Universidad de La Laguna

Escuela de Doctorado y Estudios de Posgrado

TÍTULO DE LA TESIS DOCTORAL

Ionised gas flows in the Orion Nebula: properties and environmental dependences

---

AUTOR/A

JOSE EDUARDO	MENDEZ	DELGADO

DIRECTOR/A

César Antonio	Esteban	López

CODIRECTOR/A

JORGE	GARCIA	ROJAS

DEPARTAMENTO O INSTITUTO UNIVERSITARIO

FECHA DE LECTURA

23/09/22

UNIVERSIDAD Ð LA LAGUNA
Departamento de Astrofísica

Universidad de La Laguna

Ionised gas flows in the Orion Nebula: properties and environmental dependences

A dissertation submitted by
José Eduardo Méndez Delgado
in partial fulfilment of the requirements for the degree of
Doctor of Philosophy in Astrophysics

INSTITUTO Ð ASTROFISICA Ð CANARIAS
september 2022

Examination date: 23 September, 2022
Thesis supervisor: Dr. César Esteban
Thesis co-supervisor: Dr. Jorge García-Rojas

ISBN: xx-xxx-xxxx-x
Depósito legal: TF-xxxx/2022

To my beloved parents Ricardo and Margarita.
For your unconditional support.

Resumen

Esta tesis doctoral está dedicada al análisis de los objetos Herbig-Haro (HHs) de la región central de la Nebulosa de Orión y su impacto en el gas ionizado circundante. Los HHs son chorros de gas colimados, eyectados desde protoestrellas. Aunque sus propiedades físicas y mecanismo de excitación han sido extensamente estudiados en nubes de gas neutro, la situación no es la misma con respecto a los HHs inmersos en regiones H II. El estudio de estos últimos objetos requiere el uso de espectroscopía de alta resolución espectral para poder separar su emisión de la radiación nebular de fondo, usando el corrimiento Doppler. En este trabajo, empleamos principalmente espectros de alta resolución espectral obtenidos con el espectrógrafo *Ultraviolet and Visual Echelle Spectrograph* (UVES) del *Very Large Telescope* (VLT) e imágenes de alta resolución espacial del *Telescopio Espacial Hubble* (HST). Nuestros esfuerzos se centraron en HH529II, HH529III, HH204 y HH514, objetos localizados a diferentes distancias de la estrella ionizante principal de la Nebulosa de Orión, θ^1 Ori C, y con diferentes velocidades aparentes de propagación. Nuestro análisis confirma que el mecanismo de excitación principal de estos HHs es la fotoionización, a diferencia de sus contrapartes presentes en las nubes de gas neutro, excitadas por calentamiento por choques. Esta característica nos permitió analizar la muestra seleccionada como regiones H II a pequeña escala. Por ello, pudimos determinar sus propiedades físicas, cinemáticas y abundancias químicas con un nivel de detalle sin precedentes. Con las imágenes del HST y la información cinemática, hemos determinado las trayectorias tridimensionales de estos objetos, localizando su posible origen en distintas zonas de formación estelar de la Nebulosa de Orión. El impacto local de los HHs en el gas fotoionizado es importante, ya que incrementan fuertemente la densidad local y disminuyen el grado de ionización. Estos fenómenos repercuten en las abundancias químicas obtenidas en regiones limitadas de la Nebulosa de Orión cuando se emplean espectros de resolución espectral intermedia o baja, donde se mezclen las distintas

componentes cinemáticas. Los resultados de este trabajo se publicaron en una serie de tres artículos en las revistas científicas arbitradas *Monthly Notices of the Royal Astronomical Society* y *The Astrophysical Journal*, que se presentan en sendos capítulos de la presente tesis doctoral.

Abstract

This PhD thesis is dedicated to the analysis of Herbig-Haro objects (HHs) in the central region of the Orion Nebula and their impact on the surrounding ionised gas. HHs are collimated gas jets ejected from protostars. Although their physical properties and excitation mechanism have been extensively studied in neutral gas clouds, those HHs immersed in H II regions have been less explored. The study of these latter HHs require the use of high spectral resolution spectroscopy in order to separate their emission from the strong nebular background, using their Doppler shift. In this work, we mainly use high spectral resolution spectra from the *Ultraviolet and Visual Echelle Spectrograph* (UVES) of the *Very Large Telescope* (VLT) and high spatial resolution *Hubble Space Telescope* (HST) imaging. We focus on HH529II, HH529III, HH204 and HH514, located at different distances from the main ionising star of the Orion Nebula, θ^1 Ori C, and showing different apparent propagation velocities. Our theoretical and observational analysis confirms that photoionisation is the main excitation mechanism of these HHs, in contrast with their counterparts immersed in neutral gas clouds, which are excited by shock heating. This fact allowed us to analyse the selected sample of HHs as small-scale H II regions. Therefore, we were able to determine their physical properties, kinematics and chemical abundances with an unprecedented detail. With the HST imaging and kinematic data, we determined the three-dimensional trajectories of these HHs, locating their possible origin within the star-forming areas of the Orion Nebula. The local impact of HHs on the photoionised gas is important, since they strongly increase the local density and decrease the degree of ionisation. These phenomena have an important impact on the chemical abundances obtained in limited regions of the Orion Nebula when intermediate or low spectral resolution spectra are used and the different kinematic components can not be resolved. The results of this thesis have been published in a series of three articles in the peer-reviewed scientific journals *Monthly Notices of the Royal Astronomical*

Society and *The Astrophysical Journal*. These papers are presented as separate sections of this PhD Thesis.

Contents

1

Introduction

Si el Señor todo poderoso me hubiera consultado antes de embarcarse en la creación, le habría recomendado algo más simple.
Alfonso X "El sabio"

1.1 H II regions: a physical overview

H II regions are gaseous nebulae where massive star formation has taken place. They are usually located in the spiral arms of the late type galaxies and are originated from the gravitational collapse of molecular clouds that give rise to the star formation (Karttunen et al. 2017). Within each H II region, the most massive young stars (of O or early B spectral type) excite and ionise the surrounding gas through the emission of intense ultraviolet radiation. The ionised gas emits a large number of emission lines, mainly arising from collisional excitation of metallic[a] ions as well as HI and HeI recombination lines (Osterbrock & Ferland 2006).

The optical emission spectra of H II regions reveal the physical processes that are present within the gas, for instance: the Doppler shift and width of the emission lines reveal the kinematic structures and gas flows; the ratio of line intensities allows us to determine the electron density, $n_{\rm e}$, the electron temperature, $T_{\rm e}$, and the relative abundance of the ions. The Balmer and Paschen jumps in the continuum emission allow us to calculate the global $T_{\rm e}$ of the ionised volume. The study of these properties is important to understand the physics of each H II region in particular and their global analysis in the

[a] We define metal as any element with an atomic number greater than 2.

galactic context allow us to understand the formation and evolution of their host galaxies.

The basic physical principles assumed to directly determine $n_{\rm e}$, $T_{\rm e}$ and the chemical composition of the H II regions from their optical spectra –also applicable to other photoionised nebulae– are the photoionisation and thermal equilibria.

The photoionisation equilibrium is the balance reached between the ionisations caused by the radiation of the hot stars and the recombination of the free electrons with the available ions. Although elements with higher atomic number could potentially release and recapture more electrons, their abundances represent <1% of the gas, even in the most metallic regions observed in the Milky Way (Méndez-Delgado et al. 2022a) and therefore the photoionisation equilibrium is dominated by H and He. On the other hand, the thermal equilibrium is the balance between phenomena that heat and cool the gas. In this case, metals play an important role as major coolants since their atomic structures make them very sensitive to collisional excitations.

1.1.1 Photoionisation equilibrium

Fig. 1.1 shows a simplified scheme of an H II region defined by a volume where the hydrogen is totally photoionised. The central star will emit photons at all frequencies with a spectral energy distribution that depends on its effective temperature, T_{eff}. As a first approximation, let us consider that the gas is composed exclusively of H. The photons of a certain frequency ν, emitted by the star, will cause a rate of photoionisations equal to the availability of neutral[b] H ($n(\mathrm{H}^0)$), multiplied by the number of ν-photons[c] ($\frac{4\pi J_\nu}{h\nu}$), multiplied by the probability that these photons actually ionise the gas[d] (a_ν). When the H is excited, it rapidly decays to its ground atomic state (Storey & Hummer 1995). Therefore, only those photons with $h\nu \geq 13.6$ eV, the energy threshold for photoionisations from the ground level, are able to ionise the H. For those photons with $\nu < \nu_0$, $a_\nu = 0$. Now, if we want to know the total number of photoionisations that the central star will cause per cubic centimetre per second, we need to sum up the contribution of all the photons with energies $\nu \geq \nu_0$. Since the emissivity of the star is a continuous function of ν, the sum becomes an integral:

$$\text{Rate of photoionisations } [\mathrm{cm}^{-3}\ \mathrm{s}^{-1}] = n(\mathrm{H}^0) \int_{\nu_0}^{\infty} \frac{4\pi J_\nu}{h\nu} a_\nu(\mathrm{H}^0) d\nu. \qquad (1.1)$$

[b] $n(\mathrm{H}^0)$ is the number of neutral H atoms per unit of volume
[c] J_ν is the mean intensity of radiation and h the Planck's constant
[d] a_ν is the ionisation cross section.

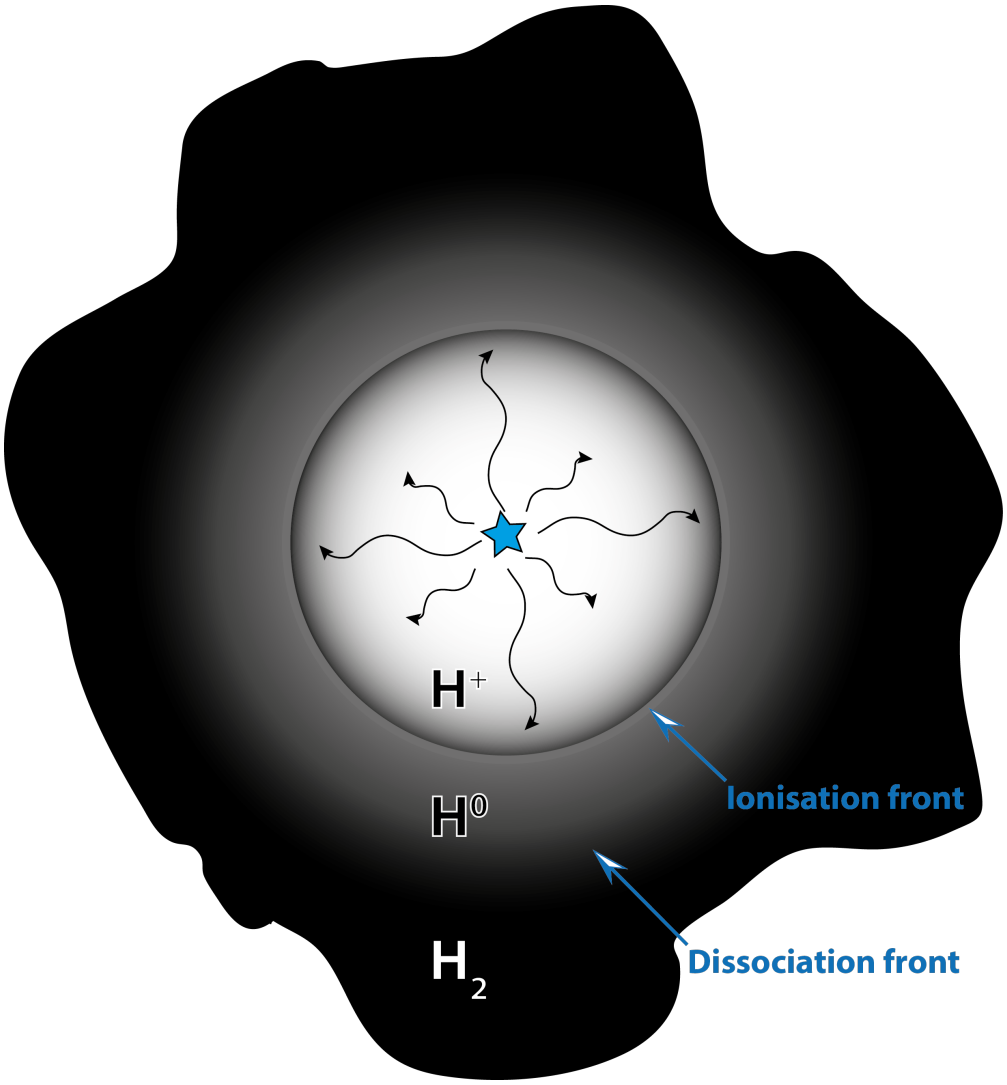

FIGURE 1.1— A simplified representation of an H II region. The central hot star ionises the surrounding H up to a certain radius. Beyond this limit, the ionisation front, the H remains neutral up to the dissociation front, where the H start to be found in molecular form.

When a photon with frequency $\nu > \nu_0$ ionises a H atom, it is expelled with a kinetic energy equal to $h(\nu - \nu_0)$. This electron quickly collides elastically with the cloud of free electrons created by other photoionisations, sharing the kinetic energy and reaching a Maxwell-Boltzmann distribution of velocities (Osterbrock & Ferland 2006). This velocity distribution is parameterised by T_e, the electron

temperature. The greater the average velocity of the free electrons, the greater $T_{\rm e}$.

The free electrons tend to recombine with the available ions. The rate of recombinations will be equal to the available number of electrons[e] ($n_{\rm e}$) multiplied by the available number of ions ($n(\mathrm{H}^+)$) and the probability that they will actually recombine[f] (included in $\alpha(\mathrm{H}^0, T_{\rm e})$). The faster electrons are harder to recapture than the slower ones. Thus, as $T_{\rm e}$ becomes greater, the chances of recombination, $\alpha(\mathrm{H}^0, T_{\rm e})$, decrease. Therefore:

$$\text{Rate of recombinations } [\mathrm{cm}^{-3}\ \mathrm{s}^{-1}] = n_{\rm e} n(\mathrm{H}^+) \alpha(\mathrm{H}^0, T_{\rm e}). \tag{1.2}$$

The photoionisation equilibrium condition is satisfied if:

$$n(\mathrm{H}^0) \int_{\nu_0}^{\infty} \frac{4\pi J_\nu}{h\nu} a_\nu(\mathrm{H}^0) d\nu = n_{\rm e} n(\mathrm{H}^+) \alpha(\mathrm{H}^0, T_{\rm e}). \tag{1.3}$$

When the radiation field of ionising photons travels through the gas, along a direction s, part of it is absorbed. Once the gas is ionised, electronic recombinations to the ground level of H produce the emission of photons with $h\nu \geq 13.6$ eV. Therefore, the change of the specific intensity of radiation of frequency ν (I_ν) along s will be equal to the decrease of I_ν due to absorptions plus the addition of the ionising radiation field produced by the recombinations, represented by[g] (j_ν). Therefore

$$\frac{dI_\nu}{ds} = -n(\mathrm{H}^0) a_\nu I_\nu + j_\nu. \tag{1.4}$$

The absorption of photons along a radius r from the source of the photons is proportional to the relative abundance of photon absorbers ($n(\mathrm{H}^0)$) and to (a_ν). This quantity is known as the optical depth:

$$\tau_\nu(r) = \int_0^{r'} n(\mathrm{H}^0, r') a_\nu dr'. \tag{1.5}$$

If the optical depth is low, the photons can travel a longer distance before being absorbed. In one of the limit cases, known as the optically thin case, the optical depth is low enough so the diffuse radiation field produced by recombinations to the ground level of H can freely escape, and therefore $j_\nu \approx 0$. In this case, in Eq. 1.3, $\alpha = \alpha_A$, where recombinations to all levels, including the ground

[e] $n_{\rm e}$ is the number of free electrons per unit of volume

[f] $\alpha(\mathrm{H}^0, T_{\rm e})$ is the total recombination coefficient, equal to the sum of the specific recombination coefficients $\alpha_{n^2L}(\mathrm{H}^0, T_{\rm e})$ for all the considered n^2L levels.

[g] j_ν is the local emission coefficient.

level, are considered. In the other extreme case, known as optically thick case, the diffuse radiation field can not longer escape, but is absorbed immediately after being emitted[h]. In this case, the total number of photons produced by the diffuse radiation field is equal to the number of recombinations to the ground level. Therefore, in this case, in Eq. 1.3, $\alpha = \alpha_B = \alpha_A - \alpha_{1^2S}$.

Integrating Eq. 1.3 for the radius r that separates the photoionisation boundary (the ionisation front from Fig. 1.1) from the central ionising star, we obtain the size of the ionised volume, known as the Strömgren sphere (Strömgren 1939):

$$r_{\text{Strömgren}} = \left(\frac{3R^2 \int_{\nu_0}^{\infty} \frac{\pi F_\nu(R)}{h\nu} d\nu}{n(\mathrm{H}^+) n_e \alpha\left(H^0, T_\mathrm{e}\right)} \right)^{\frac{1}{3}}, \tag{1.6}$$

where R is the radius of the ionising star[i]. The idealisation of the Strömgren sphere is only possible if there is enough material to ionise as shown in Fig. 1.1, which is known as a radiation-bounded nebula. The opposite case is known as a density-bounded nebula. The numerator inside the parenthesis of Eq. 1.6 is also defined as:

$$\frac{Q(\mathrm{H}^0)}{4\pi} = R^2 \int_{\nu_0}^{\infty} \frac{\pi F_\nu\left(R\right)}{h\nu} d\nu, \tag{1.7}$$

where $Q(\mathrm{H}^0)$ is the total number of ionising photons emitted by the star per unit of time.

He is the second most abundant element after H, representing a fraction of the order of 10% of the latter. Its ionisation potential is 24.6 eV, so photons capable of photoionise He will also be capable of photoionise H. Due to its relatively high abundance, recombinations to the ground level of He will be an important source of diffuse ionising radiation for H. Therefore, the photoionisation rates of He and H will be tightly coupled. In the case of metallic ions, Eq. 1.3 can be generalised as follows:

$$n(X^{+i}) \int_{\nu_i}^{\infty} \frac{4\pi J_\nu}{h\nu} a_\nu(X^{+i}) d\nu = n(X^{+1+i}) n_\mathrm{e} \alpha_G(X^{+i}, T_\mathrm{e}). \tag{1.8}$$

In this case, adopting the notation of Osterbrock & Ferland 2006, X^{+i} represents an element i times ionised and α_G is the recombination coefficient of the ground level. The contribution of the elements heavier than He to the diffuse radiation field is negligible due to their low abundances. The generalisation of

[h] This case is known as the "on the spot" approximation.

[i] It should be noted that $4\pi J_\nu = \pi F_\nu(R) \frac{R^2 e^{-\tau_\nu}}{r^2}$ due to the geometrical dilution and absorption of the stellar radiation.

the concept of Strömgren sphere to the real case –when considering the existence of elements heavier of H– produces that the ions are distributed in concentric volumes in the form of onion layers, as is shown in Fig. 1.2 for H and O.

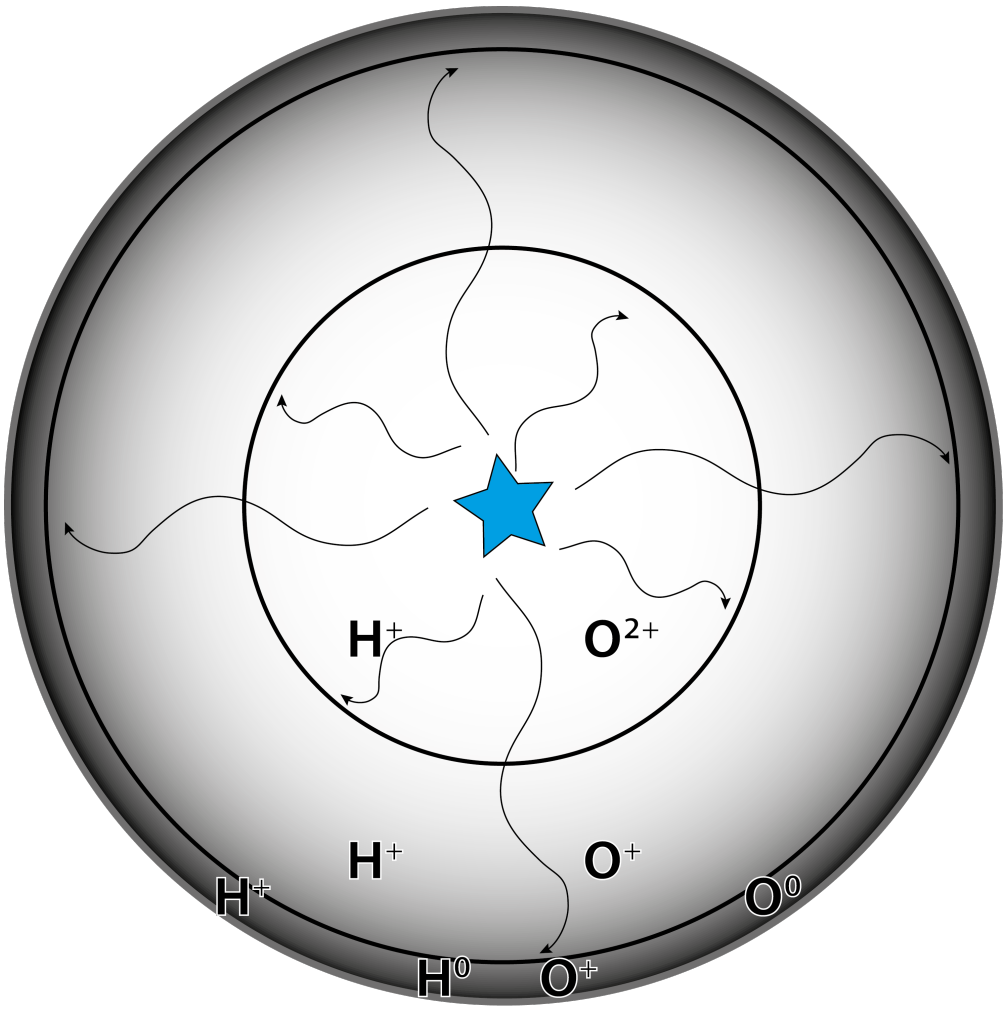

FIGURE 1.2— A simplified representation of the ionisation stratification of H and O in a spherical H II region.

1.1.2 Thermal equilibrium

As mentioned in Sec. 1.1.1, the electron temperature (T_e), parameterises the Maxwell-Boltzmann velocity distribution that is produced by collisions of free electrons produced by the photoionisations. Therefore, a change in the velocity

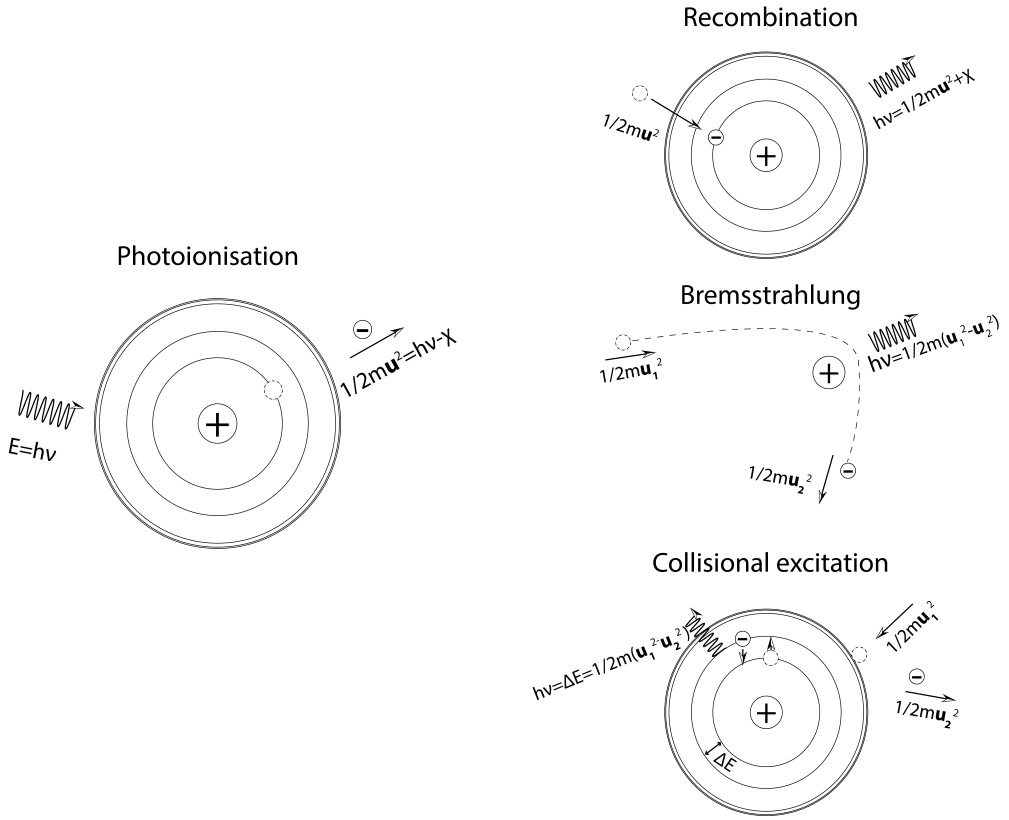

FIGURE 1.3— Representation of physical processes involved in the thermal equilibrium of a photoionised nebula. Due to photoionisations, the free electrons gain energy, whereas due to recombinations, Bremsstrahlung interactions and collisional excitations, they loose energy.

distribution of free electrons will change the characteristic temperature of the gas. As shown in Fig. 1.3, photoionisations injects energy to the free electrons system, heating it up, while basically 3 physical processes cool it down by removing part of the kinetic energy and emitting it in the form of radiation: i) the recombination process; ii) the free-free radiation or Bremsstrahlung, typically produced by the electromagnetic interaction between positive charged ions and the free electrons and, iii) the collisional excitation process, where the collisions of electrons with metallic ions are able to excite them, emitting photons produced by radiative decays.

The ionising star is the source that provides kinetic energy to the free electrons of the gas. The total energy input is the sum of the contributions of each photoionisation. As mentioned in Sec. 1.1.1, an expelled electron –a

photoelectron– will have a kinetic energy equal to $h(\nu - \nu_0)$, where ν is the frequency of the ionising photon, while ν_0 is the threshold frequency to photoionise an atom. Therefore, for the case of a pure H nebula, the energy "gain" ($G(\mathrm{H})$) will have a very similar relation to Eq. 1.1, since each photoionisation will contribute to the energy input:

$$G(\mathrm{H}) = n(\mathrm{H}^0) \int_{\nu_0}^{\infty} h(\nu - \nu_0) \frac{4\pi J_\nu}{h\nu} a_\nu(\mathrm{H}^0) d\nu. \tag{1.9}$$

Similarly to Eq. 1.2 for recombinations, the loss of energy by recombinations of H is:

$$L_R(\mathrm{H}) = n_\mathrm{e} n(\mathrm{H}^+) k T_\mathrm{e} \beta(\mathrm{H}^0, T_\mathrm{e}), \tag{1.10}$$

where $\beta(\mathrm{H}^0, T_\mathrm{e})$, the recombination cooling coefficient, integrates the probability of recombination and the energetic contribution to the emission of radiation over the Maxwell-Boltzmann velocity distribution. As in the case of the recombination coefficient, $\beta(\mathrm{H}^0, T_\mathrm{e})$ decreases its value as the temperature increases, since the faster free electrons are more difficult to recombine.

Equations 1.9 and 1.8 can be generalised to consider the presence of elements heavier than H. However, since these relationships are proportional to the abundances of the elements, only H and He have significant contributions.

The Bremsstrahlung process is also dominated by H and He, whose positively charged ions are the most numerous. According to Spitzer 1949, the energy loss produced by a given ion due to this process is:

$$L_{FF} = 1.42 \times 10^{-27} Z^2 n(X^{+i}) g_{ff} n_\mathrm{e} T_\mathrm{e}^{1/2}, \tag{1.11}$$

where $n(X^{+i})$ is the ionic abundance and Z the nuclear charge in units of charge of proton. The Gaunt factor, g_{ff}, is a function of n_e and T_e, having values between 1.0 and 1.5 (Osterbrock & Ferland 2006).

When electrons collide with other electrons, they share their kinetic energy, contributing to the establishment of a Maxwell-Boltzmann distribution of velocities. However, since the proton-electron mass ratio is ~ 1836 (Patra et al. 2018), the collision between an electron and an ion is not very efficient in moving the latter. Instead, the kinetic energy given by the electron can be used to excite the ion. The difference in energy between the ground level and the first excited level of hydrogen and helium is quite large, unlike what happens in many metal ions. In the case of the latter, the first excited energy levels are of the order of kT_e, Therefore, most of the free electrons are able to excite these metallic ions, while the hydrogen and helium can only be excited in this way by the fastest electrons, which are comparatively negligible. Therefore, although

the abundance of heavy elements is very low in gaseous nebulae, they play a fundamental role in the thermal equilibrium of the gas.

The number of collisional excitations of an ion in the ground state to an excited level is proportional to the number of free electrons (n_e), the number of ions in the base level (n_1) and the probability that it is actually excited collisionally (contained in $q_{1,2}$):

$$\text{collisional excitation rate } [\mathrm{cm^{-3}s^{-1}}] = n_\mathrm{e} n_1 q_{1,2}, \tag{1.12}$$

$q_{1,2}$ depends on the velocity of the free electrons and their Maxwellian distribution (and therefore on T_e). It is usually expressed in terms of the energy-specific collision strengths $\Omega_{1,2}(T_\mathrm{e})$ (Hebb & Menzel 1940) or the velocity-averaged collision strength $\Upsilon_{1,2}(T_\mathrm{e})$:

$$q_{1,2} = \frac{8.629 \times 10^{-6}}{T_\mathrm{e}^{1/2}} \frac{\Upsilon(1,2)(T_\mathrm{e})}{\omega_1} e^{-\Delta E/kT_\mathrm{e}}, \tag{1.13}$$

where ω is the statistical weight and ΔE the energetic threshold between levels. Once the ion is collisionally excited, two things can happen: it can decay radiatively to the ground level, or it can be collisionally deexcited. Then the equilibrium equation between collisional excitations and radiative and collisional deexcitations would be:

$$n_\mathrm{e} n_1 q_{1,2} = n_\mathrm{e} n_2 q_{2,1} + n_2 A_{2,1}, \tag{1.14}$$

where $A_{2,1}$ is the transition probability from level 2 to 1. The part of the collisional excitations that will finally contribute to the cooling of the gas is precisely that which results in the emission of radiation. Then the cooling rate by radiative excitation will be the sum of the contributions from all the ions:

$$L_C = \sum_i n_i \sum_{i>j} A_{i,j} h\nu_{i,j}. \tag{1.15}$$

The resulting thermal equilibrium is determined by Eqs.1.9, 1.10, 1.11 and 1.15:

$$G = L_R + L_{FF} + L_C. \tag{1.16}$$

To be able to solve Eq. 1.15 it is necessary to solve the complete statistical equilibrium matrix, as presented in Eq. 1.14 for a collisional system of two levels, together with the total number of ions $\sum_i n_i = n$ for each ion. The statistical equilibrium matrix for each ion is:

$$n_\mathrm{e} n_j \alpha_j(T_\mathrm{e}) + \sum_{i \neq j} n_i n_\mathrm{e} q_{i,j} + \sum_{i>j} n_i A_{i,j} = \sum_{k \neq j} n_j n_\mathrm{e} q_{j,k} + \sum_{k<j} n_j A_{j,k}. \tag{1.17}$$

The left side of Eq. 1.17 contains all the process that can populate the atomic level j: direct recombinations ($n_{\rm e} n_j \alpha_j(T_{\rm e})$), collisional excitations or deexcitations ($\sum_{i \neq j} n_i n_{\rm e} q_{i,j}$), and cascading decays ($\sum_{i>j} n_i A_{i,j}$). The right side contains the collisional and radiative processes that can depopulate level j.

1.2 Some practical examples

In the following subsections, the practical use of the equations and physical assumptions from the previous sections will be shown. These examples show intuitively the impact of the different parameters of the aforementioned equations in the determination of the physical conditions and chemical abundances of the ionised gas.

1.2.1 Typical electron temperatures of ionised nebulae.

Following Raga et al. 2020, let's consider Eq. 1.9. If we model the emissivity of the ionising star as a Planck function and we approximate the UV emissivity –the one in charge of photoionisations– by a Wien function (Raga et al. 2020), then:

$$G({\rm H}) \approx kT_{eff} \left(n({\rm H}^0) \int_{\nu_0}^{\infty} \frac{4\pi J_\nu}{h\nu} a_\nu({\rm H}^0) d\nu \right) \times \left(\frac{x_0^2 + 4x_0 + 6}{x_0^2 + 2x_0 + 2} \right), \qquad (1.18)$$

where T_{eff} is the effective temperature of the ionising star and $x_0 = h\nu_0 / kT_{eff}$. Now, assuming photionisation equilibrium (Eq. 1.3):

$$G({\rm H}) \approx kT_{eff} \left(n_{\rm e} n({\rm H}^+) \alpha({\rm H}^0, T_{\rm e}) \right) \times \left(\frac{x_0^2 + 4x_0 + 6}{x_0^2 + 2x_0 + 2} \right), \qquad (1.19)$$

on the other hand, if we consider the approximation that the cooling of the gas is produced only by the emission of the collisional excited lines $\lambda\lambda 3727, 3729$ from $\rm O^+$ then:

$$L_C(3727, 29) = n_{\rm e} n({\rm O}^+) \frac{hc}{3727 + 29} \left(q_{3727}(T_{\rm e}) + q_{3729}(T_{\rm e}) \right). \qquad (1.20)$$

It is reasonable to assume $n_{\rm e} \approx n({\rm H}^+)$. Then, considering Eq. 1.16:

$$kT_{eff} \left(\frac{x_0^2 + 4x_0 + 6}{x_0^2 + 2x_0 + 2} \right) \geq \frac{n({\rm O}^+)}{n({\rm H}^+)} \left(\frac{q_{3727}(T_{\rm e}) + q_{3729}(T_{\rm e})}{\alpha({\rm H}^0, T_{\rm e})} \right) \frac{hc}{3727 + 29}. \qquad (1.21)$$

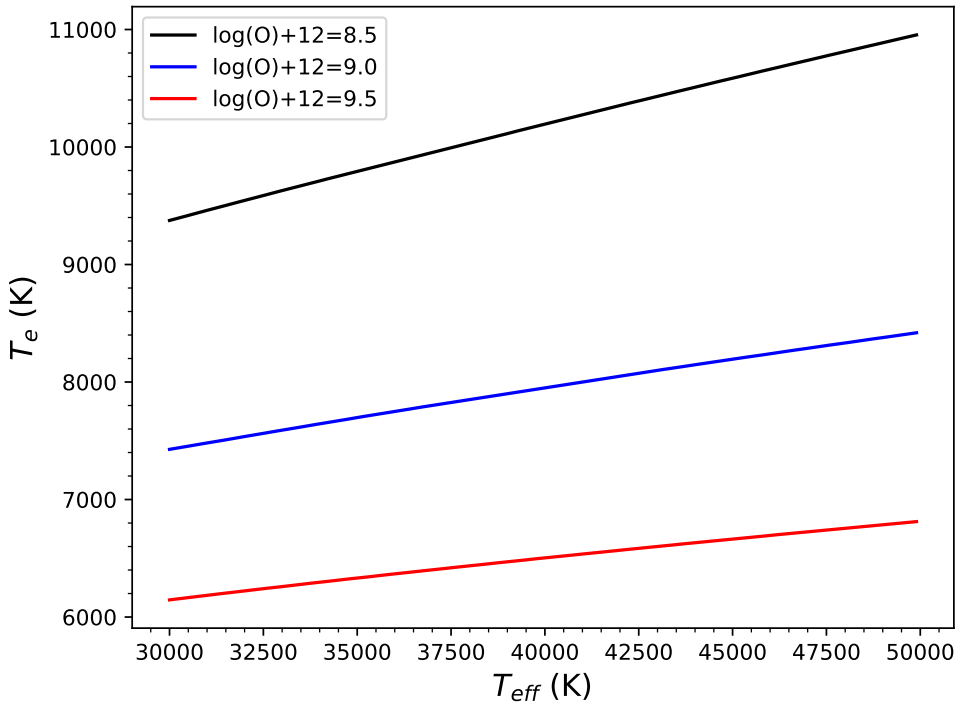

FIGURE 1.4— Electron temperature of the gas T_e as function of the effective temperature of the ionising star T_{eff} considering the case where the equality is satisfied in relation 1.21.

If we consider the case where equality is satisfied in relation 1.21, we can solve the equation by using Eq. 1.13 with the Υ and α parameters adopted from Kisielius et al. 2009 and Storey & Hummer 1995, respectively. Fig. 1.4 shows the resulting relationship between T_{eff} and T_e for different values of O abundances. It is remarkable that for a wide range of effective temperatures (from early B- to early O-type stars), the variations of T_e are relatively small. The dependence on n_e of the gas is negligible, while the dependence on the abundance of O is evident: the higher the amount of O, the lower T_e, since the gas coolers increase. Of course, this is a very simple approximation of the complete thermal equilibrium equation, since L_R and L_{FF} where not considered and it has been assumed that the cooling is only produced by O^+ ions. However, the general trend discussed above holds even with more sophisticated models that consider several metals in different ionisation stages and the contributions of L_R and L_{FF}. This is the reason why it is possible to talk of "typical electron temperatures" of ionised nebulae, assuming them to be of the order of ~ 10000

K, even if the ionising source is not well known. However, having an approximation of T_e is not enough for most of the scientific questions. It is possible to accurately determine T_e from Eq. 1.17 for some metals. An example of its use will be shown in Sec. 1.2.2.

1.2.2 Determining the physical conditions of the gas

Lets consider the single ionised nitrogen. This element has 6 electrons orbiting its nucleus, so its ground state has the configuration $1s^2 2s^2 2p^2$. Levels 1s and 2s are filled and therefore they do not contribute to the total angular momentum. The 2p level has 3 orbitals ($m_l = 1, 0, -1$) that are populated by 2 valence electrons. These electrons will prefer to be in different orbitals ($m_l = 1, 0$) with the same spin number, rather than share the orbital with opposite spins, given the electrical repulsion between particles of the same charge. This means that the total spin quantum number of the ground state will be $S = 1/2 + 1/2 = 1$. The total orbital angular momentum will be the sum of the orbital momentum of each electron in the 2p level, therefore $L = 1 + 0 = 1$. Therefore, the total angular momentum can take values of $J = |L - S|, ..., |L + S|$. According to the third Hund's rule, for an atom with less than half-filled valence shell, the level with the lowest value of J is the lowest in energy. Therefore, the term symbol[j] for the ground state of N^+ is $^3P_0$. The next level will be then $^3P_1$ and the third one $^3P_2$. These 3 levels are very close in energy, as the only difference is in J. The next excited level is where electrons fill the first orbital of the 2p level ($m_l = 1$). Following the Pauli exclusion principle (Pauli 1925), the electrons can not have all the same quantum numbers and therefore they should have opposite spin and therefore $S = 1/2 - 1/2 = 0$. In this case, since the orbital $m_l = 1$ have two electrons $L = 1 + 1 = 2$, therefore the third excited level is $^1D_2$. Following the same logic, the next excited level is $^1S_0$.

Fig. 1.5 shows an energy-level diagram for the lowest excited levels of N^+. The energies of the excited terms are of the same order of magnitude as kT_e for typical nebular temperatures ~ 10000 K. Therefore, these levels are easily populated by collisional excitations. Radiative decays can give rise to the optical lines $\lambda\lambda 5755, 6527, 6548, 6584$. The aforementioned optical lines are "forbidden" by the electric dipole interaction since they are transitions within the 2p shell, i.e. there is no change in parity [k]. These emissions occur through the magnetic dipole and/or electric quadrupole interactions. To differentiate these lines from the permited ones, they are enclosed in square brackets [N II] $\lambda\lambda 5755, 6527, 6548, 6584$. It is significant to note that not all the collisionally

[j] Defined as $^{2S+1}L_J$

[k] the parity is defined as $(-1)^l$.

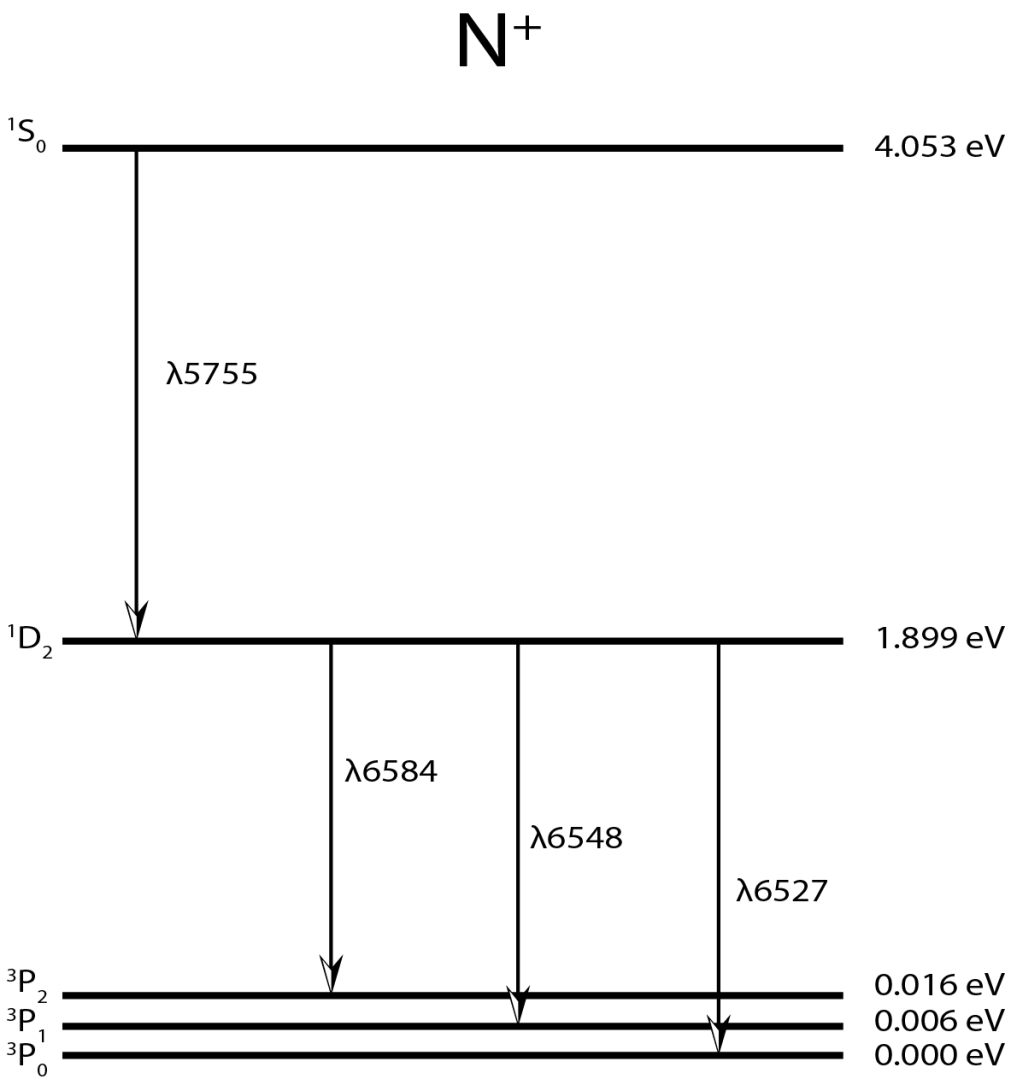

FIGURE 1.5— Grotrian diagram for the first excited levels of N^+. The energy separation of the individual levels ^3P levels has been exaggerated to be distinguishable.

excited lines are "forbidden lines". Some lines in the UV range are collisional excited but permitted lines, as C IV $\lambda\lambda 1548, 1551$.

It turns out that all ions with ground configuration np^2 and np^4 have an analogous levels ^3P, $^1D_2$ and $^1S_0$. Among them [N II], [O III], [S III], [O I] and [Ar III], being some of the most common ions found in ionised nebulae. For

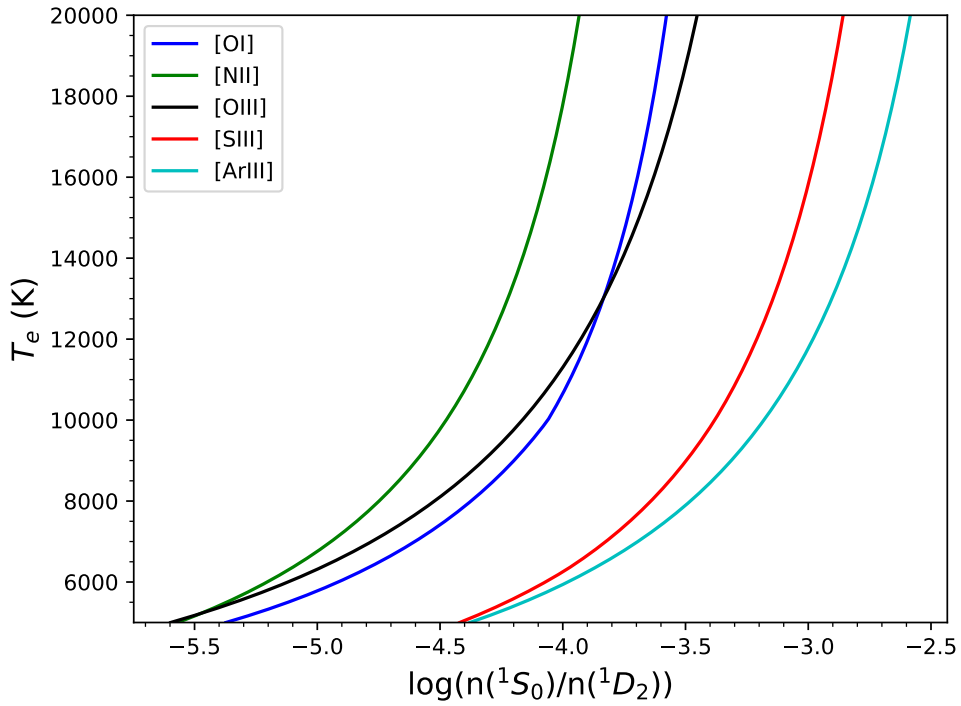

FIGURE 1.6— Ratio of the $n(^1S_0)/n(^2D_2)$ and its T_e dependence for [N II], [O III], [S III], [O I] and [Ar III] ions adopting $n_e = 100$ cm^{-3}.

these ions, the recombination term of Eq. 1.17 is only a small perturbation and can be neglected. It is necessary to adopt a set of quantum mechanically calculated transition probabilities and collision strengths to be able to solve the remaining terms of Eq. 1.17. The references to the adopted parameters are shown in Table 1.1, and the resulting ratio of the $n(^1S_0)/n(^2D_2)$ populations and its T_e dependence, considering a 5-level system with $n_e = 100$ cm^{-3}, are shown in Fig. 1.6. This result is very important since the observed flux ratio of the emission lines arising from the $n(^1S_0)$,$n(^1D_2)$ levels is proportional to $n(^1S_0)/n(^1D_2)$:

$$\frac{I(^1S_0 - ^1D_2)}{I(^1D_2 - ^3P)} = \frac{n(^1S_0)A(^1S_0 - ^1D_2)\Delta E(^1S_0 - ^1D_2)}{n(^1D_2)A(^1D_2 - ^3P)\Delta E(^1D_2 - ^3P)}. \quad (1.22)$$

Lines arising from $^1D_2 - ^3P$ transitions are named "nebular" in the literature, whereas $^1D_2 - ^3P$ and $^1S_0 - ^1D_2$ transitions are usually called "auroral" and "transauroral", respectively. Several auroral/nebular line intensity ratios,

TABLE 1.1— Atomic data set used to solve Eq. 1.17 for several ions.

Ion	Transition probabilities A	Collision Strengths (Ω)
O^0	Wiese et al. 1996	Bhatia & Kastner 1995
O^+	Froese Fischer & Tachiev 2004	Kisielius et al. 2009
S^+	Podobedova et al. 2009	Tayal & Zatsarinny 2010
Cl^{2+}	Fritzsche et al. 1999	Butler & Zeippen 1989
O^{2+}	Wiese et al. 1996, Storey & Zeippen 2000	Storey et al. 2014
N^+	Froese Fischer & Tachiev 2004	Tayal 2011
S^{2+}	Froese Fischer et al. 2006	Grieve et al. 2014
Ar^{2+}	Mendoza 1983, Kaufman & Sugar 1986	Galavis et al. 1995

such as [N II] $I(5755)/I(6584)$ or [O III] $I(4363)/I(5007)$, can be observed and be used as T_e diagnostics. Since the ionisation structure of the Strömgren sphere can be stratified as onion layers, as shown in Fig. 1.2, the different T_e-diagnostics may reflect the conditions present into different volumes of ionised gas. Now, the auroral/nebular ratios begin to have important variations with density if the collisional deexcitations are important in one or more excited levels in comparison to the radiative decays. The critical density n_c of an excited level is then defined as:

$$n_c = \frac{\sum_{i>j} A_{i,j}}{\sum_{i\neq j} q_{i,j}}. \tag{1.23}$$

n_c is higher for higher levels, since the energetic threshold required to excite them collisionally is higher while radiative decays are very important. In those cases where the gas density is much higher than the critical density of the levels involved, it is necessary to have a precise estimation of n_e to obtain an accurate estimation of T_e.

To determine n_e, it is possible to use the ratio of some lines emitted from ions with ground configuration np^3, such as S^+, O^+ or Cl^{2+}. Following Hund's rules and the Pauli exclusion principle, it is obtained that the terms of the ground and first excited levels of these ions are $^4S_{3/2}$, $^2D_{5/2}$, $^2D_{3/2}$, $^2P_{1/2}$,$^2P_{3/2}$, which are represented in Fig. 1.7 for O^+. The fact that the energy differences between the $^2D_{5/2} - ^2D_{3/2}$ or $^2P_{1/2} - ^2P_{3/2}$ is rather small, makes the line ratios coming from those levels sensitive only to the transition probabilities and/or collisional deexcitation rates, and hence to density.

In Fig. 1.8 some density-sensitive line ratios are shown, adopting $T_e = 10000$ K. To solve Eq. 1.17, the atomic parameters shown in Table 1.1 were used. It should be noted that each line ratio are density-sensitive in different density ranges. For instance, the [O II] $I(3726)/I(3729)$ or [S II] $I(6731)/I(6716)$ ra-

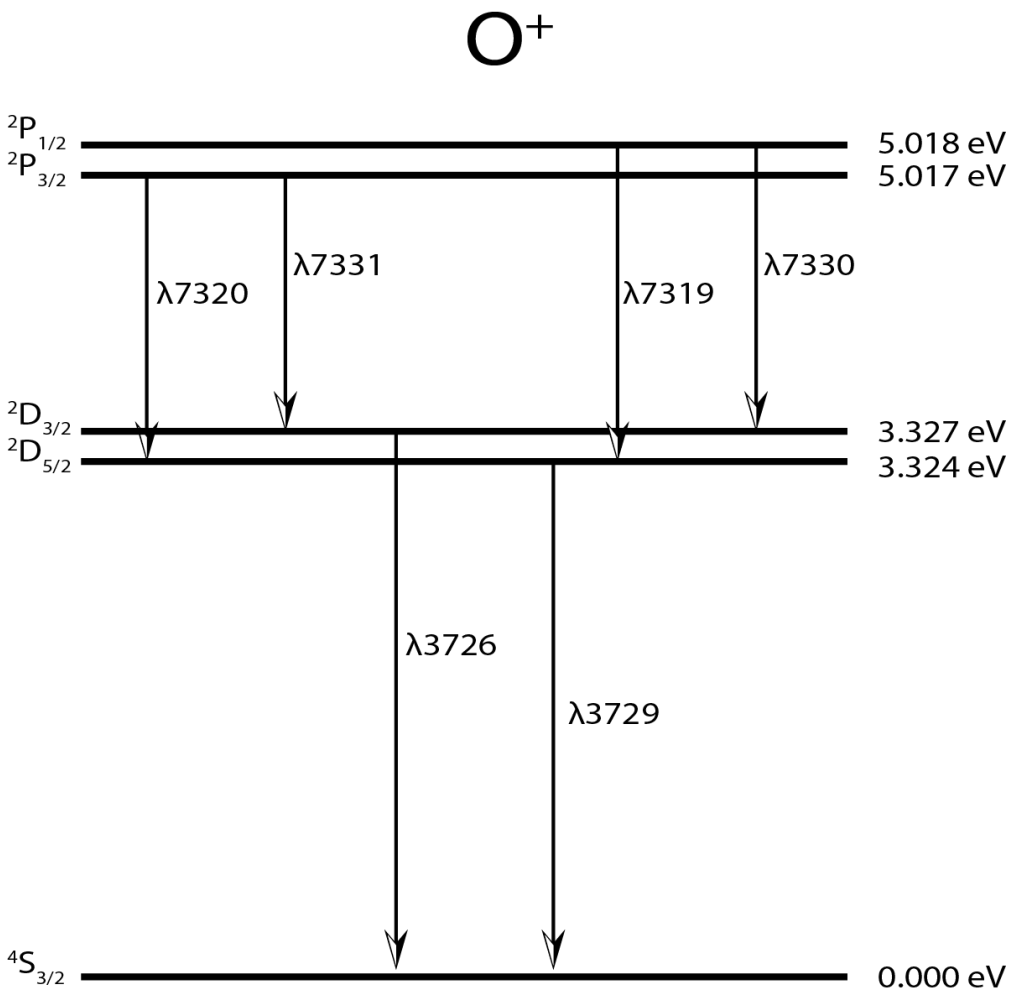

FIGURE 1.7— Grotrian diagram for the first excited levels of O^+. The energy separation of the individual ^2P and ^2D doublets has been exaggerated to be distinguishable.

tios are not good density diagnostics if the ionised gas has a density higher than 10000 cm^{-3} or smaller than 100 cm^{-3}. On the other hand, [Cl III] $I(5538)/I(5518)$ is density-sensitive up to densities of 10^6 cm^{-3}. In addition to the different sensitivities, since each ion has a different ionisation potential, each density diagnostic may reflect the conditions of a different volume of gas. For this reason, it is not recommended to use a single density diagnostic with a single temperature diagnostic to determine the physical conditions of a nebula.

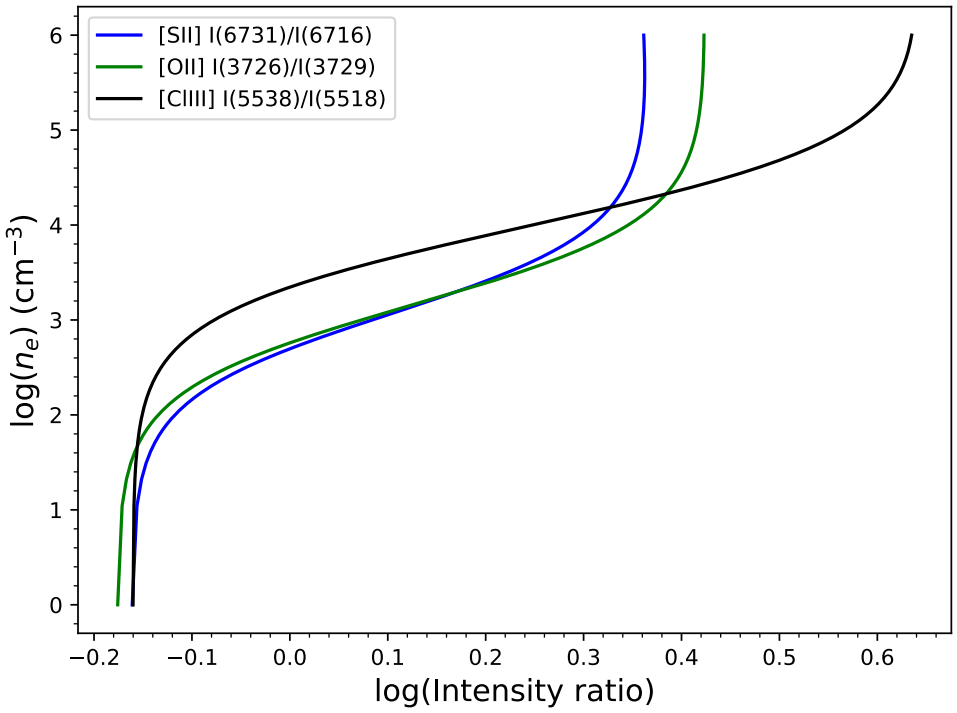

FIGURE 1.8— Line I($^2D_{3/2}$ $-^4$ $S_{3/2}$)/I($^2D_{5/2}$ $-^4$ $S_{3/2}$) ratios and their n_e dependence for [O II], [O II] and [Cl III] adopting $T_e = 10000$ K.

It is preferable to use multiple diagnostics, creating "plasma diagnostics plots", where the dependence on temperature and density is plotted as a function of observed intensity ratios. The crossing zones between the different diagnostics will give the representative physical conditions of the different volumes of ionised gas integrated in the nebular spectrum.

Fig. 1.9 shows a plasma diagnostic plot for the Orion Nebula. It was taken from Méndez-Delgado et al. 2021a, who used PyNeb (Luridiana et al. 2015) to solve Eq. 1.17 for several observed line ratios. From Fig. 1.9, it is noticeable that the density converges to a single value, whereas there seem to be 3 groups of temperatures: T_e([S II]), T_e([O II]) and T_e([N II]), representing the temperature of ions with a low degree of ionisation; T_e([O III]) and T_e([Ar III]), representing the temperature of ions with a high degree of ionisation and T_e([S III]) representing ions with an intermediate degree of ionisation.

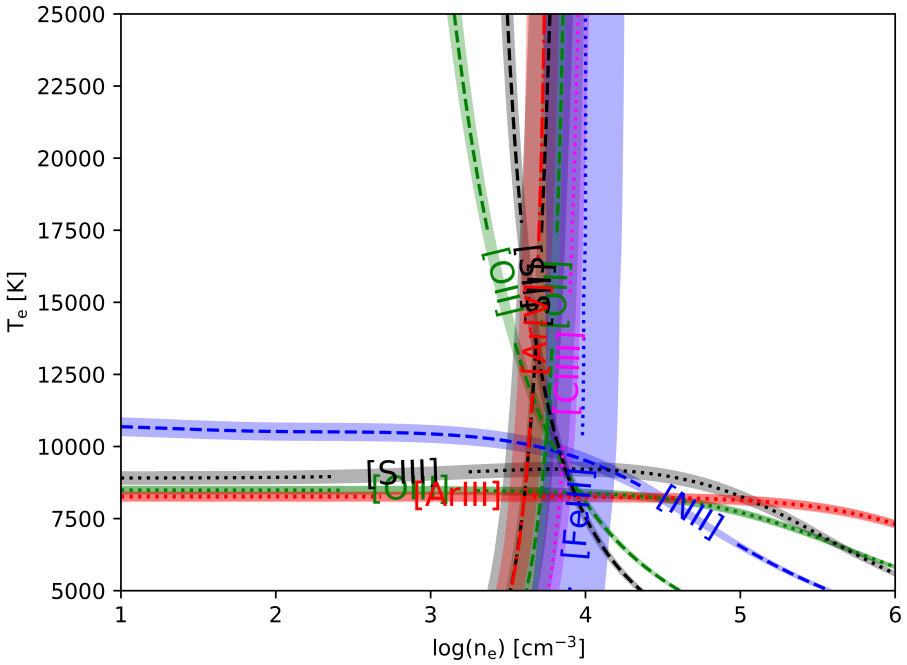

FIGURE 1.9— Plasma diagnostic plot of the Orion Nebula, taken from Méndez-Delgado et al. 2021a.

1.2.3 Deriving the chemical composition of the gas

Once the physical conditions of the gas have been determined, the abundances of the different ions can be derived. It is common to determine the relative abundance of metallic ions with respect to hydrogen using the observed intensity of CELs and Hβ, as it is shown in Eq. 1.24 [l]. In this case, there is an exponential dependence on T_e introduced by Eq. 1.13.

$$\frac{I_\lambda(X^{+i})}{I_{H\beta}(H^+)} = \frac{4861.32}{\lambda(X^{+j})} \frac{n_\lambda(X^{+i}) A_\lambda(X^{+i})}{n_e \alpha^{eff}(H\beta)} \frac{n(X^{+i})}{n(H^+)}. \tag{1.24}$$

It is also possible to obtain the relative abundances from the intensity ratio of recombination lines (RLs). In this case, the dependence with the

[l] λ is the wavelength of the emitted line, whereas $n_\lambda(X^{+i})$ is the density of X^{+i} in the excited state whose radiative transitions produce the emission of radiation of wavelength λ. This equation is valid if both ions are emitting their lines within the same line of sight Δs

physical conditions is small. Although the effective recombination coefficient, $\alpha^{eff}(X^{+i})$, depends on a power of T_e, the RL ratios reduce or cancel that dependency. Since the emissivity of the RLs depends linearly on n_e, the RL intensity ratios cancels this dependence as shown in Eq. 1.25.

$$\left(\frac{I_\lambda(X^{+i})}{I_{\lambda'}(Y^{+j})}\right)_{\rm RLs} = \frac{\lambda'(Y^{+j})}{\lambda(X^{+j})}\frac{\alpha^{eff}(X^{+i})}{\alpha^{eff}(Y^{+j})}\frac{n(X^{+i})}{n(Y^{+j})}. \tag{1.25}$$

Once the relative ionic abundances are determined, it is possible to obtain the total abundances of some elements by summing up the contributions of their ionisation stages. However, some ions do not emit optical lines or their emission is affected by telluric sky emissions or absorptions or other observational problems. In these cases it is necessary to use theoretical or empirical models called ionisation Correction Factors (ICFs) to calculate the contributions of the unseen ions, as shown in Eq. 1.26. ICFs are estimated from results of photoionisation models or use recipes based on similarities in ionisation potentials and/or depletion patterns to predict the relative abundances of the unseen ions based on other observed ions.

$$n(X) = \text{ICF} \times \left(\sum_{(\text{observed } i)} n(X^{+i})\right). \tag{1.26}$$

1.3 A more complex overview of an H II region

The physical idealisations mentioned previously are very useful to understand the main physical processes of the ionised nebulae. However, real nebulae are more complex than Strömgren spheres. Detailed observations with high spatial resolution of H II regions have revealed a wide variety of internal structures such as photoevaporating protoplanetary disks (proplyds), bowshocks, knots and jets. Fig. 1.10 shows a more realistic view of a real H II region, having several ionising stars, proplyds and high-velocity flows.

In the Orion Nebula, the existence of collimated outflows as Herbig-Haro objects (HHs) has been established decades ago (Taylor & Munch 1978; Canto et al. 1980). Since the first images of the Hubble Space Telescope (HST), the number of their identifications has grown significantly, being subject of several studies (O'Dell et al. 1993; O'Dell et al. 1997a; O'Dell et al. 1997b; Bally et al. 1998; Henney et al. 2007). These HHs have large differences with respect to their counterparts located in neutral (non-ionised) environments, since the intense ionising radiation field of the Orion Trapezium dominates the gas excitation, frequently having a negligible shock contribution in their emission

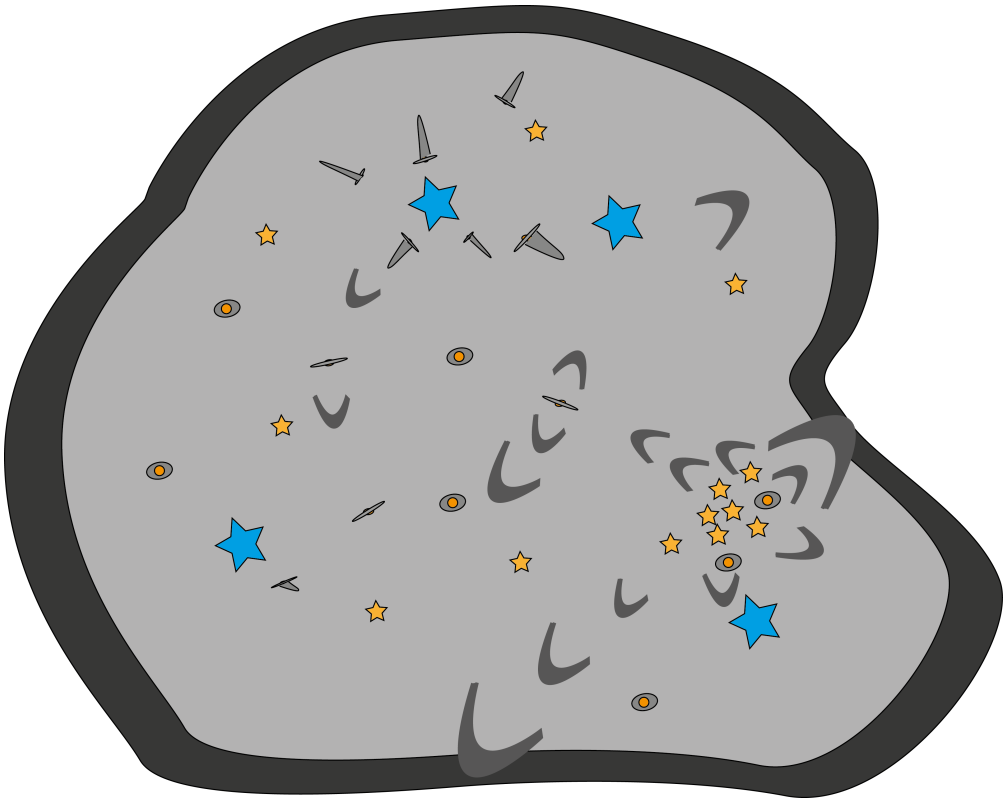

FIGURE 1.10— Representation of an H II region with several internal features as young stellar objects (yellow stars), proplyds (disks with tails) and high-velocity flows (arcs). Several hot stars, represented in blue, are responsible for the gas ionisation.

line spectra. However, the shocks produced by the supersonic flows associated with HH objects are able to compress the gas, increasing the local n_e and decreasing the degree of ionisation (Henney 2002; Mesa-Delgado et al. 2009). In addition, shocks are capable of destroying dust grains, releasing depleted metals to the gaseous phase in different ionisation stages (Blagrave et al. 2006; Mesa-Delgado et al. 2009; Méndez-Delgado et al. 2021a; Méndez-Delgado et al. 2021b). Although the impact of shocks on the physical conditions and chemical composition derived in the nebulargas is still not completely understood, the evidence indicates to be rather important (Mesa-Delgado et al. 2008; Núñez-Díaz et al. 2012).

1.3.1 Herbig-Haro objects

HHs are nebulae with relatively collimated shapes. They were initially observed by George Herbig and Guillermo Haro (Herbig 1950; Herbig 1951; Haro 1952; Haro 1953) in a dark region at the south of the Orion Nebula. Fig. 1.11 shows these first discovered objects, named as HH 1 and HH 2.

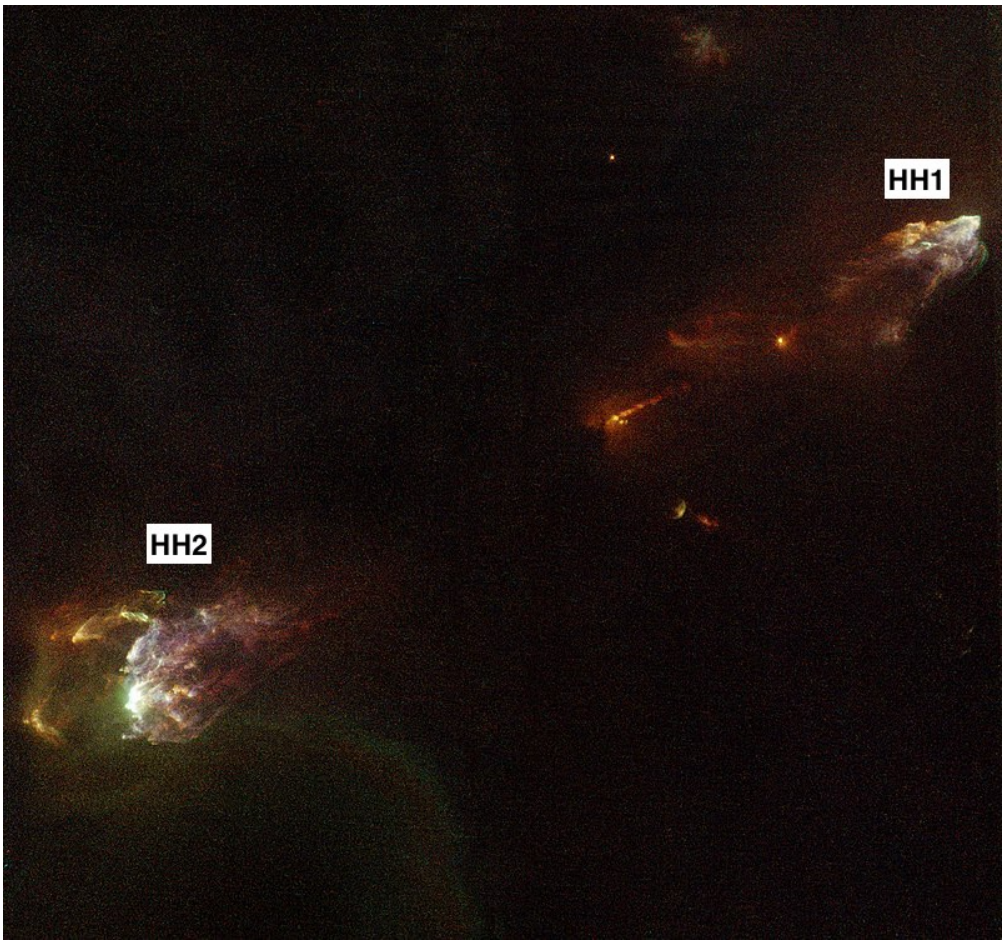

FIGURE 1.11— HST/WFC3 image of HH1-2, located at the south of the Orion Nebula. Image Credit: NASA/ESA Hubble Space Telescope WFC3 Instrument: Wide-field Camera 3 Filters: F373N, F487N, F631N, F656N, F673N (Raga et al. 2015).

The spectra of HH1/2, as well as those from the HHs found in neutral environments, differs from what is usually found in photoionised regions and their excitation source was matter of debate for the first 25 years since their discovery (Schwartz 1983). A pioneering work from Osterbrock 1958 suggested that the

dominant excitation mechanism in HH1/2 could not be the radiative processes present in photoionisation conditions, but the collisional ionisation caused by an energetic outflow from a newborn star, given the partial ionisation of hydrogen. The recognition of the similarity of the spectra of supernova remnants with those of the prototypical HHs allowed to establish that the main source of excitation were the radiative shocks created from the interaction of a supersonic stellar mass outflow with the ambient gas (Schwartz 1975; Schwartz 1983). The connection between mass outflows and young stars is well established (Mundt 1985), leading to the conclusion that there is a relationship between HHs and star formation (Canto 1985). Nowadays, it is widely accepted that their launch mechanism occurs via magneto-centrifugal interactions between the surface of an accretion disc and its associated protostellar object (Reipurth & Bally 2001; Nisini et al. 2018). Although HHs are bipolar outflows, the geometric orientation, extinction or asymmetries in the distribution of the surrounding gas or in the launch mechanism can make only one of its sides detectable.

Due to their supersonic velocities, the HHs give rise to shocks with the surrounding environment. After the shock passage, the gas is heated from T_0 up to a temperature T_1 (Zel'dovich & Raizer 1967). As shown in Eq. 1.27 for a non-magnetic shock, T_1/T_0, will depend on the Mach number, $\mathcal{M}$, which is the ratio of the propagation velocity V_{sh} and the preshock sound speed c_s. T_1 will be higher for shocks where the relative propagation velocity is higher, as the amount of kinetic energy realised by the shock increases.

$$\frac{T_1}{T_0} = \frac{1}{16}\left(5\mathcal{M}^2 - 1\right)\left(1 + 3\mathcal{M}^{-2}\right). \tag{1.27}$$

In addition to the increase in temperature, the shock front compresses the gas, increasing the density as it is shown in Eq. 1.28.

$$\frac{n_1}{n_0} = \frac{4\mathcal{M}^2}{\mathcal{M}^2 + 3}. \tag{1.28}$$

Once heated, the gas cools down through radiative emission, forming a cooling zone whose extension is proportional to $n_{\rm e}^{-1}$ (Hartigan et al. 1987). Through these strong emissions, some HHs can be very bright in comparison to their surrounding neutral clouds. On the other hand, in the presence of a magnetic field, the parallel component to the shock front increases the gas pressure by magnetic cushioning (Hartigan et al. 1994), although its treatment is far more complicated than what is shown in Eqs.1.27 and 1.28 (Bazer & Ericson 1959).

Although the existence of a large number of Young Stellar Objects (YSOs) and protoplanetary disks within H II regions ensures the existence of HHs in

the interior of these ionised nebulae, they are less noticeable than their neutral counterparts. They usually camouflage their emission with that of the nebular gas when low spectral/spatial resolution is used. In these HHs, the UV radiation field from the ionising stars plays a fundamental role in their excitation mechanism, in addition to the kinetic energy released by the shock. If the photoionisation dominates in these HHs, the physical concepts described in Sec. 1.1 can be applied directly, analogously to a small-scale H II region (Reipurth & Bally 2001).

The shock contribution to the observed flux should be equal to the kinetic energy released (Henney 2002):

$$F_{sh} = \frac{1}{2}\mu m_H n_0 V_{sh}^3, \tag{1.29}$$

where μ is the mean atomic mass per particle and m_H the hydrogen mass. For irradiated HHs, the radiative flux from the photoionisation equilibrium gas should be equal to:

$$F_{ph} = n_2^2 \Lambda_0 H, \tag{1.30}$$

where n_2 is the post-shock density of the gas in equilibrium, H the thickness of the working surface and Λ_0 the cooling coefficient (Henney 2002). After the shock, the gas forms a Mach ring (Falle & Raga 1993) due to the lateral pressure gradients, whose radius is approximately the jet radius, r_{jet}. By considering the isothermal Mach number ($\mathcal{M}_s = \gamma^{1/2} V_{sh}/c_s$) and the Bernoulli equation, it is found that:

$$H = \frac{1}{2}\frac{e^{1/2} r_{jet}}{\mathcal{M}_s}. \tag{1.31}$$

By using Eqs.1.29, 1.30 and 1.31 and $\Lambda_0 = 2.5 \times 10^{-24}$ erg cm^3 s^{-1} (Osterbrock & Ferland 2006), it is obtained:

$$\frac{F_{sh}}{F_{ph}} = 195 \times \mathcal{M}_s^2 \times \left(\frac{n_2}{\mathrm{cm}^{-3}}\right)^{-1} \times \left(\frac{r_{jet}}{10^{-3} pc}\right)^{-1}. \tag{1.32}$$

In principle, by using Eq. 1.32 it is possible to determine whether the shock contribution is small enough to treat irradiated jets as small-scale H II regions. However, determining $\mathcal{M}_s$ can be tricky, given the existence of internal shocks inside some outflows (Raga et al. 1990), making the measured propagation velocities upper limits to the relative velocity. On the other hand, it is important to point out that, although in some cases F_{sh}/F_{ph} is not negligible, the shock effects on the optical spectra can be negligible. For instance, a $\mathcal{M}_s \sim 5$ ($V_{sh} \sim 70$ km s^{-1} within the ionised gas) in the Orion Nebula would represent a post-shock temperature of ~ 70000 K (Eq. 1.27). For these conditions,

the cooling zone is mainly emitting FUV lines of high-ionisation ions (Méndez-Delgado et al. 2021a), whereas the optical spectrum is dominated by the gas in photoionisation equilibrium.

1.4 Goals of this thesis

The main objective of this thesis is to determine the physical properties and the impact on the surrounding environment of HH529II, HH529III, HH204 and HH514, HHs located in the brightest photoionised zone of the Orion Nebula, also known as the Huygens Region (Huygens(1659). The selection of these objects considers their location at different distances from the main ionising star (θ^1 Ori C), flow velocities and origin, parameters potentially relevant. The following are the specific objectives:

- Estimate the main excitation mechanism of the HHs within the photoionised gas of the Orion Nebula.
- Determine the shock heating contribution from the HHs to the local temperature of the gas.
- Verify the existence of density and/or temperature inhomogeneities within the HHs.
- Quantify the destruction of dust grains through the estimation of the gaseous abundances of Fe/H and other refractory elements.
- Compare the chemical composition of the HHs and the Orion Nebula to analyse differences in the composition of the destroyed dust grains.
- Calculate the impact of the presence of the HHs in the local ionisation degree of the gas.
- Study the implications on the derived global physical conditions and chemical abundances of having different kinematic components when low spectral resolution spectra are used.
- Reveal the most likely origin of the high-velocity jets and its relationship to the different star-forming areas within the Orion Nebula.
- Establish a relationship between the destruction of dust and the propagation velocity of the HHs.

The HHs of the sample cover a range of apparent distances between 14 and 150 arcsecs ($27 - 300 \times 10^{-3}$ pc by adopting a distance of 410 pc for the Orion Nebula (Binder & Povich 2018)) from the main ionising source, θ^1 Ori C. Their upper limits to the propagation velocity are between 70 and 135 km s^{-1}. Therefore, these HHs cover an important diversity of ionisation and propagation conditions, on which some phenomena explored in this thesis may depend.

The observational data used in this thesis are high spectral resolution spectra ($\lambda/\Delta\lambda \approx 6.5$ km s^{-1}) taken with the Ultraviolet and Visual Echelle Spectrograph (UVES) (D'Odorico et al. 2000) at the Very Large Telescope (VLT) and high spatial resolution images taken from 20 years of archival of HST imaging.

The optical emission of the Orion Nebula is not static, since as the gas is ionised, its emission is blueshifted with respect to the Orion Molecular Cloud (OMC) (Kaler 1967; Fehrenbach 1977; Goudis 1982; O'Dell & Wen 1992). However, the high spectral resolution of UVES allows to measure the spectra of the HHs of the sample, independently of the Orion Nebula emission, given the differences in their radial velocities.

The importance of this thesis transcends the field of HH objects and seeks to be the starting point to study the impact of the internal structures of star forming regions. H II regions are the basis of many studies on the formation and evolution of galaxies. Therefore, a paradigm shift in their study may also change the way we understand galactic systems. There are several open problems in the study of the chemical composition of H II regions that may be related, at least partially, to an oversimplification of the treatment of their internal structures. For instance, the discrepancy between the chemical abundances derived with RLs and CELs, being those based on RLs always higher, also known as the Abundance Discrepancy (AD) Problem. The typical value of the discrepancy of about a factor 2 measured in H II regions (García-Rojas & Esteban 2007) could be related to internal temperature fluctuations (t^2) , as proposed by Peimbert 1967 more than 50 years ago. However, the phenomena that cause t^2 are not clear and photoionisation models fail to reproduce it. This may be due, at least partially, to the neglect of shock heating, chemical inhomogeneities, mixture of different kinematic components with different ionisation and physical conditions introduced by the presence of HHs.

The thesis is organised as follows: in Chapter 1 the physical-mathematical formalism and the objectives of this thesis are presented; in Chapter 2 the steps of the reduction and analysis of the observational data are shown; in Chapters 3, 4 and 5 we show the results published in scientific journals Q1 on HH529II, HH529III, HH204 and HH514. Finally, in Chapter 6 we summarise the conclusions and future perspectives on this topic.

2

Optical spectra reduction

This chapter provides details on the reduction and analysis of the UVES spectra, observed with the VLT, on which the results of this thesis are based.

2.1 The observational sample

The spectroscopic observations were taken in service mode between October and November 2013 with the UVES spectrograph at the UT2 of the VLT as part of the program 092.C-0323(A), PI: Adal Mesa-Delgado. In addition to HH529II, HH529III, HH204, and HH514, the program also includes observations of HH202N, HH203, HH518, HH529I and HH625. These last objects will be part of the future works. HH514 is a micro-jet ejected from a nearby protoplanetary disk (170-337), whereas the rest of the sample are well defined bowshocks. These HHs were selected attempting to their brightness, distances of the main ionising source (θ^1 Ori C) and propagation velocities. The HHs were observed under photometric conditions, with the exception of HH514 and HH625, which were observed under clear conditions. The slit positions of the observed HHs are shown in Fig. 2.1. The slit width was set to 1" to achieve a spectral resolution of ~ 6.5 km s^{-1}, whereas the effective spatial coverage is 10".

UVES is a two-arm cross-dispersed spectrograph, so the blue arm covers the wavelength range 3000-4995Å, whereas the red one the range 4785-11000Å. The red arm uses two CCDs and the spatial coverage is slightly larger (12"). Two dichroic beam splitters are used to cover the full spectral range, which is divided into 6 sections, as described in Table 2.1. Due to the physical separation of both CCDs in the red arm, the spectral ranges 5773–5833 and 8540–8650Å

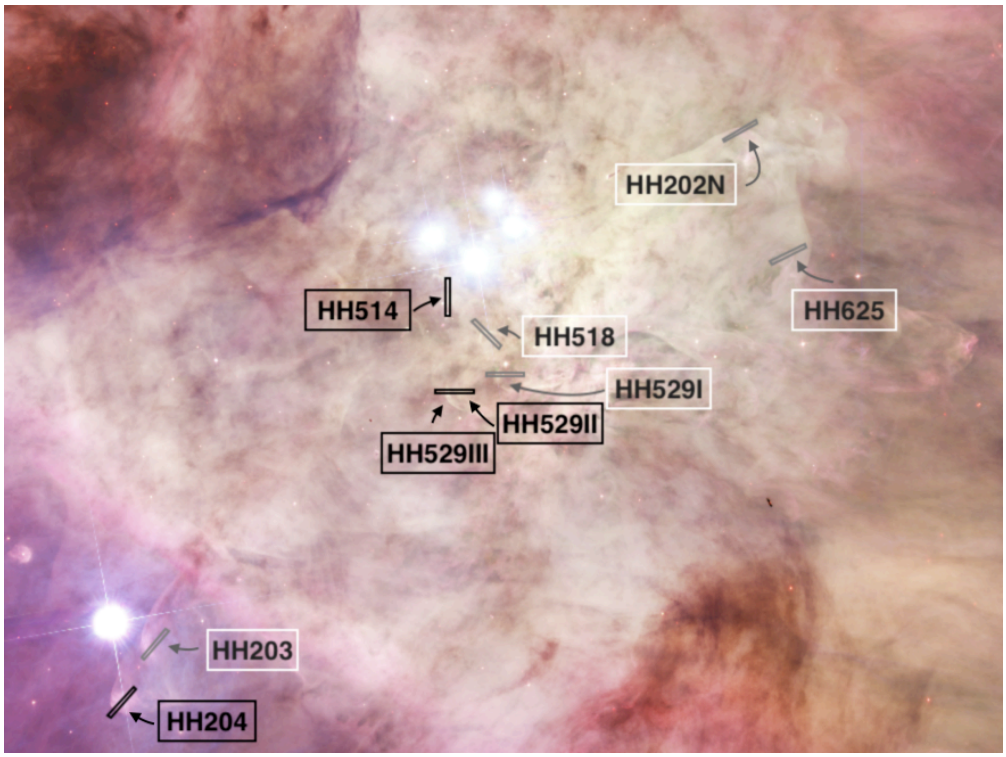

FIGURE 2.1— Composite RGB image from the Orion Nebula indicating the slit positions of the observed HHs of the ESO/UVES 092.C-0323(A) program. The HHs analysed in this thesis are marked in black while the rest are marked in grey. Acknowledgments: NASA, ESA, M. Robberto (Space Telescope Science Institute) and the Hubble Space Telescope Orion Treasury Project Team

can not be observed. Furthermore, since the redmost spectral orders do not fit entirely within the CCD, there are small gaps at the reddest wavelengths, which are: there are the following gaps: 8911–8913, 9042–9046, 9178–9182, 9317–9323, 9460–9469, 9608–9619, 9760–9774, 9918–9935, 10080–10100 and 10248–10271Å. The spatial resolutions are 0.246"/pixel and 0.182"/pixel for the blue and red arm, respectively. Given the wide spectral range covered and the high spectral and spatial resolutions required in the study of the HHs, an atmospheric dispersion corrector (ADC) (Avila et al. 1997) was used during the observations.

2.2 Getting the data

The European Southern Observatory (ESO) makes available all the public data taken from its telescopes in the following webpage: `http://archive.eso.org/`

TABLE 2.1— Wavelength coverage of each UVES arm.

Arm	Wavelength range (Å)
Blue Arm Dichroic #1	3000 - 3885
Blue Arm Dichroic #2	3750 - 4995
Red Arm Dichroic #1 lower CCD	4785 - 5773
Red Arm Dichroic #1 upper CCD	5833 - 6805
Red Arm Dichroic #2 lower CCD	6700 - 8540
Red Arm Dichroic #2 upper CCD	8650 - 11000

`eso/eso_archive_main.html`. The best way to request the data is night by night, in order to not mix the different calibration files (such as BIAS, FLATS or lamp observations). In Fig. 2.2 the request of the data of HH203 and HH518 (taken during the night of 2013-11-27) is shown. Besides the night, the program ID and the instrument are specified. At this point, it is only necessary to search for the science files and all observations of HH203, HH518 and GD71 will be listed. This last object is the calibration star. All the listed data must be requested.

As shown in Fig. 2.3, it is possible to download the associated calibration files after requesting the science files. Although the ESO portal allows you to download some processed calibrations (as combined masterbias or masterflat files), I do not recommend their use, since they were created automatically without individual supervision. The possible use of corrupt calibration files can lead up to introduce systematic observational errors. After completing the download, we will have several UNIX compressed ".Z" files that should be uncompressed.

2.3 Preparing the files

Several dead pixels have been detected in the UVES CCDs, which are not sensitive to incident radiation. If they are only a few, this problem can be solved by creating pixel masks, that extrapolate the flux values detected in the neighbouring pixels. Since there are three CCDs in UVES, it is necessary to classify the data set according to its corresponding CCD. This can be done with Image Reduction and Analysis Facility (IRAF) (Tody 1993), a set of software packages developed for the astronomical data reduction. It is possible to manage IRAF from the command language of Python via PyRAF, making it easy to write scripts with joint python and IRAF packages. Using the package "imhead" of IRAF it is possible to read the header information of the images and group them according to their CCD of origin. Once each group is established, it is

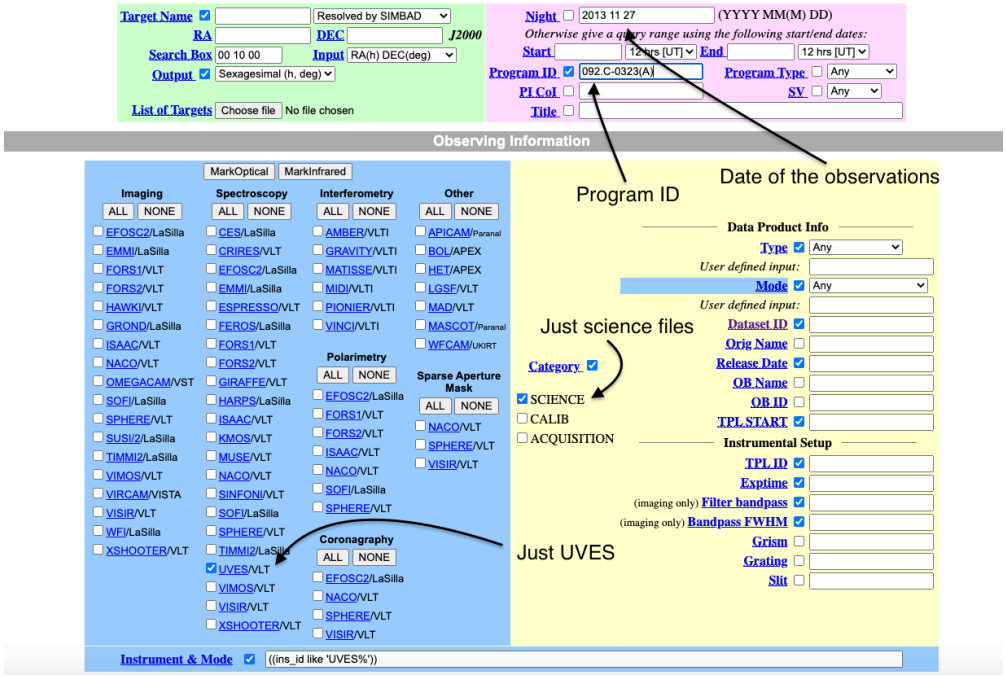

FIGURE 2.2— ESO internet portal for downloading observational data. To request the data of HH203 and HH518, the program ID, the date of interest and the instrument are specified. Only science observations are searched at this point.

FIGURE 2.3— ESO portal for the selection of the science data. In addition, the raw associated calibration files are requested.

possible to automatically fix the dead pixels with the IRAF task "fixpix".

Due to the presence of cosmic rays in almost every astronomical observation,

several individual observations of the same science object are taken during the night. When the files are combined, the effects of cosmic rays can be removed by rejecting the extreme values of the combined pixels. To combine the science files, the first step is to classify them by using the "imhead" information. In the 092.C-0323(A) program, the calibration star GD71 is classified as science object in the files header. Special care must be taken with this object, since it may be observed several times during the night in order to analyse it under different air mass conditions. Once the science observations were grouped, by object, exposure time and air mass in each configuration, it is possible to combine them with the "imcombine" task of IRAF. As mentioned previously with the calibration files, it is essential to take a look at the images before combining them. For instance, the file UVES.2013-11-28T04:09:21.467.fits from HH203 is totally defective, being probably saturated. If it is not manually removed, imcombine is unable to discard its influence.

2.4 From echellograms to wavelength calibrated spectra

Before having a wavelength calibrated spectrum, several steps are needed. For instance, the bias and flat correction, as well as the trace and extraction of the echelle orders and the wavelength calibration. For this purpose, the ESO UVES pipeline (Ballester et al. 2000) under the *Gasgano* graphic user interface was used. Once the pipeline is installed, a folder named gasgano will be created with an "UVES.prefs" file. It has to be modified in order to specify the full path to the observations. As shown in Fig. 2.4, *Gasgano* will automatically load and classify the input files. This pipeline has several recipes that require specific input files to do a specific task.

2.4.1 Reduction steps

- **Combining bias files**. It is possible to combine the bias files with the "uves_cal_mbias" recipe. Those files of the blue and red arm must be combined independently. This task gives as result a MASTERBIAS file for each configuration.

- **Estimating the approximate trace of the echelle orders and their wavelength coverage**. The recipe "uves_cal_predict" can generate tables with the approximate trace and wavelength coverage of the echelle orders by using observations from a ThAr lamp and a reference table. The results of this step allow automatising the order extraction and wavelength calibration of the spectra. The recipe requires the following files as

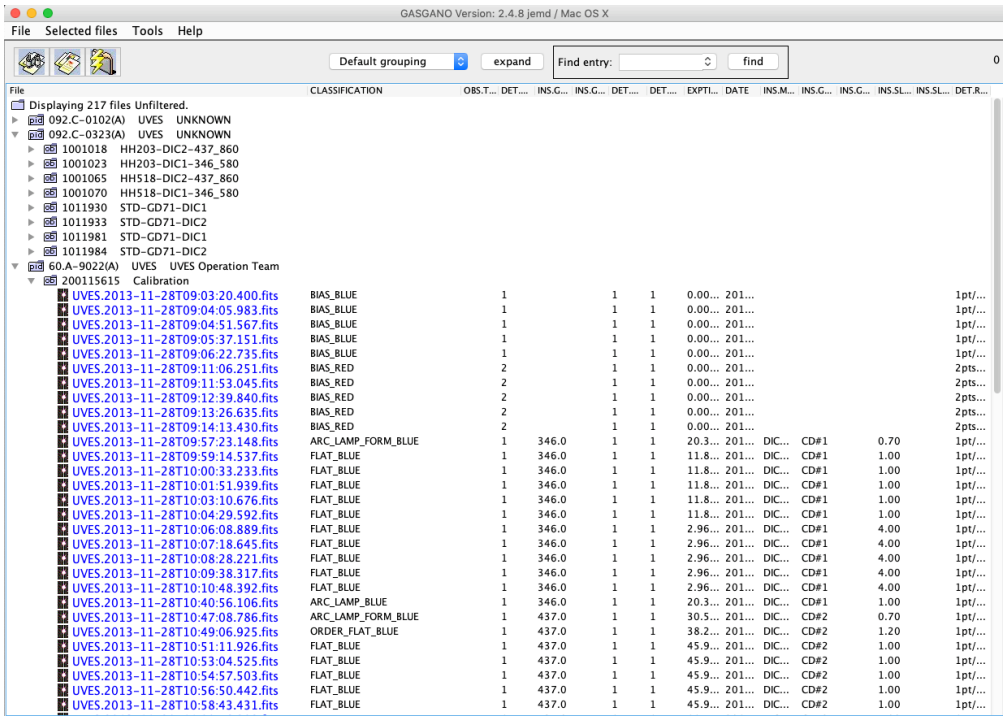

FIGURE 2.4— Overview of the UVES pipeline under *Gasgano*. The files of the input folder are automatically classified as calibration or science files.

input: MASTERBIAS, ARC_LAMP_FORM and LINE_REFER_TABLE. These first two files must be grouped according to their arm and dichroic configuration. The output files are the ORDER_GUESS_TABLE and LINE_GUESS_TABLE.

- **Estimating the precise echelle order positions**. The "uves_cal_orderpos" recipe measures the precise position of the echelle orders by using an UVES narrow slit observation of a continuum lamp. The input files are the ORDER_GUESS_TABLE and MASTERBIAS files obtained in previous steps as well as the ORDER_FLAT file, which is the continuum lamp observations. The output file of this step is a table of the echelle orders, ORDER_TABLE.

- **Combining flats**. The "uves_cal_mflat" recipe generates a combined flats file for each arm and dichroic configuration. It also subtracts the bias from the flat frames and determines the mean exposure level over the orders. It uses as input, besides the flat files, the MASTERBIAS and

the ORDER_TABLE files. In the case of the blue arm, there are two types of flat files, the standard ones and those named DFLAT files. These latter ones are optimised for the bluest region of the spectra. It is necessary to combine both blue flat groups separately and then combine them with the "uves_cal_mflat_combine" recipe to obtain the blue arm MASTERBIAS.

- **Determining the precise wavelength calibration of each order**. The recipe "uves_cal_wavecal" estimate the precise wavelength calibration of the echelle orders by using an ARC_LAMP observation together with the resulting files of the previous steps: MASTERBIAS, MASTERFLAT, LINE_GUESS_TABLE, ORDER_TABLE and the LINE_REFER_TABLE. The recipe subtracts the MASTERBIAS and divide the ARC_LAMP by the MASTERFLAT. Then the lamp spectrum is extracted using the ORDER_TABLE file that contains the echelle order positions. After this, the emission lines are detected in the extracted spectrum and their relationship with the LINE_GUESS_TABLE and LINE_REFER_TABLE is established. The wavelength calibration solution output is saved in a LINETABLE file.

- **Extracting and calibrating the science spectra**. Once we have the MASTERBIAS and MASTERFLAT files as well as the tables with the position and the wavelength calibration of the echelle orders, it is time to extract the science spectra (which includes the standard star). It is performed with the "uves_obs_scired" recipe which requires the MASTERBIAS, MASTERFLAT, ORDER_TABLE and LINETABLE files together with the science combined images (Sec. 2.3). This recipe subtracts the MASTERBIAS and divide the science files by the MASTERFLAT. The object is extracted and wavelength calibrated following the ORDER_TABLE and LINETABLE files. There are several extraction methods. The most important ones for our purposes are two: the "2D method", which extracts all the spatial coverage of the echelle orders and the "optimal" one, which fits and subtracts the sky emission and extracts a 1D spectrum. The two-dimensional extraction of the HHs is essential for our purposes, because it will allow us to define different spatial cuts to delimit the different kinematic components, maximising the HH/Orion Nebula contrast. For the calibration star GD71, it is better to choose the optimal extraction. However, it is also desirable to have a bidimensional spectrum in order to detect the presence of sky emissions, which will also be affecting the observations of the HHs. Since the echelle orders of the images are merged into a single spectrum, in

some cases there may be problems at the order boundaries. Thus, it is necessary to fix some parameters that define the extension of the overlapping of the adjacent orders. It is advisable to use the following values to the recipe parameters: "reduce.merge_delt2=4" for all the configurations and "reduce.merge_delt1=10" for the blue arm dichroic #1, "reduce.merge_delt1=12" for the blue arm dichroic #2 and the red arm dichroic #1 whereas "reduce.merge_delt1=14" for the red arm dichroic #2. These parameters define the amount in pixels of the order begin and end. Another important parameter is "reduce.ffmethod", which specify whether the flat field correction is done before or after the spectrum extraction. In all configurations except the red arm dichroic #2, it is recommended to set "reduce.ffmethod=extract" (i.e. make the flat field correction after the extraction). This method has the advantage of not introduce artifacts at the order begin and end in these configurations. In the case of the red arm dichroic #2 configuration, "reduce.ffmethod=pixel" is recommended, given the known flat-field residual fringes of this configuration.

An example of the resulting extracted spectra is shown in Fig. 2.5 for the observations of HH203 around [Fe III] λ4658 in the blue arm dichroic #2 configuration.

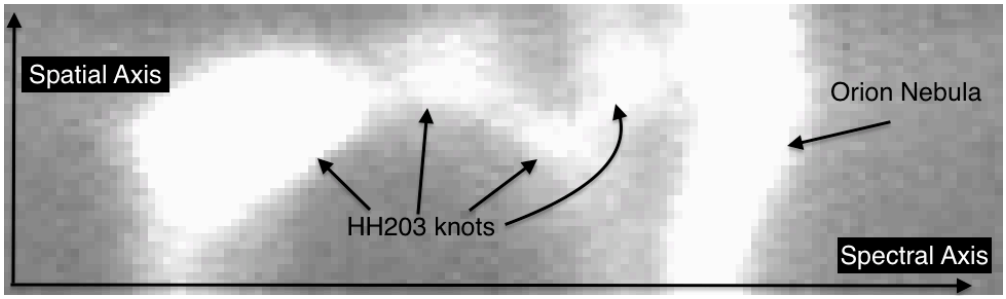

FIGURE 2.5— 2D spectrum extracted around [Fe III] λ4658 from the observations of HH203 in the blue arm dichroic #2 configuration.

2.5 Spatial cuts and flux calibration

In the bidimensional wavelength calibrated science spectra, the different kinematic components are evident and the HHs can be easily delimited. As shown in Fig. 2.5, contrary to the Orion Nebula emissions, which extend along the entire spatial axis with a relatively homogeneous shape and velocity, the HHs

have well-separated bullet shapes. This allows delimiting the spatial areas that contain the total HH emission, maximising the contrast with respect to the nebular emission. Before spatially extracting the HHs, it should be considered that the spatial coverage of the red arm spectra is 12" while that of the blue arm is 10" and that the spatial resolution of both arms is different. We have ensured the correct central alignment of the red and blue arms by checking the spatial position of the emission peak of the HHs. Approximately 5 spatial pixels must be discarded at each border of the red arm in order to limit the spatial coverage to 10". In each arm, the peak and a width of 2 or 3 sigma of the spatial coverage of the knot emission should be delimited. After these considerations, the spatial cuts can be collapsed with the "Astropy.io" package (Astropy Collaboration et al. 2013; Astropy Collaboration et al. 2018) to create 1D spectra. This collection of python software packages is designed for the manage of astronomical data. Fig. 2.6 shows an example of the defined cuts in the bidimensional spectrum of HH529II-III and the corresponding 1D spectra. Due to differences in spatial resolution of the red and blue arms, there may be slight differences in their flux counts. However, these differences will vanish during the normalisation of the spectra with respect to the flux of the Hβ line, taking advantage of the common spectral zones of each arm (see Sec. 2.1).

The basic idea of the flux calibration is to compare the observations of the calibration star (in our case GD71) with its well-known emission distribution to derive a function that gives the instrumental counts/flux response for every wavelength at observational conditions of the night. To achieve the flux calibration of the defined 1D spectra, three IRAF packages are needed: "onedspec.standard", "onedspec.sensfunc" and "calibrate". The following steps should be followed:

- **Determining the pass-bands of the calibration star**. The IRAF "onedspec.standard" task automatically covers the instrumental flux of the observed calibration star with spectral bands of a given width. As input, it requires the tabulated flux of the calibration star, containing the central wavelength, the flux and the spectral interval width. It is also desirable to input the Paranal Observatory extinction file to make second order extinction corrections. In the interactive mode, "onedspec.standard" may show some bands that fall into areas of strong telluric absorptions or emissions. These must be removed interactively with the "d" key to prevent an spurious mapping of the flux distribution. It is also possible to create new bands with the "a" key. The output file is a table with four columns, containing the central wavelength, the flux of the calibration star, the interval widht and the instrumental flux of the CCD (in counts).

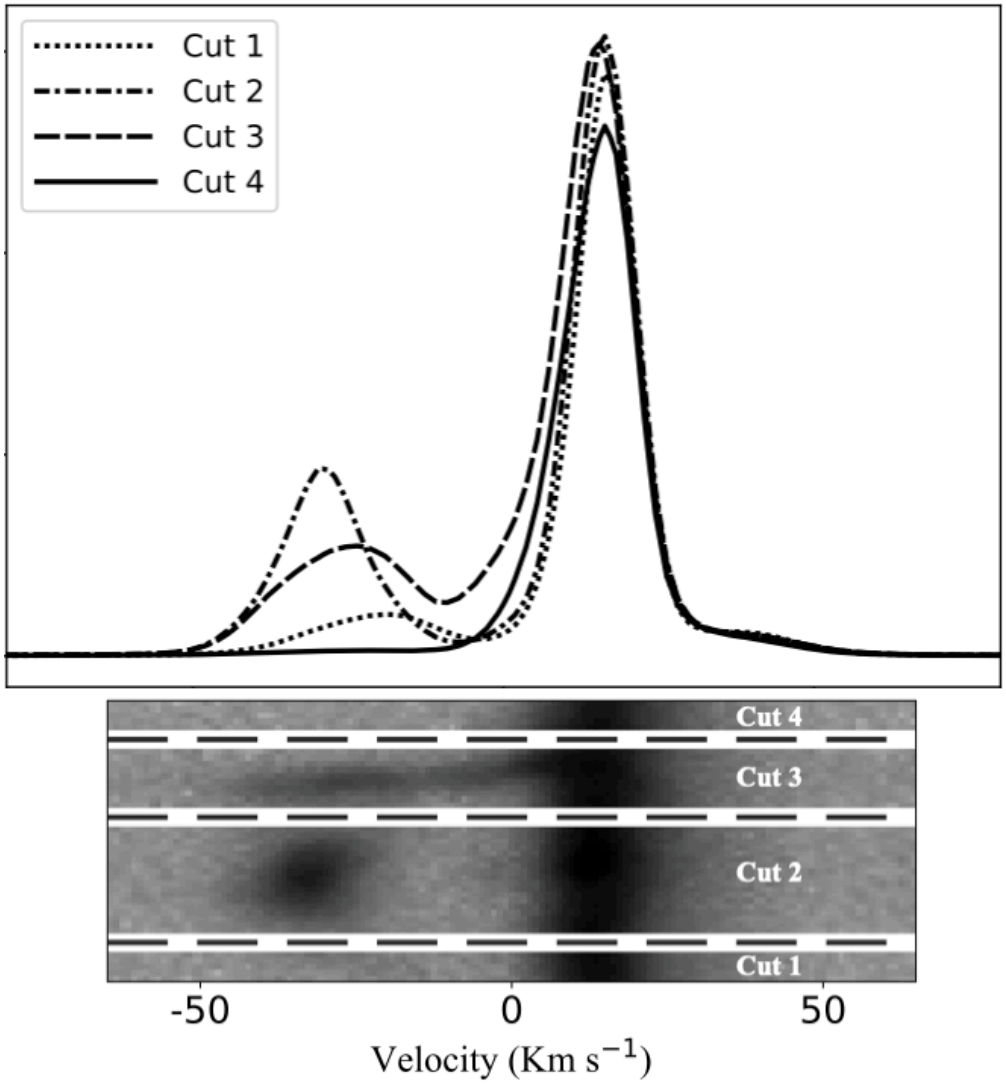

FIGURE 2.6— Comparison between the spatial cuts defined for HH529II and HH529III and the corresponding 1D spectra around [O III] λ4959. The fainter blueshifted components correspond to the emission from HHs. Figure taken from Méndez-Delgado et al. 2021a.

- **Determining the sensitivity function**. The IRAF task "onedspec.sensfunc" uses the output file from the previous step to determine the system sensitivity function for each observed wavelength. The goal of this task is to fit the observations with some polynomials such as those of Chebyshev, Legendre or spline interpolations. The interactive mode shows some graphs

containing the predefined sensitivity function, the flux calibrated spectrum and the residuals. By modifying the fitted spectral bands (which can be deleted with the "d" key) or the order of the polynomials, the sensitivity fit can be controlled. It is advisable to avoid polynomials of very high order, even if this reduces the residuals, since some abrupt changes in the flux curve may appear. The sensitivity function must be a smooth curve.

- **Flux calibrating the spectra**. By considering the airmass, the exposure time of the science images and the sensfunc output file, the task "calibrate" of IRAF determines the flux in physical units of the observed science spectra. As a control measure, it is important to perform a flux calibration of GD71. Its comparison with the tabulated flux shows differences of around 1% for the UVES spectra, being a representative percentage of the uncertainty associated with the flux calibration.

2.6 Fluxes, central wavelengths and widths of the emission lines

By using the IRAF task "splot" it is possible to estimate the flux, central wavelength and FWHM of the multiple kinematic components present in the science spectra. An example is shown in Fig. 2.7. The flux uncertainty can be estimated through a Montecarlo propagation method around the continuum noise. This can be done modifying the parameters "splot.nerrsample", "splot.invgain" and "splot.sigma0". The first one is the number of error samples, being "splot.nerrsample=100" a reasonable choice for our purposes. The second parameter is the error between the conversion of photoelectrons detected on the CCD and the flux counts registered. This quantity can be neglected in our case. The last parameter is the constant gaussian noise term, which has to be determined from the spectra. Therefore, before fitting the emission lines, it is necessary to estimate the continuum noise using the "m" key in the continuum surrounding the line. Since it is necessary to change the "splot.sigma0" parameter for each measured line, this can become a tedious and time-consuming process. However, this can be automatised in PyRAF, by creating some python routines to open the "splot" window, register the continuum noise, close the splot window, modify the splot.sigma0 parameter and reopen the "splot" window again, where it is enough just to use the "d" key to create the multi gaussian fits. In fact, it is possible to automate the search of lines by using a known list of lines (for example, those from Esteban et al. 2004), leaving the manual search for those particular lines present in the HHs that are not found in

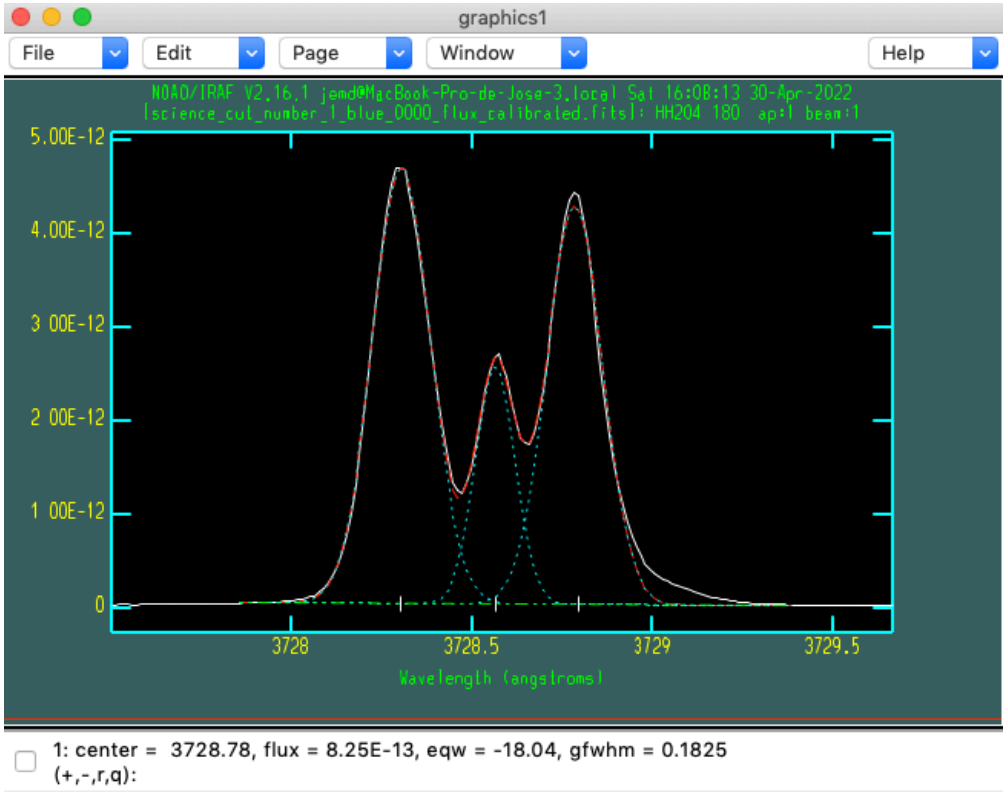

FIGURE 2.7— Multi Gaussian fit around the emission of [O II] λ3729 in one of the 1D spectra of HH204. There are three evident kinematic components: the bluest one is HH204; the central one is the Diffuse Blue Layer (DBL), one of the multiple foreground layers of gas and the main emission from the Orion Nebula.

the nebular emission (such as some [Fe II], [Fe III], [Ni II] or [Ni III] emissions). This allows obtaining detailed, carefully measured spectra of several hundred lines with several kinematic components in a reasonable amount of time.

2.7 Heliocentric motion and reddening correction.

As mentioned in Sec. 2.1, the total spatial coverage of the slit is divided into several sections for each object. These can be normalised to the Hβ flux by using the flux of H I λ3835, [O III] λ4959 and [S II] λ6731, present in the overlapping zone of each section. The normalisation of the spectrum eliminates the small differences that may exist between the spectra of the blue and red arms. Now, it is necessary to correct the spectral position of the lines due to the Earth/Sun motions. This is achieved by using the packages of Astropy "time", "units"

and "coordinates". It is necessary to specify the observed sky coordinates, date and the latitude, longitude and height of the observatory to estimate the radial heliocentric shift. Once corrected, it can be easily subtracted from the observed spectral positions, using the Doppler effect equations.

Finally, it only remains to correct for reddening due to the interstellar extinction. This was achieved by applying the Balmer decrement method using Eq. 2.1, where the left side of the equation is the corrected line intensity ratio and the right side is the measured flux ratio multiplied by 10 to the product of the extinction law ($f(\lambda)$) and the reddening coefficient, c(Hβ). We have adopted the extinction law of Blagrave et al. 2007, derived for the Orion Nebula. We calculate c(Hβ) by using the measured flux ratios of Hε, Hδ, Hγ, Hβ, Hα, P12, P11, P10, P9 and the theoretical emissivity coefficients of Storey & Hummer 1995.

$$\frac{I(\lambda)}{I(\mathrm{H}\beta)} = \frac{F(\lambda)}{F(\mathrm{H}\beta)} \times 10^{\mathrm{c}(\mathrm{H}\beta) f(\lambda)}. \tag{2.1}$$

Examples of the resulting spectra tables are shown in Tables D6, 9 and A1 from Méndez-Delgado et al. 2021a; Méndez-Delgado et al. 2021b; Méndez-Delgado et al. 2022b, shown in Chapters 3, 4 and 5, respectively.

3

HH529II-III: two prominent central bowshocks

This chapter includes the first article of the series "Photoionized Herbig-Haro objects in the Orion Nebula through deep high-spectral resolution spectroscopy", published in the Monthly Notices of the Royal Astronomical Society (MNRAS) 2021, Volume 502, Number 2, pp.1703-1739.

In this chapter, we introduce the series of papers "Photoionized Herbig-Haro objects in the Orion Nebula through deep high-spectral resolution spectroscopy" in this case dedicated to HH529II and HH529III. These are two prominent bowshocks located around 70×10^{-3} pc from θ^1 Ori C. They flow from west to east, with apparent origin in Orion South, a star-forming zone within the Orion Nebula. Since it is the first article of the series, we give a detailed introduction to the observations and methodologies used to determine the physical conditions, ionic abundances, total abundances and kinematic properties of the different kinematic components. We also lay the theoretical groundwork (summarised in Eqs. 1.29, 1.30, 1.31 and 1.32) to estimate the shock contribution to the excitation of the HHs in photoionised environments.

We find that HH529III and H529II are two bowshocks originated from the same jet beam, being HH529II an internal shock. Both high-velocity components are fully photoionised with no emission of neutral ions such as [O I] or [N I]. The shock contribution to the excitation of HH529II is up to $\sim 3\%$, whereas for HH529III it can represent up to $\sim 10\%$. Using our theoretical considerations and photoionisation models, we show that the shock excitation does not con-

tribute significantly to the optical spectrum of HH529III, as the shock-heated zone, previously at $T_e \sim 10000$ K, will reach temperatures of up to 70000 K, producing mainly UV emissions of ions such as C III] or C IV. Furthermore, optical line intensity ratios as I([O III]λ5007)/I(Hβ) or I([N II]λ6584)/I(Hα) present values consistent with photoionised regions, being very far from the range of values observed in supernova remnants and non-photoionized HHs. Therefore we treat HH529III and H529II as small-scale HII regions, adopting the formalism described in Chapter 1.

Due to the compression of the gas in HH529II and HH529III, we find very high values of the electron density, n_e, in comparison to the values found in the Orion Nebula. However, their values of T_e are basically consistent with those of the Orion Nebula, given the fixed photoionisation equilibrium. HH529II and HH529III have larger Fe abundances than the Orion Nebula, by a factor 2, given the partial destruction of dust grains in the bowshocks. We also found a slight overabundance of heavy elements (around 0.12 dex) that cannot be entirely due to dust destruction because the overabundance is also present in noble gases. This may be related to inhomogeneous gas mixing processes during the ejection of the material from the protostellar source.

By using 20 years of HST imaging, we determine the proper motions of the HHs, deriving its three-dimensional flow propagation. Given that the line emissions of HH529II have a constant radial shift, we analyse the uncertainties of the theoretical wavelengths (λ_0). We show that much of the scatter in the blister-shape kinematic structure of the Orion Nebula was due to the aforementioned λ_0-uncertainties and not to physical processes. We analyse the AD problem in each of the kinematic components, finding that temperature inhomogeneities ($t^2 > 0$) are capable to explain the AD in the nebular emission, but some additional/different phenomenon is required in the HHs.

Monthly Notices of the ROYAL ASTRONOMICAL SOCIETY

MNRAS **502,** 1703–1739 (2021) doi:10.1093/mnras/stab068
Advance Access publication 2021 January 11

Photoionized Herbig–Haro objects in the Orion Nebula through deep high-spectral resolution spectroscopy – I. HH 529 II and III

J. E. Méndez-Delgado [1,2]★ C. Esteban [1,2] J. García-Rojas [1,2] W. J. Henney [3] A. Mesa-Delgado[4] and K. Z. Arellano-Córdova [1]

[1]*Instituto de Astrofísica de Canarias (IAC), E-38205 La Laguna, Spain*
[2]*Departamento de Astrofísica, Universidad de La Laguna, E-38206 La Laguna, Spain*
[3]*Instituto de Radioastronomía y Astrofísica, Universidad Nacional Autónoma de México, Apartado Postal 3-72, 58090 Morelia, Michoacán, México*
[4]*Calle Camino Real 64, Icod el Alto, Los Realejos, E-38414 Tenerife, Spain*

Accepted 2021 January 5. Received 2021 January 5; in original form 2020 September 14

ABSTRACT

We present the analysis of physical conditions, chemical composition, and kinematic properties of two bow shocks – HH 529 II and HH 529 III – of the fully photoionized Herbig–Haro object HH 529 in the Orion Nebula. The data were obtained with the Ultraviolet and Visual Echelle Spectrograph at the 8.2m Very Large Telescope and 20 yr of *Hubble Space Telescope* imaging. We separate the emission of the high-velocity components of HH 529 II and III from the nebular one, determining n_e and T_e in all components through multiple diagnostics, including some based on recombination lines (RLs). We derive ionic abundances of several ions, based on collisionally excited lines and RLs. We find a good agreement between the predictions of the temperature fluctuation paradigm (t^2) and the abundance discrepancy factor (ADF) in the main emission of the Orion Nebula. However, t^2 cannot account for the higher ADF found in HH 529 II and III. We estimate 6 per cent of Fe in the gas phase of the Orion Nebula, while this value increases to 14 per cent in HH 529 II and between 10 and 25 per cent in HH 529 III. We find that such increase is probably due to the destruction of dust grains in the bow shocks. We find an overabundance of C, O, Ne, S, Cl, and Ar of about 0.1 dex in HH 529 II and III that might be related to the inclusion of H-deficient material from the source of the HH 529 flow. We determine the proper motions of HH 529 finding multiple discrete features. We estimate a flow angle with respect to the sky plane of $58^\circ \pm 4^\circ$ for HH 529.

Key words: ISM: abundances – Herbig–Haro objects – ISM: individual objects: Orion Nebula – ISM: individual objects: HH 529 II – ISM: individual objects: HH 529 III.

1 INTRODUCTION

Herbig–Haro (HH) objects are small emission nebulae associated with outflows from young stars interacting with the surrounding environment (Schwartz 1983). Since their discovery by George Herbig and Guillermo Haro (Herbig 1950, 1951, 1952; Haro 1952, 1953) a multitude of them have been discovered and studied. Through the *Hubble Space Telescope* (*HST*), multiple velocity features associated with HH objects have been observed in the Orion Nebula with unprecedented detail. There are several works dedicated to determine the nature and physical properties of many outflows from stars in the Orion Nebula (see Bally, O'Dell & McCaughrean 2000; Bally & Reipurth 2001; O'Dell & Henney 2008; O'Dell et al. 2015, and references therein). These have revealed that the Orion Nebula is a complex environment with multiple gas interactions. These high-velocity systems cover a wide range of velocities with noticeable differences in the conditions of their emitting gas.

Through the radiation field of the massive stars of the Orion Nebula, HH objects can be photoionized under conditions where the shock between the ambient gas and the HH merely serves to create a dense blob where we can determine the physical conditions and chemical abundances using the standard methods developed to study ionized nebulae (Reipurth & Bally 2001). Moderate velocity ($v < 100$ km s^{-1}) shocks in H II regions are predicted to be strongly radiative, showing only a thin high-T_e cooling zone immediately behind the shock, which contributes little to the total emission (Henney 2002). The bulk of the shocked gas returns to thermal equilibrium at the same T_e as the ambient gas, hence the combined front (shock plus cooling zone) can be considered isothermal. However, there are few works in the literature dedicated to analyse the chemical composition of photoionized HH objects, isolating their emission from that of the nebula in which they are immersed. Using high-spectral resolution spectroscopy, Blagrave, Martin & Baldwin (2006) and Mesa-Delgado et al. (2009) were able to separate the emission of HH 529 III+II and HH 202 S, respectively, from the main emission of the Orion Nebula. This permitted the analysis of the chemical composition of the ionized gas under the peculiar physical conditions of the HHs and the effects of their interaction with the surrounding nebular gas, such as the chemical effects of dust destruction.

As Mesa-Delgado, Esteban & García-Rojas (2008) showed through long-slit spectra, there are important spatial variations in the physical conditions of the Orion Nebula due to the presence of HH

★ E-mail: jemd@iac.es

Table 1. Main parameters of UVES spectroscopic observations.

Date	Δλ (Å)	Exp. time (s)	Seeing (arcsec)	Airmass
2013-11-29	3100–3885	5, 3 × 180	0.79	1.20
2013-11-29	3750–4995	5, 3 × 600	0.65	1.14
2013-11-29	4785–6805	5, 3 × 180	0.79	1.20
2013-11-29	6700–10420	5, 3 × 600	0.65	1.14

objects. These variations also affect some chemical properties of the gas. For example, these authors found an increase in the discrepancy between the abundances obtained from recombination lines (RLs) and collisionally excited lines (CELs) for the same heavy element at the locations of HH objects. Therefore, it is important to investigate the physical and chemical influence that HH objects exert on the gas of ionized nebula and test our knowledge of photoionized regions by analysing objects with complex conditions.

This work aims to be the first in a series devoted to the analysis of photoionized HHs in the Orion Nebula using very high resolution spectroscopy from the Ultraviolet and Visual Echelle Spectrograph (UVES; D'Odorico et al. 2000) attached to the UT2 (Kueyen) of the Very Large Telescope (VLT). This paper is dedicated to two bow shocks associated with HH 529: HH 529 II and HH 529 III. HH 529 consists of a series of shocks flowing towards the east in the central region of the Orion Nebula. It is divided into three main shocks designated as HH 529 I, HH 529 II, and HH 529 III, numbered from west to east (O'Dell & Henney 2008). We spatially separate the emission from HH 529 II and HH 529 III and isolate the blueshifted high-velocity emission of the gas of the shock from the nebular one. We analyse our high-spectral resolution observations that cover a wide spectral range (3100–10400 Å) through four spatial cuts, obtaining seven 1D spectra: four corresponding to the main emission of the Orion Nebula, one for HH 529 II, another one for HH 529 III, and one additional 1D spectrum corresponding to the sum of all the 1D spectra. This last spectrum simulates a single low-spectral resolution long-slit observation, including the mixing of the HH emission with that of the nebular gas, summing up the emission of all the velocity components for each emission line. In this paper we analyse the physical conditions, chemical composition, and kinematic properties of HH 529 II and HH 529 III as well as the Orion Nebula in several small and nearby areas.

The paper is organized as follows: in Section 2 we describe the observations and the reduction process for the spectroscopic data, as well as the *HST* imaging used to calculate the proper motions of HH 529 in the plane of the sky. In Section 3 we describe the emission line measurements, identifications, and the reddening correction as well as a comparison between our observations and those from Blagrave et al. (2006) over the common spectral range (3500–7500 Å). In Section 4 we derive the physical conditions of the gas throughout different methods, using CELs, RLs and continuum emission. In Section 5 we derive ionic abundances using both RLs and CELs. In Section 6 we describe the temperature fluctuations paradigm and estimate values of t^2, based on the different temperature diagnostics. In Section 7 we discuss the abundance discrepancy (AD) between ionic abundances derived with CELs and RLs. In Section 8 we analyse the total abundances obtained from RLs and CELs, in the second case both with and without the assumption of the existence of temperature fluctuations ($t^2 > 0$ and $t^2 = 0$, respectively). We also discuss the increase in the gaseous Fe abundance due to dust destruction in HH 529 II and HH 529 III. In Section 9 we describe the radial velocity structure of each component, both the nebular and the high-velocity ones. We also derive the electron temperature from the thermal broadening of the line profiles. In Sections 10 and 11 we calculate the proper motions of HH 529 and discuss some physical properties of the shock, such as the pre-shock density. Finally, in Section 12 we summarize our main conclusions. In the appendices, some extra information, tables, and figures are attached as Supporting Information.

2 OBSERVATIONS AND DATA REDUCTION

The observations were made under photometric conditions during the nights of 2013 November 28 and 29 using UVES in the UT2 of the Very large Telescope (VLT) in Cerro Paranal, Chile. The slit position was centred at the coordinates RA(J2000) = $05^{h}35^{m}16\overset{s}{.}80$, DEC(J2000) = $-05^{\circ}23'57\overset{''}{.}48$, with a slit length of 10 arcsec in the blue arm and 12 arcsec in the red arm in order to give an adequate interorder separation. Table 1 shows the main parameters of UVES observations. The slit width was set to 1 arcsec, which provides an effective spectral resolution $\lambda/\Delta\lambda \approx 40\,000$ (6.5 km s^{-1}). To perform the flux calibration of the data, three exposures of 150 s of the standard star GD71 (Moehler et al. 2014a, b) were taken under similar conditions of seeing and airmass than the science observations during the same night. The spatial coverage of the slit is shown in Fig. 1.

Our observations cover the spectral range between 3100 and 10420 Å, using two standard dichroic settings of UVES. Dichroic #1 setting splits the light in two wavelengths ranges: from 3100 to 3885 Å in the blue arm and from 4785 to 6805 Å in the red one, while the dichroic #2 setting covers from 3750 to 4995 Å in the blue arm and from 6700 to 10420 Å in the red one. However, in our high-resolution and wide spectral range observations, there are some observational gaps. The red arm uses two CCDs, and due to their physical separation, spectral ranges 5773–5833 and 8540–8650 Å could not be observed. Additionally, there are some narrow gaps that could not be observed in the redmost part of the red arm in the dichroic #2 setting because the spectral orders could not fit entirely within the CCD. These ranges are ∼8911–8913, 9042–9046, 9178–9182, 9317–9323, 9460–9469, 9608–9619, 9760–9774, 9918–9935, 10 080–10 100, and 10 248–10 271 Å.

We reduced the spectra using a combination of tasks from the public ESO UVES pipeline (Ballester et al. 2000) under the GASGANO graphic user interface, and tasks built by ourselves based on *IRAF*[1] (Tody 1993) and several PYTHON packages. First, we used *IRAF* tasks FIXPIX and IMCOMBINE to mask known bad pixels in our images and to combine all the images with the same exposure time. Then, we used the ESO UVES pipeline for bias subtraction, background subtraction, aperture extraction, flat-fielding, and wavelength calibration. As a product, we obtained a 2D science spectrum for each arm in each dichroic setting without flux calibration. We followed the same procedure for GD 71 but extracting both a 2D and a 1D spectrum. The 2D spectrum of the calibration star helps us to note the presence of faint sky lines that are also present in the science spectra.

One crucial step of the data reduction is to perform adequate cuts in the spatial direction of the slit to extract 1D spectra. We chose these spatial cuts in order to study in detail each observed velocity component and trying to maximise the shock/nebular emission ratio. We relied on the [Fe III] λ4658 line, which is relatively bright in the high-velocity components, to delimit the cuts. In the bi-dimensional

[1]IRAF is distributed by National Optical Astronomy Observatory, which is operated by Association of Universities for Research in Astronomy, under cooperative agreement with the National Science Foundation

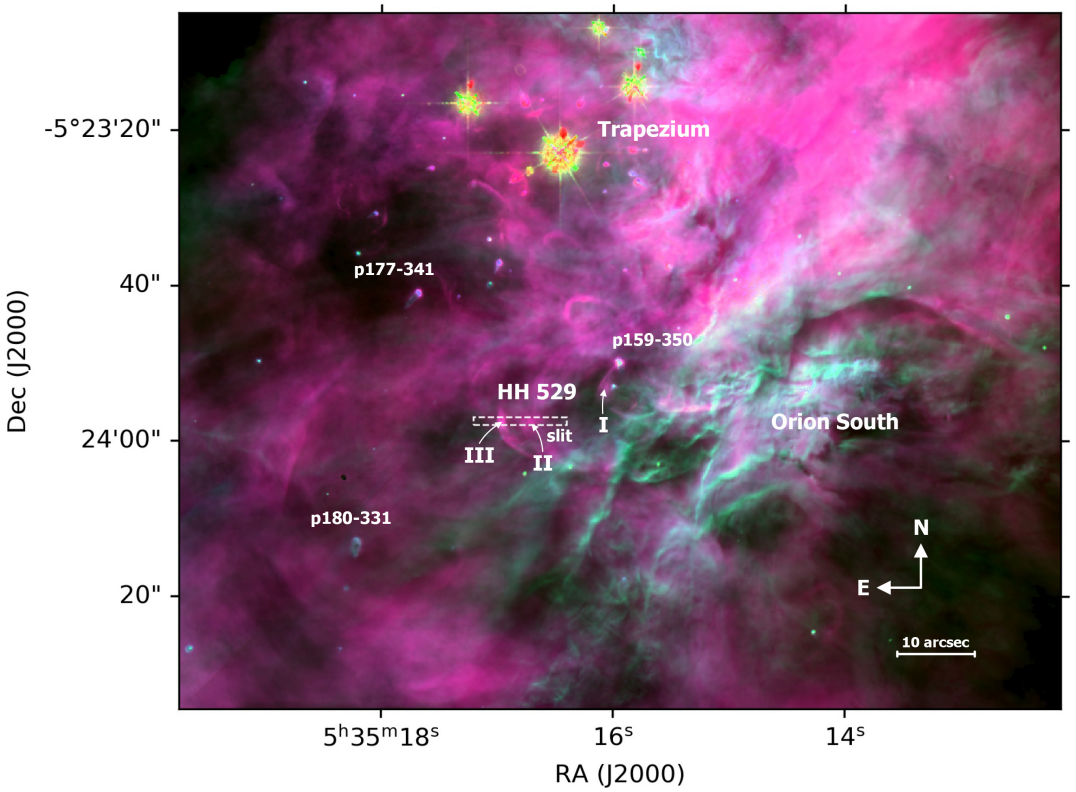

Figure 1. Composite WFPC2 *HST* image of the central Orion Nebula. Three narrow filters were used for the colour scale: F502N, F658N, and F656N for red, green, and blue, respectively (images obtained by Bally et al. 1998). The slit position of our observations is indicated. It covers HH 529 III and HH 529 II. HH 529 bowshocks I, II, and III are indicated following the designation given by O'Dell & Henney (2008). The positions of some protoplanetary discs (proplyds) are also indicated.

spectrum shown in Fig. 2 for some representative lines, we show that the seeing conditions permit us to spatially separate HH 529 II from HH 529 III. HH 529 II has a 'ball shape' while HH 529 III presents an elongated distribution along the spectral axis. This is related to the morphology of the outflow system of HH 529 (first identified by Bally et al. 2000). This system shows three prominent bright arcs, identified by the numbers I, II, and III, being numbered by their position from west to east (O'Dell & Henney 2008). However, the system is more complex than just three homogeneous arcs as we will analyse in Section 10. Lengths covered by each cut in the spatial direction are 1.23, 4.43, 2.46, and 1.23 arcsec for cuts 1, 2, 3, and 4, respectively. The numbering of the cuts has been defined from west to east. The high-velocity component of cut 3 corresponds to HH 529 III, while that of cut 2 is HH 529 II. We have also defined an additional 1D spectrum, labelled as 'combined cuts'. This was created by adding the flux of the lines in all the velocity components when they were detected at least in the nebular emission of all cuts. The spectrum of the combined cuts is useful for analysing the effect that a non-resolved shock component would have in the properties of a low-resolution spectrum. We used the PYTHON-based Astropy package (Astropy Collaboration 2013; Price-Whelan et al. 2018) to obtain 1D spectra for each cut, doing the conversion between the different pixel scale of the CCDs in the blue and the red arm. Each spatial cut covers an area larger than the seeing size during the observations, as is shown in Table 1. We used the *IRAF* tasks STANDARD, SENSFUNC, and CALIBRATE to perform the flux calibration of each 1D spectra of all cuts. The radial velocity correction was made using Astropy.

For the determination of the proper motion of HH 529, we take advantage of the 20 yr of archival *HST* imaging that is now available. We employ three epochs of observations, as detailed in Table 2. All data were downloaded from the Barbara A. Mikulski Archive for Space Telescopes.[2]

3 LINE INTENSITIES AND REDDENING

We used the SPLOT task from *IRAF* to measure line intensities and estimate their uncertainties. We applied a double Gaussian profile fit for the nebular and the high-velocity component, delimiting the continuum by eye. The error estimations are carried out by SPLOT by Monte Carlo simulations around a Gaussian sigma defined as the average *rms* measured on the continuum on both sides of each line with 100 iterations. The error estimates are 1σ estimates. We also

[2]MAST, https://archive.stsci.edu/

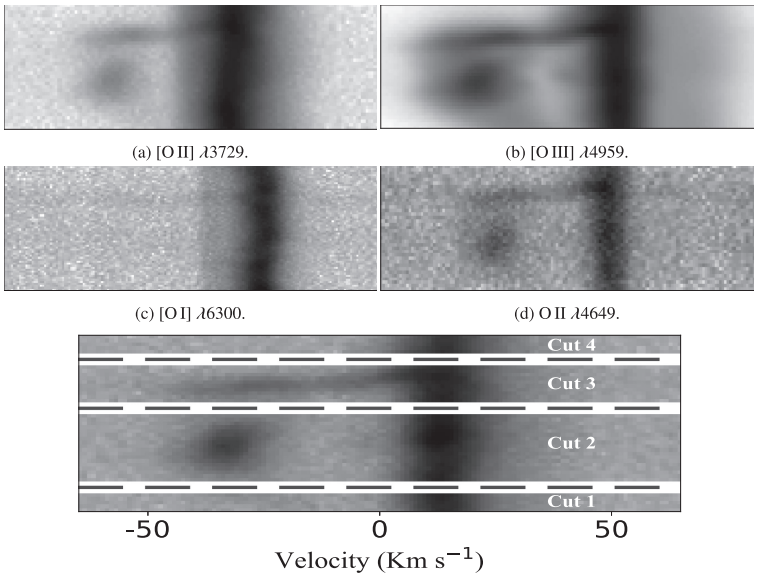

(a) [O II] λ3729. (b) [O III] λ4959. (c) [O I] λ6300. (d) O II λ4649. (e) [Fe III] λ4658. The 4 cuts are identified. Bottom: Cut 1, Top: Cut 4.

Figure 2. Upper panels: Sample of representative lines in the bi-dimensional spectrum. The *Y* axis corresponds to the spatial direction (up east, down west, see Fig. 1 for the spatial location of the slit) while the *X* axis is the spectral axis. All figures are centred at λ_0, the rest-frame reference wavelength of each line. The 'ball-shaped' emission corresponds to HH 529 II while the elongated one to HH 529 III. The blueshifted high-velocity components do not present emission from neutral elements as [O I] and rather faint emission from low ionization ions such as [O II]. Bottom panel: Emission of the [Fe III] λ4658.17 line as well as the limits and extension of the different spatial cuts selected to analyse each velocity component. Cut 1 is at the bottom, which corresponds to the westernmost one. The spatial coverage is 1.23, 4.43, 2.46, and 1.23 arcsec for cuts 1, 2, 3, and 4, respectively. The velocity scale is heliocentric.

Table 2. *HST* observations used in proper motion study.

Date	Program	Camera, CCD, Filter	Reference
1995-03	5469	WFPC2, PC, F656N	Bally et al. (1998)
2005-04	10246	ACS, WFC, F658N	Robberto et al. (2013)
2015-01	13419	WFC3, UVIS, F656N	Bally & Reipurth (2018)

consider an error of the absolute flux calibration of 2 per cent, added quadratically. In case of evident line blending, we applied as many Gaussians as necessary to properly reproduce the line profile. As was mentioned in Section 2, the observed wavelength range (3100–10420 Å) was covered in four sections (two dichroic settings splitting the light into two spectrograph arms). Between each section, there is an overlapping zone from where we used the most intense lines to normalize the entire spectrum with respect to Hβ. The measured flux of H I λ3835, [O III] λ4959, and [S II] λ6731 lines were used to normalize the spectra from the blue arm of dichroic #1, the red arm of dichroic #1, and the red arm of dichroic #2 settings, respectively (Hβ is in the blue arm of dichroic #2 setting). This normalization eliminates the differences in flux between each part of the spectrum due to the different pixel scale between the blue and the red arms.

The emission lines were corrected for reddening using equation (1), where $f(\lambda)$ is the adopted extinction curve from Blagrave et al. (2007), normalized to Hβ. We calculate the reddening coefficient, c(Hβ), by using the ratios of Hε, Hδ, Hγ, and Hα Balmer lines and the P12, P11, P10, and P9 Paschen lines with respect to Hβ and the emissivity coefficients of Storey & Hummer (1995):

$$\frac{I(\lambda)}{I(\mathrm{H}\beta)} = \frac{F(\lambda)}{F(\mathrm{H}\beta)} \times 10^{c(\mathrm{H}\beta) f(\lambda)}. \quad (1)$$

Table 3. Reddening coefficients for each component.

	c(Hβ)	
	High velocity	Nebula
Cut 1	–	0.82 ± 0.02
Cut 2	0.90 ± 0.03	0.83 ± 0.02
Cut 3	0.89 ± 0.05	0.84 ± 0.03
Cut 4	–	0.83 ± 0.02
Combined cuts	–	0.85 ± 0.02

The final adopted c(Hβ) value is the weighted average value obtained from the aforementioned Balmer and Paschen lines and is shown in Table 3 for each component. The selected H I lines are free of line-blending or telluric absorptions that may affect the determination of c(Hβ). Despite the existence of further isolated and bright Balmer and Paschen lines in the spectra, we did not use them since their emission depart from the case B values. This behaviour was reported previously in the Orion Nebula (Mesa-Delgado et al. 2009), the Magellanic Clouds (Domínguez-Guzmán et al. 2019), and in several planetary nebulae (PNe; see Rodríguez 2020).

Blagrave et al. (2006, hereinafter BMB06) observed a zone of the Orion Nebula that includes HH 529 II+III using the 4m Blanco telescope at the Cerro Tololo Inter-American Observatory, covering the 3500–7500Å spectral region. Fig. 3 shows a comparison between

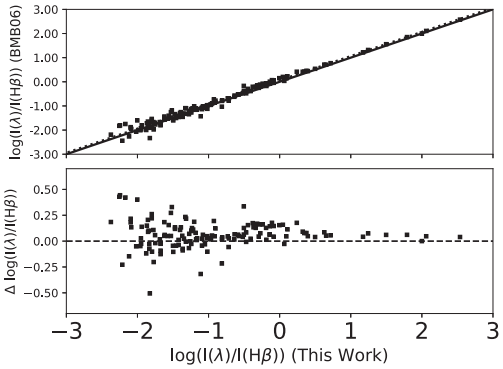

Figure 3. Upper panel: Comparison between the reddening corrected nebular spectrum (log(I(λ)/I(Hβ))) from Blagrave et al. (2006) and this work. The dotted line represents the linear fit $y = 1.00x + 0.05$, while the solid line represents $y = x$. Bottom panel: Difference of the logarithm of line intensity ratios with respect to I(Hβ) in the spectrum of BMB06 and ours.

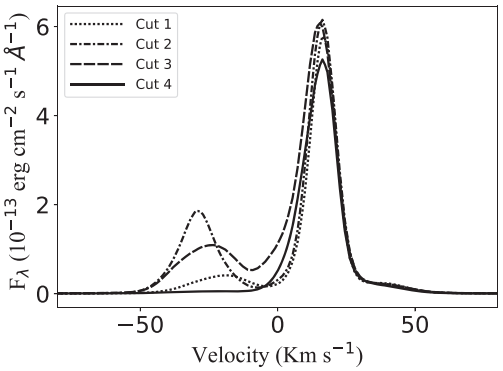

Figure 4. Profile of [O III] λ4958.91 line in each of the analysed spatial cuts. The velocity scale is heliocentric.

their reddening corrected nebular spectrum and ours (from cut 2). For the comparison, we have excluded lines flagged with notes of 'Avg', 'blend', or 'small FWHM' in table 1 of BMB06, due to their uncertain fluxes. For example, [Ne III] λ3967.46 line, marked with an 'Avg', is inconsistent with the measured intensity of [Ne III]λ3868.75, since their observed ratio is 2.02, quite far from the theoretical one of 3.29 (McLaughlin et al. 2011). A least-squares linear fit of the data represented in Fig. 3 yields the relationship $y = 1.00(\pm 0.01)x + 0.05(\pm 0.02)$, indicating that the BMB06's spectrum (y values) presents systematically larger (by a factor of ∼1.12) line ratios (relative to Hβ) than ours (x values). This is very noticeable in the spectral region of the high-level Balmer lines (3660–3720Å), where this difference can reach up to 50 per cent. This may be due to the relative weakness of these lines, coupled with the abrupt change in the continuum level due to the closeness to the Balmer discontinuity. In Table D1, we compare our values of some selected reddening-corrected Balmer line ratios with those obtained by BMB06. The Balmer line ratios with respect to Hβ obtained by BMB06 for both components differ significantly from the theoretical values. However, this does not seem to be the case when we use ratios of Balmer lines excluding Hβ. An underestimation of around 10 per cent in the flux of Hβ in the BMB06's spectrum explains the systematic trend observed in Fig. 3. We do not compare the high-velocity component of BMB06 with our data of HH 529 II and HH 529 III since their slit position and spatial coverage is slightly different than ours.

Fig. 4 shows the [O III] λ4958.91 line profile in the different cuts. As can be seen, the reddest component of each profile (corresponding to the nebular component) shows practically the same shape in all cuts except in cut 3, where the line is broadened by the presence of a larger velocity dispersion in the high-velocity component. The complexity of the velocity components of HH 529 is discussed in more detail in Section 10.

Line identifications were consistently made by adopting the theoretical wavelengths of Peter Van Hoof's latest Atomic Line List v2.05b21[3] (Van Hoof 2018) for all ions except for Cl III , Cl IV and Ne III due to some inconsistencies found (see Section 9 for a detailed discussion). The number of lines we have identified in our spectra is very large. Line identifications and observed and dereddened flux line ratios are presented in 4 online tables, one for each analysed cut. Tables of cut 2 and cut 3 contain, in addition to the observed nebular component, the spectra of HH 529 II and HH 529 III, respectively. These tables contain, for each measured line, the identified rest-frame wavelength (λ_0), the identified ion, the observed wavelength (λ), the radial velocity with respect to λ_0 (v_r), the full width at half-maximum (FWHM), the observed flux relative to $F(\mathrm{H}\beta) = 100$ ($F(\lambda)/F(\mathrm{H}\beta)$), the reddening corrected intensity relative to $I(\mathrm{H}\beta) = 100$ ($I(\lambda)/I(\mathrm{H}\beta)$), the estimated error of the reddening corrected intensity and some notes. In the nebular components, 514, 633, 579, and 522 lines were measured in cuts 1, 2, 3, and 4, respectively. For HH 529 II and HH 529 III, 376 and 245 lines were detected, respectively. Multiline blends were counted as single detections. As an example of our line tables, in Table D2 we show a sample of 15 lines of the spectra of cut 2.

[3] https://www.pa.uky.edu/~peter/newpage/

4 PHYSICAL CONDITIONS

The estimation of the physical conditions and chemical abundances in the different components analysed in this work are based on their photoionization equilibrium state. However, since HH 529 II and HH 529 III are produced by the interaction of high-velocity flows within the photoionized gas of the Orion Nebula, some contribution of the shock in the energy balance of the ionized gas may be expected. In Section 11, we demonstrate that the shock contribution in the observed optical spectra of the high-velocity components is very small and, therefore, the physical conditions and ionic abundances of these objects can be determined by means of the usual tools for analysing ionized nebulae.

4.1 Physical conditions based on CELs

We use PyNeb (version 1.1.10) (Luridiana, Morisset & Shaw 2015) and the updated atomic data set listed in Table D3 to calculate physical conditions based on the intensity ratios of CELs from different ions.

The first step was to test all the intensity ratios of CELs that can serve as a temperature or density diagnostic using the PyNeb task *getCrossTemDen*. This task uses two line ratios at the same time: one as density diagnostic and the other one for temperature,

Table 4. Physical conditions.

	Cut 1	Cut 2		Cut 3		Cut 4	
Diagnostic	Nebula	HH 529 II	Nebula	HH 529 III	Nebula	Nebula	Combined Cuts
Density				n_e (cm^{-3})			
[O II] λ3726/λ3729	5460^{+1000}_{-750}	10570^{+3680}_{-2420}	5220^{+960}_{-720}	18020^{+17170}_{-6930}	5530^{+1000}_{-800}	5070^{+880}_{-710}	5530^{+990}_{-810}
[S II] λ6731/λ6716	4230^{+1500}_{-980}	9390^{+10170}_{-3950}	4160^{+1570}_{-1040}	13130^{+15820}_{-6550}	4130^{+2020}_{-1250}	4160^{+1400}_{-960}	4510^{+2270}_{-1330}
[Cl III] λ5538/λ5518	7020^{+960}_{-900}	8170^{+1810}_{-1610}	6670^{+920}_{-860}	15040^{+5620}_{-4490}	7370^{+1190}_{-1120}	7000^{+960}_{-900}	7420^{+1170}_{-1100}
[Fe III] λ4658/λ4702	9260^{+3700}_{-2890}	12390^{+5010}_{-3460}	8990^{+2840}_{-2350}	33800^{+13820}_{-10530}	10490^{+4240}_{-3090}	8340^{+3620}_{-2530}	9510^{+3790}_{-2750}
[Ar IV] λ4740/λ4711	4480^{+1700}_{-1640}	6410^{+1900}_{-1880}	5920^{+980}_{-940}	15050^{+13300}_{-9240}	6400^{+1690}_{-1660}	5460^{+1000}_{-1050}	6580^{+2000}_{-1870}
O II*	4710 ± 710	3490 ± 340	4390 ± 400	3600 ± 850	4920 ± 550	4350 ± 610	5420 ± 690
[Fe III]*	8530 ± 1050	11880 ± 1860	9430 ± 1010	30200 ± 8080	10330 ± 1700	9020 ± 1170	10360 ± 1410
Adopted	**5830 ± 1210**	**11880 ± 1860**	**5870 ± 970**	**30200 ± 8080**	**6180 ± 1220**	**5650 ± 1030**	**6290 ± 1130**
Temperature				T_e (K)			
T(H I)$_{Balmer}$	–	–	–	–	–	–	7520 ± 790
T(H I)$_{Paschen}$	–	–	–	–	–	–	7550 ± 1160
T(He I)	8280^{+520}_{-570}	7200 ± 550	8060^{+540}_{-510}	7340 ± 710	8090 ± 530	7390^{+470}_{-580}	7690^{+500}_{-510}
[N II] λ5755/λ6584	9910 ± 250	10150^{+570}_{-510}	9850 ± 240	11040^{+920}_{-970}	10060^{+260}_{-280}	9860^{+250}_{-270}	9990^{+250}_{-270}
[O II] λλ 3726+29/λλ7319+20+30+31	10340^{+1330}_{-940}	–	–	–	–	11230^{+1330}_{-1110}	10910^{+1320}_{-950}
[S II] λλ4069+76/λλ 6716+31	11430^{+3290}_{-1870}	–	11070^{+2420}_{-1450}	–	10550^{+2450}_{-1570}	10790^{+2340}_{-1470}	11000^{+2510}_{-1600}
[O III] λ4363/λλ4959+5007	8430 ± 90	8240 ± 80	8410^{+80}_{-90}	8600^{+110}_{-120}	8510 ± 90	8320 ± 90	8450^{+80}_{-90}
[S III] λ6312/λλ9069+9531	9220^{+290}_{-330}	8670 ± 310	8990^{+290}_{-330}	9040^{+410}_{-420}	8920^{+330}_{-300}	8850^{+290}_{-320}	8970^{+280}_{-290}
[Ar III] λ5192/λλ7136+7751	8280^{+280}_{-310}	8620^{+500}_{-540}	8390^{+220}_{-280}	–	8250^{+260}_{-290}	8280^{+380}_{-420}	8270^{+280}_{-320}
O II*	–	–	9350 ± 1090	–	–	–	–
[Fe III]*	7800 ± 800	8500 ± 1050	8450 ± 730	7900 ± 1910	7970 ± 920	7350 ± 590	8440 ± 710
Thermal broadening	–	8670 ± 50	8340 ± 410	10470:	–	–	–
T_e (low) Adopted	**9930 ± 140**	**10150^{+570}_{-510}**	**9860 ± 240**	**11040^{+920}_{-970}**	**10070 ± 270**	**9920 ± 280**	**10040 ± 210**
T_e (high) Adopted	**8470 ± 200**	**8270 ± 110**	**8440 ± 140**	**8630 ± 120**	**8510 ± 120**	**8360 ± 140**	**8480 ± 150**

* A maximum likelihood method was used.

giving their convergence to a pair n_e, T_e as a result. We tried all possible permutations for all the available diagnostics in all components from all cuts. We only discarded the use of lines strongly affected by blends, telluric emissions and/or absorptions or reflections in the optical system of the spectrograph. We did not consider the n_e diagnostic based on [N II] λλ5198/5200 owing to a significant fluorescent contribution in the Orion Nebula (Ferland et al. 2012).

Diagnostics based on [Ni III] λ_1/λ_2, where $\lambda_1, \lambda_2 \in$ [6000, 6534, 6682, 6797, 6946, 7890], do not give any useful physical information since they either did not converge or showed convergences at values highly discordant with the other diagnostics. This will be discussed in Section C. Another interesting diagnostics are based on [Fe III] λ_1/λ_2, where $\lambda_1, \lambda_2 \in$ [4658, 4702, 4734, 4881, 5011, 4925, 4987, 5271]. With the exception of [Fe III] 4658/4702, all the diagnostics converge in a fairly wide range of physical conditions. This is due to the ambivalence and/or high dependence of these ratios on both density and temperature. This will be discussed in Section 4.2.

After the initial exploration, we define the ratios we consider good indicators of electron density and temperature. Then we use Monte Carlo simulations with 1000 points to estimate uncertainties in the physical conditions given by the *getCrossTemDen* task of PyNeb. For example, using [O III] λ4363/λλ4959+5007 as a temperature indicator and the following density diagnostics: [Cl III] λ5538/λ5518, [Fe III] λ4658/λ4702, [O II]λ3726/λ3729, [S II] λ6731/λ6716, and [Ar IV] λ4740/λ4711, we estimate the convergence in T_e and n_e and their uncertainties in every case. Analogously, we use the rest of T_e-diagnostics. The central value of T_e or n_e corresponds to the median of the Monte Carlo distribution and the errors are represented by the deviations to 84th and 16th percentiles, corresponding to $\pm 1\sigma$ in the case of a Gaussian. After this procedure, all diagnostics (either T_e or n_e), will have a result for each cross-comparison.

For the nebular components on each cut, we define the representative n_e as the weighted mean[4] in each cross-comparison with all the the temperature indicators. In the case of high-velocity components, the treatment is more complex since all the density diagnostics based on CELs reveal considerably higher densities than in the nebular components, reaching values at or above the critical densities of the atomic levels involved in some diagnostics as shown in Table D5. At densities of 10^4–10^6cm^{-3}, diagnostics based on [Fe III] lines are more reliable than other classic ones such as [O II] λ3726/λ3729 or [S II] λ6731/λ6716. In addition, dust destruction processes release gaseous Fe in the shock front that should favour the larger contribution of the emission of [Fe III] lines of the post-shock gas and, therefore, the derived physical conditions would be biased to those of the post-shock zones. We adopted a maximum-likelihood method to determine the density from [Fe III] lines for the high-velocity components. This procedure and its interpretation are described in detail in Section 4.2.

Finally, using the adopted representative n_e, we calculate T_e with the available diagnostics using the *getTemDen* task of PyNeb. Assuming the scheme of two ionization zones, we define **T_e(high)** as the weighted mean T_e obtained from [Ar III] λ5192/λλ7136+7751, [O III] λ4363/λλ4959+5007, and [S III] λ6312/λλ9069+9531 line ratios. Similarly, we define **T_e(low)** based on the resulting T_e obtained from [S II] λλ4069+76/λλ 6716+31, [N II]λ5755/λ6584, and [O II] λλ3726+29/λλ7319+20+30+31 line ratios.

We note that in the nebular component of all cuts the observed [S III] λ9531/λ9069 line intensity ratio does not agree with the theoretical value. This is owing to strong telluric absorptions that affect the [S III] λ9069 line that, on the other hand, do not affect the blueshifted lines of the high-velocity components. After an

[4]The weights were defined as the inverse of the square of the error associated to each density diagnostic.

inspection in the 2D spectra of the calibration star and in the science object, we concluded that [S III] λ9531 is not affected by telluric absorptions or emissions at the Earth velocities at which the observations were taken. In the nebular component of all cuts, we assumed the theoretical ratio I([S III] 9531)/I([S III] 9069) = 2.47 obtained from the atomic data given in Table D3 to estimate T_e([S III]).

Plasma diagnostic plots shown in Fig. D1, indicate that the resulting values of each diagnostic are consistent with each other. The numerical values in each case are presented in Table 4.

4.2 Physical conditions based on [Fe III] lines

As mentioned in Section 4.1, density diagnostics based on different [Fe III] line intensity ratios give apparently discordant results. This is mainly due to the ambivalence in the density dependence of some observed intensity ratios and/or due to their high dependence on T_e as well as on n_e. These two scenarios are exemplified in Fig. 5 for [Fe III] λ4881/λ4658 and λ5271/λ4658 line ratios, upper and middle panels, respectively. λ4881/λ4658 has a broad maximum around $n_e \sim 2 \times 10^4$cm^{-3}, so only becomes an accurate density diagnostic for $n_e < 5 \times 10^3$cm^{-3} or $n_e > 10^5$cm^{-3}. In the case of λ5271/λ4658, the T_e dependence is always important except for some narrow density ranges between $\sim 10^2$ and $\sim 10^3$ cm $^{-3}$ and between $\sim 10^5$ and $\sim 10^6$ cm $^{-3}$. For the expected densities in the different components observed in this work (n_e between $\sim 10^3$ and $\sim 10^5$ cm $^{-3}$), these diagnostics are not very enlightening on their own. On the other hand, for 10^3cm$^{-3} < n_e < 10^6$cm^{-3}, λ4658/λ4702 (see bottom panel of Fig. 5) varies monotonically with n_e and is insensitive to T_e. Thus, it is the most reliable diagnostic in our case.

We consider that the option to determine the physical conditions based on the observed intensity ratios of [Fe III] lines is using a maximum-likelihood process. This method is based on a χ^2 minimization by testing a wide range of parameters. The value of χ^2 is defined in equation (2), as the sum of the quadratic differences between the abundance of ion X^i (in this case Fe^{2+}) determined with each emission line included in the procedure and the weighted average of the abundance defined in equation (3):

$$\chi^2 = \sum_{\lambda} \frac{\left(n\left(\frac{X^i}{H^+}\right)_\lambda - \overline{n\left(\frac{X^i}{H^+}\right)}\right)^2}{\Delta n\left(\frac{X^i}{H^+}\right)^2_\lambda}, \quad (2)$$

$$\overline{n\left(\frac{X^i}{H^+}\right)} = \frac{\sum_\lambda \left(n\left(\frac{X^i}{H^+}\right)_\lambda / \Delta n\left(\frac{X^i}{H^+}\right)^2_\lambda\right)}{\sum_\lambda \left(1/\Delta n\left(\frac{X^i}{H^+}\right)^2_\lambda\right)}. \quad (3)$$

This self-consistent procedure gives the physical parameters that minimize χ^2 with an associated uncertainty based on the resulting values within $\chi^2 - \chi^2_{min} \leq 1$. This method requires a strict control on the variables that affect the line fluxes, otherwise a spurious contribution appears, and can change the resulting parameters that minimize χ^2. For example, undetected blends in the studied lines can result in incorrect density and/or temperature determinations.

We have considered several aspects to choose the set of [Fe III] lines that should be included in the maximum-likelihood process. We discard lines with evident line blending or contamination by telluric emission or ghosts. To test unnoticed line blends or inaccuracies in flux estimations, we use ratios of observed lines that should depend only on transition probabilities and not on physical conditions. The results are shown in Table D6. As can be seen, there are some deviations between the theoretical and the observed values

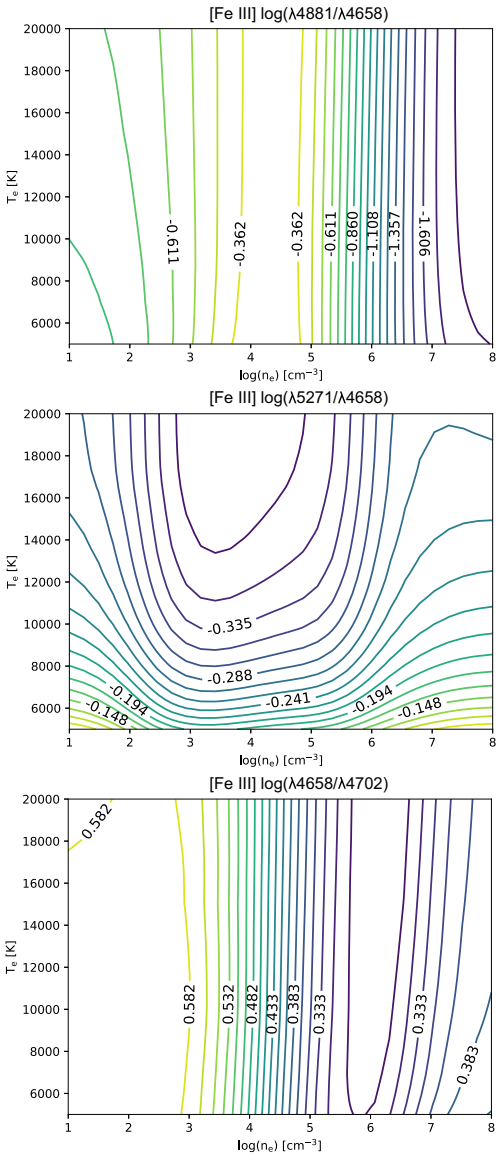

Figure 5. Predicted dependence of the [Fe III] λ4881/λ4658, λ5271/λ4658, and λ4658/λ4702 line intensity ratios with physical conditions.

in the cases of [Fe III] λ4667/λ4734, λ4778/λ4667, λ4607/λ4702, λ4607/λ4770, and λ4881/λ4987 due to the contamination of [Fe III] λ4667 by a ghost, by the blend of [Fe III] λ4607 with N II λ4607.15 and by the blend of [Fe III] λ4987.29 with N II λ4987.38. On the other hand, we detect that λ4778 line is 35 per cent wider than the rest of the [Fe III] bright lines in HH 529 II, although, this is not observed in HH 529 III. This suggests that, due to the higher signal-to-noise ratio in the cut 2 spectrum, a line blend with an emission feature is detected in HH 529 II while for HH 529 III it remains below the

detection level. The line ratio with the largest deviation is [Fe III] λ5011/λ4085. This could be mainly due to the low signal-to-noise ratio of the [Fe III] λ4085 line. However, [Fe III] λ5011 is located close to [O III] λ5007, which presents broad wings in its line profile that affects the shape of the continuum close to [Fe III] λ5011 and perhaps the measurement of its line flux. The presence of bright lines affecting the continuum shape in areas close to relatively weak [Fe III] lines may also contribute to some differences between the observed and predicted line ratios shown in Table D6. This problem is reduced by using the brightest line of each ratio in the maximum-likelihood process.

We select the following [Fe III] lines for the maximum-likelihood process: λλ4658.17, 4701.64, 4734.00, 4881.07, and 5270.57. This selection includes the brightest [Fe III] lines that are free of blends or telluric emissions and/or absorptions. Moreover, these lines lie in a relatively small spectral range and hence, uncertainties in the reddening correction would have a negligible effect. This allows us to restrict the parameter space to electron density and temperature to test χ^2. Studies of the primordial helium abundance have used similar maximum-likelihood procedures to calculate the He^+ abundance and have found that this procedure can lead to degeneracies in the fitted parameters and χ^2 (see Olive & Skillman 2004; Aver, Olive & Skillman 2011, and references therein). Because of this, it is important to have an overview of the behaviour of χ^2 in the complete parameter space. In Fig. 6 we present the convergence of χ^2 in the $n_e - T_e$ space for both high-velocity and nebular components of cut 2. As it can be seen, χ^2 falls into a single minimum in each case, corresponding to $T_e = 8500 \pm 1050$ K and $n_e = 11880 \pm 1860$ cm^{-3} for HH 529 II and $T_e = 8450 \pm 730$ K and $n_e = 9430 \pm 1010$ cm^{-3} for the nebular component. The T_e and n_e values obtained for the rest of cuts using this approach are presented in Table 4. The convergence to the resulting n_e is consistent with the diagnostic based on [Fe III] λ4658/λ4702 ratio but with a smaller uncertainty due to the application of the χ^2 maximum-likelihood procedure. It is notable that in all cases, [Fe III] lines give n_e values higher than the usual diagnostics based on CELs such as [S II] λ6731/λ6716 or [O II] λ3726/λ3729. The largest difference is found in the high-velocity components, in particular in HH 529 III. In the case of nebular components, the low dependence on density of some ratios such as λ4734/λ4658, λ4658/λ4702 or λ4734/λ4702 at density values smaller than $\sim 10^3$ cm^{-3}, gives more weight to the higher-density zones within the line of sight. On the other hand, in the high-velocity components, the larger differences suggest the presence of high densities in the range of 10^4–10^5cm^{-3}, where the usual density diagnostics, such as [S II] λ6731/λ6716 or [O II] λ3726/λ3729, are uncertain, being well above the critical densities, as is shown in Table D5. In addition, as found in HH 202 (Mesa-Delgado et al. 2009; Espíritu et al. 2017) and in this work (see Section 8.1.3), the gaseous Fe abundance is higher in the high-velocity components due to the dust destruction where the Fe is commonly depleted, thus, the flux of [Fe III] lines increase in the shock front, where the gas is being compressed. Therefore, the n_e determinations based on [Fe III] lines will be biased to the higher values of the density at the head of the shock although the volume of gas integrated in the high-velocity components include not only the denser gas of the head but also some contribution of the jet beam gas behind since it is fully photoionized and flowing towards the observer (see Section 11).

The results indicate a closer similarity between T_e([Fe III]) and T_e(high), contrary to what the ionization potential of Fe^{2+} would suggest, closer to N^+ than to O^{2+}, which are ions representative of the low and high ionization zones, respectively. In the case of the nebular components, the fact that the [Fe III] density diagnostics give more weight to the high-density zones in the line of sight, as we mentioned previously, may bias the results towards lower temperatures, which are not representative for all the Fe^{2+}. On the other hand, in the high-velocity components, this indicates that in the shock front, where further dust destruction and incorporation of Fe into the gas phase is expected, the high-ionization gas dominates over the remaining low-ionization one, which may be flowing behind of the shock front. This suggests that the optimal temperature to calculate the Fe^{2+} abundance in the high-velocity components is T_e(high). Estimates of Fe^{2+} abundances based on both T_e(low) and T_e(high) will be discussed separately in Section 8.1.3.

4.3 Physical conditions based on RLs.

4.3.1 Physical conditions based on O II RLs

To estimate physical conditions based on O II RLs, we use the effective recombination coefficients from Storey, Sochi & Bastin (2017). These coefficients fully account the dependence on electron density and temperature of the population distribution among the ground levels of O II. We follow a similar maximum-likelihood procedure as described in Section 4.2 to derive the physical conditions. For this case, we chose the observed lines from multiplet 1 and λλ4089.29, 4275.55 from 3d-4f transitions, due to the following reasons: (1) lines from multiplet 1 are the brightest O II RLs and are comparatively less affected by line blending or instrumental reflections as is illustrated in Fig. 7 for cut 2. (2) The line ratios within multiplet 1 deviate from the local thermodynamic equilibrium (LTE) values for $n_e \leq 10^5$cm^{-3} (Storey et al. 2017), providing a density diagnostic. (3) O II λλ4089.29, 4275.55 RLs corresponding to 3d-4f transitions depend slightly stronger on T_e than the lines from multiplet 1 and their ratio with O II λ4649.13 is practically insensitive to n_e, since the population of the levels that arise these lines depend on the population of the same $^3P_2$ ground level (Storey et al. 2017), giving a T_e diagnostic. Nevertheless, λλ4089.29, 4275.55 are relatively weak and we expect comparatively larger uncertainties in the T_e determinations than using diagnostics based on CELs.

Fig. 8 shows χ^2-maps in the space of T_e and n_e for both components of cut 2. As it can be seen, HH 529 II has a temperature degeneracy. This is not surprising, due to the fact that multiplet 1 is rather independent of T_e and the weak line λ4275.55 is the only one that can break the degeneracy in this component since O II λ4089.29 is blended with a ghost feature (see Section A). However, it is clear that the density dependence is well limited within a range of 3000–3700 cm^{-3}. Fixing the temperature to the adopted one for the high ionization zone using CELs, we obtain $n_e = 3490 \pm 340$ cm^{-3} for HH 529 II. On the other hand, since we were able to use the O II λ4089.29 together with λ4275.55 in the nebular component of cut 2, we have a convergence within a more limited interval of values. The physical conditions that minimizes χ^2 in this case are $n_e = 4390 \pm 400$ cm^{-3} and $T_e = 9350 \pm 1090$ K. This result is compatible with T_e([O III]) within the uncertainties, indicating that the emission of CELs and RLs of O^{2+} comes basically from the same gas (see Section 8.3).

In Table 4, we can see that the density values obtained from O II lines are similar to those obtained from other diagnostics in the nebular components but lower in the high-velocity ones. This may be because, although formally the population of the ^3P_J levels from O^{2+} do not reach the statistical equilibrium until densities of $\sim 10^5$cm^{-3}, the density dependence becomes rather weak from values above $\sim 10^4$cm^{-3}, as it is shown in Fig. 4 from Storey et al.

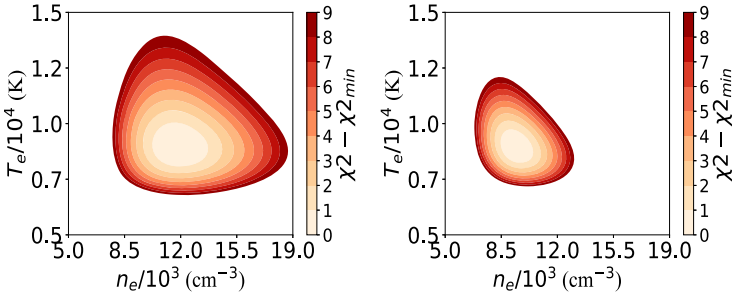

(a) HH 529 II (b) Nebular component

Figure 6. χ^2 in the space of T_e and n_e in the maximum-likelihood procedure for [Fe III] lines. Both in the case of HH 529 II (left panel) and the nebular component of cut 2 (right panel) there is a convergence to well-defined physical conditions.

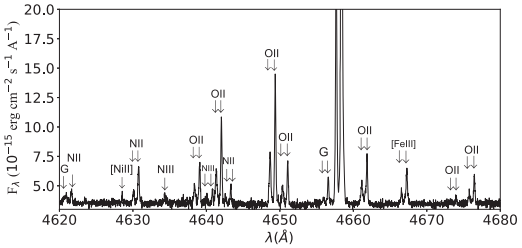

Figure 7. Section of the spectrum of the spatial cut 2 covering the spectral range 4620–4680Å. Several couples of O II lines from multiplet 1 are present, showing the quality of the spectra of HH 529 II and the nebular component. Emissions marked with a G are ghosts (see Section A).

(2017). Therefore, the values obtained by this diagnostic may not be representative of the shock front, where the density is expected to be higher than 10^4cm^{-3} but from a lower density component flowing in the jet beam. A gas component with a density around $\sim 10^3$cm^{-3} has larger deviations from LTE in the populations of the levels from which multiplet 1 arise. This might bias the results to lower values. However, this discrepancy may have a different origin, which requires further investigation.

4.3.2 *Electron temperature from He I recombination line ratios*

Following the procedure used by Zhang et al. (2005) for PNe, we have used the I(He I λ7281)/I(He I λ6678) ratio for deriving T_e (He I) in our spectra. The use of those particular lines have several advantages. First, λ7281 and λ6678 are among the brightest He I RLs and their use minimizes observational errors. Second, they are produced in transitions between singlet levels, ensuring that they are free of significant self-absorption effects. We have explored the temperature dependence of other intensity ratios of He I λ7281 with respect to other relevant singlet lines (λλ4388, 4922, 4438,, 3614, 3965, and 5016) using the recombination coefficients of Porter et al. (2012, 2013). Intensity ratios of transitions coming from 5^1D, 4^1D, 3^1D levels to 2^1P show the the strongest dependence on T_e (see Fig. D4). 2^1P is the same lower level of the transition producing the He I λ7281 line, which comes from the 3^1S level. On the other hand, comparatively, the I(He I λ7281)/I(He I λ6678) ratio has the weakest n_e dependence, in agreement with the conclusion of Zhang et al. (2005), despite using different recombination coefficients.

Fig. D5 shows that the T_e dependence of I(He I λ7281)/I(He I λ6678) ratio is practically linear in the interval 5000 K $\leq T_e \leq$ 10000 K. The deviation between the determination of T_e(He I) using a linear fit (as in equation 4) and a more complex interpolation of the recombination coefficients of Porter et al. (2012, 2013) is always smaller than 35K. At $T_e > 10000$ K, any linear fit will fail for almost all n_e values except for the lowest ones ($n_e \leq 100$ cm^{-3}). In these cases, a more complex treatment is necessary to estimate T_e(He I). The linear fit (slope and intercept) varies significantly in the lower density ranges, and tends to remain almost constant for densities $n_e \geq 10000$ cm^{-3}:

$$T_e\,(\mathrm{He\,I})\,(\mathrm{K}) = \alpha \left[\frac{I\,(\lambda 7281)}{I\,(\lambda 6678)}\right] + \beta. \quad (4)$$

In Table D7, we present the slope and intercept values given by equation (4) for a density range representative for H II regions and some PNe. The resulting T_e(He I), using the average values obtained with I(λ7281)/I(λ6678), I(λ7281)/I(λ4922), and I(λ7281)/I(λ4388) ratios, are all consistent with each other and are included in Table 4 for all components.

4.4 Electron temperature determinations from nebular continuum.

Thanks to the high signal-to-noise ratio of our spectra, we can obtain a good determination of the Balmer and Paschen discontinuities of the nebular continuum in the spectrum obtained adding all the cuts (see Fig. 9). We used equation (5), taken from Liu et al. (2001) for $He^{2+}/H^+ = 0$ to estimate $T_e(\mathrm{H\,I})_{\mathrm{Balmer}}$. This formula is based on theoretical continuum emission of H I, He I, and He II calculated by Brown & Mathews (1970) and the theoretical line emission of H I λ3770.63 (H11) from Storey & Hummer (1995). Analogously, we used equation (6), taken from Fang & Liu (2011), to estimate $T_e(\mathrm{H\,I})_{\mathrm{Paschen}}$ using the measured Paschen discontinuity and the intensity of H I λ8862.78 (P11) line:

$$T_e(\mathrm{H\,I})_{\mathrm{Balmer}}(\mathrm{K}) = 368 \times \left(1 + 0.259\frac{\mathrm{He}^+}{\mathrm{H}^+}\right)\left(\frac{\mathrm{BJ}}{\mathrm{H11}}\right)^{-3/2}. \quad (5)$$

$$T_e(\mathrm{H\,I})_{\mathrm{Paschen}}(\mathrm{K}) = 8.72 \times \left(1 + 0.52\frac{\mathrm{He}^+}{\mathrm{H}^+}\right)\left(\frac{\mathrm{PJ}}{\mathrm{P11}}\right)^{-1.77}. \quad (6)$$

The estimation of the temperature requires a precise fit to the continuum emission at both sides of 3646 and 8204 Å, the approximate

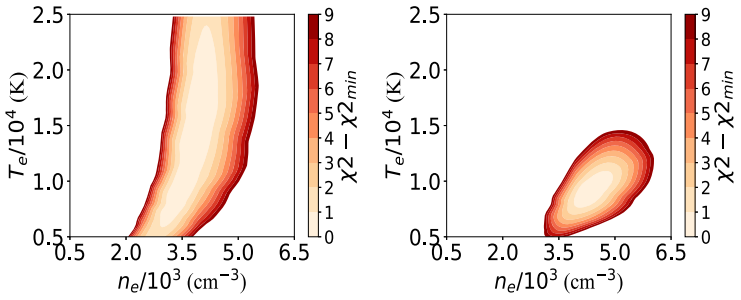

(a) HH 529 II (b) Nebular component

Figure 8. The same as in Fig. 6 but using O II lines. In this case, there is an evident T_e degeneracy in HH 529 II (left panel) because that the temperature-dependent O II RL λ4089.29 cannot be measured in its spectrum. A clear convergence can be seen in the nebular component (right panel). The uncertainties are somewhat large owing to the relative weakness of the temperature-dependent O II lines (λλ4089.23, 4275.55).

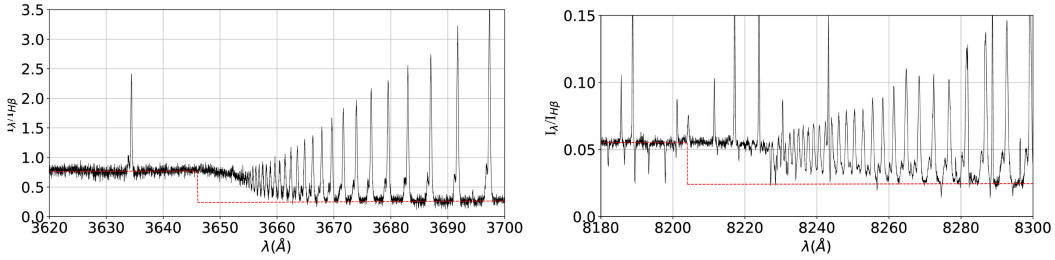

Figure 9. Reddening-corrected spectrum resulting after adding all cuts, showing the Balmer (left-hand panel) and Paschen (right-hand panel) discontinuities. Both jump estimations are shown in red.

wavelengths of the Balmer and Paschen discontinuities, respectively, since both estimations are very sensitive to changes in the jump value. We do not determine $T_e(\mathrm{H\,I})_{\mathrm{Balmer}}$ and $T_e(\mathrm{H\,I})_{\mathrm{Paschen}}$ in the remaining cuts because of the much larger noise level of the continuum in their spectra. However, using the spectrum of the combined cuts has the drawback of mixing the emission of the nebular and the high-velocity components in the continuum. In any case, as Bohigas (2015) suggests, the total T_e(H I) would be the weighted average of the individual values of the mixed components, where the weight would be the H^+ mass of each component. Thus, given that the high-velocity component should contain a much smaller mass, we can assume that the contribution of the high-velocity component to the continuum should be small, not affecting the T_e(H I) determination in a substantial manner.

Fig. 9 shows the discontinuities and the fitted Balmer and Paschen continua in the normalized and reddening corrected spectrum. The best fit is achieved with $\mathrm{BJ}/\mathrm{I}_{H\beta} = 0.532 \pm 0.036$ and $\mathrm{PJ}/\mathrm{I}_{H\beta} = 0.031 \pm 0.002$.

5 CHEMICAL ABUNDANCES

5.1 Ionic abundances from CELs

We determine the ionic abundances based on the observed CELs using the PyNeb routines and the transition probabilities and collision strengths given in Table D3. Abundances for O^+, N^+, S^+, Ni^{2+}, and Cl^+ were derived using the n_e and T_e(low) adopted for each component of each cut, while abundances for O^{2+}, Ne^{2+}, Cl^{3+}, Fe^{3+}, Ar^{2+}, and Ar^{3+} rely on the adopted T_e(high). S^{2+} and Cl^{2+} abundances were derived using T_e([S III]) (see Section B). In the case of Fe^{2+}, estimations of its abundance are presented using both T_e(high) and T_e(low) (see Tables D8 and D9). This will be analysed in Section 8.1.3. General results are presented in Table 5.

5.2 Ionic abundances from RLs

5.2.1 *He^+ abundance*

To estimate the He^+ abundance, we use the flux of some of the most intense He I lines: λλ3188, 3614, 3889, 3965, 4026, 4388, 4438, 4471, 4713, 4922, 5016, 5876, 6678, 7065, 7281. He I λλ4121, 5048 lines were discarded because they are contaminated by ghost lines (see Section A). The 15 selected lines correspond to both singlet and triplet configurations, as it is shown in Fig. D4. The fluxes of triplet lines are affected by the metastability of the 2^3S level. The comparatively much longer lifetime of 2^3S means that transitions to this level can become optically thick, altering the flux ratios predicted by recombination theory for some He I lines. For example, self-absorption of He I λ3188 photons can increase the flux of He I λλ3889, 5876, and 7065 lines at the expense of He I λ3188, which flux decreases accordingly. On the other hand, self-absorption of the He I λ3889 line is also important and increase the flux of He I λ7065 at the expense of He I λ3889. However, the sum of the fluxes of He I λλ3188, 3889, 4713, 5876, and 7065 lines should remain independent of the optical depth (parametrized by τ_{3889} or τ_{3188}; Porter, Ferland & MacAdam 2007).

Table 5. Chemical abundances based on CEL's without considering the temperature fluctuation scenario ($t^2 = 0$). The units are logarithmic with $n(H) = 12$.

	Cut 1	Cut 2		Cut 3		Cut 4	
Ion	Nebula	HH 529 II	Nebula	HH 529 III	Nebula	Nebula	Combined cuts
O^+	7.88 ± 0.04	$7.36^{+0.12}_{-0.09}$	$7.83^{+0.06}_{-0.05}$	$7.51^{+0.22}_{-0.14}$	$7.76^{+0.07}_{-0.06}$	$7.81^{+0.07}_{-0.06}$	7.75 ± 0.05
O^{2+}	8.32 ± 0.03	$8.54^{+0.03}_{-0.02}$	8.35 ± 0.03	$8.48^{+0.03}_{-0.02}$	$8.35^{+0.03}_{-0.02}$	8.36 ± 0.03	8.37 ± 0.03
N^+	7.00 ± 0.02	$6.19^{+0.06}_{-0.05}$	6.99 ± 0.03	$6.45^{+0.12}_{-0.08}$	$6.91^{+0.04}_{-0.03}$	$6.98^{+0.04}_{-0.03}$	6.89 ± 0.03
Ne^{2+}	7.67 ± 0.04	7.91 ± 0.03	$7.70^{+0.04}_{-0.03}$	7.80 ± 0.03	7.73 ± 0.03	$7.75^{+0.04}_{-0.03}$	$7.73^{+0.04}_{-0.03}$
S^+	5.58 ± 0.05	$4.88^{+0.08}_{-0.07}$	$5.57^{+0.05}_{-0.04}$	$5.17^{+0.15}_{-0.12}$	$5.53^{+0.06}_{-0.05}$	5.59 ± 0.05	5.49 ± 0.05
S^{2+}	6.79 ± 0.04	$6.92^{+0.05}_{-0.04}$	$6.85^{+0.09}_{-0.07}$	$6.89^{+0.06}_{-0.05}$	$6.86^{+0.05}_{-0.04}$	$6.82^{+0.05}_{-0.04}$	6.85 ± 0.04
Cl^+	3.72 ± 0.04	$2.95^{+0.14}_{-0.13}$	3.71 ± 0.04	<3.34	3.68 ± 0.04	3.75 ± 0.04	3.63 ± 0.04
Cl^{2+}	$4.88^{+0.06}_{-0.05}$	$5.01^{+0.06}_{-0.05}$	$4.93^{+0.06}_{-0.05}$	$5.03^{+0.08}_{-0.07}$	$4.96^{+0.06}_{-0.05}$	$4.95^{+0.06}_{-0.05}$	$4.94^{+0.05}_{-0.04}$
Cl^{3+}	3.28 ± 0.06	3.60 ± 0.05	$3.28^{+0.04}_{-0.03}$	3.40 ± 0.10	3.33 ± 0.04	3.45 ± 0.04	3.38 ± 0.05
Ar^{2+}	6.31 ± 0.03	6.39 ± 0.02	6.31 ± 0.03	6.36 ± 0.03	6.33 ± 0.02	6.29 ± 0.03	6.32 ± 0.03
Ar^{3+}	$4.39^{+0.06}_{-0.05}$	$4.67^{+0.04}_{-0.03}$	$4.47^{+0.04}_{-0.03}$	4.51 ± 0.07	4.50 ± 0.04	$4.61^{+0.04}_{-0.03}$	$4.52^{+0.05}_{-0.04}$
$^*Fe^{2+}$	5.77 ± 0.02	5.94 ± 0.05	5.82 ± 0.02	5.75 ± 0.05	5.78 ± 0.02	5.76 ± 0.03	5.80 ± 0.02
$^{**}Fe^{2+}$	5.52 ± 0.03	5.62 ± 0.07	5.57 ± 0.02	5.40 ± 0.06	5.52 ± 0.04	5.48 ± 0.03	5.53 ± 0.04
Fe^{3+}	$5.68^{+0.13}_{-0.11}$	$6.25^{+0.10}_{-0.09}$	$5.70^{+0.09}_{-0.08}$	<6.58	$5.73^{+0.11}_{-0.10}$	$5.73^{+0.13}_{-0.12}$	$5.75^{+0.11}_{-0.10}$
Ni^{2+}	4.37 ± 0.14	4.50 ± 0.08	4.33 ± 0.17	$4.28^{+0.15}_{-0.11}$	4.32 ± 0.16	4.36 ± 0.12	4.38 ± 0.10

Notes. * indicates that T_e(high) was used.
** indicates that T_e(low) was used.

In Table D13, we show the He^+ abundances determined using the fluxes of He I λλ3188, 3889, 4713, 5876, and 7065 lines and the values of n_e and T_e(He I) corresponding to each component of each cut. In the same table, we also include the He^+ abundance obtained from the sum of the fluxes of all the individual lines of the table and re-distributing them assuming $\tau_{3188} = \tau_{3889} = 0$. In Table D14 we show the He^+ abundances determined from singlet lines and those triplet ones that are expected to be less affected by self-absorption (see table 2 from Benjamin, Skillman & Smits 2002). Tables D13 and D14 show a good agreement between the average values of He^+/H^+ ratios included in Table D14 (the last row) and those obtained summing the fluxes of the lines included in Table D13. This last table also shows that the self-absorption effects are less important in the high-velocity components than in the nebular one. This is noticeable in the lower dispersion of the abundances obtained with individual lines in the high-velocity components. As discussed in Osterbrock & Ferland (2006, see their fig. 4.5) if the nebula has ionized zones at different velocities, the self-absorption effects can be reduced due to the Doppler shift between the emitting and absorbing zones. For example, the effect of self-absorption in the intense He I λ5876 line is notable in the nebular component, giving He^+ abundances about 0.05 dex higher than the sum value. In this sense, the common procedure of using a flux-weighted average of He I λ5876 and other bright optical He I lines (as λ4471 and λ6678) for obtaining the mean He^+ abundance would provide rather an upper limit of it.

Another interesting fact that can be noted in Table D14 is that the He^+ abundance determined from the He I λ5016 line is lower than the values obtained from other lines in the high-velocity components. An abnormally low flux of this line was noted by Esteban et al. (2004), and this was attributed to self-absorption effects in the singlet configuration of He I. Porter et al. (2007) discussed this, proposing that the most likely explanation is a deviation from case B of the He I λλ 537.0 and 522.0 lines, that go to the ground level, partially escaping before being reabsorbed. This is probably the case in the high-velocity components where any kind of self-absorption of photons emitted by the 'static' nebular gas should be reduced. The adopted He^+/H^+ values are presented in Table 6.

5.2.2 O^{2+} abundance

In Table D15, we present the O^{2+} abundance obtained from RLs of O II. We use T_e(high) and the values of n_e obtained from O II (see section 4.3.1) and [Fe III] lines for the nebular and high-velocity components, respectively. We used the recombination coefficients calculated by Storey et al. (2017) that consider the distribution of population among the O^{2+} levels with some improvements over similar estimates from Bastin & Storey (2006). Previous references (as Storey 1994) assumed that the O^{2+} levels are populated according to their statistical weight, which is not suitable for densities below the critical one.

In Table D15, we also present the weighted average abundance for each multiplet. In the last row of Table D15 we give the O^{2+} abundance obtained averaging the values obtained for multiplets 1, 2, 10, 20 and 3d−4f transitions. These multiplets and transitions give consistent values and were also considered by Esteban et al. (2004) for determining their mean values. However, we decided to consider only the abundance obtained from multiplet 1 as representative of the O^{2+} abundance, as we show in Table 6. This is because, although it gives values consistent with the average of the other aforementioned multiplets and transitions, the inclusion of multiplets with fainter lines increases the formal uncertainties of the final mean O^{2+} abundance.

5.2.3 Determination of the abundance of other heavy elements based on RLs

Due to the high quality of our deep spectra, we were able to determine abundances of other heavy element ions such as O^+, C^{2+}, and Ne^{2+} based on the fluxes of RLs and the recombination coefficients presented in Table D4.

O^+ abundances were obtained from the lines of multiplet 1 of O I λλ 7771.94, 7774.17, and 7775.39 together with the adopted density

Table 6. Chemical abundances based on RL's. The units are logarithmic with $n(H) = 12$.

Ion	Cut 1 Nebula	Cut 2 HH 529 II	Cut 2 Nebula	Cut 3 HH 529 III	Cut 3 Nebula	Cut 4 Nebula	Combined cuts
He^+	10.89 ± 0.02	10.95 ± 0.03	10.90 ± 0.01	10.95 ± 0.03	10.90 ± 0.02	10.91 ± 0.02	10.91 ± 0.02
O^+	8.34 ± 0.10	<7.91	8.25 ± 0.06	<7.95	8.28 ± 0.07	8.27 ± 0.07	8.19 ± 0.07
O^{2+}	8.47 ± 0.04	8.83 ± 0.07	8.52 ± 0.02	8.84 ± 0.09	8.52 ± 0.03	8.53 ± 0.03	8.58 ± 0.02
C^{2+}	8.34 ± 0.03	8.46 ± 0.02	8.35 ± 0.03	8.56 ± 0.03	8.34 ± 0.03	8.33 ± 0.02	8.37 ± 0.03
Ne^{2+}	–	8.60 ± 0.06	8.07 ± 0.03	–	8.04 ± 0.15	–	–

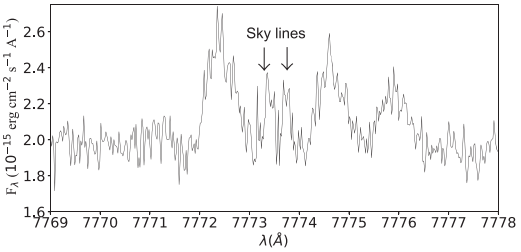

Figure 10. Lines of multiplet 1 of O I ($3s^5S^0-3p^5P$) in the spatial cut 2. No emission from HH 529 II is observed, only the nebular component is noticeable. These lines are produced from transitions of quintet levels (Grandi 1975a) and arise purely by recombination. Due to high spectral resolution and the earth motion during the observations, these lines are free of blending with sky lines.

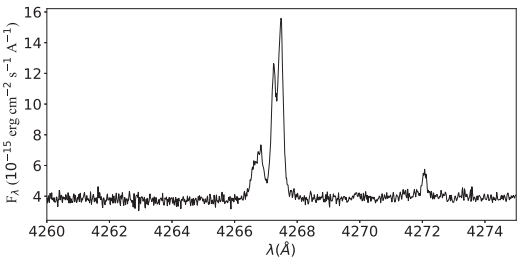

Figure 11. Lines of multiplet 6 of C II ($3d^2D-4f^2F^0$) in the spatial cut 2. Due to our high spectral resolution, we can partially separate λ4267.00 from λ4267.18 + λ4267.26 both in the component corresponding to HH 529 II and to the nebular one.

and temperature of the low ionization zone for each component of each cut. Due to the high spectral resolution of our data, these O I lines are not blended with telluric emission features, as is shown in Fig 10. We do not detect the lines of multiplet 1 of O I in the high-velocity components. In these cases, we have estimated upper limits of their intensity and corresponding abundances considering an hypothetical line with a flux of 3 σ of the rms of the adjacent continuum. The resulting O^+ abundances and the estimated upper limits for the high-velocity components are shown in Table 6.

For C^{2+} and Ne^{2+}, we adopt the temperature of the high ionization zone for each component of each cut. C II RLs from different transitions were considered to derive C^{2+} abundances, as is shown in Table D16. Multiplet 6 of C II present two lines at 4267.00 and 4267.18+4267.26 Å resolved at our spectral resolution, as shown in Fig. 11. In general, lines from all multiplets of C II considered give consistent values of C^{2+} abundances. RLs from multiplet 1 of Ne II

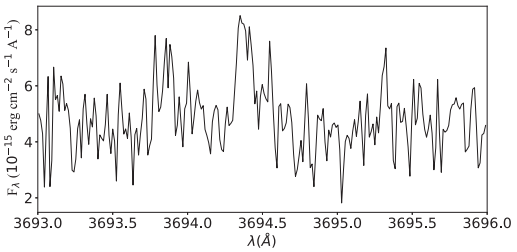

Figure 12. Lines of multiplet 1 of Ne II ($3s^4P-3p^4P^0$) in the spatial cut 2.

were used to calculate the Ne^{2+} abundance. Although they are rather faint lines (see Fig. 12), the Ne^{2+} abundances derived from Ne II λλ 3694.21 and 3766.26 lines for each component of cut 2 are consistent with each other. In addition, the Ne^{2+} abundance we derive for the nebular component in cuts 2 and 3 is in good agreement with that obtained by Esteban et al. (2004, see their table 11).

6 TEMPERATURE FLUCTUATIONS

We followed the t^2-paradigm postulated by Peimbert (1967), by using equation (10) from Peimbert & Costero (1969) and equation (10) from Peimbert et al. (2004), together with the measured T_e(H I) and T_e([O III]) in order to estimate t^2 (Peimbert 2003; Esteban et al. 2004; García-Rojas et al. 2004, 2005, 2007). Implicitly, this approach assumes that $t^2(H^+) \approx t^2(O^{2+})$ and $T_0(H^+) \approx T_0(O^{2+})$. The same procedure has been followed with equations (13) and (14) from Peimbert & Costero (1969), together with the measured T_e([S III]) and T_e([N II]), respectively, in order to estimate representative values of t^2 for different ionization zones (Peimbert & Costero 1969; Esteban et al. 1998). The analogous procedure has been used with equation (11) from Zhang et al. (2005), to use the t^2 dependence of the measured T_e(He I). In Table 7, we show the t^2 and T_0 values obtained for each combination. We have to emphasize the excellent agreement between using T_e(H I) and T_e(He I) together with the T_e diagnostics based on CEL ratios.

However, the above procedure may not be entirely accurate. From the definition of T_0 and t^2 – equations (9) and (12) from Peimbert (1967) – it is clear that these quantities depend on the integrated volume of gas. Thus, since each ion X^{i+} will have its own Strömgren sphere, each one will have a representative $t^2(X^{i+})$ and $T_0(X^{i+})$. Considering another ion, Y^{i+}, the assumption $t^2(X^{i+}) \approx t^2(Y^{i+})$ will be only correct if X^{i+} and Y^{i+} occupy the same nebular volume. Based on a set of Cloudy photoionization models with different input parameters, Kingdon & Ferland (1995) derived t^2 in two manners: as t^2_{str} from the formal definition and the t^2_{obs} obtained from the comparison of T_e(H I) and T_e([O III]). They found that generally $t^2_{str} \neq t^2_{obs}$, with the difference increasing with the T_{eff} of the ionizing

Table 7. t^2 and T_0 derived from the combinations of different temperature estimates within the formalism of Peimbert (1967) for the spectrum of all cuts combined.

	T_e([O III])		T_e([S III])		T_e([N II])	
	t^2	T_0	t^2	T_0	t^2	T_0
$T_e(H\,I)_{BJ}$	0.020 ± 0.017	7770 ± 850	0.051 ± 0.030	8240 ± 980	0.068 ± 0.023	8510 ± 960
$T_e(H\,I)_{PJ}$	0.019 ± 0.025	7800 ± 1260	0.050 ± 0.042	8250 ± 1420	0.068 ± 0.033	8530 ± 1430
T_e(He I)	0.018 ± 0.012	7840 ± 520	0.054 ± 0.024	8160 ± 570	0.075 ± 0.018	8360 ± 570

sources. However, for the $T_{\rm eff}$ typical of the ionizing stars of H II regions (between 30,000 and 50,000 K), the approximation $t^2_{\rm str} \approx t^2_{\rm obs}$ seems to be valid. The main drawback one faces in determining $t^2_{\rm obs}$ is its high intrinsic uncertainty.

Assuming the two ionization zones scheme for H II regions, a better approximation to t^2 can be obtained using equations (7) and (10) from Peimbert, Peimbert & Luridiana (2002). Then we need to estimate the fraction of O^+ in the total O abundance. For the spectrum of the combined cuts, this value varies from 0.36 to 0.23 according to whether the abundances are determined from RLs or CELs, respectively. A reasonable approximation is to take the average value ∼0.3. On the other hand, He^+ should be present in both, the O^+ and O^{2+} zones. Although there may be coexistence of He^0 and H^+, the volume that He^0 occupies should be small at the ionization conditions of the observed area of the Orion Nebula and it can be assumed that the volume containing H^+ and He^+ should be approximately the same. This assumption is reinforced by the fact that the parameter $\eta = (O^+/O^{2+})(S^{2+}/S^+)$ (Vilchez & Pagel 1988), which is a measure of the radiation hardness and is anticorrelated with the $T_{\rm eff}$ of the ionizing source, has a value of $\log(\eta) = 0.74$ for the 'combined cuts' spectrum. Pagel et al. (1992) showed that for $\log(\eta) < 0.9$, the amount of He^0 is negligible for a large variety of photoionization models. Therefore, we can assume $T_0(H^+) \approx T_0(He^+)$ and $t^2(H^+) \approx t^2(He^+)$. Based on the previous discussion, we use the $T_0 - t^2$ dependence of the measured T_e(H I) and T_e(He I), for the 'combined cuts' spectrum, obtaining $t^2(H^+) \approx 0.036$ and $T_0(H^+) \approx 8000$ K. Using these values in equation (10) from Peimbert et al. (2002) and assuming that the volume occupied by O^+ and N^+ is the same, and that to first order, $\frac{T_e([O\,III])}{T_e([N\,II])} \approx \frac{T_0(O^{2+})}{T_0(N^+)} \approx 0.85$, we obtain $T_0(O^{2+}) \approx 7580$ and $T_0(N^+) \approx 8950$. Then, we estimate $t^2_{\rm high} = t^2(O^{2+}) \approx 0.025$ and $t^2_{\rm low} = t^2(N^+) \approx 0.050$.

The remarkably good agreement between these values and those presented in Table 7 reinforces the suitability of the temperature fluctuations paradigm to describe the results in the 'combined cuts' spectrum. Considering the numerical values obtained, we adopt the average values $t^2_{\rm high} = 0.021 \pm 0.003$, $t^2_{\rm inter} = 0.051 \pm 0.009$, and $t^2_{\rm low} = 0.064 \pm 0.011$, where the uncertainties correspond to the standard deviation of the average. Unfortunately, T_e(H I) based on the Balmer and Paschen discontinuities cannot be calculated for the individual components of the different cuts, and the estimations of t^2 must rely exclusively on the calculated T_e(He I). However, calculations similar to those used to obtain the values presented in Table 7 for the individual components of each cut show similar results. These values are presented in Table D17. Considering the higher uncertainty of the estimated t^2 based on T_e(He I) without using T_e(H I), we adopt the values of the 'combined cuts' spectrum as representative for the other components of each cut.

Following the same scheme described in Section 5.1, we recalculate the ionic abundances assuming temperature fluctuations and the results are shown in Table 8.

7 THE ABUNDANCE DISCREPANCY FACTOR

A major problem in the analysis of photoionized regions is the discrepancy between the chemical abundances derived from RLs and CELs, known as the abundance discrepancy (AD) problem. The relatively weak RLs, give systematically higher abundances than CELs. This difference is commonly quantified through the abundance discrepancy factor (ADF, Liu et al. 2000), defined here as

$$\mathrm{ADF}\left(\mathrm{X}^i\right) = \log\left(\frac{n\left(\mathrm{X}^i\right)_{\rm RLs}}{n\left(\mathrm{X}^i\right)_{\rm CELs}}\right). \quad (7)$$

There is an extensive collection of works dedicated to this problem in the literature (see Torres-Peimbert, Peimbert & Daltabuit 1980; Liu et al. 2001; García-Rojas & Esteban 2007; Stasińska et al. 2007; Tsamis et al. 2011; Nicholls, Dopita & Sutherland 2012; Gómez-Llanos & Morisset 2020, and references therein). Although there is no definitive solution, there are several hypotheses to explain the AD. For example, temperature fluctuations (see Section 6), which would primarily affect abundances based on CELs, underestimating the real values; semi-ionized gas clumps, overestimating abundances based on RLs and underestimating those of CELs; chemical inhomogeneities with different physical conditions, affecting both estimates depending on each specific case and so on. It is even possible that the AD is the result of the sum of various phenomena affecting each nebula in a different degree. Using a set of deep spectra of Galactic H II regions, García-Rojas & Esteban (2007) found that the ADF is fairly constant around a factor 2, showing no trend with ionization degree, T_e or the effective temperature of the ionizing stars. They found that temperature fluctuations is the most likely explanation for the AD in H II regions.

In Table 9, we present the ADF obtained from O^+, O^{2+}, Ne^{2+}, and C^{2+} abundances determined from RLs and CELs for each component. The abundances based on CELs do not consider temperature fluctuations. In the case of C^{2+}, the value of the abundance from CELs have been taken from the UV observations reported by Walter, Dufour & Hester (1992). We have considered the mean value of their positions number 5 and 7, which are the nearest to our slit and give $12+\log(C^{2+}/H^+) = 7.835$. We do not estimate the ADF(C^{2+}) for the high-velocity component since the UV CELs values can only be compared with the nebular component. We emphasize that the estimated value of t^2 comes from the comparison of different temperature diagnostics and the formalism described in Section 6. Therefore $t^2 > 0$, does not necessarily mean ADF > 0, unless the measured value of t^2 is compatible with this.

From Table 9, it is remarkable that the ADF is slightly different for each ion and higher in the high-velocity components. Comparing the values included in Table D15 and Table 8, we can see that using the value of t^2 adopted for each ionization zone of the nebular components, the O^{2+} abundances based on CELs become fairly consistent with those determined from RLs. In the case of the O^+ abundances, although the CELs abundances obtained with $t^2 > 0$ do not agree completely with those obtained from RLs, they become

Table 8. Chemical abundances based on CELs derived within the paradigm of temperature inhomogeneities ($t^2 > 0$).The units are logarithmic with $n(H) = 12$.

	Cut 1	Cut 2		Cut 3		Cut 4	
Ion	Nebula	HH 529 II	Nebula	HH 529 III	Nebula	Nebula	Combined cuts
O^+	$8.18^{+0.10}_{-0.08}$	$7.65^{+0.20}_{-0.12}$	$8.14^{+0.12}_{-0.09}$	$7.74^{+0.34}_{-0.17}$	$8.05^{+0.13}_{-0.09}$	$8.12^{+0.13}_{-0.09}$	$8.05^{+0.11}_{-0.08}$
O^{2+}	$8.48^{+0.06}_{-0.05}$	$8.72^{+0.04}_{-0.03}$	$8.50^{+0.05}_{-0.04}$	$8.64^{+0.04}_{-0.03}$	8.51 ± 0.04	$8.52^{+0.05}_{-0.04}$	$8.53^{+0.05}_{-0.04}$
N^+	$7.18^{+0.05}_{-0.04}$	$6.36^{+0.11}_{-0.08}$	$7.17^{+0.07}_{-0.05}$	$6.59^{+0.18}_{-0.11}$	$7.09^{+0.07}_{-0.05}$	$7.16^{+0.07}_{-0.06}$	$7.07^{+0.06}_{-0.05}$
Ne^{2+}	$7.86^{+0.07}_{-0.06}$	8.12 ± 0.04	$7.89^{+0.06}_{-0.05}$	$7.99^{+0.05}_{-0.04}$	$7.91^{+0.05}_{-0.04}$	$7.94^{+0.06}_{-0.05}$	$7.93^{+0.06}_{-0.05}$
S^+	$5.75^{+0.07}_{-0.06}$	$5.04^{+0.12}_{-0.08}$	$5.75^{+0.07}_{-0.06}$	$5.30^{+0.19}_{-0.13}$	$5.70^{+0.08}_{-0.07}$	$5.77^{+0.08}_{-0.06}$	$5.66^{+0.07}_{-0.06}$
S^{2+}	$6.87^{+0.05}_{-0.04}$	$7.01^{+0.06}_{-0.05}$	$6.94^{+0.06}_{-0.05}$	$6.97^{+0.07}_{-0.06}$	$6.95^{+0.06}_{-0.05}$	6.91 ± 0.05	6.94 ± 0.05
Cl^+	3.87 ± 0.05	$3.09^{+0.16}_{-0.14}$	$3.86^{+0.06}_{-0.05}$	<3.49	$3.81^{+0.06}_{-0.05}$	$3.90^{+0.07}_{-0.06}$	$3.76^{+0.06}_{-0.05}$
Cl^{2+}	$5.00^{+0.07}_{-0.06}$	$5.15^{+0.09}_{-0.07}$	$5.06^{+0.08}_{-0.06}$	$5.15^{+0.11}_{-0.08}$	$5.09^{+0.08}_{-0.06}$	$5.08^{+0.08}_{-0.06}$	$5.07^{+0.07}_{-0.06}$
Cl^{3+}	3.30 ± 0.06	3.71 ± 0.05	3.38 ± 0.04	$3.50^{+0.11}_{-0.10}$	3.43 ± 0.04	$3.55^{+0.05}_{-0.04}$	$3.48^{+0.06}_{-0.05}$
Ar^{2+}	6.42 ± 0.04	6.51 ± 0.03	$6.42^{+0.04}_{-0.03}$	6.46 ± 0.03	6.43 ± 0.03	$6.40^{+0.04}_{-0.03}$	$6.43^{+0.04}_{-0.03}$
Ar^{3+}	$4.55^{+0.07}_{-0.06}$	$4.84^{+0.05}_{-0.04}$	$4.63^{+0.06}_{-0.05}$	$4.66^{+0.08}_{-0.07}$	$4.66^{+0.05}_{-0.04}$	$4.79^{+0.06}_{-0.05}$	$4.69^{+0.06}_{-0.05}$
Fe^{2+*}	5.93 ± 0.02	6.11 ± 0.05	5.97 ± 0.02	5.91 ± 0.05	5.94 ± 0.02	5.92 ± 0.03	5.96 ± 0.01
Fe^{2+**}	5.75 ± 0.02	5.84 ± 0.06	5.81 ± 0.02	5.57 ± 0.06	5.75 ± 0.02	5.72 ± 0.03	5.76 ± 0.02
Fe^{3+}	$5.99^{+0.16}_{-0.12}$	$6.59^{+0.12}_{-0.10}$	$6.00^{+0.12}_{-0.09}$	<6.68	$6.23^{+0.18}_{-0.16}$	$6.05^{+0.16}_{-0.13}$	$6.16^{+0.18}_{-0.15}$
Ni^{2+}	4.52 ± 0.19	4.68 ± 0.09	4.51 ± 0.18	$4.42^{+0.20}_{-0.13}$	4.48 ± 0.16	4.51 ± 0.13	4.54 ± 0.11

Notes. * indicates that T_e(high) was used.
** indicates that T_e(low) was used.

Table 9. Abundance discrepancy factor (ADF), defined in equation (7), for different ions in the components of each cut.

Cut	Component	ADF(O^+)	ADF(O^{2+})	ADF(Ne^{2+})	ADF(C^{2+})*
1	Nebular	0.46 ± 0.14	0.15 ± 0.07	–	0.51 ± 0.03
2	HH 529 II	<0.55	0.29 ± 0.10	0.79 ± 0.09	–
2	Nebular	0.42 ± 0.12	0.17 ± 0.05	0.37 ± 0.04	0.52 ± 0.03
3	HH 529 III	<0.44	0.36 ± 0.11	–	–
3	Nebular	0.52 ± 0.14	0.17 ± 0.06	0.31 ± 0.15	0.51 ± 0.03
4	Nebular	0.46 ± 0.14	0.17 ± 0.06	–	0.50 ± 0.02
	Combined cuts	0.44 ± 0.12	0.21 ± 0.05	–	0.54 ± 0.03

Note. * We adopt $12+\log(C^{2+}/H^+) = 7.835$ from UV CELs considering the slit positions 5 and 7 of Walter et al. (1992).

clearly more similar. Definitively, this is not the case for the Ne^{2+} abundances, in which values determined from CELs and RLs still do not agree even considering $t^2 > 0$. The results obtained for O^{2+} and O^+ suggest that the temperature fluctuation paradigm may be capable of explaining the ADF, at least for these ions, the ones with the best abundance determinations based on RLs. Among different scenarios, the existence of H-deficient clumps has been advocated as a possible cause of the very high ADF values found in some PNe (e.g Péquignot et al. 2002). Since the heating of ionized gas is mainly due by photoionization of H and He and the cooling by the emission of CELs of metallic ions, this scenario implies significant lower temperatures in the clumps (Péquignot et al. 2002). As we mentioned in Section 4.3.1, the T_e(O II) determined for the nebular component of cut 2 (which must be representative of the other nebular components) is consistent with T_e([O III]) within the uncertainties, which rules out the aforementioned scenario in the nebular components analysed in this work. The situation seems to be different for the high-velocity components. Assuming $t^2 > 0$, the ionic abundances obtained from CELs do not increase enough to match the values obtained from RLs. For example, in the case of HH 529 II, considering the adopted value $t^2 = 0.021$, the ADF(O^{2+}) is reduced from 0.29 to 0.11 but is not zero. Even if we consider the value of $t^2 = 0.025$ from Table D17, the ADF(O^{2+}) would be 0.08. A similar situation is found in HH 529 III, where for $t^2 = 0.021$ the ADF(O^{2+}) is 0.20 while considering $t^2 = 0.030$ the ADF(O^{2+}) would be 0.12. Since we do not find evidence of higher temperature fluctuations than those previously commented, these results suggest the presence of another physical process apart (or in addition) to the classic description of temperature inhomogeneities to explain the ADF. A similar result was found by Mesa-Delgado et al. (2009) in the case of HH 202 S (see their section 5.5). For the high-velocity components, the presence of an H-deficient material cannot be discarded as we will discuss in Section 8.3.

8 TOTAL ABUNDANCES

We have to use ionization correction factors (ICFs) to estimate the contribution of unseen ions to the total abundance of some elements. Following the detailed analysis of Arellano-Córdova et al. (2020), we have used the ICF schemes for C, N, Ne, and Ar adopted by those authors, which are shown in Table 10. In the case of S, He, Fe, and Ni, we use the ICFs from Stasińska (1978), Kunth & Sargent (1983), Rodríguez & Rubin (2005), and Delgado-Inglada et al. (2016), respectively. Results of total abundances based on CELs are presented in Tables 11 and 12, for the cases of $t^2 = 0$ and $t^2 > 0$, respectively. Total abundances based on RLs are

Table 10. ICFs used to estimate the abundance of unseen ions.

Element	ICF Reference
He	Kunth & Sargent (1983)
C	Berg et al. (2019)
N	Peimbert & Costero (1969)
Ne	Peimbert & Costero (1969)
S	Stasińska (1978)
Ar	Izotov et al. (2006)
Fe	Rodríguez & Rubin (2005)
Ni	Delgado-Inglada et al. (2016)

presented in Table 13. In this case, we do not expect significant changes in the total abundances within the temperature fluctuation paradigm due to the low dependence of RLs on temperature. The ICFs are generally based on the degree of ionization indicated by the abundance ratio of O ions. For consistency, in the case of abundances based on CELs, we use the degree of ionization determined also with CELs. An analogous procedure is applied for abundances determined from RLs.

8.1 Total abundances with CELs

8.1.1 Oxygen, chlorine, and argon

The total abundances of O, Cl, and Ar were obtained by adding the ionic abundances of the observed ions. Although in HH 529 III we could not estimate the Cl^+ abundance, its calculated upper limit shows that its contribution is negligible. It should be noted that, in the case of Ar, the ICF model of Izotov et al. (2006) indicates that the contribution of Ar^+/H^+ to the total Ar abundance is also negligible in all the analysed components. The Cl/O and Ar/O ratios are consistent with the solar values recommended by Lodders (2019) within the uncertainties, whether we use abundances determined from CELs considering $t^2 = 0$ or $t^2 > 0$. In addition, there are no appreciable differences between the Cl/O and Ar/O ratios determined in the nebular and the high-velocity components.

8.1.2 Nitrogen, neon, and sulfur

The total abundances of N, Ne, and S depend strongly on the adopted ICF values. The schemes used for these elements are indicated in Table 10. The estimated fraction N/N^+ can reach values between 4 and 16 for the nebular and the high-velocity components, respectively. This indicates that the ICF values are rather uncertain at the high degree of ionization of the high-velocity components. However, in the nebular ones, the average value of $\log(N/O) = -0.86 \pm 0.02$ is in very good agreement with the suggested solar value of -0.88 ± 0.14 (Lodders 2019), while in the case of $t^2 > 0$, $\log(N/O) = -0.98 \pm 0.02$ is still consistent within the relatively large uncertainties of the solar abundance ratio.

Rubin et al. (2011) determined the Ne/H ratio of the Orion Nebula from FIR spectra taken with the *Spitzer Space Telescope*, that permitted to detect fine-structure [Ne II] and [Ne III] lines, avoiding the use of ICFs. They obtain $12+\log(Ne/H) = 8.01 \pm 0.01$, which is consistent with the Ne/H values we obtained for the nebular component assuming $t^2 > 0$. It is important to remark that the intensity of FIR CELs has a very small dependence on T_e. Therefore, the agreement between the Ne/H ratios obtained from FIR CELs and optical ones assuming $t^2 > 0$ supports the temperature fluctuations paradigm for describing the spectral properties of the nebula.

The Ne/O and S/O ratios are rather similar in the nebular and high-velocity components. The average values of log(Ne/O) are -0.64 ± 0.02 and -0.61 ± 0.02 for $t^2 = 0$ and $t^2 > 0$, respectively, which are consistent with the solar value of -0.58 ± 0.12 (Lodders 2019) within the uncertainties. In the case of S/O, the average values of log(S/O) for $t^2 = 0$ and $t^2 > 0$ are -1.50 ± 0.05 and -1.63 ± 0.05, respectively, while the solar value is -1.58 ± 0.08 (Lodders 2019).

8.1.3 Nickel and iron

Ni/H abundances are estimated using the ICF scheme derived by Delgado-Inglada et al. (2016) and are presented in Tables 11 and 12 for $t^2 = 0$ and $t^2 > 0$, respectively. The estimation of this abundance is rather uncertain as discussed in Section C.

In the case of Fe, considering the absence of He II lines in our spectra, we do not expect to have Fe^{4+} in the nebula and therefore $Fe/H = Fe^+/H^+ + Fe^{2+}/H^+ + Fe^{3+}/H^+$. We have determined the abundance of Fe^{2+} and Fe^{3+} in all the components of each cut except in HH 529 III, where we could only estimate an upper limit to Fe^{3+}/H^+. In the high-velocity components, the absence of usually relatively intense [Fe II] lines as λλ4287, 5158 and 5262, together with the high ionization degree of the gas, indicates a negligible contribution of Fe^+ to the total abundance. Thus, in these cases $Fe/H = Fe^{2+}/H^+ + Fe^{3+}/H^+$. In the nebular components, although a large number of [Fe II] lines have been detected, their emission is mainly produced by fluorescence (Rodríguez 1999; Verner et al. 2000) and most of the observed lines will not provide reliable estimates of Fe^+ abundance. Unfortunately, [Fe II] λ8617, a line almost insensitive to fluorescence (Lucy 1995; Baldwin et al. 1996) cannot be observed due to the physical gap of the CCDs in the Red Arm of UVES. However, previous studies with direct estimations of Fe^+ in the Orion Nebula as Rodríguez (2002) or Mesa-Delgado et al. (2009), obtain Fe^+/Fe^{+2} ratios between 0.05 and 0.27. Considering the approximation $Fe/H = Fe^{2+}/H^+ + Fe^{3+}/H^+$, the neglected Fe^+/H^+ ratio would contribute to Fe/H up to 0.06 dex in the worst case (calculating Fe^{+2}/H^+ with T_e(high) and assuming $Fe^+/Fe^{+2} = 0.27$). This maximum contribution is within the range of uncertainties associated with the sum of Fe^{2+} and Fe^{3+} abundances and therefore, it seems reasonable to consider $Fe/H \approx Fe^{2+}/H^+ + Fe^{3+}/H^+$ for the nebular component as well.

Rodríguez & Rubin (2005) proposed two ICFs for Fe, one derived from photoionization models and other based on observations with detection of [Fe III] and [Fe IV] lines. The values of Fe/H obtained using both ICFs are discrepant, perhaps due to errors in the atomic data of the ions involved. The true total Fe abundance is expected to be in between the values obtained from both ICFs (Rodríguez & Rubin 2005; Delgado-Inglada, Morisset & Stasińska 2014). We use the aforementioned ICFs only for HH 529 III and we give its Fe/H ratio as the interval of values obtained from both ICFs, as it is shown in Tables 11 and 12.

In HH 529 II, the abundances of Fe/H and Fe/O are higher than in the nebular components independently of whether the temperature T_e(low) or T_e(high) is considered to derive Fe^{2+}/H^+. The same behaviour is observed in HH 529 III for $t^2 = 0$, although the uncertainty in Fe/H do not allow us to be conclusive in the case of $t^2 > 0$. However, as is discussed in Section 4.2, the representative temperature to derive Fe^{2+}/H^+ in HH 529 II and HH 529 III is likely to be T_e(high) while in the nebular components is T_e(low).

Considering the discussion above, the average log(Fe/O) value in the nebular components is -2.53 ± 0.02 while for HH 529 II

Table 11. Total abundances based on CELs with $t^2 = 0$. The units are logarithmic with $n(\mathrm{H}) = 12$.

	Cut 1	Cut 2		Cut 3		Cut 4	
Element	Nebula	HH 529 II	Nebula	HH 529 III	Nebula	Nebula	Combined cuts
O	8.45 ± 0.02	8.57 ± 0.03	8.46 ± 0.03	8.53 ± 0.03	8.45 ± 0.03	8.47 ± 0.03	8.46 ± 0.03
N	7.57 ± 0.04	$7.40^{+0.16}_{-0.10}$	$7.62^{+0.07}_{-0.05}$	$7.45^{+0.37}_{-0.17}$	$7.60^{+0.08}_{-0.07}$	$7.64^{+0.08}_{-0.06}$	$7.60^{+0.06}_{-0.05}$
Ne	7.81 ± 0.04	7.94 ± 0.03	7.82 ± 0.04	7.84 ± 0.04	7.83 ± 0.03	7.86 ± 0.04	7.82 ± 0.04
S	6.89 ± 0.04	$7.18^{+0.07}_{-0.06}$	$6.96^{+0.08}_{-0.09}$	$7.09^{+0.11}_{-0.07}$	6.98 ± 0.05	6.94 ± 0.05	6.98 ± 0.04
Cl	4.92 ± 0.06	5.03 ± 0.05	4.97 ± 0.06	5.05 ± 0.08	4.99 ± 0.06	4.99 ± 0.06	4.97 ± 0.05
Ar	6.32 ± 0.03	6.40 ± 0.02	6.32 ± 0.03	6.37 ± 0.03	6.34 ± 0.02	6.30 ± 0.03	6.33 ± 0.03
Fe*	6.03 ± 0.06	6.42 ± 0.07	6.07 ± 0.04	6.24–6.63	6.06 ± 0.05	6.05 ± 0.06	6.08 ± 0.05
Fe**	5.91 ± 0.07	6.34 ± 0.08	5.94 ± 0.05	5.90–6.28	5.94 ± 0.07	5.92 ± 0.08	5.95 ± 0.07
Ni	4.59 ± 0.14	$5.12^{+0.15}_{-0.10}$	$4.58^{+0.18}_{-0.17}$	$4.75^{+0.29}_{-0.17}$	$4.60^{+0.17}_{-0.16}$	$4.62^{+0.13}_{-0.12}$	$4.67^{+0.11}_{-0.10}$

Notes. * indicates that T_e(high) was used to compute Fe^{++}/H^+.
** indicates that T_e(low) was used to compute Fe^{++}/H^+.

Table 12. Total abundances based on CELs with $t^2 > 0$. The units are logarithmic with $n(\mathrm{H}) = 12$.

	Cut 1	Cut 2		Cut 3		Cut 4	
Element	Nebula	HH 529 II	Nebula	HH 529 III	Nebula	Nebula	Combined cuts
O	8.66 ± 0.05	8.76 ± 0.04	8.66 ± 0.05	8.70 ± 0.05	8.64 ± 0.04	8.67 ± 0.05	8.65 ± 0.05
N	$7.66^{+0.11}_{-0.08}$	$7.45^{+0.35}_{-0.16}$	$7.69^{+0.14}_{-0.10}$	$7.46^{+0.63}_{-0.28}$	$7.68^{+0.16}_{-0.10}$	$7.71^{+0.15}_{-0.10}$	$7.68^{+0.13}_{-0.09}$
Ne	8.04 ± 0.08	8.16 ± 0.04	8.05 ± 0.07	8.04 ± 0.06	8.04 ± 0.06	$8.08^{+0.08}_{-0.07}$	$8.05^{+0.07}_{-0.06}$
S	6.95 ± 0.05	$7.24^{+0.10}_{-0.07}$	7.03 ± 0.06	$7.15^{+0.14}_{-0.09}$	$7.05^{+0.07}_{-0.06}$	$7.01^{+0.06}_{-0.05}$	$7.05^{+0.06}_{-0.05}$
Cl	5.04 ± 0.06	5.17 ± 0.09	5.10 ± 0.07	5.17 ± 0.11	5.12 ± 0.07	5.12 ± 0.07	5.10 ± 0.07
Ar	6.44 ± 0.04	6.52 ± 0.03	6.43 ± 0.04	6.47 ± 0.04	6.44 ± 0.03	6.42 ± 0.04	6.44 ± 0.04
Fe*	6.26 ± 0.09	6.71 ± 0.09	6.29 ± 0.06	6.38–6.72	6.41 ± 0.12	6.29 ± 0.09	6.37 ± 0.11
Fe**	6.19 ± 0.10	6.66 ± 0.10	6.22 ± 0.07	6.04–6.37	6.35 ± 0.14	6.22 ± 0.11	6.31 ± 0.13
Ni	4.70 ± 0.19	$5.22^{+0.26}_{-0.13}$	$4.71^{+0.19}_{-0.18}$	$4.81^{+0.42}_{-0.28}$	$4.71^{+0.18}_{-0.16}$	$4.72^{+0.15}_{-0.13}$	$4.78^{+0.13}_{-0.12}$

Notes. * indicates that T_e(high) was used to compute Fe^{++}/H^+.
** indicates that T_e(low) was used to compute Fe^{++}/H^+.

Table 13. Total abundances based on RLs. The units are logarithmic with $n(\mathrm{H}) = 12$.

	Cut 1	Cut 2		Cut 3		Cut 4	
Element	Nebula	HH 529 II	Nebula	HH 529 III	Nebula	Nebula	Combined cuts
O	8.71 ± 0.03	8.83 ± 0.07	8.70 ± 0.03	8.84 ± 0.09	8.71 ± 0.03	8.72 ± 0.03	8.73 ± 0.03
He	10.94 ± 0.02	10.95 ± 0.03	10.94 ± 0.01	10.95 ± 0.03	10.94 ± 0.02	10.95 ± 0.02	10.94 ± 0.02
C*	8.56 ± 0.04	8.46 ± 0.02	8.52 ± 0.03	8.56 ± 0.03	8.52 ± 0.04	$8.51^{+0.04}_{-0.03}$	$8.51^{+0.04}_{-0.03}$
C**	$8.48^{+0.08}_{-0.07}$		8.45 ± 0.05		$8.45^{+0.07}_{-0.06}$	8.44 ± 0.06	$8.45^{+0.06}_{-0.05}$
Ne	–	8.60 ± 0.06	8.26 ± 0.04	–	8.23 ± 0.15	–	–

Notes. * Total abundances of the nebular components derived with the ICF of Berg et al. (2019).
** Total abundances of the nebular components derived with the ICF of Amayo et al. (in preparation).

it is -2.14 ± 0.08, both values computed assuming $t^2 = 0$. This represents an increase of the gaseous Fe abundance by a factor of 2.45 in HH 529 II. The same increase is observed when considering $t^2 > 0$. For HH 529 III the increase is between 1.78 and 4.37. Taking the solar value of $\log(\mathrm{Fe/O}) = -1.28 \pm 0.08$ recommended by Lodders (2019), we find that only 6 per cent of the total Fe is in gaseous phase in the nebular component, while this fraction increases to 14 per cent in HH 529 II and between 10 per cent and 25 per cent in HH 529 III. In the case of HH 202 S, Mesa-Delgado et al. (2009) found that the gaseous phase fraction is around 44 per cent. The evidence of dust destruction on HH shocks is also present in non-photoionized objects (see Hartigan et al. 2020, and references therein). This is shown by the relative enhancement of the Fe emission lines with respect to the emission of other non-depleted elements in areas where shock waves are present. These results are consistent with theoretical studies predicting that fast shocks are effective at destroying dust grains (see Jones et al. 1994; Mouri & Taniguchi 2000, and references therein). However, it is possible to have partial depletion of Fe in jets (Antoniucci et al. 2014). An evidence of surviving dust is the detection of thermal emission of dust at 11.7 μm coincident with HH 529 II and III as well as HH 202 S (Smith et al. 2005). A key factor is to explore correlations between the Fe abundance and some properties of the HH objects, such as their velocity, density or distance to the ionizing source.

8.2 Total abundances with RLs

8.2.1 Helium

Considering the absence of an ionization front in HH 529 II and HH 529 III because of the non-detection of emission lines of neutral elements in their spectra, it is likely that the He^0/H^+ ratio should be

negligible in the high-velocity components and, therefore, we can assume He/H = He^+/H^+. In the nebular components, we estimate the fraction of neutral helium within the ionized zone making use of the ICF scheme by Kunth & Sargent (1983), obtaining that the He^0/He fraction is approximately 10 per cent. This value is consistent with the other ICF schemes tested by Méndez-Delgado et al. (2020) for the Orion Nebula. In Table 13, we can see that the He/H ratios obtained for all the cuts are in complete agreement.

8.2.2 *Oxygen*

The total O abundances based on RLs are determined directly from O/H = $O^+/H^+ + O^{2+}/H^+$. In the high-velocity components, the estimated upper limits to the O^+ abundances indicate that this ion can contribute up to 0.05 to the total O abundance. Thus, for these high-velocity components the O abundance is assumed to be equal to the ionic abundance of O^{2+}.

8.2.3 *Carbon and neon*

In the case of the high-velocity components, due to the high degree of ionization estimated from the ionic O abundances based on RLs, we expect to have small or negligible contributions of the ions once ionized from Ne and C to their total abundances. For the nebular components, we use the same ICFs schemes of Peimbert & Costero (1969) and Berg et al. (2019) for Ne and C, respectively, using ionic abundances based on RLs exclusively. It is important to note that this last ICF has been optimized for low-metallicity objects (up to 12+log(O/H) = 8.0). However, Arellano-Córdova et al. (2020) have shown that its use for higher metallicity objects provides consistent results. For comparison, in Table 13, we present the C/H ratio obtained using the ICF proposed by Amayo et al. (in preparation, private communication), whose scheme is optimized for a wider range of metallicities, including the solar one.

The resulting log(Ne/O) values based on RLs are -0.44 ± 0.03 and -0.23 ± 0.10 for the nebular components and HH 529 II, respectively. This indicates an overestimation of the Ne abundance based on RLs in HH 529 II, since it is significantly larger than the solar one. In the case of C, we obtain $\log(C/O) = -0.20 \pm 0.02$ using the ICF of Berg et al. (2019) and -0.26 ± 0.02 using the scheme of Amayo et al. (in preparation) in the nebular components. This last value is more consistent with the recommended solar value of -0.26 ± 0.09 by Lodders (2019). The log(C/O) value for HH 529 II is -0.37 ± 0.08 while for HH 529 III is -0.28 ± 0.12.

8.3 A slight higher metallicity in the high-velocity components?

An interesting result of our analysis is that the metal abundances are higher in the high-velocity components, HH 529 II and HH 529 III, than in the nebular ones. In the case of the O abundance, that difference can reach up to 0.14 dex, regardless if abundances are calculated with CELs or RLs. Mesa-Delgado et al. (2009) estimated that 0.12 ± 0.03 dex of log(O/H) is depleted into dust grains in the Orion Nebula. In principle one may explain the 0.14 dex increase of O/H in the HH objects as produced by dust destruction, and that all the O locked in grains has been released to the gas phase. Nevertheless, the Ar/O, Ne/O, S/O, and Cl/O ratios remain almost the same in all components. Since Ar and Ne are noble gases, they cannot be depleted into dust grains and, therefore, lower abundance ratios would be expected if dust destruction is increasing the gaseous O abundance. In addition to this, considering that the O trapped on to dust grains is in olivine $(Mg, Fe)_2SiO_4$, pyroxene (Mg, Fe)SiO_3 or oxides like Fe_2O_3, then the gaseous O must grow in proportion to the release of elements like Fe to the gas phase. Considering this, Mesa-Delgado et al. (2009) estimated that 0.06 dex of log(O/H) can be attributed to dust destruction in HH 202 S. As we mention in Section 8.1.3, the proportion of gaseous Fe present in in HH 529 II and HH 529 III is lower than in HH 202 S, and therefore, the expected increase of log(O/H) in the two bow shocks of HH 529 should be consequently less than 0.06 dex.

BMB06 also report a higher O abundance in HH 529 with respect to the nebular one. The difference they obtained was slightly larger than ours, of around 0.2 dex. This value is confirmed in the later reanalysis of BMB06 data carried out by Simón-Díaz & Stasińska (2011). However, as we discussed in Section 3, part of the larger difference found by BMB06 with respect to our O/H ratio may be due to their underestimation of I(Hβ), as we illustrate in Table D1.

Assuming that the abundance difference between the kinematical components is real, one possible explanation is that the bulk of the material of the HH objects comes from H-deficient material expelled by the source of the gas flow. As we mentioned in Section 7, an H-deficient ionized gas should be colder than one with normal chemical composition but this in not observed (see Table 4). This may be because the possible over-metallicity is actually small, which might not significantly alter the temperature. The origin of the H-deficent material may be in the evaporation of protoplanetary discs around newly formed stars (Yuan et al. 2011), a probable scenario for the origin of HH 529. In this sense, it is a well-known fact that HH 529 is a source of IR emission (Robberto et al. 2005; Smith et al. 2005), emitting strongly at 10 and 11.7 μm. Smith et al. (2005) show that the 11.7 μm radiation arises from thermal dust emission and is visible both behind the leading bow shock and within the jet body of HH 529 (see their fig. 7). After analysing different scenarios, Smith et al. (2005) conclude that the dust may be entrained from the origin of the jet, which implies that at least part of the ejected material comes from a radius larger than the sublimation radius in the accretion disc of the source. Some of this material may originally come from H-deficient solids. However, the mechanism of expulsion of this H-deficient material and its interaction with the ambient gas requires a deeper analysis of solid body destruction in new formed stars, an idea further explored in planetary nebulae (Henney & Stasińska 2010). Tsamis et al. (2011) obtained deep optical integral field spectroscopy of the LV2 proplyd in The Orion Nebula, determining, for the first time, the chemical composition in this kind of objects. They find that the abundances of O, C and Ne in the ionized gas of the proplyd are between 0.11 and 0.52 dex higher than in the rest of the nebula. This result is somehow qualitatively consistent with the overmetallicity we find for the bow-shocks of HH 529, supporting the possibility that the entrained material of the HH objects may come from the source of the gas flow. However, the abundance pattern found for LV2 is not confirmed in the proplyd *HST* 10, where the chemical composition is not substantially different from the nebular gas (Tsamis et al. 2013).

Finally, we should keep in mind that the apparently larger metallicity of the HH objects may be simply produced by the atomic data used for the analysis. As Juan de Dios & Rodríguez (2017) have discussed, uncertainties in the atomic data may be more important for high-density objects (densities above 10^4 cm^{-3}) because there is less possibility to check them observationally. Subsequent analysis of new photoionized HH objects, whose analysis we are carrying out, can shed further light on this issue.

9 KINEMATICAL ANALYSIS FROM UVES DATA

We calculate the radial velocity of each line in the heliocentric framework by comparing its observed wavelength (after applying the radial velocity correction) with its theoretical wavelength in air. All the theoretical values have been taken from the Atomic Line List v2.05b21 (Van Hoof 2018). Wavelengths from this compilation list are mainly calculated from the theoretical energy difference between the levels connected by the transition. The exception are the hydrogenic lines, which include a weighted average of all the fine structure components.

We detect some evident inaccuracies in the theoretical wavelengths of [Cl III], [Cl IV], and [Ne III] in the Atomic Line List v2.05b21. This conclusion is based on the discrepant velocities that those lines show with respect to the rest of lines in the high-velocity components, which show fairly similar velocities independently of the ionization state of the ions and elements (see Section 9.1). For example, in the case of [Ne III] λλ3869, 3967, the Atomic Line List v2.05b21 gives λλ3869.07 ± 0.09 and 3967.79 ± 0.10 based on the works of Persson et al. (1991) and Feuchtgruber et al. (1997). These wavelengths give velocities about −20 km s^{-1} displaced with respect to the mean velocity obtained for the rest of the lines. In this case, we decided to adopt the wavelengths λλ3868.75 and 3967.46 obtained by Bowen (1955) from high-resolution spectroscopy of nebulae. The [Cl III] and [Cl IV] lines show a similar problem; in this case, we adopt the reference wavelengths used by Esteban et al. (2004) that give consistent velocities. The wavelengths adopted for [S III] lines deserve special attention. The values given by the Atomic Line List v2.05b21 are λλ6312.1 ± 0.36, 8829.4 ± 0.49, 9068.6 ± 0.52, and 9530.6 ± 0.57, taken from the work by Kaufman & Martin (1993). There is a small (but noticeable at our spectral resolution) discrepancy in the velocity obtained for [S III] λ6312 and the rest of the lines of about 10 km s^{-1}. Assuming the velocities measured for the H I lines of HH 529 II, our best estimation of the rest wavelengths of the observed [S III] lines are: λλ6312.07 ± 0.01, 8829.70 ± 0.01, 9068.93 ± 0.04, and 9530.98 ± 0.01.

9.1 Radial velocity structure

In Table D18, we present the average velocity and FWHM of each ion observed in the nebular component of cut 2 and in HH 529 II and III. The behaviour of the nebular component of cut 2 is representative of what is observed in the nebular components of the other cuts. In each column, we include in parentheses the number of lines of each kind whose values have been averaged. In this analysis, we discard lines with known blends and those affected by ghosts or by telluric emissions/absorptions. For O I, O II, C II, and Ne II lines, we include only those used in Section 5.2 for abundance determinations, which are the lines that are assumed to be produced by pure recombination and are most probably not affected by fluorescence. In the special case of [S III] lines we consider only the λ6312 line, due to the aforementioned evident inaccuracies in the theoretical wavelengths of the rest of the [S III] lines. Fig. 13 shows the heliocentric velocity as a function of ionization potential relation for the data collected in Table D18.

From the upper left panel of Fig. 13, it is clear that the nebular component presents a pattern consistent with the 'blister' model for the Huygens Region of the Orion Nebula (and references therein O'Dell 2001; Ferland 2001; O'Dell, Abel & Ferland 2020). The basic idea is that a layer of gas of the Orion Molecular Cloud (OMC) facing the direction towards the Sun is ionized by θ^1 Ori C, which is located in the foreground of OMC. As the gas gets ionized, it is accelerated towards the observer. Velocities of [O II], [C II], and [N II] are similar to the average velocity of the molecules in the OMC of ∼28 km s^{-1} (Goudis 1982; O'Dell 2018, and references therein), then a rapid drop in the observed velocity (which means an increase in velocity compared to the OMC's systemic velocity) of the ions whose ionization potential are between 6.77 and 13.6 eV is observed as well as a constant velocity after 13.6 eV. This behaviour has been observed in previous works (Kaler 1967; Fehrenbach 1977; O'Dell & Wen 1992; Esteban & Peimbert 1999).

In the lower panels of Fig. 13, we present the observed radial velocity of the ions as a function of their ionization potential for the high-velocity components: HH 529 II (lower left panel) and HH 529 III (lower right panel). Contrary to what the nebular components show, all the ions of the high-velocity components show a fairly constant radial velocity, independently of their ionization potential. Moreover, the high-velocity components do not show emission lines of neutral ions. These features are consistent with the scenario of a fully ionized slab of gas moving at a different velocity with respect to the rest of the nebular gas.

In the upper right panel of Fig. 13, we present the difference between the radial velocity pattern of the nebular component and HH 529 II (the subtraction of the upper and lower left panels of Fig. 13) rescaled using the average radial velocity of 51 H I lines in HH 529 II, whose rest-frame reference wavelengths λ_0 are the best determined among all the ions. Doing that subtraction, we can see that the dispersion of the data points represented initially in the upper left panel decreases substantially. This fact indicates that the dispersion is not due to errors associated with the determination of the wavelength of the lines or to a complex velocity structure, but to inaccuracies in the adopted rest-frame reference wavelengths or possibly in the wavelength calibration. By eliminating the aforementioned dispersion, we can demonstrate that the acceleration of the gas in the Orion Nebula is constant for ionization potential between 6.77 and 13.6 eV, becoming zero for energies above, reaching a constant velocity of 16.4 ± 0.8 km s^{-1}.

There is a difference of 5.18 ± 1.25 km s^{-1} between the radial velocities of HH 529 II and III. This is due to the presence of unresolved lower velocity components in HH 529 III, as it is shown in Fig. 14, which also contribute to increase the dispersion in the radial velocity structure of this component.

The radial velocities of the selected O I, O II, and Ne II lines are practically the same as those of [O II], [O III], and [Ne III] CELs, respectively, in the nebular component. This reinforces the assumption that they are produced by pure recombination. For example, lets consider the O I RLs from multiplet 1, which come from quintuplet levels. If these lines were produced by fluorescence, they would be emitted in neutral and partially ionized zones of the nebula and should show a radial velocity similar to the systematic one of the OMC. In fact, O I lines from transitions between triplet levels (such as multiplet 4 λλ8446.25, 8446.36, 8446.76) are displaced around ∼10 km s^{-1} with respect to the velocity of the aforementioned multiplet 1, clearly indicating the different nature of both multiplets, with the lines of multiplet 4 originating in starlight excitation (Grandi 1975b).

9.2 Electron temperature from thermal broadening of the line profiles

The observed line widths are the result of several physical processes. Apart from the instrumental width, σ_{ins}, the main contributors are the thermal width, σ_{th}, the fine structure broadening, σ_{fs} and the non-thermal contribution, σ_{nt}, which includes effects such as turbulence and any other additional broadening process. Following García-Díaz

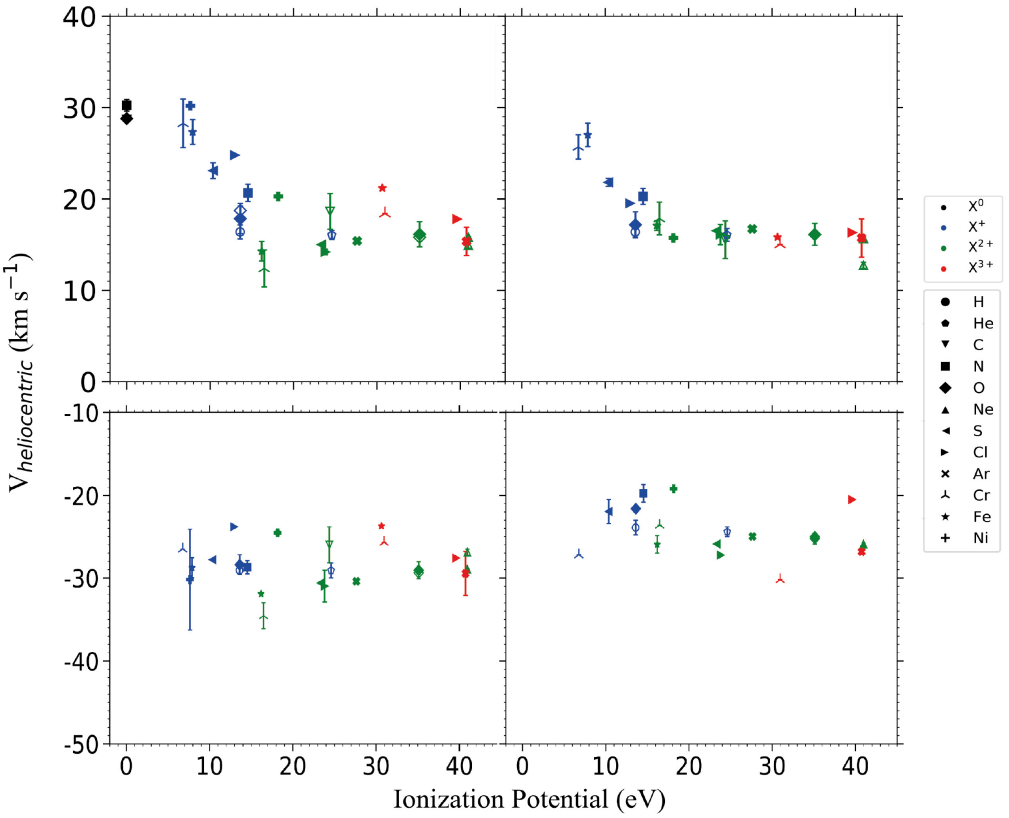

Figure 13. Observed radial velocity of the ions as function of the ionization potential. The upper left, bottom left, and bottom right panels correspond to the radial velocities derived by considering the rest-frame reference wavelength λ_0 and the observed one λ in the heliocentric frame of reference for the nebular component of the cut 2, HH 529 II, and HH 529 III, respectively. The upper right panel is defined with the difference of velocities between the nebular component and HH 529 II (subtraction of the upper and lower left panels) and rescaled using the velocity determined for H I lines, whose rest-frame reference wavelengths λ_0 are the best determined ones.

et al. (2008, hereinafter GHLD08, see their equation 2), we use equation (8) to express the relationship commented above:

$$\sigma^2_{obs} = \sigma^2_{th} + \sigma^2_{fs} + \sigma^2_{ins} + \sigma^2_{nt}. \quad (8)$$

The thermal contribution of equation (8) is the Doppler broadening and depends linearly on the temperature, $\sigma^2_{th} = 82.5\ T_4/A$ (km s^{-1})^2, where A is the atomic weight of the emitting ion and $T_4 = T_e/10^4$ (GHLD08).

In principle, using equation (8) we can estimate T_e from the subtraction of the observed widths of H I and [O III] lines. The instrumental width affects the same for both kinds of lines and should be cancelled in the subtraction. GHLD08 estimated σ^2_{fs} (H I) = 10.233 (km s^{-1})^2, finding that σ^2_{fs} ([O III]) is negligible. On the other hand, σ^2_{nt} (H I) is not strictly equal to σ^2_{nt} ([O III]), since the nebular volume occupied by both ions is different. GHLD08 define f as the fraction of the volume of H^+ occupied by O^{2+} and $(1 - f)$ the fraction filled by O^+ and other ions with lower degree of ionization, as N^+. We assume the average value $\langle f \rangle = 0.76$ estimated by GHLD08 for the Orion Nebula. Using equations 7 to 10 from GHLD08, we obtain T_e = 8340 ± 410 k for the nebular component. In the case of the high-velocity components, we assume $f = 1.0$, obtaining $T_e = 8670 \pm 50$ K and $T_e = 10470 \pm 790$ K for HH 529 II and HH 529 III, respectively.

The resulting T_e values in the nebular component of cut 2 and HH 529 II are in remarkably good agreement with T_e([O III]) from CEL ratios as shown in Table 4. In the case of HH 529 III, the large difference between the values obtained from both methods may be due to the contamination by several unresolved velocity components, as it is shown in Fig. 14 and discussed in Section 10, that broadens the lines, providing overestimated temperatures.

10 PROPER MOTIONS OF HH 529 II AND III

The plane-of-sky motions of the bow shocks in HH 529 have been previously reported in table 3 of O'Dell & Henney (2008) and in section 3.3.1.3 of O'Dell et al. (2015). However, the reported tangential velocities are very disparate, so we have re-measured the proper motions, using *HST* imaging over 20 yr as described in Section 2. The 1995 and 2015 images were aligned to the 2005 ACS image using Astrodrizzle[5] and rebinned to the ACS pixel

[5]https://drizzlepac.readthedocs.io

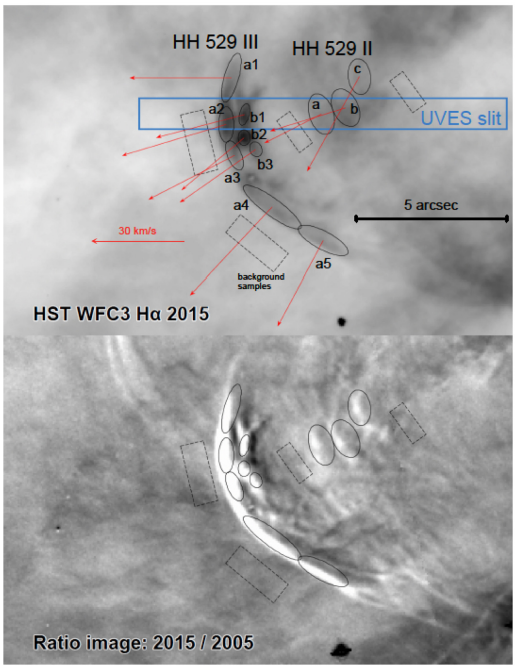

Figure 14. Tangential velocities of shock features in HH 529 II and III derived from three epochs of *HST* imaging. Upper panel shows various discrete features identified in the bow shocks (black ellipses with arrows indicating the average proper motion of each feature). Small dashed rectangles indicate regions where the nebular background brightness was measured and the large blue rectangle shows the position of the spectrograph slit. The background negative greyscale shows an *HST* WFC3 image in the F656N filter from 2015. Lower panel shows the ratio between the 2015 image and an *HST* ACS image in the F658N filter from 2005 (white means brighter in 2015). This highlights the changes in the nebula over that 10-yr period, which are principally due to motions of the shocked gas.

scale of 0.05 arcsec. The 2005 image itself has been aligned to the absolute astrometric reference of 2MASS, as painstakingly described in section 3.3 of Robberto et al. (2013). Proper motions are estimated for the two intervals, 1995–2005 and 2005–2015, using the Fourier Local Correlation Tracking (FLCT) method (Welsch et al. 2004; Fisher & Welsch 2008)[6] with a kernel width of 10 pixels (0.5 arcsec). For an assumed distance of 417 pc, a shift of 1 pixel in 10 years corresponds to approximately 10 km s^{-1}. A potential disadvantage of using the ACS data in this study is that the F658N ACS filter is relatively broad and includes both Hα λ6563 and [N II] λ6583, whereas the WFPC2 and WFC3 F656N filters are narrower and more effectively isolate λ6563. Ionization gradients in the nebula can therefore contribute to differences in the images obtained, which would obscure the signal due to the gas motions. However, the degree of ionization in HH 529 III and II is so high that this turns out not to be an issue in this object. Results are presented in Table 14 and Fig. 14.

[6]We used version 1.07 of FLCT, obtained from http://cgem.ssl.berkeley.edu/cgi-bin/cgem/FLCT/home, together with version 1.04 of the PYTHON wrapper pyflct, obtained from https://github.com/PyDL/pyflct.

Table 14. Proper motions of shock features.

Feature (1)	UVES cut (2)	V_t (km s^{-1}) (3)	PA (deg) (4)	Contrast S(Hα)/S(Hα, BG) (5)
HH 529 III a1		33 ± 3	90 ± 3	0.46 ± 0.14
HH 529 III a2	3	36 ± 1	107 ± 7	0.82 ± 0.11
HH 529 III a3		32 ± 1	117 ± 3	0.52 ± 0.14
HH 529 III a4		39 ± 2	137 ± 5	0.41 ± 0.07
HH 529 III a5		32 ± 1	152 ± 10	0.27 ± 0.07
HH 529 III b1	3	30 ± 2	105 ± 3	0.95 ± 0.09
HH 529 III b2		27 ± 1	130 ± 1	1.14 ± 0.10
HH 529 III b3		30 ± 2	125 ± 4	0.64 ± 0.07
HH 529 II a	2	21 ± 9	117 ± 58	0.25 ± 0.03
HH 529 II b	2	26 ± 5	107 ± 4	0.35 ± 0.08
HH 529 II c		35 ± 9	151 ± 87	0.22 ± 0.03

Note. COLUMNS: (1) Name of shock feature (see Fig. 14 for positions). (2) Spatial cut of the UVES spectrum where this feature appears, if any. (3) Mean tangential velocity for each feature, weighted by background-subtracted surface brightness, S(Hα), of each pixel. (4) Mean position angle of proper motion, weighted in the same way. (5) Mean relative Hα brightness with respect to nebular background (BG). For columns 3, 4, and 5, the ± uncertainties correspond to the root-mean-square variation over each sample region and do not include systematic uncertainties, which are of order 2 km s^{-1}.

We find that HH 529 III consists of at least two distinct moving structures. The large outer curved bow, which we call III a, is relatively smooth, spanning about 7 arcsec in its brightest part, but with fainter wings (best visible on the ratio image) that extend farther. We cover the bright part of the bow with five sample ellipses: a1–a5, where a3 seems to be the apex of the bow but a2 is the one that falls in the UVES slit. Roughly 0.7 arcsec to the east of III a is a smaller, knottier bow, which we call III b and cover with three sample ellipses: b1, b2, and b3. The brightest knot is b2, but it is the b1 sample that falls in the UVES slit. HH 529 II is found to consist of three distinct bows with separations of order 1 arcsec, which we call II a, II b, and II c, with II a and II b falling in the UVES slit.

Considering the OMC reference frame (28 ± 2 km s^{-1}, Goudis 1982), we obtain v_{tot} values of 62.68 ± 3.30 and 67.01 ± 3.09 km s^{-1} for HH 529 III and HH 529 II, respectively. To obtain those numbers we have used the weighted average tangential motion of 35 ± 5 km s^{-1}, calculated with components a, b, a2, and b1 of HH 529 (see Fig. 14) and the radial velocities shown in Table D18). On the other hand, using the ratio between the average tangential and radial velocities and considering a systematic uncertainty of ∼2 km s^{-1} between the OMC and the stellar source, we estimate a flow angle of 58° ± 4° for HH 529. This value is in agreement with the result of O'Dell & Henney (2008) (∼54°) but discrepant with the value obtained by O'Dell et al. (2015) (∼83°).

11 PHYSICAL ASPECTS OF THE HIGH-VELOCITY COMPONENTS

Since the material in the HH outflows is moving highly supersonically with respect to the ionized sound speed in the nebula, it will give rise to shocks where the flow and nebula interact (Hartigan, Raymond & Hartmann 1987). Further internal shocks may form inside the outflow if its velocity varies with time (Raga et al. 1990). It is important to investigate the degree to which direct excitation by the shocks might be affecting our emission line analysis.

In this section, we first calculate the heating and compression expected behind a shock wave and then we use results of non-equilibrium Cloudy simulations to predict the relative contributions of the post-shock cooling zone and the equilibrium photoionized shell to the emission line spectrum of the knots.

11.1 Shock compression and heating

A non-magnetized hydrodynamic shock is characterized by its Mach number $\mathcal{M} = V_{\rm sh}/c_{\rm s}$, where $V_{\rm sh}$ is the shock velocity and $c_{\rm s}$ is the pre-shock adiabatic sound speed. On passing through the shock, the gas is heated (Zel'Dovich et al. 1967) to a temperature T_1, which is higher than the equilibrium photoionized temperature, T_0:

$$\frac{T_1}{T_0} = \frac{1}{16}\left(5\mathcal{M}^2 - 1\right)\left(1 + 3\mathcal{M}^{-2}\right), \tag{9}$$

while at the same time it is compressed by a factor

$$\frac{\rho_1}{\rho_0} = \frac{4\mathcal{M}^2}{\mathcal{M}^2 + 3}. \tag{10}$$

In both cases, a ratio of specific heats $\gamma = 5/3$ is assumed, as is appropriate for ionized and atomic gas. The post-shock gas then cools in a radiative relaxation layer until it returns to the equilibrium temperature $T_2 \approx T_0$, reaching a final density compression factor of

$$\frac{\rho_2}{\rho_0} = \frac{5}{3}\mathcal{M}^2. \tag{11}$$

The adiabatic sound speed in the equilibrium ionized gas is given by $c_{\rm s} = (\gamma k T_0/\mu m_{\rm H})^{1/2}$,where k is the Boltzmann constant, T_0 is the temperature, $m_{\rm H}$ is the hydrogen mass and μ is the mean atomic mass per particle. Assuming that all He is singly ionized with y = He/H = 0.087 (Table 13) yields $\mu \approx (1 + 4y)/(2 + 2y) \approx 0.62$, which combined with $T_0 = 8480$ K (Table 4) implies an adiabatic sound speed of $\sim 13.7\,{\rm km\,s^{-1}}$.

The case of a magnetized shock is considerably more complicated (Bazer & Ericson 1959), but the principle effect is that the component of the magnetic field, B, parallel to the shock front provides extra pressure support (magnetic cushioning) in the post-shock gas (Hartigan, Morse & Raymond 1994; Hartigan & Wright 2015). An approximate way to account for this is to replace the sound speed in the above equations by the fast magnetosonic speed: $V_{\rm fast} = (c_{\rm s}^2 + V_{\rm A}^2)^{1/2}$, where $V_{\rm A} = B/(4\pi\rho)^{1/2}$ is the Alfvén speed. The ambient gas inside an H II region is expected to have a low Alfvén speed of $V_{\rm A} \approx 2\,{\rm km\,s^{-1}} \ll c_{\rm s}$ (Arthur et al. 2011) so that the magnetic cushioning will be negligible in shocks propagating in the ambient medium. On the other hand, the Alfvén speed in the jet itself (Hansen, Frank & Hartigan 2015; Pudritz & Ray 2019) may be sufficiently high so as to limit the compression behind shocks driven into the jet.

Considering the *isothermal* Mach number $\mathcal{M}_{\rm s} = \gamma^{1/2} V_{\rm sh}/c_{\rm s}$, we estimate $\mathcal{M}_{\rm s} = 5.31 \pm 0.28$ and $\mathcal{M}_{\rm s} = 5.68 \pm 0.27$ for HH 529 III and HH 529 II, respectively, on the assumption that both are external working surfaces. By using the estimated densities of the HH objects as post-shock densities, n_2, in equation (11), we can estimate a value for the pre-shock densities, n_0. In the case of HH 529 III, we obtain $n_0 = 1070 \pm 310\,{\rm cm^{-3}}$, a value that is consistent with photoionized areas of the Orion Nebula outside the Huygens region, where the density decreases radially (Mesa-Delgado et al. 2008). This would place HH 529 III in the foreground of the main ionization front. For HH 529 II, the pre-shock density, $n_0 = 370 \pm 70\,{\rm cm^{-3}}$, would indicate that the impact with the ambient gas is taking place in a more external zone from where HH 529 III does, being located farther from the main ionization front (and closer to the observer). However, this scenario seems unlikely.

Considering the complex velocity structure of HH 529 II+III (see Fig. 14), that HH 529 III is almost a factor 3 denser than HH 529 II, that both objects present similar velocities (in the frame of reference of the OMC) and ionization degree, it is likely that HH 529 II is rather an internal working surface of the jet beam (Masciadri & Raga 2001). In this case, the relevant $\mathcal{M}_{\rm s}$ would be substantially smaller than 5.68. This internal shock may be due to temporal velocity variations in the jet from the common source of HH 529 (possibly located at the star COUP 666, O'Dell et al. 2015).

The absence of [O I] CELs (see Fig. 2) and the weakness of lines of low ionization potential ions (e.g. [O II] or [N II]) demonstrate that HH 529 II and HH 529 III are fully photoionized objects and do not contain a trapped ionization front (Masciadri & Raga 2001), contrary to what was found by Mesa-Delgado et al. (2009) in the case of HH 202 S. Therefore, the entire jet beam should be observable in optical emission lines, contrary to partially ionized or neutral HH objects, where only limited regions can be observed in the optical (Raga et al. 2000a, b). Since HH 529 is flowing at an angle of $\sim 58^\circ$ with reference to the plane of the sky, the observed spectra of the HH objects should integrate both the compressed gas at the leading working surface and the gas of the jet beam behind. Which of these dominates the total emission depends on the relative densities of the jet and the ambient medium (Hartigan 1989). In the case of HH 529 III, it is possible that the two components, a and b, resolved by *HST* (see Fig. 14) represent respectively the bowshock (shocked ambient medium) and Mach disk (shocked jet). However, these are unresolved in our slit spectra.

11.2 Shock emission versus shell emission

In order to estimate the shock contribution to the line emission from the working surface, we are going to consider the high-temperature radiative relaxation layer (cooling zone) that lies immediately behind the shock.

The post-shock gas in the working surface will be accelerated away from the jet axis by lateral pressure gradients, flowing sideways out of the working surface at the isothermal sound speed through a 'Mach ring' (Falle & Raga 1993), with radius approximately equal to that of the jet, $r_{\rm jet}$. In a steady state, the outward mass flux through the Mach ring must be equal to the inward mass flux through the shock, while the isothermal Bernoulli equation shows that the density at the Mach ring is $e^{-1/2}\rho_{\rm ws}$, where $\rho_{\rm ws}$ is the density of the working surface. This yields the thickness of the working surface as $H = \frac{1}{2}e^{1/2} r_{\rm jet}/\mathcal{M}_{\rm s}$. We assume that $r_{\rm jet} = 2$ mpc, which is half the observed lateral extent of the HH 529 II knots.[7] The thickness of the cooling zone, $d_{\rm cool}$ is approximately the immediate post-shock velocity multiplied by the cooling time. This implies that, in our case, $d_{\rm cool}/H \approx 0.1$, being thin compared with the total thickness of the working surface.

The contribution of this thin cooling zone should be equal to the kinetic energy flux through the shock:

$$F_1 = \frac{1}{2}\rho_0 V_{\rm s}^3 \quad {\rm erg\,cm^{-2}\,s^{-1}}, \tag{12}$$

whereas the radiative flux from the cooled equilibrium gas in the working surface is

$$F_2 = n_2^2 \Lambda_0 H \quad {\rm erg\,cm^{-2}\,s^{-1}}, \tag{13}$$

[7] At the distance of the Orion Nebula, 1 arecsec $\approx$ 2 mpc.

where Λ_0 is the cooling coefficient of the equilibrium gas. Assuming $\Lambda_0 = 2.5 \times 10^{-24}$ erg cm^3 s^{-1}(Osterbrock & Ferland 2006), the ratio of equations (12) and (13) is then

$$\frac{F_1}{F_2} = 195 \times \mathcal{M}_s^2 \times \left(\frac{n_2}{\mathrm{cm}^{-3}}\right)^{-1} \times \left(\frac{r_{\mathrm{jet}}}{\mathrm{mpc}}\right)^{-1}. \quad (14)$$

We find that $F_1/F_2 \approx 0.1$ for HH 529 III, whereas for HH 529 II, assuming that HH 529 II moves at 20 km s^{-1} with respect to the internal velocity of the jet beam, $F_1/F_2 \approx 0.03$. However, it should be noted that the F_1/F_2 value found for HH 529 III is rather an upper limit to the real contribution of the cooling area since we have used the total velocity with respect to the OMC to define the Mach number, while a shock within the photoionized gas of the Orion Nebula must consider its internal velocity structure, which moves radially towards the observer (see Section 9.1), as well as partially does HH 529. In addition to this, although HH 529 III is observed as a prominent arch, the possibility that it is preceded by other shocks cannot be ruled out. As recent analyzes have shown, there is at least one high ionization shock to the east of HH 529 III that may be related to the gas flow of HH 529 (labelled as 'East Shock' in O'Dell et al. 2015), in which case it would imply a lower Mach number than the one used.

From an observational point of view, the spectrum of HH 529 III have logarithmic values of $I(\,[\mathrm{O\,III}]\,\lambda5007)/I(\mathrm{H}\beta) = 0.69$ and $I(\,[\mathrm{N\,II}]\,\lambda6584)/I(\mathrm{H}\alpha) = -1.34$, while HH 529 II have $I(\,[\mathrm{O\,III}]\,\lambda5007)/I(\mathrm{H}\beta) = 0.69$ and $I(\,[\mathrm{N\,II}]\,\lambda6584)/I(\mathrm{H}\alpha) = -1.60$. These values are in complete agreement with those expected in star-forming regions, as shown by the curve derived by Kauffmann et al. (2003) in their equation (1), based in photoionization models. Furthermore, the values of $\log(I(\,[\mathrm{S\,II}]\,\lambda6716 + 31)/I(\mathrm{H}\alpha))$ in both components are ~ -2.45, also consistent with the typical values of ionized nebulae and very far from the range of values observed in objects ionized by shock energy (between -0.5 and 0.5), such as supernova remnants and non-photoionized HH-objects (Canto 1981; Riera et al. 1989).

Finally, a value of $F_1/F_2 \approx 0.1$ in HH 529 III (i.e. a Mach number $\sim$5) would imply a post-shock temperature as high as 70 000 K (see equation 9) in the thin cooling zone. At such high-temperature, the gas emits pre-dominantly at far-ultraviolet (FUV) wavelengths, via lines such as C III] λ1909 and C IV λ1549, whereas most of the optical lines studied in this paper are minor coolants in such conditions. Therefore, even in this extreme case, the optical spectra analysed in this work would have a contribution probably much smaller than a factor of 0.1.

We have calculated time-dependent photoionized shock models using the Cloudy plasma physics code (Ferland et al. 2013, 2017) in order to investigate this, taking the [O III] λ5007 line as a typical example. We find that for gas in photoionization equilibrium with the radiation field from the Trapezium stars, a fraction $f_{5007} = 0.33$ of the total radiative cooling is due to this line. For the cooling zones behind low-velocity shocks, this fraction initially increases slightly with shock velocity, reaching a maximum value $f_{5007} = 0.37$ for $V_s \approx 20\,\mathrm{km\,s^{-1}}$, but subsequently declines, falling to $f_{5007} = 0.11$ for $V_s \approx 70\,\mathrm{km\,s^{-1}}$ as the FUV lines take over the majority of the cooling. The 5007-emission-weighted average temperature of the cooling zone saturates at $T \approx 16000\,\mathrm{K}$ for $V_s > 50\,\mathrm{km\,s^{-1}}$, indicating that the conditions in the post-shock [O III] emission zone become insensitive to the shock velocity. For recombination lines such as Hα, the emissivity declines with increasing temperature, so that the contribution of the post-shock zone to the total emission is negligible. On the other hand, for some weak lines we would expect a relatively larger shock-excited contribution. For instance, an auroral line such as [O III] λ4363 has an excitation temperature that is roughly double that of λ5007, so will be relatively enhanced in the cooling zone. However, in both high-velocity components, T_e([O III]) is consistent with the values of the Orion Nebula, which implies that there are no significant effects. Although in our case, all the indicators used show that the shock contribution in the observed optical spectra of HH 529 II and HH 529 III is negligible, the detailed effects of post-shock cooling on an optical spectrum clearly deserves a deeper study.

12 SUMMARY AND CONCLUSIONS

We have observed two of the bow shocks of the photoionized Herbig-Haro object HH 529: HH 529 II and HH 529 III, inside the Orion Nebula, under photometric conditions with the UVES echelle spectrograph at VLT. Our observations have an effective spectral resolution of $\sim$6.5 km s^{-1} and cover a spectral range of 3100–10420Å. We defined 4 spatial cuts in our 10 arcsecs-long slit to separate HH 529 II from HH 529 III. Our spatial and spectral resolution permitted us to resolve the blueshifted high-velocity components of HH 529 II and III from the nebular emission of the Orion Nebula. Thus, we analysed six 1D spectra: four of the nebular emission and one of each bow shock. We measured up to 633 emission lines in the Orion Nebula and 376 and 245 in the cases of HH 529 II and III, respectively. We defined an additional spectrum labelled as 'combined cuts' with the sum of all components to study the impact of the HH objects in a single low-spectral resolution long-slit observation. We also take advantage of the 20 yr of archival *HST* imaging to analyse proper motions of HH 529 and their physical impact.

Considering the absence of emission lines of neutral elements such as [O I] and the rather faint emission from low ionization ions such as [O II] in HH 529 II and III, we conclude that they are fully photoionized and present a high ionization degree. We analyse the influence of the shock energy in our spectra of HH 529 II and HH 529 III and all evidences indicate a certainly minor contribution, presenting values consistent with normal H II regions. We analysed five density diagnostics based on CEL ratios. We found a mean value of $n_e \approx 6000 \pm 1000\,\mathrm{cm^{-3}}$ for the nebular components. We obtain $n_e = 11880 \pm 1860\,\mathrm{cm^{-3}}$ and $n_e = 30200 \pm 8080\,\mathrm{cm^{-3}}$ for HH 529 II and III, respectively, concluding that at so high values, the density diagnostics based on [Fe III] lines are more suitable than the usual ones. We determined the density of each component using the RLs of multiplet 1 of O II, finding that it does not differ from the one derived from CELs in the nebular components. However, the results based on O II RLs are inconsistent with other diagnostics in the case of HH 529 II and III.

Using CEL ratios, we study six T_e-diagnostics. We derive mean values of T_e(low) $\approx 10000 \pm 200$ K and T_e(high) $\approx 8500 \pm 150$ K for the temperature of the low and high ionization degree zones, respectively, in the nebular components. For HH 529 II we obtain $T_e(\mathrm{low}) = 10150^{+570}_{-510}$ K and $T_e(\mathrm{high}) = 8270 \pm 110$ K. For HH 529 III, we derive $T_e(\mathrm{low}) = 11040^{+920}_{-970}$ K and $T_e(\mathrm{high}) = 8630 \pm 120$ K. These results indicate that the temperature are very similar in the nebular and the high-velocity components, although there is a slight increase in temperature in the shock front (HH 529 III). For the nebular component of cut 2, we were able to estimate T_e from O II RLs, obtaining $T_e(\mathrm{O\,II}) = 9350 \pm 1090$. The good agreement between T_e(O II) and n_e(O II) with the physical conditions obtained with CELs in the nebular components demonstrate that the emission of CELs and RLs of O^{2+} come basically from the same gas, ruling out the possibility of cold clumps dominating the emission in RLs. For all components, we derive T_e(He I) from

He I RL ratios while in the 'combined cuts' spectra we were also able to derive T_e(H I) using both the Balmer and the Paschen discontinuities of the nebular continuum. In all the derived physical conditions, we found no significant deviation between the results of the 'combined cuts' spectrum and the individual nebular ones. We conclude that the emission of HH 529 II and HH 529 III do not alter the physical conditions and abundances derived from low spectral resolution spectra in areas of size of the order or larger than 10 arcsecs.

Based on the different temperature determinations available and following the Peimbert's t^2−formalism, we estimate $t^2_{\rm high} = 0.021 \pm 0.003$, $t^2_{\rm inter} = 0.051 \pm 0.009$ and $t^2_{\rm low} = 0.064 \pm 0.011$ for the high-, intermediate-, and low-ionization zones both for the nebular and the high-velocity components. We derive ionic abundances of O^+, N^+, S^+, Cl^+, Ni^{2+}, Fe^{2+}, S^{2+}, Cl^{2+}, O^{2+}, Ne^{2+}, Ar^{2+}, Cl^{3+}, Ar^{3+}, and Fe^{3+} based on CELs both in the case of $t^2 = 0$ and $t^2 > 0$. We estimated ionic abundances of He^+, O^+, O^{2+}, C^{2+} and Ne^{2+} based on RLs. The mean ADF values for the nebular components are ADF(O^+) $\approx 0.50 \pm 0.13$ dex, ADF(O^{2+}) $\approx 0.20 \pm 0.05$ dex, ADF(C^{2+}) $\approx 0.50 \pm 0.03$ dex, and ADF(Ne^{2+}) $\approx 0.35 \pm 0.10$dex. For HH 529 II, we obtained ADF(O^{2+}) $= 0.29 \pm 0.10$ dex and ADF(Ne^{2+}) $= 0.79 \pm 0.09$ dex while for HH 529 III we obtained ADF(O^{2+}) $= 0.36 \pm 0.11$ dex. The t^2 values we obtained are capable of account for the ADF(O^{2+}) in the nebular components but not in the ones corresponding to HH 529 II and III, where larger t^2 values would be needed to reproduce their ADF(O^{2+}).

We estimate the total abundances of O, Cl, Ar, and Fe without ICFs in the nebular components. In the cases of HH 529 II and III, in addition to the aforementioned elements (except Fe in HH 529 III), we were also able to estimate the total abundances of He and C without using an ICF. By using the Solar value of Fe/O as reference, we estimate that 6 per cent of the total Fe is in gaseous phase in the nebular components while in HH 529 II this fraction reaches 14 per cent and between 10 and 25 per cent in HH 529 III. This increase should be due to destruction of dust grains in the shock fronts. We found a slight overabundance of heavy elements (around 0.12 dex) in the high-velocity components that cannot be entirely due to dust destruction processes since it affects also the noble gases. We speculate that its possible origin may lie in the inclusion of H-deficient gas entrained after the evaporation of material in the outer part of the protoplanetary disc of the source of HH 529.

We found a constant value of the radial velocity of the emission lines, irrespective of the ionization potential of the observed ions in HH 529 II ($v_r = -29.08 \pm 0.36$ km s^{-1}) and HH 529 III ($v_r = -23.90 \pm 0.89$ km s^{-1}). In the nebular emission of the Orion Nebula, we demonstrate that the velocity varies linearly with the ionization potential for ions with ionization potential between 6.77 and 13.6 eV, reaching a constant velocity of 16.4 ± 0.8 km s^{-1} for ionization potentials greater than 13.6. From the thermal broadening of the line profiles, we derived $T_e = 8340 \pm 410$, $T_e = 8670 \pm 50$, and $T_e = 10470 \pm 50$ for the nebular components, HH 529 II and III, respectively. The determination for HH 529 III is anomalously large due to the contamination by unresolved velocity components.

We determined the proper motions of HH 529 II and III by using *HST* imaging over 20 yr. We found several discrete features identified in the bow shocks. We estimated an average tangential velocity of 35 ± 5 km s^{-1} for the HH 529 II-III system. We also estimate a flow angle with respect to the sky plane of $58^\circ \pm 4^\circ$. Several indicators evidence that HH 529 II corresponds to an internal working surface of the jet beam.

ACKNOWLEDGEMENTS

This work is based on observations collected at the European Southern Observatory, Chile, proposal number ESO 092.C-0323(A). We are grateful to the anonymous referee for his/her helpful comments. We acknowledge support from the Spanish State Research Agency (AEI) of the Spanish Ministry of Science, Innovation and Universities (MCIU) and the European Regional Development Fund (FEDER) under grant with references AYA2015-65205-P and AYA2017-83383-P. JG-R acknowledges support from an Advanced Fellowship from the Severo Ochoa excellence program (SEV-2015-0548). The authors acknowledge support under grant P/308614 financed by funds transferred from the Spanish Ministry of Science, Innovation and Universities, charged to the General State Budgets and with funds transferred from the General Budgets of the Autonomous Community of the Canary Islands by the MCIU. KZA-C acknowledges support from Mexican CONACYT posdoctoral grant 364239. JEM-D acknowledges support of the Instituto de Astrofísica de Canarias under the Astrophysicist Resident Program and acknowledges support from the Mexican CONACYT (grant CVU 602402). AM-D acknowledges support from the FONDECYT project 3140383. WJH acknowledges support from DGAPA, UNAM PAPIIT IN107019.

DATA AVAILABILITY

The lines measured in the spectra are entirely available in online tables annexed to this article. Table D2 is an example of the content found in the online tables. The rest of information is found in tables or references of this paper.

REFERENCES

Antoniucci S., La Camera A., Nisini B., Giannini T., Lorenzetti D., Paris D., Sani E., 2014, A&A, 566, A129
Arellano-Córdova K. Z., Esteban C., García-Rojas J., Méndez-Delgado J. E., 2020, MNRAS, 496, 1051
Arthur S. J., Henney W. J., Mellema G., de Colle F., Vázquez-Semadeni E., 2011, MNRAS, 414, 1747
Astropy Collaboration, 2013, A&A, 558, A33
Aver E., Olive K. A., Skillman E. D., 2011, J. Cosmol. Astropart. Phys., 2011, 043
Baldwin J. A. et al., 1996, ApJ, 468, L115
Ballester P., Modigliani A., Boitquin O., Cristiani S., Hanuschik R., Kaufer A., Wolf S., 2000, The Messenger, 101, 31
Bally J., Reipurth B., 2001, ApJ, 546, 299
Bally J., Reipurth B., 2018, Res. Notes Am. Astron. Soc., 2, 46
Bally J., Sutherland R. S., Devine D., Johnstone D., 1998, AJ, 116, 293
Bally J., O'Dell C. R., McCaughrean M. J., 2000, AJ, 119, 2919
Bastin R. J., Storey P. J., 2006, in Barlow M. J., Méndez R. H., eds, IAU Symp. Vol. 234, Planetary Nebulae in our Galaxy and Beyond. Kluwer, Dordrecht, p. 369
Bautista M. A., 2001, A&A, 365, 268
Bazer J., Ericson W. B., 1959, ApJ, 129, 758
Benjamin R. A., Skillman E. D., Smits D. P., 2002, ApJ, 569, 288
Berg D. A., Erb D. K., Henry R. B. C., Skillman E. D., McQuinn K. B. W., 2019, ApJ, 874, 93
Berg D. A., Pogge R. W., Skillman E. D., Croxall K. V., Moustakas J., Rogers N. S. J., Sun J., 2020, ApJ, 893, 96
Blagrave K. P. M., Martin P. G., Baldwin J. A., 2006, ApJ, 644, 1006
Blagrave K. P. M., Martin P. G., Rubin R. H., Dufour R. J., Baldwin J. A., Hester J. J., Walter D. K., 2007, ApJ, 655, 299
Bohigas J., 2015, MNRAS, 453, 1281
Bowen I. S., 1955, ApJ, 121, 306
Brown R. L., Mathews W. G., 1970, ApJ, 160, 939

Butler K., Zeippen C. J., 1989, A&A, 208, 337
Canto J., 1981, in Kimeswenger S., Van de Steene G. C., Avison A., Zijlstra A. A., Guzman-Ramirez L., Herwig F., Hajduk M., eds, Investigating the Universe, Herbig-Haro Objects: Recent Observational and Theoretical Developments. Reidel, Dordrecht, p. 95
Davey A. R., Storey P. J., Kisielius R., 2000, A&AS, 142, 85
Delgado-Inglada G., Morisset C., Stasińska G., 2014, MNRAS, 440, 536
Delgado-Inglada G., Mesa-Delgado A., García-Rojas J., Rodríguez M., Esteban C., 2016, MNRAS, 456, 3855
D'Odorico S., Cristiani S., Dekker H., Hill V., Kaufer A., Kim T., Primas F., 2000, in Bergeron J., ed., Proc. SPIE Vol. 4005, Performance of UVES, the Echelle Spectrograph for the ESO VLT and Highlights of the First Observations of Stars and Quasars. SPIE, Bellingham, p. 121
Domínguez-Guzmán G., Rodríguez M., Esteban C., García-Rojas J., 2019, in Cardaci M., Hägele G., Pérez-Montero E., eds, II Workshop of Chemical Abundances in Gaseous Nebulae, AAA Workshop Series,11. p. 113
Ellis D. G., Martinson I., 1984, Phys. Scr., 30, 255
Espíritu J. N., Peimbert A., Delgado-Inglada G., Ruiz M. T., 2017, Rev. Mex. Astron. Astrofis., 53, 95
Esteban C., Peimbert M., 1999, A&A, 349, 276
Esteban C., Peimbert M., Torres-Peimbert S., Escalante V., 1998, MNRAS, 295, 401
Esteban C., Peimbert M., García-Rojas J., Ruiz M. T., Peimbert A., Rodríguez M., 2004, MNRAS, 355, 229
Falle S. A. E. G., Raga A. C., 1993, MNRAS, 261, 573
Fang X., Liu X. W., 2011, MNRAS, 415, 181
Fang X., Liu X. W., 2013, MNRAS, 429, 2791
Fehrenbach C., 1977, A&AS, 29, 71
Ferland G. J., 2001, PASP, 113, 41
Ferland G. J., Henney W. J., O'Dell C. R., Porter R. L., van Hoof P. A. M., Williams R. J. R., 2012, ApJ, 757, 79
Ferland G. J. et al., 2013, Rev. Mex. Astron. Astrofis., 49, 137
Ferland G. J. et al., 2017, Rev. Mex. Astron. Astrofis., 53, 385
Feuchtgruber H. et al., 1997, ApJ, 487, 962
Fisher G. H., Welsch B. T., 2008, in Howe R., Komm R. W., Balasubramaniam K. S., Petrie G. J. D., eds, ASP Conf. Ser. Vol. 383, Subsurface and Atmospheric Influences on Solar Activity. Astron. Soc. Pac., San Francisco, p. 373
Fritzsche S., Fricke B., Geschke D., Heitmann A., Sienkiewicz J. E., 1999, ApJ, 518, 994
Froese Fischer C., Tachiev G., 2004, At. Data Nucl. Data Tables, 87, 1
Froese Fischer C., Rubin R. H., Rodríguez M., 2008, MNRAS, 391, 1828
Galavis M. E., Mendoza C., Zeippen C. J., 1995, A&AS, 111, 347
García-Díaz M. T., Henney W. J., López J. A., Doi T., 2008, Rev. Mex. Astron. Astrofis., 44, 181
García-Rojas J., Esteban C., 2007, ApJ, 670, 457
García-Rojas J., Esteban C., Peimbert M., Rodríguez M., Ruiz M. T., Peimbert A., 2004, ApJS, 153, 501
García-Rojas J., Esteban C., Peimbert A., Peimbert M., Rodríguez M., Ruiz M. T., 2005, MNRAS, 362, 301
García-Rojas J., Esteban C., Peimbert A., Rodríguez M., Peimbert M., Ruiz M. T., 2007, Rev. Mex. Astron. Astrofis., 43, 3
García-Rojas J., Peña M., Morisset C., Delgado-Inglada G., Mesa-Delgado A., Ruiz M. T., 2013, A&A, 558, A122
García-Rojas J., Madonna S., Luridiana V., Sterling N. C., Morisset C., Delgado-Inglada G., Toribio San Cipriano L., 2015, MNRAS, 452, 2606
Gómez-Llanos V., Morisset C., 2020, MNRAS, 497, 3363
Goudis C., 1982, The Orion Complex: A Case Study of Interstellar Matter. D. Reidel Publ. Company, Dordrecht
Grandi S. A., 1975a, ApJ, 196, 465
Grandi S. A., 1975b, ApJ, 199, L43
Grieve M. F. R., Ramsbottom C. A., Hudson C. E., Keenan F. P., 2014, ApJ, 780, 110
Hansen E. C., Frank A., Hartigan P., 2015, ApJ, 800, 41
Haro G., 1952, ApJ, 115, 572
Haro G., 1953, ApJ, 117, 73
Hartigan P., 1989, ApJ, 339, 987
Hartigan P., Wright A., 2015, ApJ, 811, 12
Hartigan P., Raymond J., Hartmann L., 1987, ApJ, 316, 323
Hartigan P., Morse J. A., Raymond J., 1994, ApJ, 436, 125
Hartigan P., Hillenbrand L. A., Matuszewski M., Borges A. C., Neill J. D., Martin D. C., Morrissey P., Moore A. M., 2020, AJ, 160, 165
Henney W. J., 2002, Rev. Mex. Astron. Astrofis., 38, 71
Henney W. J., Stasińska G., 2010, ApJ, 711, 881
Herbig G. H., 1950, ApJ, 111, 11
Herbig G. H., 1951, ApJ, 113, 697
Herbig G. H., 1952, J. R. Astron. Soc. Can., 46, 222
Izotov Y. I., Stasińska G., Meynet G., Guseva N. G., Thuan T. X., 2006, A&A, 448, 955
Johansson S., Zethson T., Hartman H., Ekberg J. O., Ishibashi K., Davidson K., Gull T., 2000, A&A, 361, 977
Jones A. P., Tielens A. G. G. M., Hollenbach D. J., McKee C. F., 1994, ApJ, 433, 797
Juan de Dios L., Rodríguez M., 2017, MNRAS, 469, 1036
Kaler J. B., 1967, ApJ, 148, 925
Kauffmann G. et al., 2003, MNRAS, 346, 1055
Kaufman V., Martin W. C., 1993, J. Phys. Chem. Ref. Data, 22, 279
Kaufman V., Sugar J., 1986, J. Phys. Chem. Ref. Data, 15, 321
Kingdon J. B., Ferland G. J., 1995, ApJ, 450, 691
Kisielius R., Storey P. J., Davey A. R., Neale L. T., 1998, A&AS, 133, 257
Kisielius R., Storey P. J., Ferland G. J., Keenan F. P., 2009, MNRAS, 397, 903
Kunth D., Sargent W. L. W., 1983, ApJ, 273, 81
Liu X. W., Storey P. J., Barlow M. J., Danziger I. J., Cohen M., Bryce M., 2000, MNRAS, 312, 585
Liu X. W., Luo S. G., Barlow M. J., Danziger I. J., Storey P. J., 2001, MNRAS, 327, 141
Lodders K., 2019, The Oxford Research Encyclopedia of Planetary Science. Oxford Univ. Press, UK
Lucy L. B., 1995, A&A, 294, 555
McLaughlin B. M., Lee T.-G., Ludlow J. A., Land i E., Loch S. D., Pindzola M. S., Ballance C. P., 2011, J. Phys. B: At. Mol. Phys., 44, 175206
Luridiana V., Morisset C., Shaw R. A., 2015, A&A, 573, A42
Masciadri E., Raga A. C., 2001, A&A, 376, 1073
McNabb I. A., Fang X., Liu X. W., Bastin R. J., Storey P. J., 2013, MNRAS, 428, 3443
Méndez-Delgado J. E., Esteban C., García-Rojas J., Arellano-Córdova K. Z., Valerdi M., 2020, MNRAS, 496, 2726
Mendoza C., 1983, in Aller L. H., ed., IAU Symp. Vol. 103, Planetary Nebulae. Kluwer, Dordrecht, p. 143
Mendoza C., Zeippen C. J., 1982a, MNRAS, 198, 127
Mendoza C., Zeippen C. J., 1982b, MNRAS, 199, 1025
Mendoza C., Zeippen C. J., 1983, MNRAS, 202, 981
Mesa-Delgado A., Esteban C., García-Rojas J., 2008, ApJ, 675, 389
Mesa-Delgado A., Esteban C., García-Rojas J., Luridiana V., Bautista M., Rodríguez M., López-Martín L., Peimbert M., 2009, MNRAS, 395, 855
Moehler S., Dreizler S., LeBlanc F., Khalack V., Michaud G., Richer J., Sweigart A. V., Grundahl F., 2014a, A&A, 565, A100
Moehler S. et al., 2014b, A&A, 568, A9
Mouri H., Taniguchi Y., 2000, ApJ, 534, L63
Nicholls D. C., Dopita M. A., Sutherland R. S., 2012, ApJ, 752, 148
O'Dell C. R., 2001, ARA&A, 39, 99
O'Dell C. R., 2018, MNRAS, 478, 1017
O'Dell C. R., Henney W. J., 2008, AJ, 136, 1566
O'Dell C. R., Wen Z., 1992, ApJ, 387, 229
O'Dell C. R., Ferland G. J., Henney W. J., Peimbert M., García-Díaz M. T., Rubin R. H., 2015, AJ, 150, 108
O'Dell C. R., Abel N. P., Ferland G. J., 2020, ApJ, 891, 46
Olive K. A., Skillman E. D., 2004, ApJ, 617, 29
Osterbrock D. E., Ferland G. J., 2006, Astrophysics of Gaseous Nebulae and Active Galactic Nuclei. University Science Books, Sausalito, CA
Osterbrock D. E., Tran H. D., Veilleux S., 1992, ApJ, 389, 305
Pagel B. E. J., Simonson E. A., Terlevich R. J., Edmunds M. G., 1992, MNRAS, 255, 325
Peimbert M., 1967, ApJ, 150, 825
Peimbert A., 2003, ApJ, 584, 735

Peimbert M., Costero R., 1969, Bol. Obs. Tonantzintla Tacubaya, 5, 3
Peimbert A., Peimbert M., 2013, ApJ, 778, 89
Peimbert A., Peimbert M., Luridiana V., 2002, ApJ, 565, 668
Peimbert M., Peimbert A., Ruiz M. T., Esteban C., 2004, ApJS, 150, 431
Pequignot D., Petitjean P., Boisson C., 1991, A&A, 251, 680
Péquignot D., Amara M., Liu X. W., Barlow M. J., Storey P. J., Morisset C., Torres-Peimbert S., Peimbert M., 2002, Rev. Mex. Astron. Astrofis. Ser. Conf., 12, 142
Persson W., Wahlström C.-G., Jönsson L., Di Rocco H. O., 1991, Phys. Rev. A, 43, 4791
Podobedova L. I., Kelleher D. E., Wiese W. L., 2009, J. Phys. Chem. Ref. Data, 38, 171
Porter R. L., Ferland G. J., MacAdam K. B., 2007, ApJ, 657, 327
Porter R. L., Ferland G. J., Storey P. J., Detisch M. J., 2012, MNRAS, 425, L28
Porter R. L., Ferland G. J., Storey P. J., Detisch M. J., 2013, MNRAS, 433, L89
Price-Whelan A. M. et al., 2018, AJ, 156, 123
Pudritz R. E., Ray T. P., 2019, Front. Astron. Space Sci., 6, 54
Quinet P., 1996, A&AS, 116, 573
Raga A. C., Canto J., Binette L., Calvet N., 1990, ApJ, 364, 601
Raga A. C., López-Martín J., López J. A., Meaburn J., 2000a, Rev. Mex. Astron. Astrofis. Ser. Conf., 9, 191
Raga A. et al., 2000b, MNRAS, 314, 681
Ramsbottom C. A., Bell K. L., 1997, At. Data Nucl. Data Tables, 66, 65
Reipurth B., Bally J., 2001, ARA&A, 39, 403
Riera A., Mampaso A., Phillips J. P., Vilchez J. M., 1989, A&A, 210, 351
Robberto M. et al., 2005, AJ, 129, 1534
Robberto M. et al., 2013, ApJS, 207, 10
Rodríguez M., 1999, A&A, 348, 222
Rodríguez M., 2002, A&A, 389, 556
Rodríguez M., 2020, MNRAS, 495, 1016
Rodríguez M., Rubin R. H., 2005, ApJ, 626, 900
Rubin R. H., Simpson J. P., O'Dell C. R., McNabb I. A., Colgan S. W. J., Zhuge S. Y., Ferland G. J., Hidalgo S. A., 2011, MNRAS, 410, 1320
Schwartz R. D., 1983, ARA&A, 21, 209
Simón-Díaz S., Stasińska G., 2011, A&A, 526, A48
Smith N., Bally J., Shuping R. Y., Morris M., Kassis M., 2005, AJ, 130, 1763
Stasińska G., 1978, A&A, 66, 257
Stasińska G., Tenorio-Tagle G., Rodríguez M., Henney W. J., 2007, A&A, 471, 193
Storey P. J., 1994, A&A, 282, 999
Storey P. J., Hummer D. G., 1995, MNRAS, 272, 41
Storey P. J., Zeippen C. J., 2000, MNRAS, 312, 813
Storey P. J., Sochi T., Badnell N. R., 2014, MNRAS, 441, 3028
Storey P. J., Sochi T., Bastin R., 2017, MNRAS, 470, 379
Tayal S. S., 2004, A&A, 418, 363
Tayal S. S., 2011, ApJS, 195, 12
Tayal S. S., Zatsarinny O., 2010, ApJS, 188, 32
Tody D., 1993, in Hanisch R. J., Brissenden R. J. V, Barnes J, eds, Astronomical Data Analysis Software and Systems II. p. 173
Torres-Peimbert S., Peimbert M., Daltabuit E., 1980, ApJ, 238, 133
Tsamis Y. G., Walsh J. R., Vílchez J. M., Péquignot D., 2011, MNRAS, 412, 1367
Tsamis Y. G., Flores-Fajardo N., Henney W. J., Walsh J. R., Mesa-Delgado A., 2013, MNRAS, 430, 3406
Van Hoof P. A. M., 2018, Galaxies, 6, 63
Verner E. M., Verner D. A., Baldwin J. A., Ferland G. J., Martin P. G., 2000, ApJ, 543, 831
Vilchez J. M., Pagel B. E. J., 1988, MNRAS, 231, 257
Walter D. K., Dufour R. J., Hester J. J., 1992, ApJ, 397, 196
Welsch B. T., Fisher G. H., Abbett W. P., Regnier S., 2004, ApJ, 610, 1148
Wesson R., Jones D., García-Rojas J., Boffin H. M. J., Corradi R. L. M., 2018, MNRAS, 480, 4589
Wiese W. L., Fuhr J. R., Deters T. M., 1996, J. Phys. Chem. Ref. Data Monogr., 7, 403
Yuan H.-B., Liu X.-W., Péquignot D., Rubin R. H., Ercolano B., Zhang Y., 2011, MNRAS, 411, 1035
Zel'Dovich Y. B., Raizer Y. P., Hayes W. D., Probstein R. F., Gill S. P., 1967, J. Appl. Mech., 34, 1055
Zhang H. L., 1996, A&AS, 119, 523
Zhang H. L., Pradhan A. K., 1997, A&AS, 126, 373
Zhang Y., Liu X. W., 2006, in Barlow M. J., Méndez R. H., eds, IAU Symp., Vol. 234, Planetary Nebulae in our Galaxy and Beyond. Kluwer, Dordrecht, p. 547
Zhang Y., Liu X.-W., Liu Y., Rubin R. H., 2005, MNRAS, 358, 457

SUPPORTING INFORMATION

Supplementary data are available at *MNRAS* online.

Table D2. Sample of 15 lines of the spectra of cut 2.

Please note: Oxford University Press is not responsible for the content or functionality of any supporting materials supplied by the authors. Any queries (other than missing material) should be directed to the corresponding author for the article.

APPENDIX A: THE ALLEGED OBSERVATION OF SI IV λ4088.86. LINE

Several authors used the I(O II λ4649.13)/I(O II λ4089.29) ratio to derive T_e based on its theoretical dependence on T_e and insensitivity to n_e (see e.g. García-Rojas & Esteban 2007; Fang & Liu 2013; McNabb et al. 2013; Wesson et al. 2018). Nevertheless, Peimbert & Peimbert (2013) discourages its use, due (among other reasons) to the possible contamination of O II λ4089.29 by the Si IV λ4088.86 line, which would lead to underestimating T_e. The authors consider that Si IV λ4088.86 has been detected in 2 H II regions observed with UVES echelle spectrograph at VLT telescope: the Orion Nebula (Esteban et al. 2004) and 30 Doradus (Peimbert 2003). Although it is a real possibility that a line like Si IV λ4088.86 may be detected in an H II region, much of the flux attributed to this line is actually due to an observational artefact of UVES spectrum.

Fig. D2 shows the echelle orders extracted in an UVES blue arm spectrum using dichroic #2 (Δλ = 3750–4995). Optical reflections produced by the dichroic #2 in the blue arm can be noted as vertical lines crossing the echelle orders. These artefacts are negligible with the exception of those produced by the most intense lines: [O III] λ4959, Hβ, and [O III] λ5007. The last of those lines does not enter in any complete echelle order in this arm, but it is partially observed at the edge of the CCD, together with its associated high-velocity component. As a consequence four main sources of 'ghost lines' can be noticed. The third of them (from left to right), affects exactly the λ4089.07 position in the echelle order number 11 (bottom up) in our observations. Approximately at this wavelength we expect to have the high-velocity component of O II λ4089.29 in cuts 2 and 3, but it must be free of emission from HH 529 II and III in cut 4. Fig. D6 shows the emission around λ4089.29 in the spectra of cut 4, a pretty similar image than the Fig. 2 from Peimbert & Peimbert (2013).

In our spectra, an hypothetical Si IV λ4088.86 line should be observed at λ4089.08, considering the kinematical structure of the nebular component and the high ionization potential of the line (see Section 9.1). This means that in case of being detected, the Si IV λ4088.86 line would be indistinguishable from the ghost line at λ4089.07. We have measured the intensity of ghost lines coming from the same source than λ4089.07 along the echelle orders but excluding those ones which are blended with other nebular lines. Fig. D3 shows the decreasing trend of the intensity of ghost emission

with respect to its source from higher to lower orders, as well as a least-squares fit to predict ghost emission in order 11, where the emission feature at λ4089.07 lies. The predicted ghost emission in λ4089.07 is $F(\lambda)/F(\mathrm{H}\beta) = 0.007$ while the rms of the noise associated with the continuum in cut 4 around λ4089.07 represents a possible contribution of $F(\mathrm{rms})/F(\mathrm{H}\beta) = 0.004$. On the other hand, the measured flux of λ4089.07 is $F(\lambda)/F(\mathrm{H}\beta) = 0.012$. Thus, the emission observed at λ4089.07 is consistent with purely ghost emission. This ghost emission affects in a similar way the spectra of the Orion Nebula and 30 Dor analysed by Esteban et al. (2004) and Peimbert (2003), respectively.

The main drawback of the T_e diagnostic based on the I(O II λ4649.13)/I(O II λ4089.29) ratio in H II regions is that λ4089.29 is rather weak, providing uncertain T_e values. Therefore, this diagnostic will only be useful when the O II lines are well measured, or when the object shows significant difference between the T_e of the zone where the O II lines are formed and the rest of the nebula (Wesson et al. 2018). Finally, although Si IV lines are expected to be rather faint in normal H II regions, this may not be the case in high-ionization planetary nebulae (PNe) as NGC 3918 (García-Rojas et al. 2015).

APPENDIX B: CL^{2+} AND CL ABUNDANCES

Domínguez-Guzmán et al. (2019) have proposed the use of T_e([N II]) to determine the Cl^{2+} abundance in a sample of 37 Galactic and extragalactic H II regions, including the Orion Nebula (using the data of Esteban et al. 2004). They argue that T_e([N II]) reduces the dispersion of the Cl/O ratio and remove trends in the Cl/O versus O/H relation. However, in a detailed study of each specific object, the optimal temperature to adopt can differ from what statistically would be the best choice. Considering the IP of 23.8 eV of Cl^{2+}, in between of those of N^+ (14.5 eV) and O^{2+} (35.1 eV), we expect that a T_e representative of an intermediate ionization zone as T_e([S III]) should be more appropriate for determining the Cl^{2+} abundance. The relationship of T_e([S III]) with T_e([N II]) and T_e([O III]) may depend on the ionization degree of the gas (Berg et al. 2020). In our spectra, we are able to calculate the total Cl abundance because we measure CELs of all the ionization species of Cl that are expected to be present in the Orion Nebula. We test the resulting Cl abundance considering three different temperatures: T_e(low), T_e([S III]) and T_e(high) for deriving the Cl^{2+}/H^+ ratio. In Table D10, we present the Cl^{2+} and Cl abundances as well as their corresponding log(Cl/O) values using the three aforementioned temperatures.

Using T_e(low), we obtain a log(Cl/O) value in the high-velocity components about 0.1 dex lower with respect to the value found in the nebular ones of the different cuts. This suggests that T_e(low) is slightly underestimating the Cl/H ratio, although within the uncertainties. Conversely, the Cl/O ratio becomes more consistent when using T_e([S III]) or T_e(high) to estimate the Cl^{2+} abundance. We obtain a mean log(Cl/O) value of -3.63 ± 0.04, -3.42 ± 0.03, and -3.50 ± 0.03 when adopting T_e(low), T_e(high), or T_e([S III]) to calculate the Cl^{2+} abundance, respectively. The log(Cl/O) value obtained using T_e([S III]) is the one closest to the solar value of -3.50 ± 0.09 recommended by Lodders (2019). Therefore, we finally adopt T_e([S III]) to estimate the Cl^{2+} abundance.

APPENDIX C: NI^{2+} ABUNDANCE

The first estimation of the Ni abundance in an H II region was made by Osterbrock, Tran & Veilleux (1992) for the Orion Nebula. They used estimates of the atomic data of Ni ions, considering [Ni II] and [Ni III] lines. Since then, the number of Ni abundance determinations in ionized nebulae is still very limited, both for PNe (Zhang & Liu 2006; García-Rojas et al. 2013; Delgado-Inglada et al. 2016) and H II regions (Mesa-Delgado et al. 2009; Delgado-Inglada et al. 2016). There is a considerable amount of [Ni II] and [Ni III] lines in our spectra. However, [Ni II] lines are affected by fluorescence (Lucy 1995) and their use to calculate the abundance of Ni^+ is restricted to some particular cases as low-excitation nebulae (Zhang & Liu 2006). On the other hand, [Ni III] lines are, in principle, not affected by fluorescence effects and can be used to derive Ni^{2+} abundances. From all the detected [Ni III] lines, we chose [Ni III] λλ6000, 6534, 6682, 6797, 6946 and 7890 because they are not affected by blends or telluric absorption.

As we commented in Section 4, all tested diagnostics based on [Ni III] lines fail to provide reliable values of physical conditions, indicating inaccuracies between the observed lines and the theoretical predictions. Delgado-Inglada et al. (2016) studied the Fe/Ni ratio in eight PNe and three H II regions, including the Orion Nebula. They used different data sets for these last objects, including the high spectral resolution ones from Esteban et al. (2004) and Mesa-Delgado et al. (2009) (which includes HH 202 S), and some previously unpublished observations covering approximately the same area as the Position 1 of Esteban et al. (1998) and the brightest part of the Orion Bar. We have compared our data with some observed flux ratios compiled by Delgado-Inglada et al. (2016) looking for possible undetected line blends or observational inaccuracies. For convenience, we have compared the predicted and observed flux ratios of [Ni III] λλ6000, 6534 and 6946 lines that arise from the same atomic level and therefore we expect that their intensity ratios should be constant. In Table D11, we compare the observed flux ratios and the predicted ones using the atomic data of Ni^{2+} by Bautista (2001). As Table D11 shows, the [Ni III] λ6534/λ6000 and λ6946/λ6000 intensity ratios are not inconsistent with the predicted ones. The most discrepant case is HH 529 II, although it is the component with the greatest dispersion. The intensity ratios based on the data sets with smaller dispersion seems to indicate a systematic value of λ6534/λ6000 ∼ 1.6 and λ6534/λ6000 ∼ 0.30 that are compatible with an overestimation of the flux of the [Ni III] λ6000 line. However, we discard the presence of sky emission affecting this line. Besides this, we do not find strong candidates of unusual lines in the literature or in the Atomic Line List v2.05b21 with a wavelength difference below 0.15 Å (a conservative limit for an appropriate deblending of Gaussian profiles at our spectral resolution). In addition, as can be seen in Table D12, we find an inconsistent pattern of Ni^{2+} abundances in all cuts and components for the six selected lines, with differences up to 0.8 dex. This may be a problem of the currently available atomic data of Ni^{2+}, which could not be accurate enough for deriving confident values of its ionic abundances. Therefore, our Ni^{2+}/H^+ abundances must be interpreted with care, since they may include unknown uncertainties.

APPENDIX D: SUPPORTING MATERIAL

In this appendix we include the following material:

(i) Table D1: Comparison of the Balmer line ratios between Blagrave et al. (2006) and this work.

(ii) Table D2: Sample of 15 lines of the spectra of cut 2. The complete line list of all cuts is appended in the online supporting material.

(iii) Table D3: Atomic data set (Transition probabilities and collision strengths) used in this work for the analysis of CELs.

Table D1. Reddening-corrected Balmer line ratios from Blagrave et al. (2006) and this work.

	BMB06		This Work			
Ratio	High-velocity	Nebular	HH 529 II	HH 529 III	Nebula	Predicted Value
Hα/Hβ	3.65 ± 0.18	3.19 ± 0.03	2.77 ± 0.08	2.87 ± 0.11	2.82 ± 0.09	2.85
Hγ/Hβ	0.74 ± 0.04	0.69 ± 0.01	0.46 ± 0.01	0.46 ± 0.01	0.46 ± 0.01	0.47
Hδ/Hβ	0.34 ± 0.02	0.40 ± 0.01	0.26 ± 0.01	0.26 ± 0.01	0.26 ± 0.01	0.26
Hε/Hβ	0.27 ± 0.02	0.31 ± 0.01	0.16 ± 0.01	0.15 ± 0.01	0.16 ± 0.01	0.16
Hγ/Hα	0.20 ± 0.01	0.22 ± 0.01	0.17 ± 0.01	0.16 ± 0.01	0.17 ± 0.01	0.17
Hδ/Hα	0.09 ± 0.01	0.13 ± 0.01	0.09 ± 0.01	0.09 ± 0.01	0.09 ± 0.01	0.09
Hε/Hα	0.07 ± 0.01	0.10 ± 0.01	0.06 ± 0.01	0.05 ± 0.01	0.06 ± 0.01	0.06

Table D2. Sample of 15 lines of the cut 2 spectra. This cut includes emission from HH 529 II and the Orion Nebula. F(Hβ)=100. This is an example of the content found in the online tables for all cuts.

		HH 529 II						The Orion Nebula						
λ_0(Å)	Ion	λ(Å)	v_r (km s^{-1})	FWHM (km s^{-1})	F(λ)/F(Hβ)	I(λ)/I(Hβ)	Error (%)	λ(Å)	v_r (km s^{-1})	FWHM (km s^{-1})	F(λ)/F(Hβ)	I(λ)/I(Hβ)	Error (%)	Notes
4638.86	O II	4638.40	−29.44	20.68 ± 1.67	0.091	0.098	6	4639.08	14.51	14.86 ± 0.60	0.042	0.045	4	
4640.64	N III	4640.07	−36.53	22.68 ± 3.59	0.037	0.040	10	4640.81	11.27	11.95 ± 0.98	0.013	0.014	6	
4641.81	O II	4641.35	−29.42	18.60 ± 0.58	0.152	0.164	4	4642.04	15.15	13.76 ± 0.24	0.083	0.089	2	
4643.09	N II	4642.64	−28.76	16.21 ± 5.62	0.026	0.028	21	4643.32	15.15	12.01 ± 1.52	0.015	0.016	9	
4649.13	O II	4648.67	−29.36	18.90 ± 0.38	0.240	0.258	3	4649.37	15.78	12.51 ± 0.07	0.114	0.122	2	
4650.84	O II	4650.38	−29.35	18.89 ± 1.45	0.088	0.095	6	4651.06	14.49	13.28 ± 0.52	0.040	0.043	4	
4658.17	[Fe III]	4657.67	−31.86	13.52 ± 0.04	0.887	0.950	2	4658.38	13.83	13.32 ± 0.01	0.770	0.820	2	
4661.63	O II	4661.18	−29.26	27.59 ± 1.91	0.124	0.133	6	4661.86	14.47	15.76 ± 0.60	0.048	0.051	4	ghost in neb comp
4667.11	[Fe III]	4666.57	−35.00	19.53 ± 1.62	0.064	0.068	7	4667.28	10.61	18.95 ± 0.59	0.042	0.045	4	ghost
4673.73	O II	4673.30	−27.88	29.00 ± 13.54	0.021	0.022	29	4674.00	17.02	11.80 ± 2.54	0.007	0.007	16	
4676.23	O II	4675.79	−28.51	19.68 ± 2.89	0.046	0.049	11	4676.47	15.09	13.21 ± 0.69	0.026	0.028	5	
4699.22	O II	*	*	*	*	*	*	4699.42	12.50	24.18 ± 9.72	0.011	0.012	33	
4701.64	[Fe III]	4701.13	−32.77	12.63 ± 0.25	0.299	0.315	3	4701.85	13.14	13.39 ± 0.05	0.247	0.260	2	
4704.55	Ni III?	*	*	*	*	*	*	4704.88	20.78	26.83 ± 3.26	0.014	0.015	9	
4705.35	O II	*	*	*	*	*	*	4705.60	15.68	14.40 ± 1.02	0.017	0.018	5	

Table D3. Atomic data set used for collisionally excited lines.

Ion	Transition Probabilities	Collision Strengths
O^+	Froese Fischer & Tachiev (2004)	Kisielius et al. (2009)
O^{2+}	Wiese, Fuhr & Deters (1996), Storey & Zeippen (2000)	Storey, Sochi & Badnell (2014)
N^+	Froese Fischer & Tachiev (2004)	Tayal (2011)
Ne^{2+}	McLaughlin et al. (2011)	McLaughlin et al. (2011)
S^+	Podobedova, Kelleher & Wiese (2009)	Tayal & Zatsarinny (2010)
S^{2+}	Podobedova et al. (2009)	Grieve et al. (2014)
Cl^+	Mendoza & Zeippen (1983)	Tayal (2004)
Cl^{2+}	Fritzsche et al. (1999)	Butler & Zeippen (1989)
Cl^{3+}	Kaufman & Sugar (1986), Mendoza & Zeippen (1982b), Ellis & Martinson (1984)	Galavis, Mendoza & Zeippen (1995)
Ar^{2+}	Mendoza (1983), Kaufman & Sugar (1986)	Galavis et al. (1995)
Ar^{3+}	Mendoza & Zeippen (1982a)	Ramsbottom & Bell (1997)
Fe^{2+}	Quinet (1996) , Johansson et al. (2000)	Zhang (1996)
Fe^{3+}	Froese Fischer, Rubin & Rodríguez (2008)	Zhang & Pradhan (1997)
Ni^{2+}	Bautista (2001)	Bautista (2001)

Table D4. Effective recombination coefficients used for recombination lines.

Ion	Reference
H^+	Storey & Hummer (1995)
He^+	Porter et al. (2012), Porter et al. (2013)
O^+	Pequignot, Petitjean & Boisson (1991)
O^{2+}	Storey et al. (2017)
C^{2+}	Davey, Storey & Kisielius (2000)
Ne^{2+}	Kisielius et al. (1998)

Table D5. Critical densities of density diagnostics for T_e = 10000K.

Ion	λ(Å)	n_{crit} (cm^{-3})
[O II]	3729, 3726	1.30×10^3, 4.06×10^3
[S II]	6731, 6716	3.06×10^3, 1.16×10^3
[Cl III]	5538, 5518	3.57×10^4, 7.23×10^3
[Fe III]	4658, 4702	5.17×10^6, 3.09×10^6
[Ar IV]	4740, 4711	1.26×10^5, 1.39×10^4

Table D6. Comparison of the observed [Fe III] intensity ratios and theoretical ones predicted by the transition probabilities adopted in Table D3.

	Cut 1	Cut 2		Cut 3		Cut 4		
Ratio	Nebula	HH 529 II	Nebula	HH 529 III	Nebula	Nebula	Combined cuts	Prediction
4667/4734*	–	0.52 ± 0.04	0.42 ± 0.02	–	0.45 ± 0.03	0.43 ± 0.03	–	0.28
4778/4734	0.51 ± 0.04	0.70 ± 0.06	0.51 ± 0.03	0.48 ± 0.12	0.44 ± 0.04	0.43 ± 0.03	0.51 ± 0.04	0.48
4778/4667*	–	1.35 ± 0.14	1.22 ± 0.06	–	1.09 ± 0.07	1.00 ± 0.09	–	1.74
4607/4702**	0.24 ± 0.01	0.22 ± 0.02	0.24 ± 0.01	0.24 ± 0.05	0.23 ± 0.02	0.24 ± 0.02	0.23 ± 0.02	0.17
4607/4770**	0.72 ± 0.05	0.60 ± 0.06	0.64 ± 0.03	0.52 ± 0.11	0.64 ± 0.06	0.68 ± 0.05	0.64 ± 0.05	0.51
4702/4770	2.96 ± 0.15	2.68 ± 0.16	2.73 ± 0.10	2.22 ± 0.27	2.74 ± 0.19	2.87 ± 0.14	2.72 ± 0.14	2.93
4658/4755	5.50 ± 0.20	5.28 ± 0.24	5.26 ± 0.15	4.70 ± 0.51	5.32 ± 0.24	5.30 ± 0.19	5.31 ± 0.19	5.49
5011/5085	3.19 ± 0.72	2.51 ± 0.93	5.00 ± 1.00	2.96 ± 1.22	3.61 ± 0.46	3.84 ± 0.94	3.66 ± 0.96	5.94
5271/5412	10.41 ± 1.36	9.39 ± 1.49	10.48 ± 0.81	–	10.37 ± 0.85	9.51 ± 1.24	10.84 ± 1.06	11.01
4881/4987***	4.88 ± 0.31	4.90 ± 0.38	5.07 ± 0.23	2.41 ± 0.46	5.27 ± 0.41	5.98 ± 0.35	4.85 ± 0.37	5.76

Notes. * λ4667 affected by ghost.
** [Fe III] λ4607.12 blended with N II λ4607.15.
*** [Fe III] λ4987.29 blended with N II λ4987.38.

(iv) Table D4: Effective recombination coefficients used in this work for recombination lines.
(v) Table D5: Critical densities of some lines whose ratios are commonly used as density diagnostics.
(vi) Table D6: Comparison of some observed [Fe III] intensity ratios with the theoretical predictions.
(vii) Table D7: Slopes and intercepts calculated to estimate T_e(He I) using equation (4) for a range of usual densities.
(viii) Tables D8 and D9: Ionic abundances of Fe^{2+}/H^+ derived in all studied components with 11 CELs by using T_e(low) and T_e(high), respectively.
(ix) Table D10: Cl^{2+}/H^+, Cl/H and log(Cl/O) abundances derived with T_e(low), T_e([S III]) and T_e(high), respectively, for all studied components.
(x) Table D11: Comparison between the predicted and the measured intensity ratios of Ni^{2+} 2F multiplet (λλ6000, 6534, 6946).
(xi) Table D12: Ionic abundances of Ni^{2+}/H^+ derived per line in all studied components.
(xii) Table D13: He^+/H^+ abundances derived from He I lines highly affected by self-absorption effects.
(xiii) Table D14: He^+/H^+ abundances derived from He I lines not affected by self-absorption effects.
(xiv) Table D15: O^{2+}/H^+ abundances derived with RLs of several multiplets and transitions.
(xv) Table D16: O^+/H^+, C^{2+}/H^+ and Ne^{2+}/H^+ abundances derived with RLs.
(xvi) Table D17: values of t^2 derived for each component, estimated by using T_e(He I), T_e([O III]), T_e([S III]) and T_e([N II]).
(xvii) Table D18: Average radial velocity ⟨V⟩ and Full Width at Half Maximum ⟨FWHM⟩ of the lines observed in the nebular component and in HH 529 II-III.
(xviii) Fig. D1: Plasma diagnostics used in each analysed component to determine physical conditions based on CEL ratios.
(xix) Fig. D2: Echelle orders extracted using the UVES blue arm with the dichroic #2.
(xx) Fig. D3: Least squares fit of the ghost emission that affects the spectral position λ = 4089.07.
(xxi) Fig. D4: Grotrian diagram of the levels of He I.
(xxii) Fig. D5: Dependence of I(He I λ7281)/I(He I λ6678) on the physical conditions.
(xxiii) Fig. D6: Emission spectrum of cut 4 around ∼λ4089.

Table D7. Slope and intercept for equation (4) for a range of densities.

n_e (cm^{-3})	α	β
100	92984	−7455
500	81830	−6031
1000	77896	−5527
2000	69126	−4378
3000	65040	−3851
4000	62517	−3529
5000	60744	−3305
6000	59402	−3137
7000	58334	−3004
8000	57456	−2895
9000	56715	−2804
10000	56077	−2726
12000	55637	−2676
15000	55087	−2611
20000	54364	−2523
25000	53796	−2452
30000	53329	−2392
40000	52591	−2297
45000	52289	−2257
50000	52019	−2222

Table D8. Fe^{2+}/H^+ abundances based on T_e(low). The units are logarithmic with $n(H) = 12$.

	Cut 1	Cut 2		Cut 3		Cut 4	
λ	Nebula	HH 529 II	Nebula	HH 529 III	Nebula	Nebula	Combined cuts
4658	5.51 ± 0.02	$5.59^{+0.08}_{-0.06}$	$5.56^{+0.04}_{-0.03}$	$5.34^{+0.15}_{-0.09}$	5.51 ± 0.04	$5.47^{+0.05}_{-0.04}$	5.52 ± 0.03
4702	5.51 ± 0.02	$5.59^{+0.08}_{-0.06}$	$5.56^{+0.04}_{-0.03}$	$5.38^{+0.15}_{-0.10}$	5.52 ± 0.04	$5.47^{+0.05}_{-0.04}$	$5.52^{+0.04}_{-0.03}$
4734	5.48 ± 0.03	$5.58^{+0.09}_{-0.07}$	5.56 ± 0.04	$5.36^{+0.16}_{-0.10}$	$5.50^{+0.05}_{-0.04}$	$5.47^{+0.05}_{-0.04}$	5.52 ± 0.04
4755	$5.51^{+0.03}_{-0.02}$	$5.61^{+0.09}_{-0.07}$	$5.58^{+0.04}_{-0.03}$	$5.41^{+0.16}_{-0.10}$	$5.52^{+0.05}_{-0.04}$	$5.49^{+0.05}_{-0.04}$	$5.54^{+0.04}_{-0.03}$
4770	5.51 ± 0.03	$5.63^{+0.09}_{-0.07}$	5.59 ± 0.04	$5.50^{+0.15}_{-0.10}$	$5.55^{+0.05}_{-0.04}$	$5.48^{+0.05}_{-0.04}$	$5.56^{+0.04}_{-0.03}$
4778	5.51 ± 0.04	$5.75^{+0.09}_{-0.07}$	5.59 ± 0.04	$5.36^{+0.18}_{-0.12}$	$5.51^{+0.05}_{-0.04}$	$5.42^{+0.06}_{-0.05}$	5.55 ± 0.04
4881	5.53 ± 0.02	$5.61^{+0.09}_{-0.06}$	$5.58^{+0.04}_{-0.03}$	$5.38^{+0.15}_{-0.10}$	5.53 ± 0.04	$5.49^{+0.05}_{-0.04}$	5.54 ± 0.03
5011	5.52 ± 0.04	$5.78^{+0.08}_{-0.07}$	5.56 ± 0.04	$5.55^{+0.15}_{-0.11}$	$5.51^{+0.05}_{-0.04}$	$5.51^{+0.06}_{-0.05}$	5.57 ± 0.04
5271	5.55 ± 0.02	$5.61^{+0.08}_{-0.06}$	$5.58^{+0.04}_{-0.03}$	$5.40^{+0.14}_{-0.09}$	5.55 ± 0.04	5.52 ± 0.04	5.55 ± 0.03
5412	$5.57^{+0.06}_{-0.05}$	$5.68^{+0.10}_{-0.08}$	$5.60^{+0.05}_{-0.04}$	–	$5.57^{+0.05}_{-0.04}$	$5.58^{+0.07}_{-0.06}$	5.56 ± 0.05
8838	$5.37^{+0.11}_{-0.10}$	$5.41^{+0.19}_{-0.15}$	$5.48^{+0.08}_{-0.07}$	–	$5.34^{+0.09}_{-0.08}$	$5.47^{+0.11}_{-0.09}$	$5.34^{+0.09}_{-0.08}$
Weighted Average	**5.52 ± 0.03**	**5.62 ± 0.07**	**5.57 ± 0.02**	**5.40 ± 0.06**	**5.52 ± 0.04**	**5.48 ± 0.03**	**5.53 ± 0.04**

Table D9. Fe^{2+}/H^+ abundances based on T_e(high). The units are logarithmic with $n(H) = 12$.

	Cut 1	Cut 2		Cut 3		Cut 4	
λ	Nebula	HH 529 II	Nebula	HH 529 III	Nebula	Nebula	Combined cuts
4658	$5.77^{+0.05}_{-0.04}$	$5.92^{+0.03}_{-0.02}$	5.81 ± 0.03	5.72 ± 0.03	5.78 ± 0.03	5.75 ± 0.03	5.79 ± 0.03
4702	$5.76^{+0.05}_{-0.04}$	5.92 ± 0.03	5.80 ± 0.03	5.75 ± 0.04	5.78 ± 0.03	5.74 ± 0.03	$5.79^{+0.04}_{-0.03}$
4734	$5.74^{+0.05}_{-0.04}$	$5.91^{+0.04}_{-0.03}$	$5.81^{+0.04}_{-0.03}$	5.73 ± 0.06	$5.77^{+0.04}_{-0.03}$	$5.75^{+0.04}_{-0.03}$	5.79 ± 0.04
4755	$5.76^{+0.05}_{-0.04}$	5.94 ± 0.03	5.83 ± 0.03	5.79 ± 0.05	5.79 ± 0.03	5.76 ± 0.03	5.81 ± 0.03
4770	$5.76^{+0.05}_{-0.04}$	5.96 ± 0.03	5.84 ± 0.03	5.87 ± 0.05	$5.81^{+0.04}_{-0.03}$	$5.75^{+0.04}_{-0.03}$	$5.82^{+0.04}_{-0.03}$
4778	$5.76^{+0.06}_{-0.05}$	6.08 ± 0.04	$5.84^{+0.04}_{-0.03}$	5.74 ± 0.10	$5.78^{+0.04}_{-0.03}$	$5.70^{+0.05}_{-0.04}$	5.82 ± 0.04
4881	5.79 ± 0.04	5.94 ± 0.03	5.83 ± 0.03	5.76 ± 0.04	5.79 ± 0.03	5.76 ± 0.03	5.80 ± 0.03
5011	$5.76^{+0.06}_{-0.05}$	6.09 ± 0.04	5.79 ± 0.03	$5.90^{+0.07}_{-0.06}$	5.76 ± 0.03	$5.77^{+0.05}_{-0.04}$	5.82 ± 0.04
5271	5.77 ± 0.04	5.91 ± 0.03	5.81 ± 0.03	5.74 ± 0.04	5.79 ± 0.03	5.77 ± 0.03	5.79 ± 0.03
5412	$5.80^{+0.07}_{-0.06}$	$5.97^{+0.07}_{-0.06}$	5.83 ± 0.04	–	5.81 ± 0.04	5.83 ± 0.06	5.80 ± 0.05
8838	$5.73^{+0.12}_{-0.11}$	5.87 ± 0.13	$5.83^{+0.07}_{-0.06}$	–	$5.72^{+0.08}_{-0.07}$	5.86 ± 0.09	$5.72^{+0.09}_{-0.08}$
Weighted Average	**5.77 ± 0.02**	**5.94 ± 0.05**	**5.82 ± 0.02**	**5.75 ± 0.05**	**5.78 ± 0.02**	**5.76 ± 0.03**	**5.80 ± 0.02**

Table D10. Cl^{2+}/H^+, Cl/H, and log(Cl/O) abundances using T_e(low), T_e([S III]), and T_e(high). The units are logarithmic with $n(H) = 12$.

			T_e(low)			T_e([S III])			T_e(high)		
Cut	Component	O^{2+}/O	Cl^{2+}/H^+	Cl/H	log(Cl/O)	Cl^{2+}/H^+	Cl/H	log(Cl/O)	Cl^{2+}/H^+	Cl/H	log(Cl/O)
1	Nebular	0.73 ± 0.04	4.78 ± 0.02	4.83 ± 0.02	-3.63 ± 0.03	$4.88^{+0.06}_{-0.05}$	4.92 ± 0.06	-3.53 ± 0.07	5.01 ± 0.03	5.04 ± 0.03	-3.42 ± 0.05
2	HH 529 II	0.94 ± 0.04	$4.80^{+0.08}_{-0.06}$	4.83 ± 0.07	-3.74 ± 0.07	$5.01^{+0.06}_{-0.05}$	5.03 ± 0.05	-3.54 ± 0.05	5.08 ± 0.03	5.10 ± 0.03	-3.47 ± 0.04
2	Nebular	0.77 ± 0.05	$4.81^{+0.04}_{-0.03}$	4.86 ± 0.04	-3.61 ± 0.06	$4.93^{+0.06}_{-0.05}$	4.97 ± 0.06	-3.49 ± 0.07	5.03 ± 0.03	5.06 ± 0.03	-3.41 ± 0.05
3	HH 529 III	0.90 ± 0.05	$4.77^{+0.13}_{-0.09}$	4.80 ± 0.12	-3.72 ± 0.13	$5.03^{+0.08}_{-0.07}$	5.05 ± 0.08	-3.48 ± 0.09	$5.09^{+0.05}_{-0.04}$	5.11 ± 0.05	-3.42 ± 0.06
3	Nebular	0.79 ± 0.05	$4.80^{+0.04}_{-0.03}$	4.85 ± 0.04	-3.60 ± 0.06	$4.96^{+0.06}_{-0.05}$	4.99 ± 0.06	-3.46 ± 0.07	$5.03^{+0.03}_{-0.02}$	5.06 ± 0.03	-3.39 ± 0.05
4	Nebular	0.78 ± 0.05	4.79 ± 0.04	4.85 ± 0.04	-3.62 ± 0.06	$4.95^{+0.06}_{-0.05}$	4.99 ± 0.06	-3.48 ± 0.07	5.03 ± 0.03	5.06 ± 0.03	-3.41 ± 0.05
–	Combined cuts	0.81 ± 0.05	4.79 ± 0.03	4.84 ± 0.03	-3.62 ± 0.05	$4.94^{+0.05}_{-0.04}$	4.97 ± 0.05	-3.50 ± 0.06	5.02 ± 0.03	5.05 ± 0.03	-3.41 ± 0.05

Table D11. Comparison of the observed [Ni III] intensity ratios and theoretical ones predicted by the transition probabilities adopted in Table D3.

		Mesa-Delgado et al. (2009)	Delgado-Inglada et al. (2016)	This work		
Ratio	Esteban et al. (2004)	HH 202 S	Orion Bar	Nebular	HH 529 II	Prediction
6534/6000	2.09 ± 0.94	1.58 ± 0.38	1.46 ± 0.40	1.54 ± 0.39	3.35 ± 1.40	2.19
6946/6000	–	0.28 ± 0.09	–	0.31 ± 0.11	0.82 ± 0.52	0.39

Table D12. Ni^{2+}/H^+ abundances per line. The units are logarithmic with $n(H) = 12$.

	Cut 1	Cut 2		Cut 3		Cut 4	
λ	Nebula	HH 529 II	Nebula	HH 529 III	Nebula	Nebula	Combined cuts
6000	4.52 ± 0.08	$4.42^{+0.13}_{-0.11}$	$4.34^{+0.07}_{-0.06}$	–	4.40 ± 0.07	$4.42^{+0.10}_{-0.09}$	4.35 ± 0.08
6534	$4.22^{+0.10}_{-0.11}$	4.61:	4.19 ± 0.06	4.32:	4.16 ± 0.07	4.18 ± 0.11	4.26 ± 0.07
6682	$4.76^{+0.14}_{-0.13}$	–	$4.70^{+0.14}_{-0.13}$	–	$4.44^{+0.14}_{-0.13}$	–	–
6797	$4.50^{+0.23}_{-0.22}$	4.94:	4.79 ± 0.08	–	4.77 ± 0.10	4.81:	4.77 ± 0.14
6946	$3.94^{+0.26}_{-0.23}$	$4.75^{+0.19}_{-0.17}$	4.23 ± 0.11	4.37:	4.21 ± 0.11	$4.23^{+0.15}_{-0.14}$	4.31:
7890	4.42 ± 0.04	$4.52^{+0.08}_{-0.06}$	4.49 ± 0.04	$4.28^{+0.15}_{-0.11}$	$4.45^{+0.05}_{-0.04}$	$4.45^{+0.05}_{-0.04}$	4.46 ± 0.04
Weighted Average	$\mathbf{4.37 \pm 0.14}$	$\mathbf{4.50 \pm 0.08}$	$\mathbf{4.33 \pm 0.17}$	$\mathbf{4.28^{+0.15}_{-0.11}}$	$\mathbf{4.32 \pm 0.16}$	$\mathbf{4.36 \pm 0.12}$	$\mathbf{4.38 \pm 0.10}$

Table D13. He^+/H^+ abundances determined using He I triplet lines highly affected by self-absorption. The row of 'sum' is the result of adding the measured intensity of the triplets presented and redistributing it assuming negligible self-absorption effects ($\tau = 0$). The units are logarithmic with $n(H) = 12$.

λ_0	Cut 1	Cut 2		Cut 3		Cut 4	
(Å)	Nebula	HH 529 II	Nebula	HH 529 III	Nebula	Nebula	Combined Cuts
3188	10.67 ± 0.02	10.92 ± 0.02	10.63 ± 0.02	10.97 ± 0.05	10.62 ± 0.02	10.68 ± 0.02	10.71 ± 0.02
3889	10.60 ± 0.02	10.93 ± 0.02	10.52 ± 0.02	10.75 ± 0.02	10.42 ± 0.02	10.55 ± 0.02	10.61 ± 0.02
4713	11.01 ± 0.03	11.10 ± 0.03	11.04 ± 0.03	$11.02^{+0.03}_{-0.04}$	11.07 ± 0.02	11.11 ± 0.02	11.07 ± 0.02
5876	10.96 ± 0.01	10.95 ± 0.01	10.97 ± 0.01	10.92 ± 0.01	10.98 ± 0.01	10.96 ± 0.01	10.97 ± 0.01
7065	11.34 ± 0.04	$11.22^{+0.05}_{-0.04}$	11.35 ± 0.04	11.18 ± 0.06	11.34 ± 0.04	11.37 ± 0.04	11.34 ± 0.04
Sum	$\mathbf{10.91 \pm 0.02}$	$\mathbf{10.97 \pm 0.02}$	$\mathbf{10.90 \pm 0.02}$	$\mathbf{10.93 \pm 0.03}$	$\mathbf{10.89 \pm 0.02}$	$\mathbf{10.90 \pm 0.02}$	$\mathbf{10.91 \pm 0.02}$

Table D14. He^+/H^+ abundances determined with He I singlet lines and triplet lines less affected by self-absorption effects. The units are logarithmic with $n(H) = 12$.

λ_0	Cut 1	Cut 2		Cut 3		Cut 4	
(Å)	Nebula	HH 529 II	Nebula	HH 529 III	Nebula	Nebula	Combined Cuts
3614	10.93 ± 0.02	10.85 ± 0.04	10.89 ± 0.02	11.09 ± 0.05	10.86 ± 0.02	10.85 ± 0.02	10.89 ± 0.02
3965	10.88 ± 0.01	10.86 ± 0.02	10.89 ± 0.01	10.93 ± 0.02	10.87 ± 0.01	10.88 ± 0.01	10.89 ± 0.01
4026	10.89 ± 0.01	10.97 ± 0.01	10.90 ± 0.01	11.00 ± 0.01	10.93 ± 0.01	10.93 ± 0.01	10.93 ± 0.01
4388	10.90 ± 0.01	10.96 ± 0.01	10.92 ± 0.01	10.97 ± 0.01	10.91 ± 0.01	10.91 ± 0.01	10.92 ± 0.01
4438	10.95 ± 0.03	10.88 ± 0.04	10.92 ± 0.02	11.08 ± 0.07	10.92 ± 0.02	10.91 ± 0.03	10.94 ± 0.03
4471	10.87 ± 0.01	10.96 ± 0.01	10.90 ± 0.01	10.93 ± 0.01	10.91 ± 0.01	10.93 ± 0.01	10.91 ± 0.01
4922	10.90 ± 0.01	10.94 ± 0.01	10.92 ± 0.01	10.94 ± 0.01	10.92 ± 0.01	10.92 ± 0.01	10.92 ± 0.01
5016	10.87 ± 0.01	10.78 ± 0.02	10.88 ± 0.01	10.84 ± 0.02	10.88 ± 0.01	10.88 ± 0.01	10.87 ± 0.01
6678	10.90 ± 0.02	10.94 ± 0.02	10.91 ± 0.01	10.93 ± 0.02	10.92 ± 0.02	10.90 ± 0.01	10.92 ± 0.02
7281	10.90 ± 0.03	10.95 ± 0.03	10.92 ± 0.03	10.93 ± 0.04	10.92 ± 0.03	10.91 ± 0.03	10.93 ± 0.03
Average	$\mathbf{10.89 \pm 0.02}$	$\mathbf{10.95 \pm 0.03}$	$\mathbf{10.90 \pm 0.01}$	$\mathbf{10.95 \pm 0.03}$	$\mathbf{10.90 \pm 0.02}$	$\mathbf{10.91 \pm 0.02}$	$\mathbf{10.91 \pm 0.02}$

Table D15. O^{2+} abundances based on RLs. The units are logarithmic with $n(H) = 12$.

Mult.	Transition	λ_0	Cut 1	Cut 2		Cut 3		Cut 4	Combined Cuts
			Nebula	HH 529 II	Nebula	HH 529 III	Nebula	Nebula	
1	$3s^4P\text{-}3p^4D^0$	4638.86	8.547 ± 0.038	8.938 ± 0.027	8.546 ± 0.019	$8.742^{+0.113}_{-0.111}$	8.566 ± 0.067	$8.519^{+0.031}_{-0.032}$	8.632 ± 0.044
		4641.81	$8.433^{+0.017}_{-0.018}$	$8.809^{+0.017}_{-0.018}$	$8.516^{+0.014}_{-0.013}$	$8.824^{+0.027}_{-0.026}$	$8.502^{+0.014}_{-0.013}$	$8.509^{+0.017}_{-0.018}$	$8.575^{+0.017}_{-0.018}$
		4649.13	$8.473^{+0.024}_{-0.022}$	8.793 ± 0.014	8.520 ± 0.011	$8.782^{+0.026}_{-0.027}$	8.536 ± 0.015	$8.534^{+0.018}_{-0.016}$	$8.589^{+0.016}_{-0.015}$
		4650.84	$8.469^{+0.032}_{-0.031}$	8.912 ± 0.027	8.509 ± 0.019	$9.016^{+0.044}_{-0.043}$	8.521 ± 0.023	$8.558^{+0.029}_{-0.028}$	8.602 ± 0.028
		4661.63	8.534:	$9.021^{+0.027}_{-0.026}$	8.550:	$8.974^{+0.032}_{-0.031}$	8.602:	8.609:	8.672:
		4673.73	$8.579^{+0.152}_{-0.149}$	9.041 ± 0.120	$8.478^{+0.070}_{-0.069}$	8.960:	$8.790^{+0.062}_{-0.060}$	$8.749^{+0.088}_{-0.087}$	$8.730^{+0.099}_{-0.095}$
		4676.23	$8.400^{+0.052}_{-0.053}$	$8.748^{+0.047}_{-0.049}$	8.475 ± 0.022	$8.926^{+0.068}_{-0.069}$	8.497 ± 0.026	$8.507^{+0.031}_{-0.030}$	$8.543^{+0.034}_{-0.035}$
		Average	$\mathbf{8.465 \pm 0.043}$	$\mathbf{8.830 \pm 0.073}$	$\mathbf{8.515 \pm 0.018}$	$\mathbf{8.843 \pm 0.085}$	$\mathbf{8.517 \pm 0.033}$	$\mathbf{8.525 \pm 0.026}$	$\mathbf{8.584 \pm 0.022}$
2	$3s^4P\text{-}3p^4P^0$	4317.14	$8.498^{+0.052}_{-0.054}$	$9.099^{+0.030}_{-0.031}$	8.671 ± 0.022	–	$8.644^{+0.047}_{-0.048}$	8.656 ± 0.035	8.723:
		4345.56	8.582 ± 0.057	$9.194^{+0.043}_{-0.044}$	8.714 ± 0.026	$9.139^{+0.072}_{-0.073}$	8.659 ± 0.031	8.726 ± 0.030	$8.829^{+0.043}_{-0.044}$
		4349.43	8.659 ± 0.040	$9.015^{+0.022}_{-0.021}$	8.678 ± 0.013	$8.996^{+0.051}_{-0.052}$	$8.650^{+0.021}_{-0.022}$	$8.715^{+0.026}_{-0.025}$	8.767 ± 0.030
		4366.89	$8.631^{+0.041}_{-0.040}$	$9.237^{+0.026}_{-0.025}$	8.710 ± 0.022	$9.210^{+0.056}_{-0.055}$	$8.672^{+0.030}_{-0.031}$	$8.724^{+0.031}_{-0.030}$	8.835 ± 0.030
		Average	8.595 ± 0.062	9.085 ± 0.091	8.686 ± 0.016	9.074 ± 0.097	8.656 ± 0.009	8.706 ± 0.027	8.802 ± 0.033
5	$3s^2P\text{-}3p^2D^0$	4414.90	$8.807^{+0.053}_{-0.051}$	$8.939^{+0.046}_{-0.047}$	8.754 ± 0.025	–	$8.772^{+0.026}_{-0.027}$	$8.689^{+0.053}_{-0.052}$	$8.753^{+0.036}_{-0.035}$
		4416.97	$8.622^{+0.049}_{-0.063}$	–	$8.769^{+0.031}_{-0.030}$	–	8.734 ± 0.039	$8.712^{+0.043}_{-0.044}$	$8.680^{+0.046}_{-0.034}$
		Average	8.710 ± 0.093	$8.939^{+0.046}_{-0.047}$	8.760 ± 0.007	–	8.759 ± 0.018	8.702 ± 0.011	8.712 ± 0.037
10	$3p^4D^0\text{–}3d^4F$	4069.62	$8.459^{+0.064}_{-0.060}$	–	8.246:	–	8.352:	$8.657^{+0.071}_{-0.069}$	8.299:
		4069.88	$8.352^{+0.050}_{-0.049}$	8.431:	8.297:	8.341:	8.386:	$8.412^{+0.096}_{-0.091}$	8.353:
		4072.15	8.449 ± 0.026	$8.608^{+0.035}_{-0.034}$	$8.421^{+0.017}_{-0.018}$	8.758 ± 0.064	$8.423^{+0.021}_{-0.022}$	$8.372^{+0.027}_{-0.026}$	8.467 ± 0.026
		4075.86	8.436:	8.757:	–	–	–	$8.407^{+0.030}_{-0.029}$	–
		4078.84	$8.299^{+0.166}_{-0.159}$	$8.998^{+0.093}_{-0.092}$	$8.503^{+0.040}_{-0.039}$	–	8.787:	–	–
		4085.11	8.212 ± 0.150	9.385:	8.509 ± 0.035	9.385:	8.408 ± 0.065	$8.699^{+0.044}_{-0.043}$	8.810:
		4092.93	–	8.550:	$8.598^{+0.049}_{-0.047}$	8.553:	$8.453^{+0.073}_{-0.071}$	8.627:	9.013:
		Average	8.421 ± 0.048	8.623 ± 0.093	8.450 ± 0.052	8.758 ± 0.064	8.423 ± 0.009	8.413 ± 0.099	8.467 ± 0.026
15	$3s^2D\text{-}3p^2F^0$	4590.97	$8.414^{+0.062}_{-0.060}$	$8.595^{+0.062}_{-0.061}$	$8.385^{+0.034}_{-0.033}$	$8.681^{+0.073}_{-0.072}$	8.387 ± 0.031	8.415 ± 0.057	$8.433^{+0.045}_{-0.043}$
19	$3p^4P^0\text{–}3d^4P$	4121.46	8.791:	–	8.865 ± 0.030	–	8.806:	8.862:	8.762:
		4132.80	$8.451^{+0.069}_{-0.071}$	9.029 ± 0.056	$8.565^{+0.027}_{-0.026}$	$9.023^{+0.154}_{-0.148}$	8.512 ± 0.035	8.579 ± 0.044	$8.651^{+0.053}_{-0.051}$
		4153.30	$8.622^{+0.038}_{-0.037}$	9.059 ± 0.031	8.605 ± 0.019	$8.976^{+0.053}_{-0.051}$	$8.603^{+0.023}_{-0.024}$	8.623 ± 0.037	8.725 ± 0.032
		Average	8.565 ± 0.079	9.051 ± 0.013	8.616 ± 0.093	8.812 ± 0.153	8.568 ± 0.044	8.603 ± 0.022	8.701 ± 0.034
20	$3p^4P^0 - 3d^4D$	4104.99	–	8.761:	$8.363^{+0.126}_{-0.123}$	–	$8.458^{+0.102}_{-0.098}$	8.494 ± 0.097	–
		4110.79	8.811:	9.584:	8.805:	9.167:	8.766:	9.250:	9.030:
		4119.22	$8.563^{+0.049}_{-0.048}$	$8.842^{+0.061}_{-0.059}$	$8.626^{+0.023}_{-0.022}$	–	$8.475^{+0.072}_{-0.074}$	$8.722^{+0.036}_{-0.034}$	$8.605^{+0.044}_{-0.043}$
		Average	$8.563^{+0.049}_{-0.048}$	$8.842^{+0.061}_{-0.059}$	8.626 ± 0.087	9.167:	8.469 ± 0.008	8.674 ± 0.087	$8.605^{+0.044}_{-0.043}$
36	$3p^2F^0\text{–}3d^2G$	4185.44	$8.095^{+0.062}_{-0.061}$	8.034 ± 0.112	$7.971^{+0.045}_{-0.043}$	8.425:	$8.079^{+0.065}_{-0.066}$	$8.108^{+0.071}_{-0.070}$	$8.074^{+0.092}_{-0.088}$
		4189.79	$8.344^{+0.047}_{-0.044}$	8.638 ± 0.048	$8.307^{+0.031}_{-0.029}$	8.808 ± 0.120	$8.329^{+0.071}_{-0.070}$	$8.380^{+0.055}_{-0.052}$	$8.418^{+0.062}_{-0.063}$
		Average	8.200 ± 0.128	8.279 ± 0.323	8.107 ± 0.172	8.808 ± 0.120	8.146 ± 0.119	8.217 ± 0.138	8.211 ± 0.176
3d-4f	$3d^4F\text{-}4fG^2\ [3]^0$	4087.15	8.588 ± 0.092	$8.868^{+0.117}_{-0.119}$	$8.644^{+0.065}_{-0.067}$	9.142 ± 0.099	$8.431^{+0.057}_{-0.056}$	$8.526^{+0.096}_{-0.095}$	8.651 ± 0.082
	$3d^4F\text{-}4fG^2\ [5]^0$	4089.29	$8.451^{+0.058}_{-0.057}$	8.939:	$8.518^{+0.032}_{-0.030}$	8.752:	$8.422^{+0.028}_{-0.027}$	$8.412^{+0.051}_{-0.048}$	8.555 ± 0.036
	$3d^4F\text{-}4fG^2\ [3]^0$	4095.64	–	8.824 ± 0.100	$8.499^{+0.054}_{-0.053}$	9.385:	8.545:	–	–
	$3d^4F\text{-}4fG^2\ [4]^0$	4097.26	$8.547^{+0.059}_{-0.056}$	–	$8.551^{+0.029}_{-0.028}$	–	8.577 ± 0.031	$8.592^{+0.039}_{-0.040}$	$8.497^{+0.036}_{-0.035}$
	$3d^4D\text{-}4fF^2\ [4]^0$	4275.55	$8.464^{+0.070}_{-0.068}$	$8.680^{+0.106}_{-0.110}$	$8.520^{+0.046}_{-0.047}$	–	$8.475^{+0.053}_{-0.052}$	$8.554^{+0.063}_{-0.060}$	$8.497^{+0.062}_{-0.061}$
		Average	8.494 ± 0.052	8.767 ± 0.082	8.534 ± 0.032	9.142 ± 0.099	8.468 ± 0.067	8.507 ± 0.081	8.525 ± 0.041
	Mult. 1, 2, 10, 20 and 3d-4f transitions	Average	8.465 ± 0.072	8.838 ± 0.143	8.539 ± 0.084	8.857 ± 0.115	8.512 ± 0.075	8.523 ± 0.108	8.541 ± 0.137

Table D16. O^+, C^{2+}, and Ne^{2+} abundances based on RLs. The units are logarithmic with $n(H) = 12$.

			Cut 1	Cut 2		Cut 3		Cut 4	
Mult.	Transition	λ_0	Nebula	HH 529 II	Nebula	HH 529 III	Nebula	Nebula	Combined Cuts
					O^+				
1	$3s^5S^0-3p^5P$	7771.94 7774.17 7775.39	8.344 ± 0.100	<7.91	8.250 ± 0.064	<7.95	8.275 ± 0.073	$8.274^{+0.068}_{-0.069}$	8.187 ± 0.073
					C^{2+}				
6	$3d^2D-4f^2F^0$	4267.00 4267.18 4267.26	$8.349^{+0.030}_{-0.031}$	8.457 ± 0.017	8.347 ± 0.017	8.557 ± 0.026	8.339 ± 0.013	$8.328^{+0.021}_{-0.022}$	8.371 ± 0.026
16.04	$4d^2D-6f^2F^0$	6151.27 6151.53	–	9.054:	8.376:	–	8.441 ± 0.120	–	–
17.02	$4f^2F^0-5g^2G$	9903.46 9903.89	$8.326^{+0.043}_{-0.045}$	$8.465^{+0.066}_{-0.063}$	8.363 ± 0.035	$8.622^{+0.138}_{-0.136}$	$8.301^{+0.057}_{-0.056}$	$8.353^{+0.043}_{-0.042}$	$8.377^{+0.057}_{-0.056}$
17.04	$4f^2F^0-6g^2G$	6461.95 6462.13	8.354 ± 0.091	8.704:	8.298 ± 0.065	–	8.318 ± 0.060	8.351 ± 0.071	$8.353^{+0.118}_{-0.116}$
17.06	$4f^2F^0-7g^2G$	5342.38 5342.50	8.619:	–	$8.449^{+0.059}_{-0.060}$	–	$8.502^{+0.064}_{-0.065}$	–	–
		Adopted	$\mathbf{8.342 \pm 0.030}$	$\mathbf{8.458 \pm 0.021}$	$\mathbf{8.351 \pm 0.025}$	$\mathbf{8.560 \pm 0.026}$	$\mathbf{8.340 \pm 0.029}$	$\mathbf{8.334 \pm 0.022}$	$\mathbf{8.371 \pm 0.026}$
					Ne^{2+}				
1	$3s^4P-3p^4P^0$	3694.21	–	$8.643^{+0.072}_{-0.073}$	$8.095^{+0.063}_{-0.065}$	–	8.315:	–	–
		3766.26	–	$8.515^{+0.137}_{-0.135}$	$8.034^{+0.089}_{-0.092}$	–	$8.036^{+0.153}_{-0.150}$	–	–
		Adopted	–	$\mathbf{8.603 \pm 0.057}$	$\mathbf{8.072 \pm 0.029}$	–	$\mathbf{8.036 \pm 0.150}$	–	–

Table D17. Values of t^2 estimated for each component, based on the combination of T_e(He I), T_e([O III]), T_e([S III]), and T_e([N I]I).

Cut	Component	$t^2(O^{2+})$	$t^2(S^{2+})$	$t^2(N^+)$
1	Nebular	0.004 ± 0.012	0.040 ± 0.026	0.053 ± 0.018
2	HH 529 II	0.025 ± 0.013	0.062 ± 0.026	0.095 ± 0.024
2	Nebular	0.008 ± 0.012	0.039 ± 0.025	0.058 ± 0.018
3	HH 529 III	0.030 ± 0.017	0.072 ± 0.034	0.120 ± 0.038
3	Nebular	0.010 ± 0.013	0.036 ± 0.026	0.064 ± 0.019
4	Nebular	0.022 ± 0.014	0.062 ± 0.027	0.079 ± 0.020

Table D18. Average velocities and FWHM for the observed ions in each component. The number of lines used in the average are shown in parentheses.

		Nebular Cut 2		HH 529 II		HH 529 III	
Ion	I.P. (eV)	$\langle V \rangle$ (km s^{-1})	$\langle$FWHM$\rangle$ (km s^{-1})	$\langle V \rangle$ (km s^{-1})	$\langle$FWHM$\rangle$ (km s^{-1})	$\langle V \rangle$ (km s^{-1})	$\langle$FWHM$\rangle$ (km s^{-1})
[O II]	0.00	28.80 ± 0.03(2)	11.80 ± 0.02(2)	–	–	–	–
[C II]	0.00	28.70 ± 0.03(3)	9.49 ± 0.10(3)	–	–	–	–
[N II]	0.00	30.25 ± 0.64(3)	9.51 ± 0.60(3)	–	–	–	–
[Cr II]	6.77	28.28 ± 2.66(5)	9.71 ± 1.19(5)	− 26.50 ± 1.00(1)	25.60 ± 1.00(1)	− 27.20 ± 1.00(1)	39.40 ± 1.00(1)
[Ni II]	7.64	30.20 ± 0.08(10)	11.75 ± 0.63(10)	− 30.20 ± 6.09(3)	15.81 ± 2.83(3)	–	–
[Fe II]	7.90	27.33 ± 1.36(34)	11.84 ± 2.29(34)	− 28.76 ± 1.21(2)	13.66 ± 0.97(2)	–	–
[S II]	10.36	23.10 ± 0.86(4)	21.52 ± 0.90(4)	− 27.80 ± 0.03(4)	16.29 ± 0.45(4)	− 21.94 ± 1.46(6)	22.92 ± 1.00(6)
[Cl II]	12.97	24.80 ± 1.00(1)	20.40 ± 1.00(1)	− 23.80 ± 1.00(1)	18.90 ± 1.00(1)	–	–
H I	13.60	16.39 ± 0.78(51)	24.95 ± 0.16(51)	− 29.08 ± 0.36(51)	27.20 ± 0.01(51)	− 23.90 ± 0.89(45)	33.12 ± 0.44(45)
[O II]	13.62	17.85 ± 1.65(2)	18.69 ± 0.69(2)	− 28.40 ± 1.20(2)	20.04 ± 1.10(2)	− 21.60 ± 0.03(2)	25.27 ± 0.53(2)
O I	13.62	18.73 ± 0.50(3)	23.29 ± 0.86(3)	–	–	–	–
[N II]	14.53	20.67 ± 0.95(4)	19.45 ± 0.05(4)	− 28.70 ± 0.80(4)	18.13 ± 0.45(4)	− 19.75 ± 1.05(3)	25.98 ± 0.19(3)
[Fe III]	16.19	13.83 ± 1.09(21)	12.10 ± 0.32(21)	− 31.90 ± 0.02(17)	13.56 ± 0.34(17)	− 26.43 ± 1.07(13)	25.11 ± 2.47(13)
[Cr III]	16.49	12.40 ± 2.02(4)	16.98 ± 4.86(4)	− 34.54 ± 1.56(3)	20.24 ± 1.56(3)	− 23.60 ± 1.00(1)	10.80 ± 1.00(1)
[Ni III]	18.17	20.28 ± 0.15(2)	15.36 ± 0.87(2)	− 24.54 ± 0.24(2)	12.80 ± 1.57(2)	− 19.20 ± 1.00(1)	25.70 ± 1.00(1)
[S III]	23.34	15.00 ± 1.00(1)	12.70 ± 1.00(1)	− 30.60 ± 1.00(1)	15.10 ± 1.00(1)	− 25.90 ± 1.00(1)	25.10 ± 1.00(1)
[Cl III]	23.81	14.20 ± 0.30(4)	12.44 ± 0.29(4)	− 30.98 ± 1.91(3)	16.16 ± 1.06(3)	− 27.24 ± 0.08(2)	25.81 ± 1.08(2)
C II	24.38	18.63 ± 1.95(6)	13.71 ± 0.69(6)	− 26.00 ± 2.18(5)	21.61 ± 1.82(5)	− 23.39 ± 1.93(2)	46.05 ± 4.30(2)
He I	24.59	15.87 ± 0.53(75)	15.81 ± 0.33(75)	− 29.08 ± 0.90(66)	21.52 ± 1.23(66)	− 24.42 ± 0.60(42)	26.51 ± 0.63(42)
[Ar III]	27.63	15.40 ± 0.04(2)	11.10 ± 0.04(2)	− 30.40 ± 0.04(2)	16.10 ± 0.04(2)	− 25.00 ± 1.00(1)	25.10 ± 1.00(1)
[Fe IV]	30.65	21.20 ± 1.00(1)	12.30 ± 1.00(1)	− 23.70 ± 1.00(1)	19.40 ± 1.00(1)	–	–
[Cr IV]	30.96	18.40 ± 1.00(1)	12.10 ± 1.00(1)	− 25.70 ± 1.00(1)	21.90 ± 1.00(1)	− 30.20 ± 1.00(1)	39.40 ± 1.00(1)
[O III]	35.12	16.13 ± 1.37(3)	11.75 ± 0.45(3)	− 29.07 ± 1.03(3)	17.60 ± 0.01(3)	− 25.03 ± 0.42(3)	25.02 ± 0.70(3)
O II	35.12	15.80 ± 0.03(6)	12.64 ± 0.44(6)	− 29.38 ± 0.12(6)	18.89 ± 0.43(6)	− 25.23 ± 0.68(6)	31.78 ± 3.46(6)
[Cl IV]	39.61	17.80 ± 1.00(1)	10.50 ± 1.00(1)	− 27.60 ± 1.00(1)	21.90 ± 1.00(1)	− 20.50 ± 1.00(1)	33.10 ± 1.00(1)
[Ar IV]	40.74	15.35 ± 1.55(2)	11.69 ± 0.69(2)	− 29.45 ± 2.65(2)	21.20 ± 2.20(2)	− 26.83 ± 0.07(2)	27.88 ± 2.92(2)
[Ne III]	40.96	15.80 ± 0.10(2)	12.35 ± 0.05(2)	− 28.95 ± 0.05(2)	16.22 ± 0.04(2)	− 25.90 ± 0.03(2)	25.50 ± 0.03(2)
Ne II	40.96	14.92 ± 0.33(2)	14.44 ± 1.49(2)	− 26.89 ± 0.37(2)	22.28 ± 0.14(2)	–	–
N I	14.53	29.82 ± 0.25(16)	9.47 ± 0.20(16)	− 29.80 ± 1.00(1)	36.00 ± 1.00(1)	− 25.40 ± 1.00(1)	29.40 ± 1.00(1)
Si II	16.35	19.25 ± 2.45(10)	19.42 ± 1.35(10)	− 29.18 ± 1.06(8)	17.35 ± 1.78(8)	− 26.90 ± 1.16(7)	23.89 ± 2.25(7)
Si III	33.49	12.91 ± 1.00(1)	13.23 ± 2.79(1)	− 31.80 ± 1.00(1)	10.80 ± 1.00(1)	–	–
Ne I	21.57	16.66 ± 2.38(6)	15.66 ± 0.65(6)	− 31.78 ± 5.50(3)	23.81 ± 2.20(3)	–	–
S II	23.34	16.50 ± 0.69(5)	16.69 ± 4.21(5)	− 26.88 ± 0.44(3)	25.49 ± 3.34(3)	− 34.90 ± 1.00(1)	33.10 ± 1.00(1)
N II	29.60	15.07 ± 2.57(25)	13.65 ± 1.94(25)	− 29.93 ± 1.10(10)	18.33 ± 2.29(10)	− 25.31 ± 3.86(7)	24.49 ± 7.94(7)
S III	34.79	16.06 ± 0.80(4)	13.83 ± 2.61(4)	− 29.04 ± 1.87(4)	25.21 ± 3.48(4)	− 38.86 ± 4.34(3)	15.85 ± 4.12(3)
N III	47.45	11.52 ± 0.81(2)	11.94 ± 0.16(2)	− 36.50 ± 1.00(1)	22.70 ± 1.00(1)	–	–

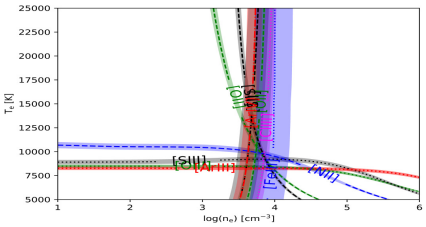

(a) Cut 1, nebular component.

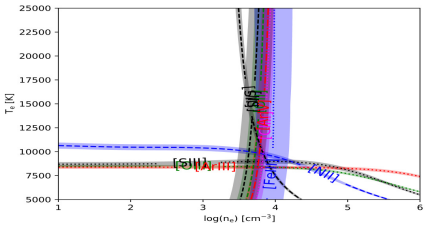

(b) Cut 2, nebular component.

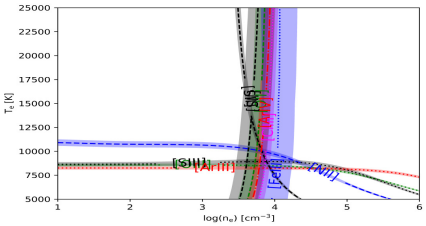

(c) Cut 3, nebular component.

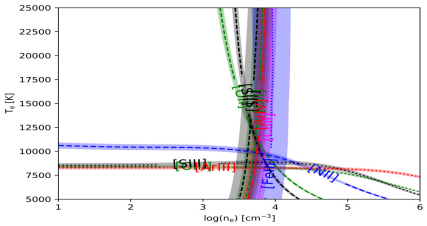

(d) Cut 4, nebular component.

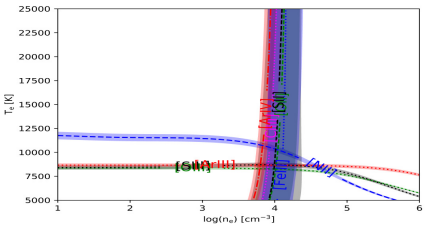

(e) HH 529 II

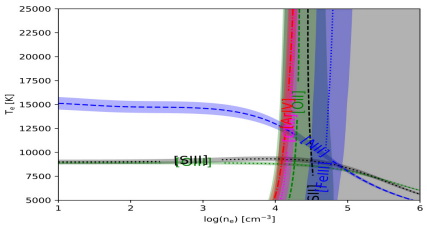

(f) HH 529 III

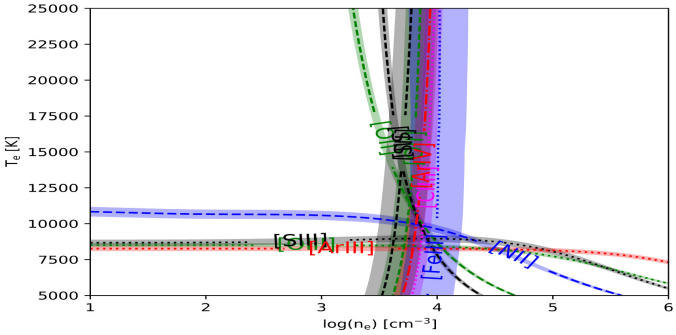

(g) All cuts combined.

Figure D1. Plasma diagnostic plots for each of the seven components analysed in this work. The labelled diagnostics correspond to those discussed in Section 4.1, whose results are presented in Table 4.

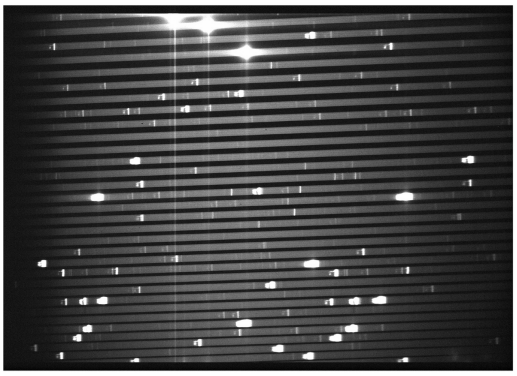

Figure D2. Image of part of the echelle orders extracted in the UVES blue arm using dichroic #2 setting ($\Delta\lambda$ = 3750–4995 Å). The contrast highlights reflections in the optical system of the spectrograph that can affect some lines. We have established that order 1 is the order at the bottom and 31 at the top.

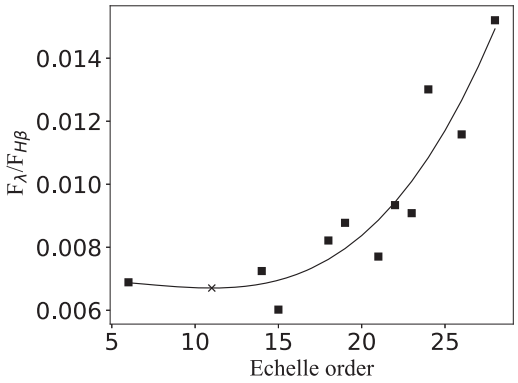

Figure D3. Least-squares fit of the flux emission for the third source of 'ghost lines' in the echelle orders. The prediction for the ghost line at λ = 4089.07 (in the order 11) is marked with a cross.

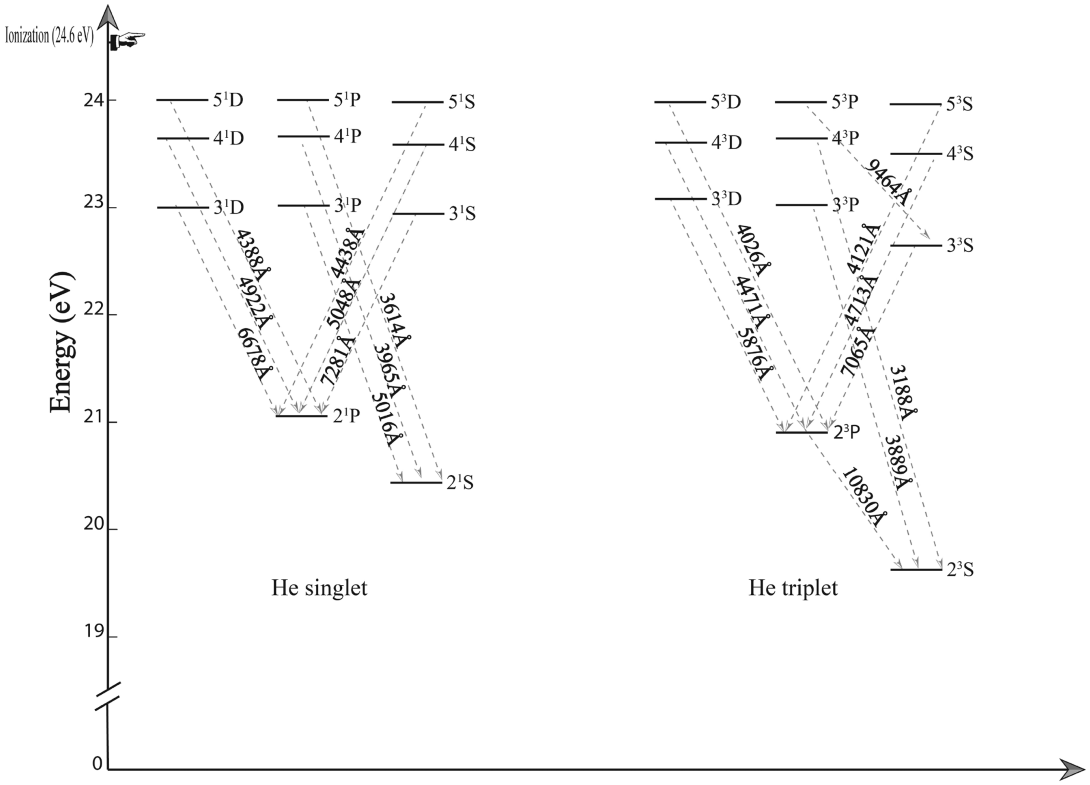

Figure D4. Grotrian diagram of He I for both configurations: triplet and singlet.

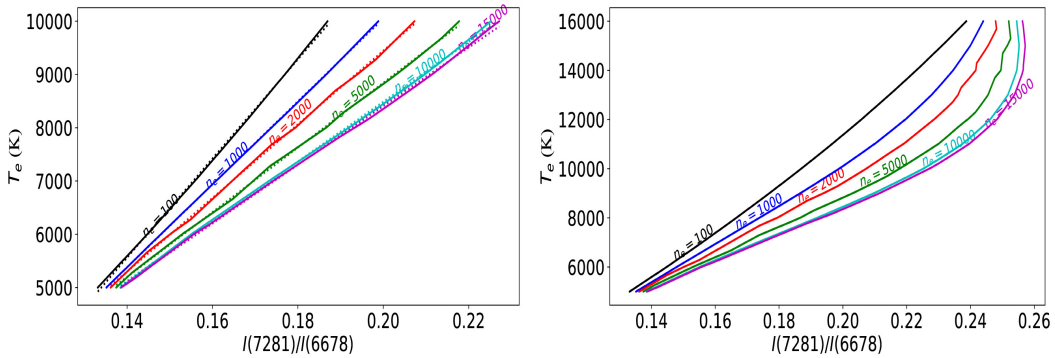

Figure D5. Dependence of I(He I λ7281)/I(He I λ6678) on the physical conditions.

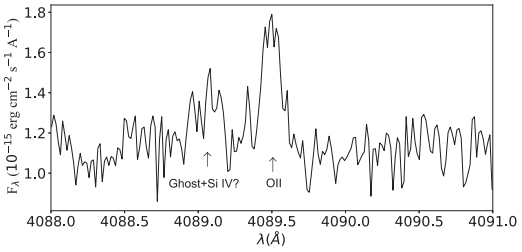

Figure D6. Emission spectrum of the spatial cut 4 around λ4089.29. There are no high-velocity components in this spatial cut.

This paper has been typeset from a TEX/LATEX file prepared by the author.

4

HH204: a spatially-resolved study of a HH object

This chapter provides the second article of the series "Photoionized Herbig-Haro objects in the Orion Nebula through deep high-spectral resolution spectroscopy", published in the Astrophysical Journal (ApJ) 2021, Volume 918, Number 1, id.27, 28 pp. The article was the main subject of several press releases[a]

In this chapter, we analyse HH204, one of the most prominent HHs of the Orion Nebula. It is located around 3×10^{-1} pc from θ^1 Ori C, at the south of the Orion Bar. Its emission lines have fluxes similar or even brighter than those of the main nebular emission, presenting a spectrum with a very high signal to noise ratio. Due to this, in addition to the global analysis of its integrated spectrum, we analyse its spatial properties pixel by pixel along the slit. We resolve its dependencies at a scale of 4×10^{-4} pc, unveiling the different gas layers of the working surface and their interactions with the environmental gas.

We estimate than more than 99% of the gas of HH204 is in photoionisation equilibrium, being composed by ions of low and intermediate ionisation stages. The remnant gas with a high degree of ionisation is mostly shock heated. These conditions permitted us to observe and analyse the layer stratification of a photoionised HH, which until now had only been modelled theoretically. The chemical analysis of the gas in photoionisation equilibrium of HH204 shows good agreement with the composition of the Orion Nebula (except for Fe and Ni). In fact, in HH204 we find no AD. This allows us to constrain this problem in H II

[a] `https://www.iac.es/en/outreach/news/anatomy-impact-protostellar-jet-orion-nebula`.

regions, which may rely on temperature inhomogeneities, starlight fluorescence and/or chemical inhomogeneities, which we show do not affect HH204. Given the pixel by pixel analysis of HH204, we demonstrate a constant depletion and ionisation pattern between Fe and Ni. These two elements have higher abundances than the Orion Nebula by a factor of 3.5, due to the destruction of dust particles in the bowshock.

By using HST images, we find several large-scale flow candidates to be driving HH204. However, the evidences are not conclusive enough, so HH204 may have its origin in a stellar source near to the Orion Trapezium or close to the southern region of Orion South. HH204 shows deuterium line emission, which are produced by fluorescence excitation which indicates, together with other evidence, the existence of a trapped ionisation front. The effects of HH204 within the surrounding environment are important and can lead to large errors in the calculation and interpretation of the chemical composition of the Orion Nebula when not using enough spectral resolution. By simulating an intermediate spectral and spatial resolution spectrum where the kinematic components are blended, we show that we can underestimate the O abundance by $\sim$40% (this effect can be seen in other elements in different proportions), due to an underestimation of the electron density. Finally, we analyse the Diffuse Blue Layer (DBL), a layer of ionised gas with a slightly different radial velocity than that of the Orion Nebula and HH204. This is the first time its chemical composition has been derived.

The Astrophysical Journal, 918:27 (28pp), 2021 September 1 https://doi.org/10.3847/1538-4357/ac0cf5

Photoionized Herbig–Haro Objects in the Orion Nebula through Deep High Spectral Resolution Spectroscopy. II. HH 204

J. E. Méndez-Delgado[1,2], W. J. Henney[3], C. Esteban[1,2], J. García-Rojas[1,2], A. Mesa-Delgado[4], and K. Z. Arellano-Córdova[5]
[1] Instituto de Astrofísica de Canarias (IAC), E-38205 La Laguna, Spain; jemd@iac.es
[2] Departamento de Astrofísica, Universidad de La Laguna, E-38206 La Laguna, Spain
[3] Instituto de Radioastronomía y Astrofísica, Universidad Nacional Autónoma de México, Apartado Postal 3-72, 58090 Morelia, Michoacán, Mexico
[4] Calle Camino Real 64, Icod el Alto, Los Realejos, E-38414, Tenerife, Spain
[5] Department of Astronomy, The University of Texas at Austin, 2515 Speedway, Stop C1400, Austin, TX 78712, USA
Received 2021 May 4; revised 2021 June 8; accepted 2021 June 16; published 2021 September 1

Abstract

We analyze the physical conditions, chemical composition, and other properties of the photoionized Herbig–Haro (HH) object HH 204 through Very Large Telescope echelle spectroscopy and Hubble Space Telescope imaging. We kinematically isolate the high-velocity emission of HH 204 from the emission of the background nebula and study the subarcsecond distribution of physical conditions and ionic abundances across the HH object. We find that low- and intermediate-ionization emission arises exclusively from gas at photoionization equilibrium temperatures, whereas the weak high-ionization emission from HH 204 shows a significant contribution from higher-temperature shock-excited gas. We separately derive the ionic abundances of HH 204, the emission of the Orion Nebula, and the fainter diffuse blue layer. In HH 204, the O^{+} abundance determined from collisional excited lines matches the one based on recombination lines, while the O^{2+} abundance is very low, so that the oxygen abundance discrepancy is zero. The ionic abundances of Ni and Fe in HH 204 have similar ionization and depletion patterns, with total abundances that are a factor of 3.5 higher than in the rest of the Orion Nebula due to dust destruction in the bow shock. We show that a failure to resolve the kinematic components in our spectra would lead to significant error in the determination of chemical abundances (for instance, a 40% underestimate of O), mainly due to incorrect estimation of the electron density.

Unified Astronomy Thesaurus concepts: Interstellar medium (847); Chemical abundances (224); Herbig-Haro objects (722); H II regions (694)

Supporting material: machine-readable table

1. Introduction

Collimated matter jets and Herbig–Haro (HH) objects are phenomena associated with star formation (see Mundt & Fried 1983; Hartigan 1989; Reipurth & Bally 2001; Nisini et al. 2005, and references therein). These objects are considered to have originated through a centrifugal-magnetic launch mechanism from young stellar objects (YSOs; see Schwartz 1983; Strom et al. 1983; Nisini et al. 2018, and references therein). These jets have a doubly important role: on the one hand, from their origin, they regulate the stellar accretion by removing the angular momentum, modifying the conditions of the matter of the disk (see Hartigan et al. 1994; Giannini et al. 2013, 2015, and references therein); on the other hand, as it passes through the surrounding medium, they modify the physical conditions of the environment.

Within the strong radiation field of the Orion Nebula, the HH objects immersed in it are photoionized, so the emission of the gas in photoionization equilibrium of the HH objects dominates the global emission over the thin cooling layer that is formed after the shock passage (Henney 2002). This makes it possible to study the chemical composition of the gas of these HH objects—which, in principle, must be the same as in the Orion Nebula—with standard methods for studying photoionized regions.

The HH object HH 204 is located in the central region of the Orion Nebula, just southeast of the Orion Bar, apparently close to the θ^2 Ori A star. It was observed by Münch & Wilson (1962) and classified as an HH by Cantó et al. (1980). The origin of the jet is usually associated with the Orion south molecular cloud (Orion-S; O'Dell et al. 2017a), an active star formation area of the Orion Nebula. However, the source of the driving jets that feed HH 204 is not entirely clear, as we discuss in this paper. Object HH 204 is photoionized by θ^1 Ori C from behind its direction of propagation through the cavity formed by the shock (O'Dell et al. 1997a, 2017a). Through long-slit spectra, Mesa-Delgado et al. (2008) studied the effects of HH 204 on the gas of the Orion Nebula, finding peaks in the density and temperature distributions when crossing its surrounding area, as well as increases in the emission flux of [Fe III] lines produced by dust destruction. Using integral field spectroscopy, Núñez-Díaz et al. (2012) studied the influence of HH 204 in the Orion Nebula in an area of 16×16 arcsec^2, finding the presence of a trapped ionization front, as well as arguments in favor of the location of the object within the main body of the Orion Nebula and not in the Veil. Work by Mesa-Delgado et al. (2008), Núñez-Díaz et al. (2012), and O'Dell et al. (2017a) shows the presence of a high-T_e([N II]) zone, attributed to shock heating. However, this effect and the coincidental fall in the total abundance of O may be related to an underestimation of the electron density, n_e, an alternative explanation that will be discussed in Section 7.

This is the second paper in a series dedicated to studying photoionized HH objects in the Orion Nebula using high-resolution spectroscopy obtained with the Ultraviolet and Visual Echelle Spectrograph (UVES; D'Odorico et al. 2000) of the Very Large Telescope (VLT) and Hubble Space Telescope

The Astrophysical Journal, 918:27 (28pp), 2021 September 1

Table 1
Main Parameters of UVES Spectroscopic Observations

Date	Δλ (Å)	Exp. Time (s)	Seeing (arcsec)	Airmass
2013 Oct 29	3100–3885	5, 3 × 180	0.85	1.10
2013 Oct 29	3750–4995	5, 3 × 600	0.70	1.16
2013 Oct 29	4785–6805	5, 3 × 180	0.85	1.10
2013 Oct 29	6700–10420	5, 3 × 600	0.70	1.16

(HST) imaging. In this work, we analyze the physical conditions, chemical composition, and dynamical properties of HH 204, separating the emission of the Orion Nebula from the HH object and other ionized gas components present in the line of sight. Previous to the present paper, there were few works dedicated to high-resolution spectroscopy of photo-ionized HH objects of the Orion Nebula, such as HH 202 S (Mesa-Delgado et al. 2009), HH 529 II, and HH 529 III (Blagrave et al. 2006; Méndez-Delgado et al. 2021).

This paper has the following content. In Section 2, we describe the observational data and their treatment. In Section 3, we describe the measurement of spectral lines and the reddening correction. In Section 4, we derive the physical conditions and ionic abundances of each of the observed velocity components, while in Section 5, we focus exclusively on HH 204, deriving its physical conditions, ionic abundances, and some properties pixel by pixel along the UVES slit, as well as studying the spatial distribution of the emission of HH 204 with HST imaging. In Section 6, we estimate the total abundances of the observed gas components. In Section 7, we study the effects of mixing three gas components of very different densities along the line of sight, simulating a spectrum with lower spectral resolution. In Section 8, we investigate the origin of HH 204 and its relationship with HH 203. In Section 9, we discuss the main results of this work and their implications. Finally, in Section 10, we summarize the conclusions. In Appendix A, we show the reliability of the [Fe III] atomic data that we use. In Appendix B, tables of data and figures are added as support material.

2. Observations and Data Reduction

The observations were made during the nights of 2013 October 28 and 29 under photometric conditions using UVES in the UT2 of the VLT in Cerro Paranal, Chile. The slit position was centered at the coordinates R.A.(J2000) = $05^h35^m22^s.72$, decl.(J2000) = $-05°25'20''.42$ with a position angle (PA) of 137°. The slit width provides an effective spectral resolution $\lambda/\Delta\lambda \approx 6.5\,\mathrm{km\,s^{-1}}$, covering the spectral range between 3100 and 10420 Å. Three exposures of 150 s of the standard star GD 71 (Moehler et al. 2014a, 2014b) were taken on the same night under similar observational conditions as the science images to achieve the flux calibration of the data. The observational settings are shown in Table 1, and the spatial coverage is presented in Figure 1. The instrumental configuration and data reduction procedure are described in Méndez-Delgado et al. (2021, hereafter Paper I). The 2D spectra (see Figure 2) show three evident components: (1) the nebular one (the emission of the Orion Nebula), which is rather homogeneously distributed along the spatial axis of the slit and occupies the reddest spectral position; (2) the "diffuse blue layer" (DBL), a slightly blueshifted homogeneous diffuse component (previously detected by Deharveng 1973) that may correspond to a different H II region along the same line of sight (García-Díaz & Henney 2007); and (3) HH 204, the "ball-shaped" blueshifted

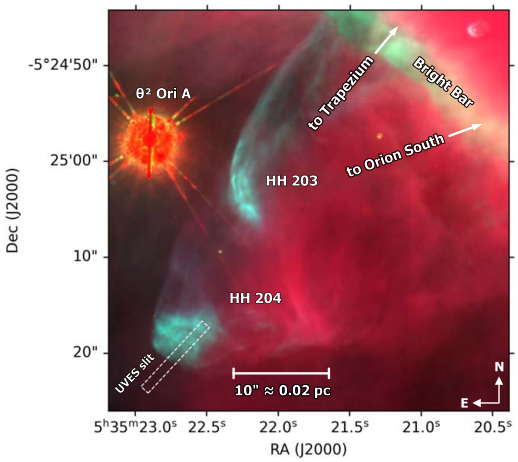

Figure 1. Location of the UVES spectrograph slit at the head of the HH 204 bow shock. The background RGB images show the immediate environs of HH 203 and 204, derived from HST WFPC2 observations (O'Dell & Wong 1996) in filters of [O III] (red), [N II] (green), and Hα (blue).

component. We define two spatial cuts—shown in Figure 2—covering a spatial area of 7.″38 for cut 1 and 1.″97 for cut 2. In cut 2, we can separate the emission of the DBL and the nebular component. However, due to the strong contribution of HH 204, we cannot separate those components in cut 1. In this case, we study the emission of the combined spectrum of the nebular component and the DBL. We also take advantage of the quality of the data, performing a pixel-by-pixel analysis of various emission lines in order to detect small variations in physical conditions and/or the chemical composition of HH 204 along the slit.

The study of the spatial distribution of the emission of HH 204 and the gas flows that may give rise to it are based in the HST WFPC2 imaging in the F502N ($\overline{\lambda} = 5012$), F547M ($\overline{\lambda} = 5446$), F656N ($\overline{\lambda} = 6564$), and F658N ($\overline{\lambda} = 6591$) filters from program GO 5469 (O'Dell & Wong 1996). The spatial pixel size of these data is 0.″045. Flux calibration and correction for contamination by continuum and nontarget lines was performed using the coefficients given in O'Dell (2009).

3. Line Intensities and Reddening

We use the SPLOT task from IRAF[6] (Tody 1993) to measure the line intensities and estimate their uncertainties, as described in detail in Paper I. In the case of the spectra of cuts 1 and 2, we measure a complete set of ∼500 and ∼300 emission lines, respectively, while in the case of the pixel-by-pixel measurements for HH 204, we limit the analysis to some representative lines: H9, Hβ, Hα; He I λλ4471, 5876, 6678; [N II] λλ5755, 6584; O I λ7772; [O I] λ6300; [O II] λ3726; [O III] λλ4363, 4959; [Ne III] λ3869; [S II] λλ6716, 6731; [S III] λλ6312, 9531; [Cl II] λ9124; [Cl III] λ5538; [Ar III] λ7136; [Ca II] λ7324; [Cr II] λ8000; [Fe II] λ9052; [Fe III] λλ4658, 4702, 4881; [Ni II] λ7378; and [Ni III] λ7890. The reddening correction was done using the extinction curve from Blagrave et al. (2007) and the emissivity coefficients of Storey & Hummer (1995) for the Hε, Hδ, Hγ, Hβ,

[6] IRAF is distributed by National Optical Astronomy Observatory, which is operated by the Association of Universities for Research in Astronomy, under cooperative agreement with the National Science Foundation.

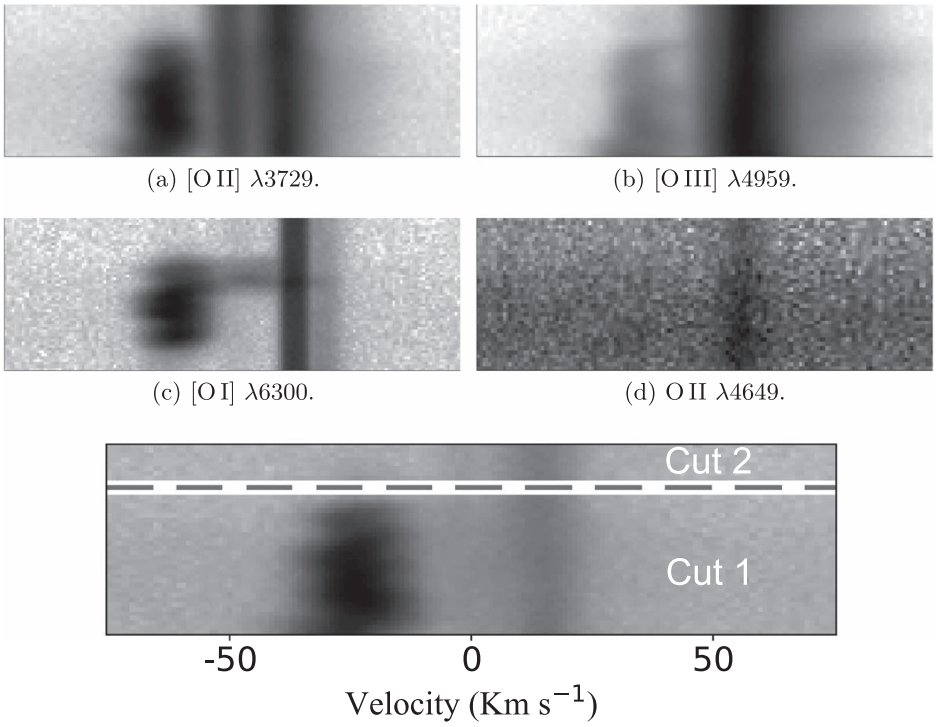

Figure 2. Top panels: sample of representative lines in the bidimensional spectrum. The *Y*-axis corresponds to the spatial direction (up southeast, down northwest; see Figure 1 for the spatial location of the slit), while the *X*-axis is the spectral axis. All figures are centered at λ_0, the rest-frame reference wavelength of each line. The "ball-shaped" emission corresponds to HH 204. The slightly blueshifted component with respect to the nebular one is the DBL (Deharveng 1973; García-Díaz & Henney 2007), mainly noticeable in the emission of low-ionization ions such as [O II]. Bottom panel: emission of the [Fe III] λ4658 line, as well as the limits and extension of the different spatial cuts selected to analyze each velocity component. Cut 1 is at the bottom, which corresponds to the westernmost one. The spatial coverage is 7.″38 and 1.″97 for cuts 1 and 2, respectively. The velocity scale is heliocentric.

Table 2
Reddening Coefficients for Each Component

	$c(\mathrm{H}\beta)$	
	HH 204	Nebula + DBL
Cut 1	0.42 ± 0.02	0.31 ± 0.03
	DBL	Nebula
Cut 2	0.42 ± 0.09	0.30 ± 0.04

and Hα Balmer lines and the P12, P11, P10, and P9 Paschen lines. The values of the extinction coefficient, $c(\mathrm{H}\beta)$, are presented in Table 2. In the case of pixel-by-pixel measurements, a value of $c(\mathrm{H}\beta) = 0.42 \pm 0.02$ was used. An example of the spectra that can be found in the online material is shown in Table 9, where some lines of the spectra of cut 1 are shown.

4. Analysis of Integrated Spectra of Each Component

4.1. Physical Conditions

We use version 1.1.13 of PyNeb (Luridiana et al. 2015) to obtain the physical conditions of the gas from the intensity ratios of collisionally excited lines (CELs) and recombination lines (RLs). PyNeb is a Python-based tool to compute line emissivities and derive physical conditions and chemical abundances of ionized gas. We have used the atomic data set presented in Tables 10 and 11 for the calculations made with PyNeb. We first estimate the n_e values given by each diagnostic of CELs by calculating each convergence of $T_e - n_e$ with the available diagnostics of electron temperature, T_e, using the PyNeb task `getCrossTemDen`, as described in detail in Paper I. The density and temperature diagnostics used are shown in Table 3. Then, in the nebular and DBL components, we adopt the weighted mean[7] of the available values of n_e obtained with the following diagnostics: [O II] λ3726/λ3729, [S II] λ6731/λ6716, and [Cl III] λ5538/λ5518. For consistency, in the case of HH 204, we rely on the n_e derived from the [Fe III] lines, since values of 10^4–10^6 cm^{-3} are above the critical densities of the CELs involved in the more common diagnostics. The simultaneous estimation of n_e([Fe III]) and T_e([Fe III]) in HH 204 is achieved by a maximum-likelihood procedure, as described in Paper I. In this procedure, different

[7] The weights were defined as the inverse of the square of the error associated with each density diagnostic.

Table 3
Physical Conditions Determined from Several Diagnostics

Diagnostic	Cut 1		Cut 2	
	HH 204	Nebula + DBL	DBL	Nebula
		n_e(cm^{-3})		
[O II] λ3726/λ3729	$15{,}420^{+7740}_{-3850}$	1130^{+150}_{-110}	400^{+140}_{-120}	1480^{+190}_{-180}
[S II] λ6731/λ6716	$11{,}350^{+9920}_{-3890}$	1350^{+290}_{-260}	300^{+140}_{-120}	1230^{+250}_{-230}
[Cl III] λ5538/λ5518	$13{,}370^{+1990}_{-1830}$	1630^{+370}_{-320}	⋯	1930^{+720}_{-650}
[Fe II] λ9268/λ9052	$13{,}100^{+2860}_{-2990}$	⋯	⋯	
[Fe III] λ4658/λ4702	$13{,}040^{+3830}_{-3130}$	3380^{+1810}_{-1340}	⋯	3200^{+2540}_{-1540}
n_e(O II)	⋯	1350 ± 150	⋯	1050 ± 200
[Fe III]*	13,540 ± 1210	⋯	⋯	⋯
Adopted	**13,540 ± 1210**	**1230 ± 160**	**350 ± 50**	**1440 ± 170**
		T_e (K)		
T_e(He I)	8790^{+480}_{-430}	9760:	5650:	7980:
[O I] λ5577/$\lambda\lambda$ 6300+64	8290^{+430}_{-320}	⋯	⋯	⋯
[N II] λ5755/λ6584	8760^{+170}_{-180}	8530^{+150}_{-190}	8120^{+390}_{-360}	8440^{+170}_{-210}
[O II] $\lambda\lambda$3726+29/$\lambda\lambda$7319+20+30+31	⋯	⋯	$10{,}390^{+730}_{-640}$	9120^{+430}_{-470}
[S II] $\lambda\lambda$4069+76/$\lambda\lambda$6716+31	8260^{+640}_{-500}	$11{,}470^{+950}_{-630}$	$10{,}440^{+1360}_{-1030}$	9890^{+650}_{-610}
[O III]λ4363/$\lambda\lambda$4959+5007	$12{,}430^{+180}_{-220}$	8010^{+90}_{-80}	⋯	8120^{+90}_{-100}
[S III] λ6312/$\lambda\lambda$9069+9531	9310^{+220}_{-330}	8180^{+190}_{-230}	7710^{+510}_{-400}	8010^{+250}_{-210}
[Fe III]*	8210 ± 220	⋯	⋯	⋯
T_e (low) adopted	**8760 ± 180**	**8530 ± 190**	**8120 ± 390**	**8440 ± 210**
T_e (high) adopted	**12,430 ± 220**	**8030 ± 60**	**7710 ± 510**	**8110 ± 90**

Note. An asterisk indicates that a maximum-likelihood method was used. The bold values are those adopted for the determination of chemical abundances.

combinations of T_e and n_e are tested to obtain the abundance of Fe^{2+}/H^+ with several [Fe III] lines, giving as a result the combination of T_e–n_e that minimizes the dispersion between the abundances obtained with all of the lines. In HH 204, we have confident detections of [Fe III] $\lambda\lambda$3240, 3335 lines from the $^5D - {}^3D$ transitions, whose ratios with lines from the multiplets $^5D - {}^3F$ and $^5D - {}^3P$ are highly dependent on T_e, as shown in Figure 3. We include the following lines in the maximum-likelihood calculation: [Fe III] $\lambda\lambda$3240, 3335, 4658, 4702, 4734, 4881, 5011, 5271. This collection of lines allows us to obtain well-constrained values of T_e([Fe III]) and n_e([Fe III]). The intensity ratios of these selected lines are consistent with the predicted ones when using transitions coming from the same atomic level (which are independent of the physical conditions of the gas), as we show in Table 12. Another density indicator that can be used with our data is n_e(O II), but only for the nebular component, which is the only one where we detect RLs of multiplet 1 of O II.

Once the representative n_e is adopted for each component, we estimate T_e through several diagnostics based on CELs, as shown in Table 3. In the case of T_e([S III]), telluric absorptions affect the line λ9069 in the nebular and DBL components. Thus, we adopt I([S III] 9531)/I([S III] 9069) = 2.47 (Podobedova et al. 2009) in these cases. In HH 204, we were able to separate the auroral [O I] λ5577 line from sky emission contamination, which permitted us to estimate T_e([O I]). In the DBL, the estimations of T_e([O II]) and T_e([S II]) are affected by some extended residual emission of HH 204 in the auroral lines that crosses the cut border, affecting the first pixels of cut 2. The T_e(He I) was estimated using the average values obtained from He I $I(\lambda7281)/I(\lambda6678)$, $I(\lambda7281)/I(\lambda4922)$, and $I(\lambda7281)/I(\lambda4388)$ line intensity ratios. Finally, we define T_e(low) as the weighted mean of T_e([N II]), T_e([O II]), and T_e([S II]), while T_e(high) is the weighted mean of T_e([O III]) and T_e([S III]).

The resulting physical conditions for all components are shown in Table 3.

4.2. Ionic Abundances

We assume the appropriate values of the n_e and T_e diagnostics for each ion—assuming a three-zone approximation—to derive the ionic abundances of the different components. We use T_e(low) for N^+, O^+, S^+, Cl^+, Ca^{2+}, Cr^+, Fe^+, Fe^{2+}, Ni^+, and Ni^{2+} and T_e([S III]) for S^{2+} and Cl^{2+}. In the case of Ne^{2+}, O^{2+}, and Ar^{3+}, we use T_e(high). We also use T_e(high) to derive the He^+, C^{2+}, and Ar^{2+} abundances for the nebular component but T_e(low) for HH 204, as we discuss in Section 5.1. We follow the same methodology described in Paper I for abundance calculations, except in some particular cases that are discussed below, together with some abundance determinations for ions whose lines were not reported in Paper I.

4.3. Ionic Abundances of Fe and Ni Ions

In HH 204, the emission lines of [Fe II], [Ni II], [Fe III], and [Ni III] are considerably enhanced in comparison with what is observed in the nebular component. Due to the low ionization degree of HH 204, we expect that Fe^+ and Ni^+ have an important contribution to the total Fe and Ni abundances. Therefore, it seems pertinent to discuss in some detail the degree of confidence of the abundance determinations based on these two ions.

Optical lines coming from the upper levels of the Fe^+ atom can be affected by continuum pumping (Lucy 1995; Rodríguez 1999; Verner et al. 2000). However, lower levels that produce the emission lines of multiplet $a^4F - a^4P$ are mostly populated by collisions (Baldwin et al. 1996). One of the strongest lines of this multiplet, [Fe II] λ8617 ($a^4F_{9/2} - a^4P_{5/2}$), could not be

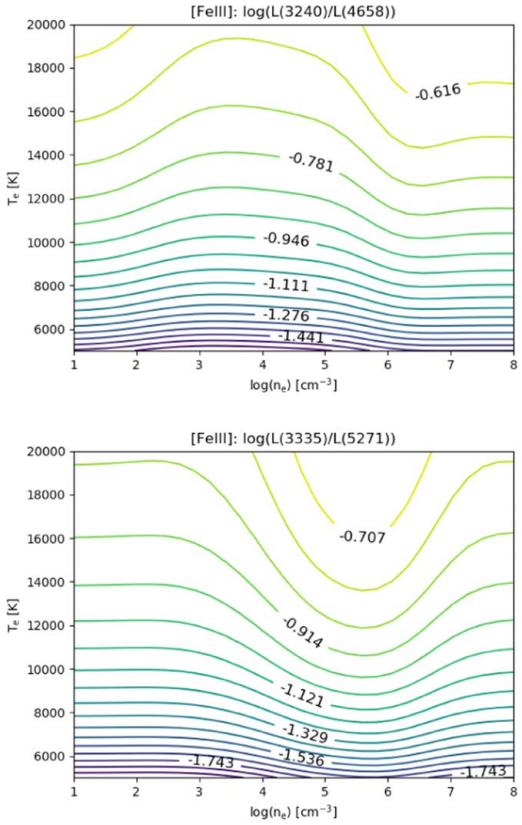

Figure 3. Predicted dependence of the [Fe III] $\lambda3240/\lambda4658$ and $\lambda3335/\lambda5271$ line intensity ratios with physical conditions.

detected due to the instrumental gap of UVES in the red arm. However, weaker lines arising from the same upper level as $\lambda\lambda9052$, 9399 ($a^4F_{7/2} - a^4P_{5/2}$, $a^4F_{5/2} - a^4P_{5/2}$), detected in HH 204, must be useful for the same purpose. Although the transition probabilities of the weakest detected lines coming from the $a^4P_{1/2}$, $a^4P_{3/2}$, and $a^4P_{5/2}$ levels still need to be tested (since these lines may be affected by undetected telluric absorptions), there is a good agreement between the measured and predicted line ratios of [Fe II] $\lambda9052/\lambda9399$, $\lambda8892/\lambda9227$, and $\lambda9268/\lambda9034$, as it is shown in Table 13. In order to make a simple test of the chosen atomic data, we take advantage of the theoretical density dependence between the population of the $a^4P_{1/2}$ and $a^4P_{5/2}$. By using the estimated T_e(low) for HH 204 and the [Fe II] $\lambda9268/\lambda9052$ intensity ratio, we obtain n_e([Fe II]) $= 13, 100^{+2860}_{-2990}$ cm^{-3}, which is consistent with the rest of the density diagnostics shown in Table 3. In cut 2, we derive the Fe^+ abundance of the nebular component by using the uncontaminated [Fe II] $\lambda8892$ line.

The $a^4F - a^4P_{5/2}$ transitions of [Fe II] and the $a^2D - a^2F_{7/2}$ ones of [Ni II] have practically the same excitation energy, giving an origin for lines that are close in wavelength (Bautista et al. 1996). However, there is an important difference in their sensitivity to fluorescence by continuum pumping due to the multiplicity of their ground states. Photoexcitations from the Fe^+ ^6D ground state to the quartet levels have low probability, and lines produced by intercombination transitions from sextet to quartet levels should be very weak (Bautista & Pradhan 1998). However, Rodríguez (1999) pointed out that the lowest quartet level, $a^4F_{9/2}$, may be metastable and promote excitations to higher quartet levels. The main pumping routes starting from this level were studied by Verner et al. (2000) at densities above 10^4 cm^{-3}, finding that this pumping populates the levels a^4H, b^4F, b^4P, and a^4G. Since transitions from any of these levels to a^4P are rather weak, its population remains practically unaffected. Nevertheless, in the case of [Ni II], the ground state and participating levels are doublets that make fluorescence effects by continuum pumping more likely (Bautista et al. 1996). However, an important factor that plays against the influence of fluorescence effects in [Ni II] in the case of HH 204 is its relatively large distance from θ^1 Ori C (150.″4), the main ionization source of the nebula (O'Dell et al. 2015, 2017b). In a simple procedure, following the formalism developed by Bautista et al. (1996, their Equation (8)), for a three-level model (level 1: $a^2D_{5/2}$, level 2: $a^2F_{7/2}$, and level 3: $z^2D^0_{5/2}$), the critical densities n_{cf}—for which if $n_e > n_{cf}$, collisional excitations dominate over fluorescence—in two zones of the Orion Nebula (a and b), both excited by θ^1 Ori C, should be related as follows:

$$\frac{n_{cf,\,a}}{n_{cf,\,b}} = \left(\frac{J_{13,\,a}}{J_{13,\,b}}\right)\left(\frac{q_{12,\,b}}{q_{12,\,a}}\right), \quad (1)$$

where q_{12} is the Maxwellian-averaged collisional strength for transitions from level 1 to level 2, and J_{13} is the intensity of the continuum at energies of the $1 \rightarrow 3$ transitions. If we choose zone a as the one observed by Osterbrock et al. (1992) and zone b as HH 204, we can assume $q_{12,b}/q_{12,a} \approx 1$, because the T_e determined by Osterbrock et al. (1992) and us are very similar (9000 and 8760 K, respectively). On the other hand, by estimating the geometrical dilution of J_{13} in both areas (the zone observed by Osterbrock et al. 1992 is located 63.″98 from θ^1 Ori C), we get $n_{cf,a}/n_{cf,b} \approx 5.53$. By adopting the $n_{cf,a}$ estimated by Bautista et al. (1996), we obtain $n_{cf,b} \approx 2.17 \times 10^3$ cm^{-3}, which is rather small compared with the density we obtain for HH 204 and therefore collisional excitation should dominate. Nevertheless, it must be considered that the apparently closer star θ^2 Ori A may also be a source of fluorescence for HH 204. However, by using the [Ni II] $\lambda7378$ ($a^2D_{5/2} - a^2F_{7/2}$) line to obtain the Ni^+ abundance and comparing with the Fe^+/H^+ ratio, we obtain $\log(Ni^+/Fe^+) = -1.27 \pm 0.06$, which is in complete agreement with the solar value of $\log(Ni/Fe)_\odot = -1.25 \pm 0.05$ (Lodders 2019), suggesting the absence of significant fluorescence effects (as discussed before, we expect larger fluorescence effects in Ni^+). Therefore, we can assume that θ^2 Ori A is not a significant source of photon pumping of [Ni II] lines in HH 204. We do not estimate the Ni^+ abundances for the rest of the velocity components because it requires a detailed analysis of the fluorescence conditions in the ionized gas, which goes beyond the scope of this paper.

We derive the Fe^{2+} abundance using the [Fe III] lines indicated in Section 4.1. The good agreement is noticeable between T_e([Fe III]), T_e([O I]), and T_e([S II]) in the case of HH 204, contrary to what was found in HH 529 II and HH 529 III, where T_e([Fe III]) was more consistent with the

temperature obtained for high-ionization ions (Méndez-Delgado et al. 2021). This is not surprising due to the different ionization degrees of HH 204 and HH 529 II+III (see Section 5).

In Paper I, we pointed out the inconsistency between the predicted and measured intensity ratios of [Ni III] $^3F - {}^3P_2$ transitions ($\lambda\lambda$6534, 6000, 6946) in HH 529 II, HH 529 III, HH 202 S, and several zones of the Orion Nebula (see Table D11 of Paper I). We obtain a similar result for HH 204, $\lambda6534/\lambda6000 = 1.38 \pm 0.18$, which is rather far from the predicted value of 2.19 (Bautista 2001). This indicates that the transition probabilities of the aforementioned lines may have errors (for a more detailed discussion, see Appendix C in Méndez-Delgado et al. 2021). We have a different situation for the intensity ratios of lines arising from the $^1D_2$ level. After subtracting the small contribution of [Cl III] λ8499.60 to the measured intensity of [Ni III] λ8499.62, we obtain [Ni III] $\lambda7890/\lambda8500 = 2.65 \pm 0.19$, in agreement with the predicted value of 2.47 (Bautista 2001). This indicates that, with the available atomic data, the most confident determinations of the Ni^{2+} abundance can be obtained with these last lines. Thus, we will adopt the Ni^{2+} abundances determined from the [Ni III] λ7890 line. Unfortunately, this line is affected by a telluric emission feature in the nebular component; therefore, we have to rely on the [Ni III] λ6534 line to determine the Ni^{2+} abundance for this component.

4.4. Ionic Abundances of Ca^+ and Cr^+

We measure some [Ca II] and [Cr II] lines with a good signal-to-noise ratio in HH 204. Thus, it allows one to estimate Ca^+ and Cr^+ abundances. However, [Cr II] lines may be affected by fluorescence similarly to [Ni II] ones. As we discuss in Section 4.3, in HH 204, collisional excitations dominate over fluorescence in the aforementioned [Ni II] transitions, and this may also be the case for [Cr II]. With this assumption, we obtain an abundance of $12 + \log(Cr^+/H^+) = 4.28 \pm 0.03$. By comparing this value with the Fe^+ and Ni^+ abundances, we obtain $\log(Cr^+/Ni^+) = -0.61 \pm 0.05$ and $\log(Cr^+/Fe^+) = -1.88 \pm 0.07$, in agreement with the solar values of $\log(Cr/Ni)_\odot = -0.57 \pm 0.05$ and $\log(Cr/Fe)_\odot = -1.82 \pm 0.04$, respectively (Lodders 2019). Nevertheless, the spatial distribution of the Cr^+/Ni^+ and Cr^+/Fe^+ ratios along the HH 204 jet is not completely constant, as described in Section 5.2, which may be indicative of different ionization/depletion patterns between these elements. Unfortunately, although several [Cr III] lines are detected, we cannot derive the Cr^{2+} abundance due to the lack of atomic data for this ion.

In the case of the Ca^+ abundance, we base our estimations on the [Ca II] λ7324 line, since λ7291 is affected by a telluric absorption in our observations. Due to its low ionization potential, much smaller than that of hydrogen, and owing to the presence of an ionization front in HH 204 (Núñez-Díaz et al. 2012), the resulting abundance may not represent the real gaseous Ca^+ abundance in the photoionized gas of HH 204.

4.5. Ionic Abundances Based on RLs

For the nebular component, the He^+ abundance is derived using T_e(high) and the lines considered in Table D14 of Paper I, which are the least affected ones by the metastability of the 2^3S level. However, we have used T_e(low) for HH 204. In this component, our determination of T_e(He I) is more consistent with T_e(low). This is because in HH 204, [O III] emission arises from a small localized area of higher-ionized gas, and T_e([O III]) may not be representative of the He^+ volume, as we describe in Section 5.1.

The C II λ4267 is partially blended in the two velocity components of cut 1; therefore, we base our calculations on C II λ9903. We use C II λ4267 in cut 2. The C^{2+} abundance estimations based on both lines are in complete agreement in cut 2. Due to the similar ionization potentials of C^+ and He^0 and the considerations outlined in the previous paragraph, T_e(low) is also used for determining the C^{2+} abundance in HH 204.

Contrary to the situation presented in Paper I, in HH 204, O I RLs from multiplet 1 are severely affected by telluric emission features, with the exception of O I λ7772. We derive the O^+ abundance of the HH object using the intensity of this line and the predicted line strengths from Wiese et al. (1996) following Equation (2) of Esteban et al. (1998).

Estimations of the O^{2+} abundance from RLs are based on the available O II lines of multiplet 1. These are not detected in the case of HH 204 (see Figure 4). We use an estimate of the upper limit to the intensity of the λ4649 line for this component.

5. Unveiling HH 204

As mentioned in Section 3, we measure several lines pixel by pixel along the slit. The spatial resolution in the blue and red arms of UVES is slightly different (0.″246 and 0.″182 pixel^{-1}, respectively). Cut 1 includes 30 pixels in the blue arm and 42 in the red one. In the pixel-by-pixel measurements, renormalization between lines in common in each arm is not enough to dilute possible differences in the integrated flux. However, Hβ is observed in the spectra of both arms; therefore, we split our pixel spectra into two parts, 27 blue pixel spectra and 37 red pixel spectra, both groups normalized with respect to F(Hβ). The missing first pixels (from east to west) of cut 1 of both arms were not included, since the emission of HH 204 was too faint. We proceeded as follows: based on the [Fe III] $\lambda4658/\lambda4702$ line ratios, we derived n_e along HH 204 in the blue arm. Once the density distribution was estimated, the calculation of T_e([O III]) was done, also in the blue arm, through the [O III] $\lambda4363/\lambda4959$ line ratio. The spatial distribution of n_e was linearly interpolated in the red arm to estimate T_e([S III]) and T_e([N II]). Once the physical conditions are determined, we estimate the ionic abundances using the same procedure followed in Section 4.2. The zero-point of the spatial distribution is located at coordinates R.A.(J2000) = $05^h35^m22^s.81$, decl.(J2000) = $-05°25'21.''86$, just at the apparent eastern—external—edge of the bow shock. To estimate the distance from the bow shock along the jet, we adopt a heliocentric distance of 410 ± 10 pc (Binder & Povich 2018) to the Orion Nebula, based on Gaia DR2 parallaxes (Gaia Collaboration et al. 2018). The integrated emission is dominated by the blueshifted jet bullet component centered around ~ -20 km s^{-1} (in a heliocentric velocity scale) within a 1σ range of ± 10 km s^{-1}, being well separated from the DBL and the nebular emission.

5.1. Small-scale Physical Conditions

The resulting pixel-by-pixel distribution of physical conditions is shown in Figure 5. At the shock front, we can see that n_e([Fe III]) reaches values up to a factor of about 2 higher than at a distance of $\sim$13 mpc from the bow shock. The distribution

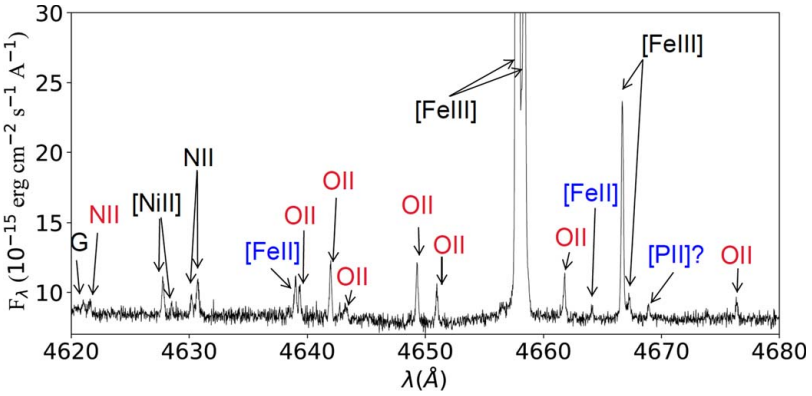

Figure 4. Section of the spectrum of spatial cut 1 covering the spectral range 4620–4680 Å. Lines emitted exclusively by HH 204 are marked in blue, while those of the Orion Nebula are marked in red. The lines observed in both components are highlighted in black. Several O II RLs from multiplet 1 are present in the nebular component, but they are not observed in HH 204 due to its low ionization degree. The emission marked with a G is a ghost feature.

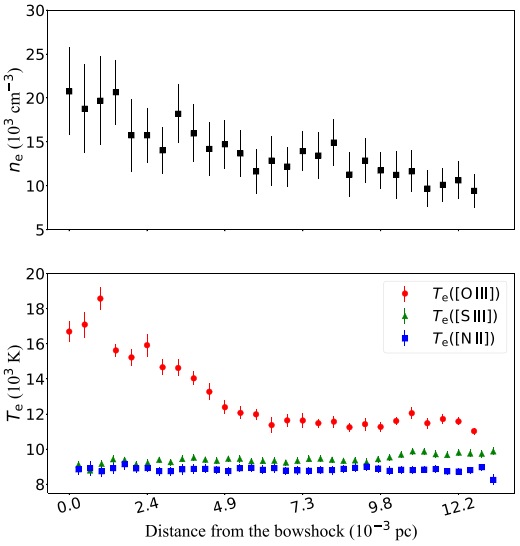

Figure 5. Spatial distribution of physical conditions as a function of the distance to the eastern—external—edge of the bow shock of HH 204. Top panel: n_e([Fe III]). The gas compresses as it approaches to the shock front, increasing its density. Bottom panel: T_e estimates with three diagnostics. While T_e([S III]) and T_e([N II]) remain unaltered, T_e([O III]) shows a strong increase when approaching the shock.

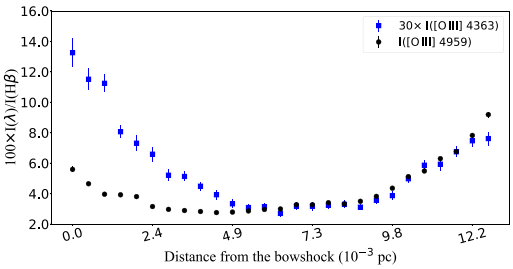

Figure 6. Same as Figure 5 but for the intensities of the [O III] $\lambda\lambda$4363, 4959 lines. Line intensity ratios with respect to H(β) have been normalized for a clearer comparison.

of T_e([N II]) is practically constant, while T_e([S III]) decreases slightly at the edge of the bow shock.

Conversely, T_e([O III]) strongly increases at distances closer to the bow shock as it is shown in Figure 6, where the intensity of the auroral line λ4363 is increased more than that of the nebular line λ4959. In the presence of a shock, a photoionized gas can be heated at a temperature higher than that fixed by photoionization equilibrium (Zel'dovich & Raizer 1967; see Section 11 of Paper I). After the shock passage, the gas cools down by radiative emission until reaching an equilibrium temperature, forming a cooling zone whose extension will be inversely proportional to the electron density (Hartigan et al. 1987). If we assume that the high-T_e([O III]) area corresponds to the cooling zone formed after the shock, the fact that T_e([S III]) and T_e([N II]) are not affected in the same way suggests that the high ionization degree emission should come (at least partially) from a different gas volume than the one that originates the low-ionization emission. Therefore, we suggest that we are seeing the superposition of two different emission components: one from the bow shock and one from the Mach disk (the shock internal to the jet). This model will be discussed in Section 9.3.1.

5.2. Small-scale Patterns in the Ionic Abundances

Figure 7 shows the spatial distribution of the ionic abundances of O. As described in Section 5.1, the increase of T_e([O III]) may be related to shock heating. Therefore, we highlight in red the O^{2+} abundances in this area in the bottom panel of Figure 7. In the top panel, we show the O^+ abundances along the full distance range and the O ones in the area where T_e([O III]) remains constant. This panel shows that practically all O is in O^+ form. It should be noted that an increase of a factor of ∼2 in the O^{2+} abundance would represent less than 1% of the total O, well below the associated

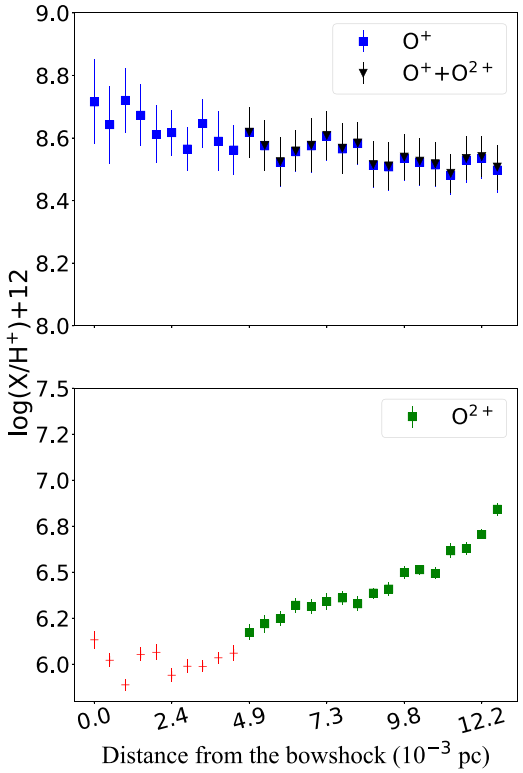

Figure 7. Same as Figure 5 but for ionic and total abundances of O. Top panel: O^+ and total O abundances. The total abundance of O was calculated as the sum of O^+ and O^{2+} in the area where T_e([O III]) remains constant: distances between 4.9 and 13 mpc from the bow shock. The contribution of O^{2+} to the total O abundance is negligible compared to the abundance of O^+. Bottom panel: O^{2+} abundances. The red crosses show the zone clearly affected by the shock (see Figures 5 and 6 and Section 5.1). The green squares indicate the area where T_e([O III]) remains constant.

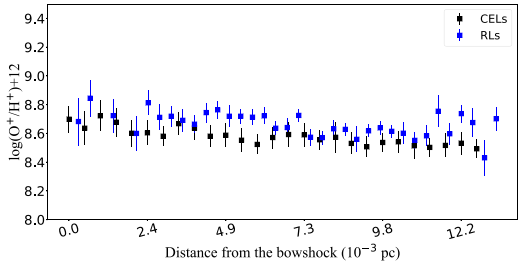

Figure 8. Same as Figure 5 but for O^+ abundances determined with CELs and RLs.

uncertainties; therefore, this increase would be undetected in analyses lacking our spatial and spectral resolutions.

In Tables 4 and 5, we can see that the O^+ abundances determined from CELs and RLs for HH 204 are the same within the errors, so we do not find an abundance discrepancy (AD) for this ion, contrary to the situation found in practically all photoionized nebulae. Figure 8 indicates the absence of systematical trends of the AD in the observed areas of HH 204. Although some fluctuations seem to be present, they are very small in any case.

In Figure 9, we present the ionic abundances of Cl and S. The species of the same ionic stage of both elements show similar pixel-by-pixel distributions. The variations of the S^{2+}/H^+ and Cl^{2+}/H^+ ratios along HH 204 are comparatively much smaller than those of S^+/H^+ and Cl^+/H^+, which show a decrease of 0.8 dex along the diagram as the distance from the bow shock increases. At distances to the bow shock smaller than ∼4.9 mpc, the abundances of S^+ and Cl^+ seem to stabilize, and presumably, almost all S and Cl must be only once or twice ionized. This allows the estimation of their total abundances without an ionization correction factor (ICF).

The pixel-by-pixel distributions of the ionic abundances of Fe and Ni are clearly correlated, as shown in Figure 10. Similar to those found for S and Cl (see Figure 9), close to the bow shock, the contribution of species of Fe and Ni with ionic charges higher than Fe^{2+} and Ni^{2+} to their total abundances should be negligible. The ratios of the ionic abundances between both elements remain constant, as shown in Figure 11, being $\log(Fe^+/Ni^+) = 1.26 \pm 0.03$, $\log(Fe^{2+}/Ni^{2+}) = 1.37 \pm 0.03$, and $\log(Fe/Ni) = 1.33 \pm 0.03$. Although the value of $\log(Fe^{2+}/Ni^{2+})$ is slightly

Table 4
Chemical Abundances Obtained with CELs of the Integrated Spectra of Each Component

	Cut 1		Cut 2	
Ion	HH 204	Nebula + DBL	DBL	Nebula
O^+	8.62 ± 0.05	8.14 ± 0.05	$8.26^{+0.13}_{-0.09}$	$8.18^{+0.06}_{-0.05}$
O^{2+}	6.34 ± 0.02	7.96 ± 0.02	$7.33^{+0.15}_{-0.10}$	8.04 ± 0.02
N^+	7.72 ± 0.03	7.34 ± 0.03	$7.40^{+0.08}_{-0.06}$	$7.29^{+0.04}_{-0.03}$
Ne^{2+}	5.05 ± 0.03	7.16 ± 0.02	⋯	$7.23^{+0.03}_{-0.02}$
S^+	6.60 ± 0.04	5.93 ± 0.03	$5.92^{+0.07}_{-0.06}$	$5.86^{+0.04}_{-0.03}$
S^{2+}	6.80 ± 0.03	6.84 ± 0.03	$6.85^{+0.10}_{-0.08}$	6.89 ± 0.04
Cl^+	4.72 ± 0.03	4.17 ± 0.03	$4.08^{+0.10}_{-0.09}$	4.05 ± 0.04
Cl^{2+}	$4.77^{+0.04}_{-0.03}$	4.93 ± 0.04	$4.99^{+0.16}_{-0.12}$	$4.98^{+0.06}_{-0.05}$
Ar^{2+}	5.66 ± 0.03	6.10 ± 0.02	$5.99^{+0.10}_{-0.08}$	6.12 ± 0.02
Ar^{3+}	⋯	$3.64^{+0.13}_{-0.12}$	⋯	⋯
Fe^+	6.16 ± 0.04	⋯	⋯	4.72 ± 0.08
Fe^{2+}	6.49 ± 0.02	5.72 ± 0.04	$5.56^{+0.10}_{-0.08}$	5.77 ± 0.04
Fe^{3+}	<5.11	5.73 ± 0.13	⋯	⋯
Ni^+	4.89 ± 0.02	⋯	⋯	⋯
Ni^{2+}	5.13 ± 0.03	4.37 ± 0.09	⋯	⋯
Ca^+	3.50 ± 0.03	⋯	⋯	⋯
Cr^+	4.28 ± 0.03	⋯	⋯	⋯

Note. Abundances in units of $12+\log(X^{n+}/H^+)$.

Table 5
Chemical Abundances Obtained with RLs of the Integrated Spectra of Each Component

	Cut 1		Cut 2	
Ion	HH 204	Nebula + DBL	DBL	Nebula
He^+	10.53 ± 0.02	10.85 ± 0.03	10.66 ± 0.06	10.92 ± 0.04
O^+	8.57 ± 0.03	⋯	⋯	⋯
O^{2+}	<7.54	8.25 ± 0.06	⋯	8.40 ± 0.03
C^{2+}	7.76 ± 0.07	8.22 ± 0.04	⋯	8.37 ± 0.02

Note. Abundances in units of $12+\log(X^{n+}/H^+)$.

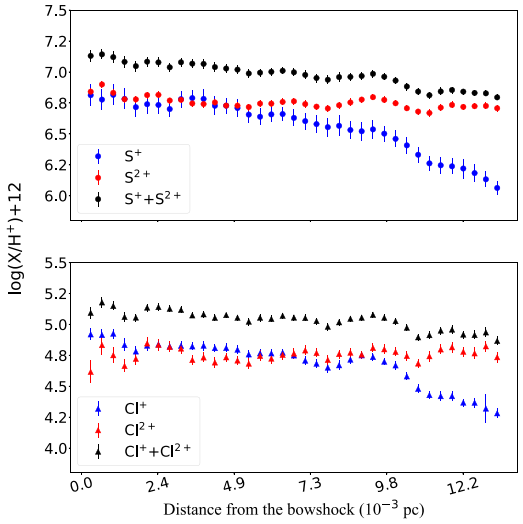

Figure 9. Same as Figure 5 but for ionic abundances of S (top panel) and Cl (bottom panel).

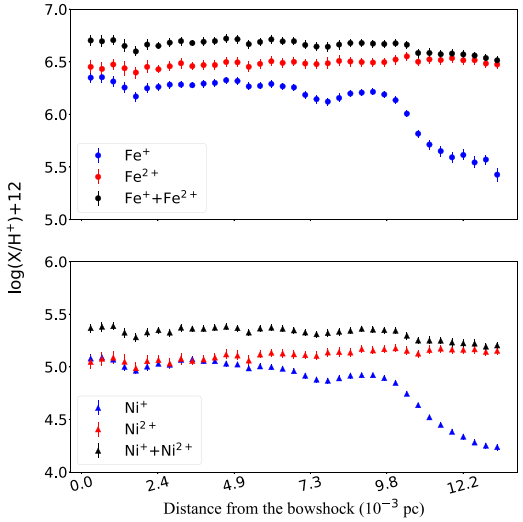

Figure 10. Same as Figure 5 but for ionic abundances of Fe (top panel) and Ni (bottom panel).

above the recommended solar value ($\log(\mathrm{Fe/Ni})_\odot = 1.25 \pm 0.05$; Lodders 2019), this may be the consequence of a slight systematic underestimation of Ni^{2+} abundance because, as we discussed in Section 4.3, the atomic data for this ion seem to show some inaccuracies.

In Figure 12, we show the similar pixel-by-pixel distributions of the He^+ and Ar^{2+} abundances. Both quantities decrease as we approach the bow shock due to the decrease of the ionization parameter as n_e increases. A slight increase is observed at distances less than ∼2.4 mpc, probably due to the same process discussed in Section 9.3.1 for the case of [O III] lines. However, the impact of the shock contribution seems to

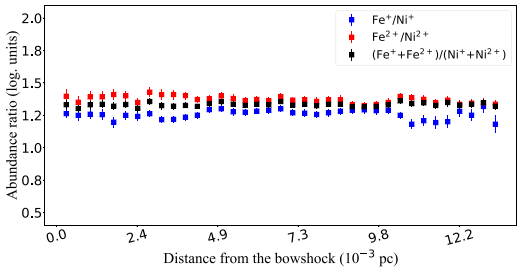

Figure 11. Same as Figure 5 but for the ratios of ionic abundances of Fe and Ni.

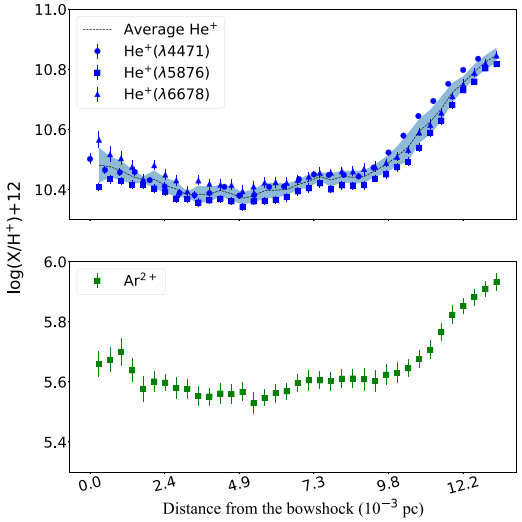

Figure 12. Same as Figure 5 but for He^+ (top panel) and Ar^{2+} (bottom panel) abundances. In the top panel, the black line indicates the average He^+ abundance obtained with He I λλ4471, 5876, 6678. The color band indicates the associated dispersion.

be negligible for these ions. For example, the fact that T_e(He I) is consistent with T_e([N II]) (see Section 4.1) reflects that the populations of the singlet levels, which are the ones used for determining T_e(He I), are largely unaffected.

In Figure 13, we show that the abundance of N^+ increases as we move toward the bow shock from $12 + \log(N^+/H^+) = 7.53 \pm 0.03$ to an apparently constant value of 7.75 ± 0.02. That plateau indicates that all nitrogen should be only once ionized. Figures 14 and 15 show the pixel-by-pixel distributions of the Cr^+ and Ca^+ abundances, respectively, which are somewhat different from the ones of Fe^+ or Ni^+ (Figure 10). This indicates that the distributions of Fe^+/Cr^+ and Fe^+/Ca^+ ratios are not constant, contrary to what is obtained for Fe^+/Ni^+ (Figure 16). In the case of the Fe^+/Cr^+ ratio, the observed trend may be related to the slight differences between their ionization energies or different depletion patterns. The curve defined by the Fe^+/Ca^+ abundance ratio may be due to the coexistence of this ion and H^0 in the trapped ionization front of HH 204 (see Section 5.3).

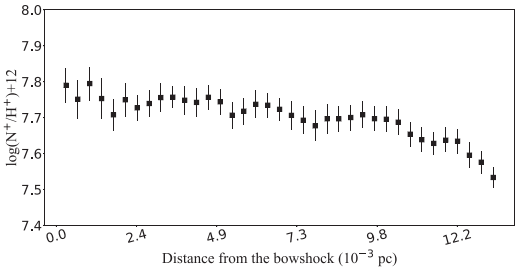

Figure 13. Same as Figure 5 but for N^+ abundances.

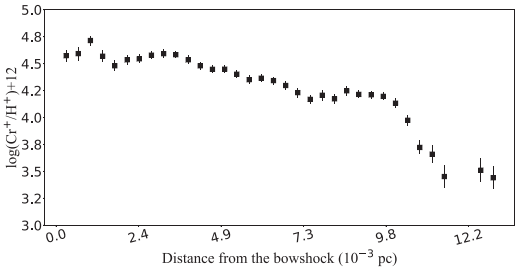

Figure 14. Same as Figure 5 but for Cr^+ abundances.

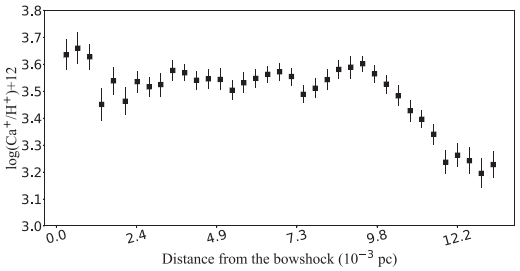

Figure 15. Same as Figure 5 but for Ca^+ abundances.

5.3. Deuterium Lines in HH 204

Deuterium emission lines were first identified in the Orion Nebula by Hébrard et al. (2000a). Unlike the expected isotopic shift of $-81.6\,\mathrm{km\,s^{-1}}$ with respect to the hydrogen lines, they observed a shifted emission around $\sim -71\,\mathrm{km\,s^{-1}}$ from Hα and Hβ. The difference of $\sim 10\,\mathrm{km\,s^{-1}}$ is essentially due to the fact that their emission is produced in different areas of the nebula, where the bulk of the gas is moving at different radial velocities. Since the hydrogen lines are produced by recombination in the ionized area that expands toward the observer, the deuterium emission is mainly due to fluorescence excitation by nonionizing far-UV continuum in areas slightly beyond the ionization front, such as the photon-dominated region (PDR), or in the H I–H II interface (O'Dell et al. 2001). After the identification of deuterium emission lines in the Orion nebula, they were also identified in other H II regions, such as M8, M16, DEM S 103, M20, and Sh 2-311 (Hébrard et al. 2000b; García-Rojas et al. 2005, 2006, 2007). As in the Orion Nebula, the deuterium emission in these H II regions has a narrow line width, consistent with their origin in colder areas.

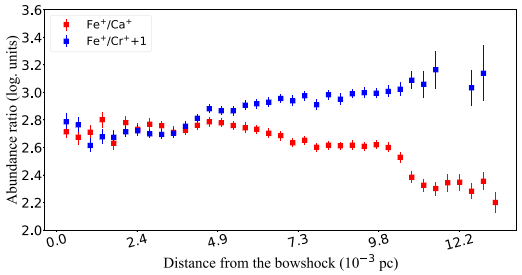

Figure 16. Same as Figure 5 but for Fe^+/Ca^+ and Fe^+/Cr^+ abundance ratios.

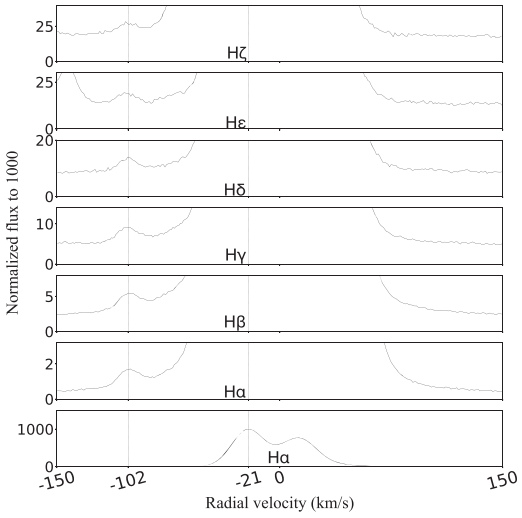

Figure 17. Deuterium lines observed in the spectra of cut 1. Vertical lines indicate the position of the deuterium lines and the H I emission from HH 204. The flux is normalized to the peak emission of HH 204 in each case.

In this work, we detect the emission of Dζ, Dε, Dδ, Dγ, Dβ, and Dα, as shown in Figure 17. In Table 6, we present the characteristics of these emissions, including the radial velocity of the D I and H I lines with respect to the laboratory wavelength of the H I ones. The observed isotopic shift of $-81.4\,\mathrm{km\,s^{-1}}$ between the deuterium and hydrogen lines indicates that both kinds of lines arise from HH 204. The observed D I/H I intensity ratios are in good agreement with the predictions of the standard model developed by O'Dell et al. (2001) for the Orion Nebula, confirming the fluorescent nature of the D I emission. Considering that the emission of deuterium occurs in areas slightly beyond the ionization front, the detection of these lines implies that the ionization front must be trapped in HH 204, moving along with it, consistent with the results of Núñez-Díaz et al. (2012), as well as other evidence that will be discussed in Section 9.3.

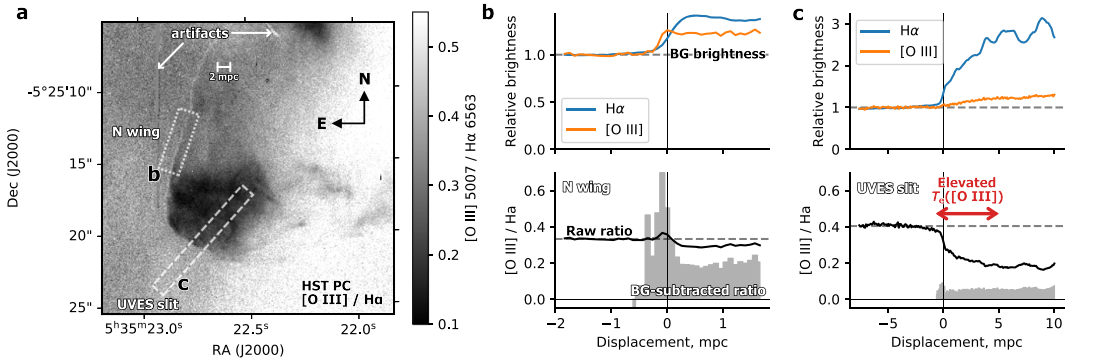

Figure 18. (a) Map of the line ratio [O III] λ5007/Hα λ6563, calculated from HST images with the PC chip of the WFPC2 camera. The position of the UVES spectrograph slit is outlined by a dashed box, while a further region of interest in the north wing of the bow shock is indicated by a dotted box. The vertically oriented "scar" at upper left is an artifact due to the bright star θ^2 Ori A, located just north of the field of view. (b) Average cut profiles of the HST images for the box in the north wing that is outlined in panel (a). The upper graph shows surface brightness profiles in the two emission lines, normalized to the mean nebular background value outside of the shock. The lower graph shows the line ratio, with the raw ratio indicated by the black solid line and the background-subtracted ratio indicated by the gray histogram. The zero-point of the displacement axis is taken to be the location of the maximum gradient in the Hα surface brightness. (c) Same as panel (b) but showing average profiles of the HST images along the UVES slit. The region of the slit that shows T_e([O III]) > 12,000 K in the blueshifted component is indicated by the red arrow.

Table 6
Characteristics of Deuterium and Hydrogen Lines in HH 204

	D I		H I		
λ_0	v_r[a] (km s^{-1})	FWHM (km s^{-1})	v_r (km s^{-1})	FWHM (km s^{-1})	I(D I)/I(H I)×1000
3889.05[b]	−103.34	13.80 ± 1.39	…	…	…
3970.07	−103.10	14.20 ± 3.40	−21.54	24.62 ± 0.02	2.99 ± 0.45
4101.73	−102.83	13.53 ± 0.86	−20.97	24.49 ± 0.01	2.24 ± 0.15
4340.46	−103.02	16.17 ± 1.40	−20.83	24.66 ± 0.01	2.10 ± 0.16
4861.32	−102.26	14.31 ± 1.90	−21.47	24.67 ± 0.01	1.06 ± 0.11
6562.80	−101.82	14.90 ± 0.79	−21.88	24.94 ± 0.01	0.58 ± 0.03

Notes.
[a] With respect to the laboratory wavelength of the closest H I line (first column).
[b] The H I λ3889.05 emission of HH 204 is blended with the nebular one of He I λ3888.65.

5.4. Subarcsecond Imaging of HH 204

Figure 18(a) shows the ratio of surface brightnesses, R([O III]) = S([O III] λ5007)/S(Hα λ6563), calculated from HST WFPC2 observations in the F502N, F547M, F656N, and F658N filters from program GO 5469 (O'Dell & Wong 1996). It can be seen that the line ratio in the background nebula shows a pronounced gradient from R([O III]) ≈ 0.3 in the northeast to R([O III]) ≈ 0.5 in the southwest.[8] Inside the bow shock, the ratio is significantly smaller, for instance, falling from ≃0.4 to ≃0.2 along the length of the UVES slit.

However, the most interesting feature of the R([O III]) image is the slight increase in the ratio that is seen in a thin layer along the leading edge of the bow shock. This is most clearly visible in the northern wing of HH 204, such as the area highlighted by a dotted box in the figure. The average profiles across the shock for this region are shown in Figure 18(b). The lower panel shows that the raw ratio (solid black line) increases only slightly above its value in the background nebula, which is because the brightness increase across the bow shock is only a small fraction of the background brightness, as can be appreciated in the upper panel. In order to isolate the emission of the shocked gas from that of the nebula, we calculate the background-subtracted line ratio,

$$R'([\mathrm{O\ III}]) = \frac{S([\mathrm{O\ III}]) - S_{\mathrm{BG}}([\mathrm{O\ III}])}{S(\mathrm{H}\alpha) - S_{\mathrm{BG}}(\mathrm{H}\alpha)}, \quad (2)$$

under the assumption that S_{BG} for each line is constant along the profile. The result is shown as a gray histogram in the lower panel of the figure, which reveals a sharp peak of width ≈0.3 mpc that reaches a maximum value R'([O III]) ≈ 2R_{BG}([O III]) and is centered on a displacement of ≈−0.1 mpc. The origin of the displacement axis is set to the peak in the spatial gradient of the Hα surface brightness, corresponding to the outer edge of the dense shocked shell. The negative displacement of the R'([O III]) peak means that this occurs outside the dense shell, closer to the shock front itself.

Figure 18(c) shows the same quantities calculated along a cut that coincides with our UVES slit at the head of HH 204. In this case, R'([O III]) is always significantly less than R_{BG}([O III]), but it does still show a small local peak with a position and width that are similar to the more impressive ones

[8] For comparison with results from our UVES spectra, and using the average reddening for the HH 204 region (Weilbacher et al. 2015), the conversion is λ4959/Hβ ≈ 1.1R([O III]).

in the northern wing. These peaks in R'([O III]) occur over a much smaller scale than any of the spatial gradients that we find in our UVES slit spectra and are only detectable because of the high spatial resolution of the HST.[9] For example, the increase in T_e([O III]) that we detect in the blueshifted emission near the shock front (Figure 5) occurs over a scale of 5 mpc, indicated by the red arrow in the figure, which is more than 10 times larger than the width of the R'([O III]) peak.

What is the origin of the narrow peak in the [O III]/Hα ratio that is seen just outside the shocked shell? When a shock propagates into low-ionization gas (predominantly O^+), there are three zones where enhanced [O III] emission might be expected (Cox & Raymond 1985; Sutherland & Dopita 2017): first, the radiative precursor in the preshock gas; second, the nonequilibrium collisional ionization zone immediately after the shock; and third, the radiative relaxation zone, where the postshock gas cools back down to the photoionization equilibrium temperature of $\sim 10^4$ K. The first of these can be ruled out in the case of HH 204 because the preshock photoionization of O^+ would require shock velocities greater than 150 km s^{-1}, and observed proper motion and radial velocities imply a shock velocity around 100 km s^{-1}. The second zone has a high temperature (>50,000 K for shock velocities >55 km s^{-1}) but is severely underionized, resulting in line emissivities that are far in excess of the equilibrium values in a very thin layer. The third zone, in which oxygen is recombining through the O^{++} stage while cooling through the range 30,000–10,000 K, is predicted to be somewhat thicker and with a higher electron density, yielding a greater contribution to the total [O III] emission. Given the electron density that we derive of 13,540 cm^{-3} (Table 3), and assuming a shock velocity <70 km s^{-1}, the cooling length should be approximately 0.05 mpc, or 0.″025, which is a few times smaller than the HST resolution. However, this analysis applies only to the head of the bow shock. In the wings, the shock is not perpendicular to the upstream gas velocity but is oblique at an angle α. This yields a postshock equilibrium density that is smaller by a factor of $\cos^2 \alpha$ and a cooling length that is larger by the same factor. Hence, the cooling length is expected to be resolved for α smaller than about 45°, which is consistent with our observations of the narrow peak in the [O III]/Hα ratio in the north wing. The reason that the same behavior is not seen in the opposite wing is probably that the ambient nebular emission is much more highly ionized there, which masks the effect.

6. Total Abundances

In the case of the nebular and DBL components, total abundances of O, Cl, and S were estimated by simply adding the abundances of all of their observed ions. Although there may be some contribution of S^{3+} and Cl^{3+}, the ICFs of Stasińska (1978) and Esteban et al. (2015), respectively, predict negligible amounts of those species. In the case of N, Ne, Ar, and C, we adopt the same ICFs used by Arellano-Córdova et al. (2020). For Fe, we use the two ICFs proposed by Rodríguez & Rubin (2005). Since the real value of Fe should be between the predictions of both ICFs (Rodríguez & Rubin 2005), in Table 7, we present those determinations as lower and upper limits of the Fe abundance.

In the case of HH 204, based on the results of Section 5, we decided not to derive the total abundances of elements for which we only observe highly ionized ions, such as He, Ne, Ar, and C, due to the low ionization degree of the gas and the large contribution of the ICFs. In the cases of O, N, Cl, S, Fe, and Ni, we can determine their total abundances without ICFs. As seen in Section 5, the spatial distribution of the abundances of the once- and twice-ionized ions of Cl, S, Fe, and Ni reach constant values at positions close to the bow shock, where the degree of ionization becomes very low. In this zone, the contribution of three or more times ionized ions of these elements should be negligible. A similar situation occurs with N, where the contribution of N^{2+} is expected to be very small close to the bow shock. Therefore, in Table 7, we present the total abundances obtained by adding the mean abundances of the once- and twice-ionized ions of Cl, S, Fe, and Ni for distances less than 4.9 mpc from the bow shock. In the case of O and N, we only consider the abundance of once-ionized ions in the same range of distances. At these distances, the pixel-by-pixel values of the O^+ abundance determined from RLs have large errors (see Figure 8) because of the faintness of the O I λ7772 line. In this case, we use the O^+ abundance obtained from the integrated spectrum presented in Table 4 to determine the total O abundance based on RLs.

Table 7
Total Abundances

Element	Cut 1		Cut 2	
	HH 204	Nebula + DBL	DBL	Nebula
O	8.62 ± 0.05	8.36 ± 0.03	8.31 ± 0.12	8.42 ± 0.04
O[a]	8.57 ± 0.03	⋯	⋯	⋯
N	7.75 ± 0.02	$7.56^{+0.04}_{-0.03}$	$7.45^{+0.09}_{-0.08}$	7.53 ± 0.05
Ne	⋯	7.56 ± 0.04	⋯	7.61 ± 0.05
S	7.07 ± 0.03	6.90 ± 0.03	6.90 ± 0.09	6.94 ± 0.04
Cl	5.10 ± 0.04	5.00 ± 0.03	5.04 ± 0.14	5.03 ± 0.05
Ar	⋯	6.14 ± 0.02	6.09 ± 0.10	6.17 ± 0.02
Fe	6.67 ± 0.03	5.91–6.09	5.64–6.19	5.97–6.13
Ni	5.35 ± 0.03	⋯	⋯	⋯
C[a]	⋯	8.49 ± 0.05	⋯	8.64 ± 0.04

Notes. Abundances in units of 12+log(X/H).
[a] Based on RLs.

7. The Effects of Lowering the Spatial and Spectral Resolution

In this section, we simulate a spectrum with lower spatial and spectral resolution by adding the flux of all of the velocity components, which includes the emission of HH 204, the DBL, and the emission of the Orion Nebula along the whole UVES slit. Following the reddening correction procedure described in Section 3, we obtain $c(\mathrm{H}\beta) = 0.36 \pm 0.02$ for this integrated spectrum.

In Figure 19, we present the resulting plasma diagnostics of the low-resolution spectrum. This diagram can be compared with those of the individual components, shown in Figure 25. If one only has the information provided by this degraded spectrum and applies the classic procedure of averaging n_e([O II]), n_e([S II]), and n_e([Cl III])—excluding n_e([Fe III]), since the sometimes-discrepant values given by this diagnostic are generally interpreted as the effect of incorrect atomic data—we would obtain $n_e = 3430 \pm 580$. Using this value of density, we would obtain T_e([O II]) = 12140^{+950}_{-930}, T_e([S II]) = 19220^{+9020}_{-2530}, T_e([N II]) = 9200 ± 200, T_e([S III]) = 8740^{+230}_{-200}, and T_e([O III]) = 8530^{+100}_{-120} K. It must

[9] Pixel size of 0.″045, which well samples the point-spread function width at an Hα of 0.″083.

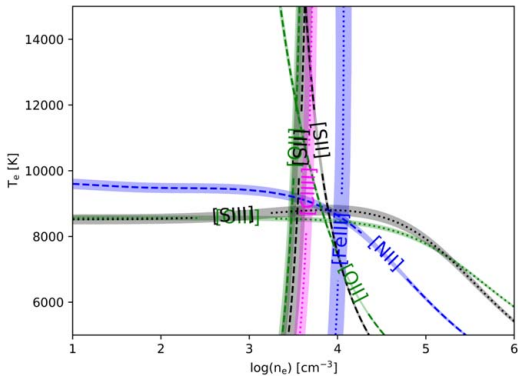

Figure 19. Plasma diagnostics of the spectrum defined by adding all of the observed velocity components along the whole UVES slit.

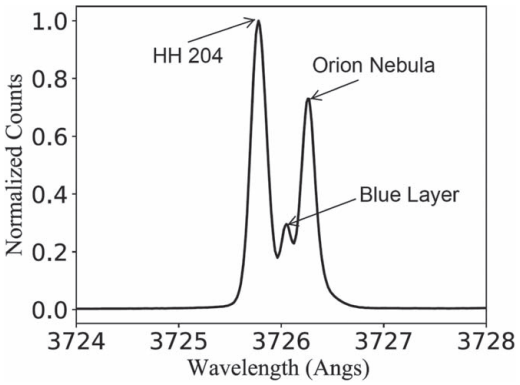

Figure 20. Normalized f([O II] λ3727) in the spectrum that results from adding all of the spatial pixels in the UVES slit. Each of the velocity components is identified.

be noted that the resulting T_e([N II]) is higher than the ones obtained for each individual component analyzed in Section 4.1. Moreover, T_e([O II]) and T_e([S II]), the most density-dependent diagnostics, show much higher values. However, their effect on abundance determinations could be somehow mitigated, as their associated uncertainties are very high, and the use of a weighted mean of the different temperature indicators would reduce their contribution. The T_e([N II]) always has much lower uncertainties and is generally the preferred temperature diagnosis for low ionization degree ions.

Following the usual procedure and assuming the physical conditions determined in the previous paragraph, we would determine the O^+ abundance using T_e([N II]) and the O^{2+} one with T_e([O III]), obtaining $O^+ = 8.15 \pm 0.04$, $O^{2+} = 7.63 \pm 0.02$, and a total abundance of $O = 8.26 \pm 0.03$. This value of the O/H ratio is lower than the one determined for all of the individual components. The only exception could be the DBL in cut 2, which shows $O = 8.31 \pm 0.12$ (see Table 7), whose uncertainty is large enough to encompass the value obtained for the low-resolution spectrum. However, this does not mean that the DBL dominates the observed abundance of O, since it is the weakest component. This is demonstrated in Figure 20, which shows the line profile of f([O II] λ3727), one of the most intense lines in the spectrum of the DBL.

The low O abundance obtained in the low-resolution spectrum is due to the use of the classical diagnostics to estimate n_e, which do not adequately account for the high density of HH 204. The critical densities of the levels involved in those diagnostics are below the density of HH 204 (see Table D5 of Paper I). Likewise, the sensitivity of I([O II] λ3726)/I([O II] λ3729) and I([S II] λ6731)/I([S II] λ6716) at $n_e \sim 10^4$ cm^{-3} is much lower than at $n_e \sim 10^2$–10^3 cm^{-3}, the normal range of densities in H II regions. The degree of ionization of each component also plays an important role. Although I([Cl III] λ5538)/I([Cl III] λ5518) is more density-sensitive than I([O II] λ3726)/I([O II] λ3729) or I([S II] λ6731)/I([S II] λ6716) at densities of around $n_e \sim 10^4$ cm^{-3}, HH 204—the component with the highest density—has a very low degree of ionization. Therefore, in the combined emission of HH 204 and the Orion Nebula, the last component has a greater weight in n_e([Cl III]). On the other hand, I([Fe III] λ4658)/I([Fe III] λ4702) is practically insensitive at densities smaller than $n_e \sim 10^3$ cm^{-3}, and the critical density of this diagnostic is above $\sim 10^6$ cm^{-3}. In addition, most of the [Fe III] emission comes from HH 204 due to its higher abundance of gaseous Fe with respect to the Orion Nebula and DBL. These properties make it an excellent indicator of the presence of high-density gas as in HH objects. In our case, the n_e([Fe III]) = $10,790^{+3230}_{-2620}$ cm^{-3} we obtain for the low-resolution spectrum is rather close to the density of HH 204. This confirms the importance of the warning given by Morisset (2017), who, through photoionization models, predicted large errors in the determination of the physical conditions and chemical abundances in nebulae if one assumes a single component when, in fact, there are several, and some of them are composed of high-density gas. The exercise we present in this section is an observational confirmation.

If instead of using the classical diagnostics to determine n_e, we take the average of the densities obtained for each component (see Table 3) weighted by their observed $F(H\beta)$, we get $n_e = 6820 \pm 810$ cm^{-3}. This value is roughly between the predictions of classical diagnostics and n_e([Fe III]). Note that in Figure 19, close to this value of density, T_e([O II]) and T_e([S II]) converge to T_e([N II]). Using that density, we obtain $T_e([O\,II]) = 8650^{+410}_{-520}$, $T_e([S\,II]) = 9890^{+1100}_{-990}$, $T_e([N\,II]) = 8850^{+210}_{-180}$, $T_e([S\,III]) = 8800^{+250}_{-160}$, and $T_e([O\,III]) = 8490^{+90}_{-120}$ K. Calculating the ionic abundances of oxygen with these physical conditions, we obtain $O^+ = 8.36^{+0.06}_{-0.05}$ and $O^{2+} = 7.64 \pm 0.02$, which implies $O = 8.44 \pm 0.05$. These values are more consistent with those obtained in the analysis of the individual components.

It is clear that the discrepancy between the different density diagnostics is not necessarily an artifact of the atomic data used. Instead, each diagnostic may be revealing the changing conditions of the gas along the line of sight of the spectrum differently. Relying uncritically only on those density diagnostics that are consistent with each other could lead to significant systematic errors.

8. Origin of the Jet that Drives HH 204

At least two different high-velocity flows converge on the general HH 203/204 region from the direction of the inner Orion Nebula (see Figure 21), but it is not clear if either of them are directly responsible for driving the HH 204 bow shock. One flow is at a PA of ≈118° and transitions from a high-ionization state northwest of the Bright Bar (cyan

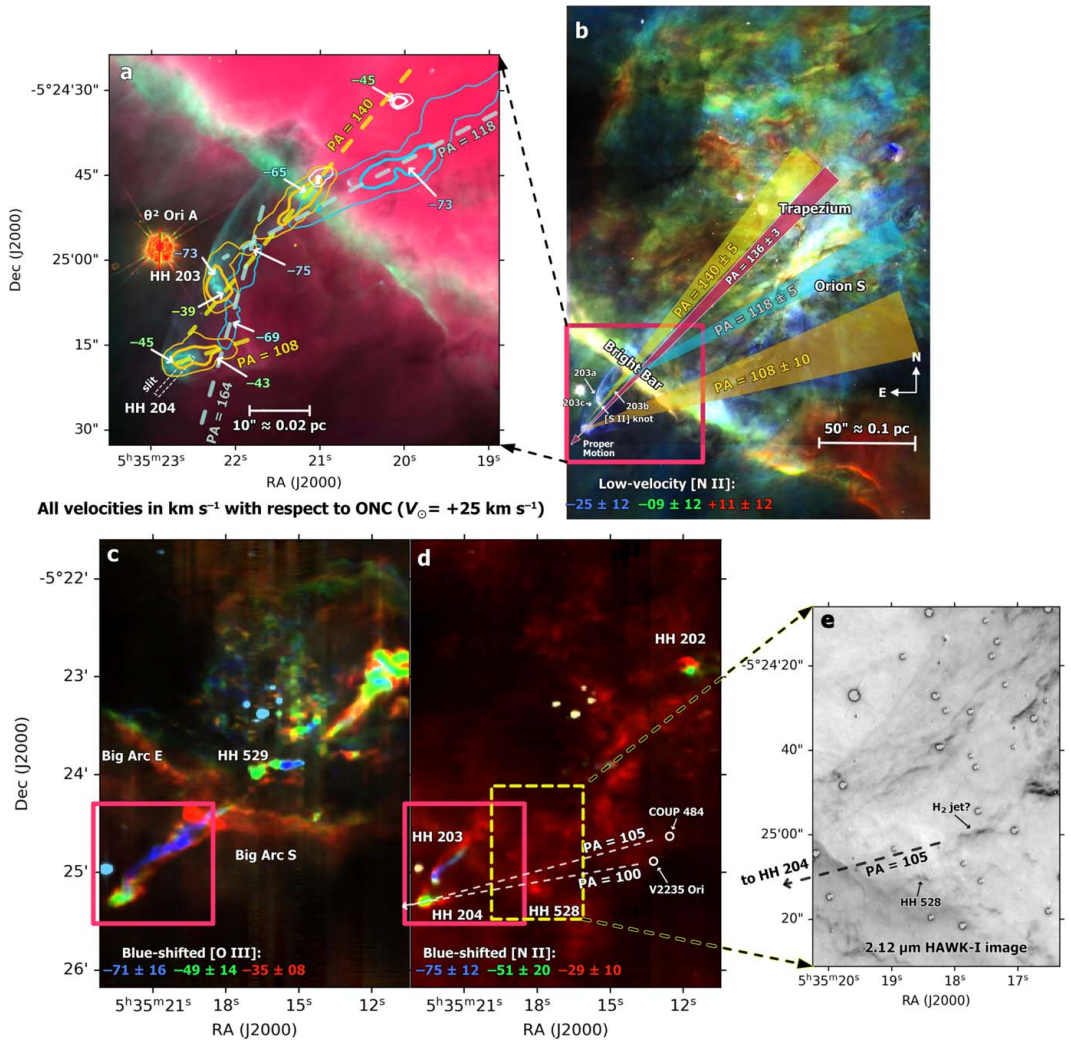

Figure 21. Location of HH 204 within the Orion Nebula. (a) Same as Figure 1 but showing an expanded view of the bow shocks and possible driving jets. Contours show highly blueshifted emission of [O III] (cyan, centered on −70 km s^{-1}) and [N II] (yellow, centered on −50 km s^{-1}, and white, centered on −35 km s^{-1}) derived from multiple long-slit spectra (Doi et al. 2004, as recalibrated in the spectral atlas of García-Díaz et al. 2008). Mean velocities with respect to the Orion Nebular Cluster of particular features related to the HH objects are indicate by arrows. (b) Location of HH 204 with respect to the inner Orion Nebula. The intensity of the image comes from the [N II] HST WFPC2 observations but colorized according to the velocity of the slow-moving nebular gas (within about 30 km s^{-1} of the systemic velocity) as derived from the long-slit spectra; see color key in figure. (c) Highly blueshifted [O III] emission for a field of view similar to that of panel (b). (d) Same as panel (c) but for highly blueshifted [N II] emission. Two candidate stellar sources along the back-projection of the PA 108 flow are indicated by white circles (see discussion in text). (e) Near-infrared HAWK-I imaging of the region outlined by a yellow dashed box in panel (d) in the 2.12 μm H_2 line (Kissler-Patig et al. 2008), showing an emission filament that may be associated with HH 204.

contours in Figure 21(a)) to a lower-ionization state (yellow contours) to the southeast of the Bright Bar. The other is at PA $\approx 140°$ and is of low ionization for its entire detected length. Both of these flows give the appearance of driving HH 203, which implies that HH 203 may be a superposition of two unrelated bow shocks. Such a superposition is consistent with the detection of two different velocity components (−73 and −39 km s^{-1}) at the head of the bow shock and also with the complex structure apparent in high-resolution HST images (see Figure 21(b)). O'Dell et al. (2015) noted that in addition to the main bow shock (HH 203a), there appears to be a second faint bow shock (HH 203b), associated with the PA 118 flow. We also detect a third faint bow shock, which we denote HH 203c, situated in front (southwest) of HH 204a. Note that O'Dell et al. (2015) gave PAs of 124° and 127°, respectively, for HH 203 and HH 204, which probably represent an average of the PA 118 and PA 140 flows.

The southern portion of HH 203a, which we label as "[S II] knot" in the figure, is particularly strong in the [S II] and [O I] filters and coincides with the peak of the $-39\,\mathrm{km\,s^{-1}}$ feature. The spatial alignment and the similarity in velocity and ionization make it likely that this knot is part of the PA 140 flow. It is conceivable that this flow may extend farther to the southwest and be driving the HH 204 bow shock, although there is no direct evidence for this. On the other hand, a third flow at PA $\approx 108°$ is seen to feed into HH 204 from the west. This jet, first noted by Doi et al. (2004), is very short and stubby and can be traced back only 10″ (20 mpc) from the bow shock. There is another faint filament of high-velocity [O III] emission that extends between the HH 203 and HH 204 regions at PA $\approx 108°$ (see Figure 21(a)). This appears to provide a connecting bridge between the PA 140 and PA 108 flows, although the difference in velocity and ionization with respect to the PA 108 flow argues against a physical association with HH 204.

We have searched archival observations in other wave bands for any evidence of jets along the back-projection of the PA 108 axis. The most convincing association is with a molecular hydrogen filament seen in the 2.12 μm line (see Figure 21(e)). At the position of this filament, HH 204 is at PA = 105°, which is well within the uncertainties, and the orientation of the filament is consistent with the same PA. Unfortunately, no kinematic observations are currently available for this filament, so its association with HH 204 can only be tentative. The stellar source that best aligns with the H_2 filament is COUP 484; see Figure 21(e). However, this is a rather low-luminosity star and therefore seems an unlikely candidate for driving such an impressive large-scale outflow. The star V2235 Ori is also marginally consistent within the uncertainty with the PA 108 axis and is roughly 100 times brighter than COUP 484 in the *K* and *L* infrared bands (Muench et al. 2002), but its position is completely inconsistent with being the source of the H_2 filament. There is also marginal evidence from MUSE observations (Weilbacher et al. 2015) for a blueshifted [Fe III] filament that extends from the position of the H_2 filament toward HH 204, but the data are noisy.

A further important line of evidence for the flow direction is provided by proper-motion measurements. We have remeasured the proper motions using HST images over an interval of 19 yr (1996–2015) using the methodology described in Section 1 of Paper I. For the "nose" of the HH 204 bow shock, we find a plane-of-sky velocity of $(71 \pm 9)\,\mathrm{km\,s^{-1}}$ at PA = (136 ± 3)°. After correcting to a common distance of 417 pc, the previous measurements of Doi et al. (2002) are $(83 \pm 10)\,\mathrm{km\,s^{-1}}$ at PA = (137 ± 7)°, which are consistent with our measurements within the uncertainties. The proper-motion axis is shown by a large red arrow in Figure 21(b) for comparison with the candidate axes from the high radial velocity jets. It is marginally consistent with the PA 140 axis but not with the PA 108, PA 118, or PA 164 axes.

In summary, convincing evidence for which large-scale flow might be driving the HH 204 bow shock is frustratingly absent. Although the PA 108 flow is clearly associated with HH 204, its short length means that the exact orientation is very uncertain. The PA 140 flow has a much better defined direction, but its extension beyond the position of the [S II] knot in order to feed into the HH 204 bow shock is purely speculative. However, the close agreement between this flow direction and the proper-motion axis is an additional argument in its favor. The only thing that can be said with any degree of certainty is that the high-ionization PA 118 flow is not driving HH 204, only HH 203.

In Figure 21(b), we show the back-projection of all three of these flows into the core of the nebula, assuming an uncertainty of ±10° for the PA 108 flow and ±5° for the other two. The PA 118 flow is consistent with an origin in the Orion-S star-forming region, as has been remarked many times previously (O'Dell et al. 1997b; Rosado et al. 2002; O'Dell & Doi 2003). However, neither of the other flows are consistent with an origin in that region, unless the flow has suffered a relatively large-angle deviation. The back-projection of PA 108 falls significantly to the south of the main Orion-S region in an area with no convincing candidates for the driving source (see above discussion of the possible H_2 jet). The back-projection of the PA 140 flow intersects the Trapezium stars in the very center of the nebula, which raises the possibility that the source may be a proplyd, which are highly concentrated in that region.

9. Discussion

The high spectral resolution of our data ($\lambda/\Delta\lambda \approx 6.5\,\mathrm{km\,s^{-1}}$) allows us to identify and properly separate three kinematical components of ionized gas: the DBL, the emission of the Orion Nebula, and HH 204. In the following, we will discuss in detail the results concerning each of these components.

9.1. The DBL

The component designated as the DBL was first reported by Deharveng (1973), although it has been little studied, since high spectral resolution is required to separate its emission from that of the Orion Nebula. García-Díaz & Henney (2007) analyzed the velocity structure of the Orion Nebula through the emission of [O I], [S II], and [S III] lines using echelle spectroscopy. They detected the emission of the [S II] doublet from the DBL, estimating a density of $\sim 400\,\mathrm{cm^{-3}}$, which is in complete agreement with our estimates. These authors did not detect the emission of [O I] or [S III] in this component, although the emission of other low-ionization ions such as [O II] and [N II] was detected in previous works (Jones 1992; Henney & O'Dell 1999). This limited spectroscopic evidence led to interpreting the DBL as composed of fully ionized gas whose ionizing radiation field was rather soft, probably coming from θ^2 Ori A. We have detected all of these lines, along with [O I] and [S III] ones, in the spectrum of this component extracted from cut 2 (see upper and middle panels of Figure 22). These emissions were also reported by O'Dell (2018) in a later reanalysis of the atlas of lines of García-Díaz & Henney (2007). In addition, we detect a weak [O III] emission, indicative of the presence of gas with a high degree of ionization, as shown in the lower panel of Figure 22.

Through observations of H I 21 cm emission, van der Werf et al. (2013) determined the existence of several H I velocity components in the Orion Nebula. In the southeast, in the area where the DBL is located, these authors identified a blueshifted component named "D," interpreted as an expanding shell centered on θ^2 Ori B, which is consistent with a scenario where this star ionizes the DBL. The observed [O I] emission is consistent with the presence of an ionization front in this nebular feature. However, with the new information provided by the ionic abundances of the DBL—estimated for the first time in this work—the simple model where the gas is photoionized

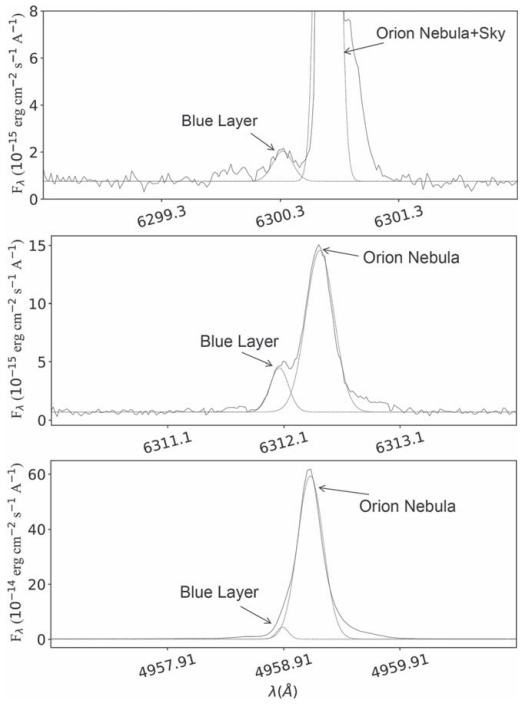

Figure 22. Spectrum of cut 2 showing the emission of [O I] λ6300 (upper panel), [S III] λ6312 (middle panel), and [O III] λ4959 (lower panel) of the DBL and Orion Nebula.

exclusively by θ^2 Ori B may not be correct. Although small, the contribution of O^{2+} to the total abundance is not negligible, being around 10%. On the other hand, assuming that the DBL should have a chemical composition similar to the Orion Nebula, this implies that the estimated N^+ abundance is approximately 75% of the total nitrogen abundance; therefore ,N^{2+} should be present in this component. Since θ^2 Ori B is a B0.7V star (Simón-Díaz 2010), we do not expect such a star to emit a number of photons capable of maintaining a significant proportion of highly ionized ions. This is reinforced by the spectroscopic results of Galactic H II regions ionized by B-type stars such as Sh 2-32, Sh 2-47, Sh 2-82, Sh 2-175, Sh 2-219, Sh 2-270, Sh 2-285, Sh 2-297, and IC 5146 (García-Rojas et al. 2014; Esteban & García-Rojas 2018; Arellano-Córdova et al. 2021). In all of these regions, nitrogen is only once ionized, and the contribution of O^{2+} to the total oxygen is lower than 2%, with the exception of the faint Sh 2-47, although the O^{2+} abundance determination in this object is very uncertain.

As we can see in the discussion above, the spectroscopic properties of the DBL suggest some ionization by radiation leakage from the Orion Nebula. Simón-Díaz et al. (2011) found abnormal emission of CELs of highly ionized species (mainly [O III]) in the external zones of M43, an H II region ionized by a B0.5V star located to the northeast of the Orion Nebula. As those authors demonstrated, the spectral properties of this abnormal emission are consistent with contamination by scattered light from the Huygens Region. In our case, we can discard the scattered nature of the emission of highly ionized ions in the DBL because (i) it has the same velocity as the lines of low-ionization ions, and (ii) we do not detect anomalies in the Balmer decrement of the spectrum of the DBL, which would be a signature of the presence of scattered emission (see Simón-Díaz et al. 2011). Further observations with a longer exposure time, similar spectral resolution, and covering different areas of the Orion Nebula would shed more light on the extension and physical, chemical, and geometrical properties of the DBL.

9.2. The Nebular Component

There are notable differences in the degree of ionization and physical conditions of the gas of the nebular component studied in this work and Paper I. The degree of ionization in the area of the Orion Nebula observed in this paper is $O^{2+}/O = 0.42 \pm 0.04$, while it is $O^{2+}/O \sim 0.8$ in the area observed in Paper I. This is an expected behavior considering the different distances of both areas with respect to the main ionizing star. The density in the nebular component in the direction of HH 204 is $n_e = 1440 \pm 170\,cm^{-3}$, significantly lower than the values of $n_e \sim 6000\,cm^{-3}$ obtained around HH 529 II and III in Paper I. This result is again consistent with the more external position of HH 204 with respect to θ^1 Ori C and the center of a blister-shaped nebula. There is a remarkable consistency between the T_e([O III]) and T_e([N II]) values we obtain in this paper and the predictions of the radial distribution of those quantities given in Equations (4) and (5) of Mesa-Delgado et al. (2008), confirming that the temperature decreases rather linearly with the radial distance from θ^1 Ori C in the Orion Nebula.

As expected, the total abundances of O, N, S, and Cl shown in Table 7 are in good agreement with those included in Table of Paper I. However, the abundances of Ne and Ar are somewhat different because of the use of different ICFs to estimate the contribution of unseen Ar^+ and Ne^+, which is larger due to the lower degree of ionization of the nebular component in the direction to HH 204. A similar situation occurs with the C abundance, which requires large corrections to estimate the important contribution of C^+. Although the total abundance of $O = 8.42 \pm 0.04$ we obtain using CELs is consistent with the value of $O = 8.46 \pm 0.03$ derived in Paper I, both are somewhat lower than the value of $O = 8.51 \pm 0.03$ obtained by Esteban et al. (2004) and Mesa-Delgado et al. (2009) in two different areas of the Orion Nebula. It is important to note that this difference seems to be correlated with the AD factor (ADF) of O^{2+} estimated in each observed area. However, there are other explanations for the different O abundances obtained in different zones of the nebula. One can be related to a different depletion factor of O onto dust grains. This element may be trapped in the form of oxides, pyroxenes, or olivines, compounds that would include atoms of metals such as Fe. However, the total abundance of Fe does not differ substantially between the aforementioned four zones of the the Orion Nebula, and, unfortunately, the relatively large uncertainties associated with the Fe/H ratio do not permit one to trace differences in depletion factors.

9.3. HH 204

9.3.1. Two-zone Model for Observed Temperature Structure

Our spectroscopic observations allow us to analyze the physical conditions and ionic abundances of HH 204 with unprecedented detail. As shown in Section 5.1, the gas density is

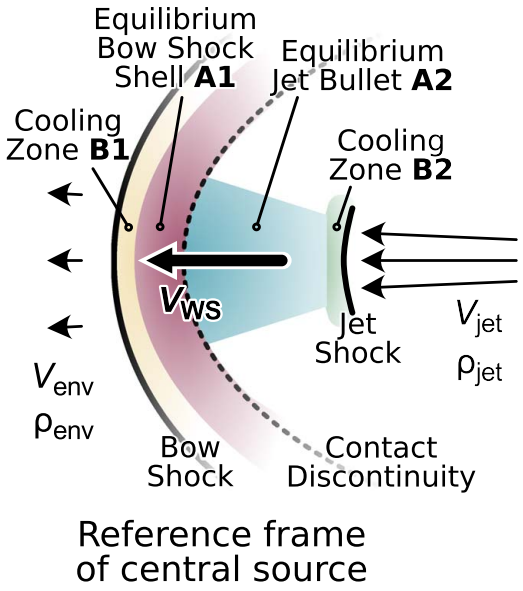

Figure 23. Simple model for the principal working surface of the HH 204 jet. The shocked gas can be divided conceptually into four zones: A1, A2, B1, and B2 (see text for details).

higher near the bow shock. On the other hand, only T_e([O III]) seems affected by the shock, while T_e([N II]) and T_e([S III]) maintain their photoionization equilibrium values. This result may be explained by the weakness of high-ionization emission from the densest postshock gas in the bow shock and jet, allowing a greater relative contribution of the immediate postshock cooling zone to the [O III] lines.

At each position along the spectrograph slit, the line of sight will cross several zones with different physical conditions, as illustrated in Figure 23:

A1: the compressed shell behind the bow shock, which is in photoionization equilibrium;
A2: the main body of the jet bullet, also in photoionization equilibrium;
B1: the immediate postshock cooling zone of the bow shock; and
B2: the postshock cooling zone of the jet shock.

In HH 204, the relative velocity between the unshocked jet and the working surface is very low ($\approx$15 km s^{-1}), so the jet shock is much weaker than the bow shock, implying that the emission from zone B2 can be neglected compared with B1. Zones A1 and A2 should have similar conditions and so can be merged into a single zone with density n_A and temperature T_A. Although zone B1 should have a range of temperatures, for simplicity, we assume a single characteristic temperature T_B. The density of zone B is found by assuming a pressure equilibrium with zone A: $n_B = n_A T_A / T_B$. We define f_B for a given ion as the fraction of the total ionic emission measure, $\int n_e\, n_{ion}\, dz$, that comes from zone B, with the remainder, $f_A = 1 - f_B$, coming from zone A.

The appropriate value of T_B is rather uncertain, since it depends on the nonequilibrium evolution of ionization and temperature in the postshock radiative relaxation layer. Most published shock models (Cox & Raymond 1985; Sutherland & Dopita 2017) are calculated on the assumption that the far upstream and downstream ionization states are determined by the radiation from the shock itself. Care must therefore be exercised when translating their results to cases such as HH 204, where external irradiation from O stars is a dominant factor. The curved bow shock in HH 204 should give a range of shock velocities up to a maximum of $V \approx 84$ km s^{-1} (assuming the preshock medium is stationary). In principle, this corresponds to postshock temperatures as high as 2×10^5 K, but the gas at such temperatures will be too highly ionized to significantly emit optical lines. The cooling timescale is generally shorter than the recombination timescale, so the gas is overionized as it cools. It is only when the temperature falls below about 50,000 K that the abundance of O^{++} becomes significant (e.g., Figure 11 of Allen et al. 2008), allowing the emission of the optical [O III] lines. A similar situation is seen in middle-aged supernova remnants, such as the Cygnus Loop (Raymond et al. 2020).

We look for solutions where both T_A and T_B are constant along the slit, so that any spatial variation in the temperature diagnostics is driven primarily by variation in f_B. Although the density diagnostics do show a gradient with position, both T([O III]) and T([S III]) are relatively insensitive to density, so for simplicity, we assume n_A is constant. We use the Python library PyNeb to calculate the per-zone emission coefficients, $j(T_A, n_A)$ and $j(T_B, n_B)$, for each emission line. For a given diagnostic line pair, 1 and 2, the ratio is calculated as

$$R_{12} = \frac{(1 - f_B)\, j_1(T_A, n_A) + f_B j_1(T_B, n_B)}{(1 - f_B)\, j_2(T_A, n_A) + f_B j_2(T_B, n_B)}. \quad (3)$$

This is then fed into PyNeb's `getTemDen` function to find the equivalent single-zone temperature that would give the same ratio (assuming a density of n_A). It is clear from Equation (3) that for $f_B = 0$, one must recover $T_e = T_A$, and that for $f_B = 1$, one must recover $T_e = T_B$. But for intermediate values of f_B, the derived temperature will differ between ions because of variations in the temperature sensitivity of the diagnostic ratios.

We first investigate the case of a common f_B for all ions, but we find that this is unable to reproduce the observations. This is demonstrated in Figure 24(a), which shows the relation between T_e([O III]) and T_e([S III]) for four different values of T_B between 15,000 and 50,000 K. We set $T_A = 9000$ K and $n_A = 20{,}000$ cm^{-3} in all cases, and f_B increases from left to right along each curve. The gray rectangle shows the observed range of temperatures along the spectrograph slit (Figure 5); T_e([O III]) shows a systematic decline from $\approx$17,000 K near the bow shock to $\approx$12,000 K further away, while T_e([S III]) is roughly constant at 9000–10,000 K, with no apparent correlation with T_e([O III]). The two-zone models with $T_B \geqslant 30{,}000$ K all show T_e([O III]) > T_e([S III]) as f_B increases, but this is insufficient to explain the observations. For example, in order to achieve T_e([O III]) = 17,000 K, the models predict T_e([S III]) > 11,000 K, which is significantly higher than observed.

In Figure 24(b), we relax the assumption of a common f_B for all ions, separately showing the predicted values of T_e([N II]), T_e([S III]), and T_e([O III]) as a function of f_B, assuming T_B = 30,000 K. The ranges of observed values are shown by colored bands, blue for [O III] and orange for [N II] and [S III]. From the figure, it is apparent that a decline from f_B([O III]) ≈ 0.1 at $x = 0$ to f_B([O III]) ≈ 0.02 for $x > 5$ mpc is required to explain the

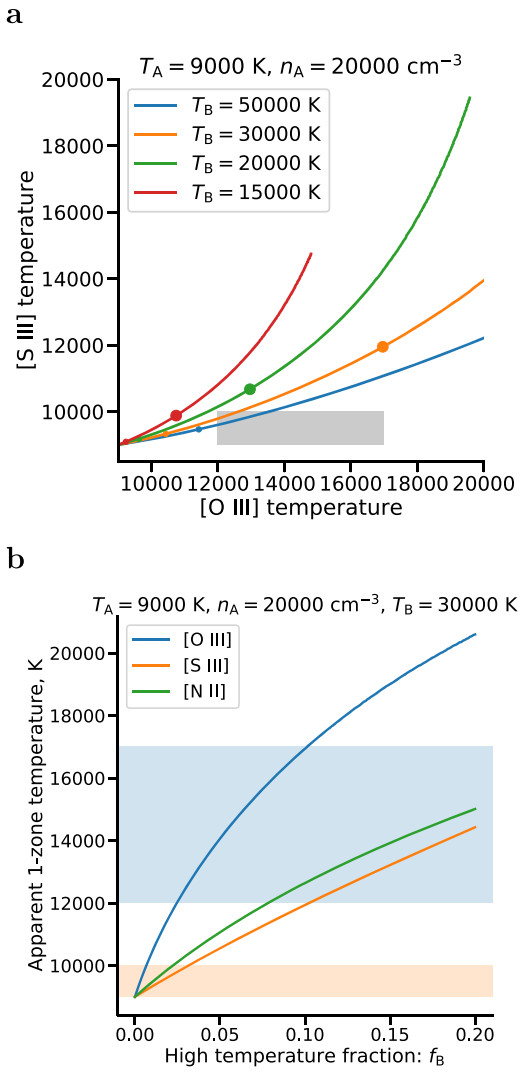

Figure 24. Simple two-zone model for spatial variations in temperature diagnostics. (a) Correlation between derived T_e from the [O III] and [S III] lines, assuming that the fraction f_B of the ionic emission measure that arises in the hot component (with temperature T_B) is the same for both ions. Values of $f_B = 0.01$ (small dots) and 0.1 (large dots) are indicated on each curve. The gray rectangle shows the observed range of values, which cannot be explained under this assumption (see text). (b) Derived T_e for [O III], [S III], and [N II] lines as a function of f_B, assuming $T_B = 30{,}000$ K. Colored bands show the observed ranges, which imply that f_B([O III]) must be larger than for the other ions (see text).

T_e([O III]) profile, whereas f_B([S III]) < 0.01 and f_B([N II]) < 0.01 are required at all positions.

It is not surprising that f_B should vary between ions, since the photoionization equilibrium ion fraction of O^{2+} from zone A is much lower than that of N^+ or S^{2+}. Assuming $f_B \ll 1$, the ionic abundances given in the "Cut 1, HH 204" column of Table 4 correspond to zone A. These yield $O^{2+}/O = 0.005$ and $S^{2+}/S = 0.61$ if the abundances of unobserved ion stages are negligible. The lack of [N III] lines means that N^+/N cannot be estimated directly but is likely of order unity. The fact that O^{2+} is only present in trace amounts in the photoionization equilibrium gas means that the relative contribution from the postshock cooling zone is much larger than for S^{2+} and N^+. This is confirmed by emission line imaging of HH 204 (Weilbacher et al. 2015), which shows a morphology in [S III] and [N II] that is clearly dominated by the compact jet bullet, whereas the emission in [O III] is more diffuse within the parabolic envelope of the bow shock.

Although part of this high ionization degree gas may be out of photoionization equilibrium, fortunately, its impact is negligible in the global abundance analysis of HH 204. The fact that T_e([N II]) and T_e([S III]) are kept in balance in HH 204 proves that the low and medium ionization degree gas, which comprises more than ∼99% of the total, is in photoionization equilibrium.

9.3.2. A Trapped Ionization Front

The detection of emission lines of neutral elements such as [O I] and [N I] and the high density and low degree of ionization of HH 204 suggest that it contains an ionization front. In previous studies, the detection of these lines has been interpreted as a product of the interaction of HH 204 with neutral material, such as that found in Orion's Veil (O'Dell et al. 1997a, 1997b; Takami et al. 2002). However, there are several arguments against this scenario and in favor of the existence of a trapped ionization front. (i) The spatial distribution of the [O I] emission, shown in Figure 2, is more concentrated than that of [O II] or [O III], located at the southeast of HH 204, in the opposite direction to θ^1 Ori C, consistent with a zone shielded from the ionizing radiation. (ii) As we discussed in Section 5.3, deuterium lines are produced by fluorescence excitation areas beyond an ionization front. Finally, (iii) the combination of the tangential and radial motions of HH 204 allows one to know the 3D trajectory of its associated jet. From its apparent distance to Orion-S (its likely origin), Doi et al. (2004) estimated that HH 204 has moved ∼0.15 pc radially toward the observer. Although van der Werf et al. (2013) argued that the Orion Veil lies ∼0.3 pc apart from Orion-S, Abel et al. (2016) established that the distance must be significantly larger, and therefore a direct interaction between HH 204 and the Veil is unlikely. If those distance estimations are correct, HH 204 would be located within the main ionized gas volume of the Orion Nebula or interacting with the nearer ionized layer (see Abel et al. 2019; O'Dell et al. 2020).

9.3.3. The ADF and the "True" O Abundance

The origin of the AD problem has been related to temperature, density, or chemical inhomogeneities in the nebulae or fluorescence effects on the intensity of RLs (see Peimbert 1967; Torres-Peimbert et al. 1980; Pequignot et al. 1991; Liu et al. 2001; García-Rojas & Esteban 2007; Escalante et al. 2012, and references therein). As mentioned in Section 5.2, the O^+ abundances calculated with RLs and CELs are equal in HH 204. Since practically all oxygen is singly ionized in this object, this implies that HH 204, contrary to what is usually found in ionized nebulae, does not show an ADF in total O abundance. Therefore, the "true" O abundance should be ∼8.6 in this object, slightly lower than the recommended solar O abundance (8.73 ± 0.07;

Table 8
Oxygen Abundances in the Orion Nebula Based on UVES Spectroscopy

Region	RLs			CELs			Reference
	O^+	O^{2+}	O	O^+	O^{2+}	O	
Orion Nebula	8.15 ± 0.13	8.57 ± 0.01	8.71 ± 0.03	7.76 ± 0.15	8.43 ± 0.01	8.51 ± 0.03	Esteban et al. (2004)
	8.01 ± 0.12	8.46 ± 0.03	8.59 ± 0.05	8.00 ± 0.06	8.35 ± 0.03	8.51 ± 0.03	Mesa-Delgado et al. (2009)
	8.25 ± 0.06	8.52 ± 0.02	8.70 ± 0.03	7.83 ± 0.05	8.35 ± 0.03	8.46 ± 0.03	Méndez-Delgado et al. (2021)
	...	8.40 ± 0.03	8.60 ± 0.03[a]	8.18 ± 0.06	8.04 ± 0.02	8.42 ± 0.04	This work
HH 202 S	8.25 ± 0.16	8.44 ± 0.03	8.65 ± 0.05	8.29 ± 0.06	8.08 ± 0.03	8.50 ± 0.04	Mesa-Delgado et al. (2009)
HH 529 II	<7.91	8.83 ± 0.07	8.83 ± 0.07	7.36 ± 0.12	8.54 ± 0.03	8.57 ± 0.03	Méndez-Delgado et al. (2021)
HH 529 III	<7.95	8.84 ± 0.09	8.84 ± 0.09	7.51 ± 0.22	8.48 ± 0.03	8.53 ± 0.03	Méndez-Delgado et al. (2021)
HH 204	8.57 ± 0.03	<7.54	**8.57 ± 0.03**	8.62 ± 0.05	6.34 ± 0.02	**8.62 ± 0.05**	This work

Notes. Abundances in units of $12+\log(X^{n+}/H^+)$ or $12+\log(X/H)$. The bold values are those adopted for the determination of chemical abundances.
[a] Using the O^+ abundance based on CELs.

Lodders 2019). In this regard, there are three properties of HH 204 that we want to highlight. (i) In Section 5.1, we show that the spatial distribution of T_e([N II]) is constant; i.e., there are no significant temperature fluctuations in the plane of the sky that may be translated into fluctuations in the line of sight for ions of a low degree of ionization (see Section 9.3.1). The presence of temperature fluctuations would produce the underestimation of the O^+ abundance based on CELs. (ii) In Section 4.3, we show that the effects of starlight fluorescence are negligible in the determination of the abundances of Ni^+ and Fe^+ due to the large distance between HH 204 and the ionizing source in addition to the high density of the HH object. Thus, if there is any mechanism in which the continuum pumping can affect the population of the levels of multiplet 1 of O I, this may be diminished in a similar way. (iii) The jet geometry of HH 204, with a relatively small angle of $32° \pm 6°$ with respect to the plane of the sky (see Section 8), implies that any gradient in the electron density of the gas along the jet axis should be separated in the plane of the sky. This is a more favorable geometry for analysis than the case of a jet flowing directly toward the observer, where different zones will overlap the same line of sight. Therefore, chemical or density inhomogeneities in the line of sight appear not to be present in HH 204. Unfortunately, we cannot perform a similar analysis for the ADF(O^{2+}) because O II RLs are not detected in HH 204.

In Table 8, we compile the O abundances obtained in all chemical abundance studies of the Orion Nebula based on deep echelle spectroscopy taken with UVES. We include determinations based on both RLs and CELs, assuming $t^2 = 0$ in the last case. A first note of caution should be given concerning the fraction of O depleted onto dust grains, which may be different in different parts of the nebula. Mesa-Delgado et al. (2009) estimated this fraction to be typically ~0.12 dex, but it may be lower in HH objects due to destruction of dust grains in shock fronts. This implies a maximum extra uncertainty of ~0.1 dex in any given O abundance measurement due to depletion variations.

If we assume that the O abundances based on RLs are the "true" ones for all objects, then HH 529 II and III show higher O/H ratios than the rest. In Paper I, we discussed the possibility of having a slight overmetallicity in HH 529 II and III due to the entrainment of material from the accretion disk of the stellar source of the jets. On the other hand, the O abundances based on RLs found in the nebular components studied in Paper I and Esteban et al. (2004) are also marginally higher than what is found in HH 204. These discrepancies may have explanations of a different nature in each case, apart from dust depletion variations.

The low measured CEL abundance values found in the more highly ionized regions of the nebula could be reconciled with the HH 204 value by considering different small proportions of O depletion onto dust grains in addition to small contributions from other phenomena, such as temperature fluctuations. In this context, if we assume that half of the difference between ~8.6 —considering that the O abundance obtained in HH 204 is the true one of the Orion Nebula—and the O abundance based on CELs obtained by Esteban et al. (2004) is due to dust depletion and the rest to temperature fluctuations, this would be compatible with $t^2 \sim 0.008$, a value considerable smaller than the $t^2 \sim 0.022$ necessary to match the O abundances from RLs obtained in the same spectrum. In this case, the relevant question is why the RLs are giving higher O abundances in all cases except HH 204. An important difference between the determination of the O abundance in HH 204 and the other zones or objects included in Table 8 is that, in HH 204, the contribution of O^{2+} to the total abundance is negligible. It is important to say that Mesa-Delgado et al. (2009) also obtained an ADF(O^+) equal to zero in both HH 202 S and the nebular component. However, the contribution of O^{2+} is much larger in those spectra, and their ADF(O^{2+}) are not zero. This result suggests that the AD problem is affecting specially to the O^{2+} abundances and perhaps related to unaccounted effects on the intensity of O II RLs. It is still premature to draw any conclusions in this regard, but we will explore this important issue further in future papers of this series.

From Table 7, it is clear that the Fe abundance in HH 204 is higher than in the other components due to dust destruction at the bow shock. Following the same procedure as in Paper I, comparing the observed Fe/O values in HH 204 and the nebular component with the expected solar value (Lodders 2019), we estimate that ~6% of the total Fe is in the gaseous phase in the nebular component, while this fraction goes up to 21% in HH 204, representing an increase of a factor 3.5. A similar factor can be assumed for Ni.

9.4. On the Presence of High-density Inclusions

Last but not least, we want to discuss the influence of the presence of an unrecognized high-density component in the spectrum of a photoionized region. We have studied this scenario in Section 7, adding the nebular emission from the Orion Nebula, the DBL, and HH 204, which would be obtained

when observing with a velocity resolution lower than ∼54 km s^{-1} or $R \approx 5550$. In this case, the classical density diagnostics based on ratios of [O II], [S II], and [Cl III] do not adequately detect the high density of HH 204. The biased low-density values determined with these diagnostics lead to an overestimate of T_e([N II]) and a subsequent underestimate of the abundances of some elements. In the case of O^+, the underestimate would be ∼0.2 dex (see Section 7), producing a similar impact on the total O abundance, as O^+ is the dominant ion. In addition, there is an indirect effect on other elements in which the total abundance is derived from lines of highly ionized ions through the ICFs. This is because they depend on the degree of ionization, parameterized by $O^{2+}/(O^+ + O^{2+})$. The impact of high-density inclusions on the abundances will depend on their contribution to the integrated volume, ionization degree, and density.

Previous studies of the area of HH 204—all based on lower spectral resolution spectroscopy—reported localized peaks of T_e([N II]) (Mesa-Delgado et al. 2008; Núñez-Díaz et al. 2012; O'Dell et al. 2017a), which were interpreted as the product of shock heating. The results presented in Section 5 demonstrate that this interpretation is not correct and can be noted in Figure 2 of O'Dell et al. (2017a). That figure shows that n_e([S II]) increases when approaching the bow shock from the direction of the jet, reaching a zone where its value stabilizes around ∼5000 cm^{-3} and decreases again when moving outward. However, when using n_e([Fe III])—as shown in Figure 5—instead of stabilizing when approaching the bow shock, the density steadily increases up to ∼20,000 cm^{-3} at the bow shock of HH 204. Considering that the T_e([N II]) diagnostic tends to be density-sensitive for values larger than ∼1000 cm^{-3}, an underestimate of n_e implies an overestimate of T_e; consequently, we will obtain significantly lower ionic abundances based on CELs, whose intensity is strongly dependent on temperature.

In Table 3, we can see that, for HH 204, even the classical density diagnostics give values consistent with those obtained from the ratio of [Fe III] lines. This is because HH 204, due to its orientation and the spectral resolution of the observations, can be interpreted basically as a single slab of high-density gas. This would be different in the case of an HH object moving directly toward us and observed with low-resolution spectroscopy. We would most likely have a density gradient in the line of sight, because it would cross the compressed gas at the bow shock and the less dense material traveling behind along the jet axis. In situations like this, a way to detect the presence of high-density inclusions—as HH objects—can be the use of the I([Fe III] λ4658)/I([Fe III] λ4702) ratio as a density diagnostic. This diagnostic will be biased to the higher-density component, while classical ones will be biased in the opposite direction. A significant discrepancy between the [Fe III] diagnostic and classical ones in a region of apparently low n_e may serve as an indicator of this type of situation. However, factors such as the degree of ionization of the gas and the relative volume occupied by each mixed component can mask density inhomogeneities. It is advisable to analyze each available density diagnostic even if they are discrepant with the others, as such discrepancies can indicate the presence of real inhomogeneities.

10. Conclusions

We have studied the physical conditions and chemical composition of the photoionized HH object HH 204 through deep high spectral resolution UVES spectroscopy and HST imaging. Our spectral resolution allows us to cleanly separate HH 204 from the various kinematic components of the Orion Nebula along the same line of sight.

We have analyzed the distribution of the physical conditions of HH 204 along the slit with subarcsecond spatial resolution. We find a steady increase of n_e from ∼10,000 cm^{-3} at ∼13 mpc behind the bow shock to ∼20,000 cm^{-3} close to it. The temperature determined from the most abundant ion stages, such as T_e([N II]) and T_e([S III]), is approximately constant at 9000 ± 500 K along the slit. In contrast, T_e([O III]) is generally higher and shows a pronounced gradient from ≈17,000 K close to the bow shock to ≈12,000 K at distances >5 mpc. We interpret this in terms of a two-zone model (Section 9.3.1). Zone A represents gas that is at the photoionization equilibrium temperature and contributes the overwhelming majority of the low- and intermediate-ionization emission. Zone B is a higher-temperature cooling layer behind the bow shock, and this contributes a significant fraction of the [O III] emission but contributes negligibly to the other ions.

We estimate that ∼99% of the gas in the observed area of HH 204 is composed of low- and intermediate-ionization stages (ionization potential <25 eV). Based on the intensity of CELs, we determine the ionic abundances of O^+, O^{2+}, N^+, Ne^{2+}, S^+, S^{2+}, Cl^+, Cl^{2+}, Ar^{2+}, Fe^+, Fe^{2+}, Ni^+, Ni^{2+}, Ca^+, and Cr^+. We also calculate the ionic abundances of He^+, O^+, and C^{2+} from the relative intensity of RLs. In HH 204, we find no difference when determining the O^+ abundance using CELs or RLs. Since practically all O is O^+ in this object, we can say that the AD is virtually zero for HH 204, contrary to what is found in essentially all ionized nebulae. Both CELs and RLs provide an O abundance of 12 + log(O/H) = 8.60 ± 0.05, slightly lower than the solar value of 12 + log(O/H) = 8.73 ± 0.07 recommended by Lodders (2019) but consistent with many other independent determinations for the Orion Nebula.

Due to the low degree of ionization of HH 204, we can derive the O, N, S, Cl, Fe, and Ni abundances without ICFs. In principle, those O, N, S, and Cl abundances should be representative of the Orion Nebula ones as well. The Fe and Ni abundances of HH 204 are a factor of 3.5 higher than in the Orion Nebula due to the destruction of dust grains at the bow shock. We also found direct evidence of the presence of an ionization front trapped in HH 204, such as the detection of deuterium lines produced by nonionizing far-UV photons.

From archival HST imaging with a higher spatial resolution than our spectra, we find a narrow border of high [O III]/Hα that traces the leading edge of the bow shock in HH 204 (Figure 18 and Section 5.4). We identify this with the postshock cooling layer, with a width of ≈0.1 mpc. This is the same as the high-temperature zone B, which we invoked in order to explain the spatial profile of T_e([O III]) in the UVES spectra. Note, however, that this layer is much narrower than can be spatially resolved in our spectroscopic observations, which means that the effects on temperature diagnostics are diluted. We predict that much higher values of T_e([O III]) ≈ 30,000 K would be found if the λ4363/λ5007 ratio were to be observed at a spatial resolution of 0.″05.

We investigate the origin of the driving jets of both HH 204 and the nearby HH 203 using both proper motions and channel maps of highly blueshifted emission (Section 8). We find that HH 203 is the superposition of two flows: a high-ionization and high-velocity flow at PA 118, which originates in the Orion-S region, plus a low-ionization and lower-velocity flow at PA

140, which originates near the Trapezium. The proper motion of the HH 204 bow shock is closely aligned with the PA 140 flow, suggesting that HH 204 may also be driven by this same jet, but there is little evidence of such a connection from the blueshifted channel maps. Instead, there is evidence for a third flow at PA 108 that appears to be feeding into HH 204 and may be connected to a molecular hydrogen filament originating in the region to the south of Orion-S.

Our observations allow us to separate and analyze the spectrum of the DBL, an ionized gas component with a radial velocity different from that of the Orion Nebula and HH 204. We have estimated its physical conditions, its T_e, for the first time, revealing that it has a density lower than the Orion Nebula. We have calculated its chemical composition for the first time.

Our analysis of the spectrum of the kinematic component corresponding to the Orion Nebula reveals a lower ionization degree and n_e with respect to the results of Paper I. This comparison also indicates that T_e in the Orion Nebula decreases with the radial distance from θ^1 Ori C. The chemical composition of the nebular component is similar to that found in Paper I, although there seems to be a slightly lower O abundance (less than 0.04 dex), perhaps related to different depletion factors onto dust grains of this element.

We carry out the exercise of simulating a spectrum with a lower spectral and spatial resolution, where the spectra of the different kinematic components are mixed. We find that the analysis of this integrated spectrum can lead to erroneous physical conditions and chemical abundances. For example, the estimation of n_e by averaging n_e([O II]), n_e([S II]), and n_e([Cl III]) underestimates the true density, resulting in an overestimation of the temperature of the low-ionization ions, which constitute an important fraction of the gas in HH 204, the dominant component of the integrated spectrum. This fact leads to an underestimate of the abundances and to obtaining a mistaken average degree of ionization, the parameter on which most ICF schemes are based. Therefore, the determination of the chemical abundances would be wrong in practically all elements. Indicators of density such as I([Fe III] λ4658)/I([Fe III] λ4702) may be used to detect the presence of high-density clumps associated with HH objects or shocks. A similar point is made by O'Dell et al. (2021) with respect to unrecognized heterogeneity in physical conditions leading to misleading results, and we echo the warning of that paper.

This work is based on observations collected at the European Southern Observatory, Chile, proposal No. ESO 092.C-0323 (A). We are grateful to the anonymous referee for helpful comments. We acknowledge support from the Agencia Estatal de Investigación del Ministerio de Ciencia e Innovación (AEI-MCINN) under grant *Espectroscopía de campo integral de regiones H II locales. Modelos para el estudio de regiones H II extragalácticas* with reference 10.13039/501100011033. W.J.H. is grateful for financial support provided by Dirección General de Asuntos del Personal Académico, Universidad Nacional Autónoma de México, through grant Programa de Apoyo a Proyectos de Investigación e Inovación Tecnológica IN107019. J.G.-R. acknowledges support from Advanced Fellowships under the Severo Ochoa excellence programs SEV-2015-0548 and CEX2019-000920-S. J.E.M.-D. is grateful for the support of the Instituto de Astrofísica de Canarias under the Astrophysicist Resident Program and acknowledges support from the Mexican CONACyT (grant CVU 602402). The authors acknowledge support under grant P/308614 financed by funds transferred from the Spanish Ministry of Science, Innovation and Universities, charged to the General State Budgets, and with funds transferred from the General Budgets of the Autonomous Community of the Canary Islands by the MCIU.

Appendix A
How Reliable Are the Atomic Data of [Fe III] that We Use?

Generally, the discrepancy between the physical conditions derived from diagnostics based on [Fe III] lines and those estimated from other ions has been interpreted as a result of errors in the transition probabilities and/or the collision strengths of the Fe^{2+} ion (see the introduction of Laha et al. 2017). With HH 204, we have an excellent opportunity to test the reliability of the atomic data we use for this ion for the following reasons. (i) We have enough spectral resolution to separate the emission of HH 204 from that of the Orion Nebula. (ii) Owing to its geometry and 3D trajectory, we do not expect significant inhomogeneities in the physical conditions within the line of sight for ions of low and intermediate ionization stages. Due to this, all of the density diagnostics used in Table 3 are consistent with each other, while the global gas temperature, due to the low degree of ionization, is well represented by T_e([N II]). (iii) The [Fe III] emission is enhanced owing to the destruction of dust grains containing Fe atoms in the shock, which allows one to have a good signal-to-noise ratio even for some weak lines that are difficult to detect.

We have used a set of transition probabilities compiled in PyNeb, which includes the data from Quinet (1996) and Johansson et al. (2000) for $^5D - {}^5S_2$ transitions. However, these transitions produce lines out of the spectral range covered by our observation, so we finally only use the calculations from Quinet (1996). Table 12 shows that the transition probabilities we use are in good agreement with the observed intensity ratios of lines arising from the same upper level in the case of lines used to determine physical conditions. However, the intensity ratios between lines that arise from different upper levels do depend on n_e and T_e. As discussed above and in Section 9.4, in HH 204, there are no significant density inhomogeneities that may produce a bias in some diagnostics, contrary to the case analyzed in Section 7. Thus, all of the density diagnostics included in Table 3 give consistent results, and the average of n_e([O II]), n_e([S II]), n_e([Cl III]), and n_e([Fe II]) is $n_e = 13{,}330 \pm 550$. Using this density for its calculation, T_e([N II]) remains practically unchanged from what is shown in Table 3. Considering these values of n_e and T_e([N II]), we can check the validity of [Fe III] atomic data by applying the procedure that we describe below. First, we take into account all of the observed [Fe III] lines that are not affected by blending with other lines, sky features, or telluric absorptions. Then we normalize their emission with respect to I([Fe III] λ4658)/I(Hβ) = 1000. We discard the [Fe III] $\lambda\lambda$3355.50, 7078.22 lines, since their FWHMs are much wider than the rest of the [Fe III] lines, which is indicative of line blending. The [Fe III] λ9203.85 line is also discarded because it shows a radial velocity of $\sim$10 km s^{-1}, larger than the velocities of the rest of the [Fe III] lines, which may be indicative of a doubtful identification. We also discard [Fe III] λ8838.14 because, although we deblend it from a very close sky feature, its intensity may not be completely reliable. Once we have the set

of [Fe III] lines with confident observed intensity ratios, they are compared with the predictions of the atomic data for the assumed physical conditions and considering error propagation. The results are shown in Table 14.

Table 14 does not include $^5D - {}^7S$ transitions ([Fe III] $\lambda\lambda$3322.47, 3371.35, 3406.18 lines) because their transition probabilities are not calculated in the reference of the atomic data used (their "Predicted" and "Difference" columns are empty). However, their measured intensities can be used to check other atomic data sets that do include them. In general, Table 14 shows good agreement between the predicted and observed intensity ratios of [Fe III] lines. Only four lines ($\lambda\lambda$4008.34, 4079.69, 4985.88, and 7088.46) show differences larger than 10%, exceeding the error bars. This can be attributed to errors in their atomic data. The first two lines arise from the same $^3G_4$ upper level, so their intensity ratio only depends on their transition probabilities. Although the I([Fe III] λ4008.34)/I([Fe III] λ4079.69) ratio is not included in Table 12—these lines were not used to determine physical conditions—its intensity ratio of 4.43 ± 0.30 is larger than the theoretical one of 3.92. Therefore, it is plausible that part of the observed discrepancy is due to incorrect transition probabilities. The largest differences reported in Table 14 are for the [Fe III] $\lambda\lambda$4985.88, 7088.46 lines, but we cannot find an obvious explanation for this. In addition to the atomic data used, we have checked other sets: for transition probabilities, Nahar & Pradhan (1996) and Bautista et al. (2010), and for collision strengths, Bautista et al. (2010) and Badnell & Ballance (2014). We have tried all possible combinations of these data. Of the nine combinations, the atomic data we use in this paper minimize the difference between the predicted and measured intensity ratios. The results of this Appendix indicate that the atomic data used in this work for [Fe III] lines contribute little to errors in the derived physical conditions and Fe^{2+} abundances, at least for the conditions of HH 204. As we discuss in Section 7, the discrepancy normally found between n_e([Fe III]) and the classical diagnostics—such as n_e([O II]) or n_e([S II])—may be rather indicative of the presence of high-density inclusions within the line of sight. For a complete test of the atomic data, similar studies would be necessary in different ranges of physical conditions. We will continue investigating this topic in other HH objects in future papers of this series.

Appendix B
Supporting Material

In this Appendix, we include the following material.

1. Figure 25. Plasma diagnostics for the individual components analyzed in this work.
2. Table 9. Sample of lines of the spectra of cut 1. The full version is included in the .tar.gz package in machine-readable format. The package also contains the cut 2, combined, and individual blue and red pixel data.
3. Table 10. Atomic data set used for CELs.
4. Table 11. Atomic data set used for RLs.
5. Table 12. Measured and predicted [Fe III] intensity ratios from lines that arise from a common upper level.
6. Table 13. Measured and predicted [Fe II] intensity ratios from lines that arise from a common upper level.
7. Table 14. Measured and predicted [Fe III] intensity ratios for all detected lines using the atomic data chosen in this work.
8. Table 15. Pixel-to-pixel spatial distribution of the physical conditions and ionic abundances of HH 204 in the UVES blue arm spectra.

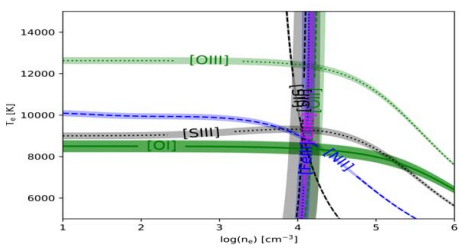

(a) Cut 1, HH 204.

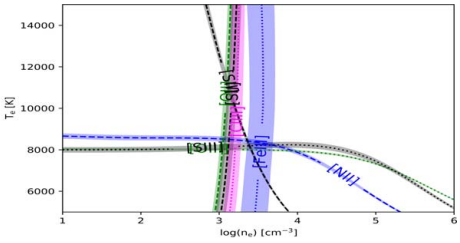

(b) Cut 1, nebular emission plus Blue Layer emission.

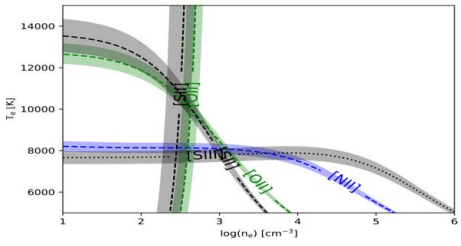

(c) Cut 2, Blue Layer.

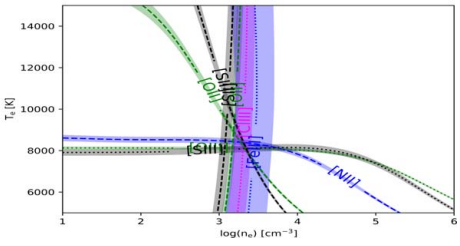

(d) Cut 2, nebular component.

Figure 25. Plasma diagnostic plots for the individual analyzed components. The labeled diagnostics correspond to those discussed in Section 4.1.

Table 9
Sample of 15 Lines from the Spectra of Cut 1

		HH 204						The Orion Nebula+The DBL						
λ_0 (Å)	Ion	λ_{obs}	Vel. (λ_0) (km s^{-1})	FWHM (km s^{-1})	$F(\lambda)/F(H\beta)$	$I(\lambda)/I(H\beta)$	Err. %	λ_{obs}	Vel. (λ_0) (km s^{-1})	FWHM (km s^{-1})	$F(\lambda)/F(H\beta)$	$I(\lambda)/I(H\beta)$	Err. %	Notes
4701.64	[Fe III]	4701.25	−24.76	18.30 ± 0.02	1.424	1.460	2	4701.83	12.22	23.27 ± 0.33	0.193	0.197	3	
4713.14	He I	4712.80	−21.48	18.57 ± 0.31	0.206	0.211	3	4713.35	13.51	27.03 ± 0.30	0.436	0.443	3	
4728.07	[Fe II]	4727.75	−20.08	13.57 ± 0.36	0.072	0.073	4	4728.45	24.31	8.18 ± 4.17	0.004	0.004	30	
4734.00	[Fe III]	4733.57	−27.00	18.18 ± 0.05	0.634	0.647	2	4734.15	9.74	23.81 ± 1.68	0.067	0.068	6	
4740.17	[Ar IV]	*	*	*	*	*	*	4740.35	11.65	14.86 ± 6.68	0.006	0.006	29	
4754.81	[Fe III]	4754.42	−24.90	18.29 ± 0.04	0.800	0.813	2	4755.00	11.67	22.95 ± 0.58	0.127	0.128	4	
4769.53	[Fe III]	4769.14	−24.77	18.23 ± 0.04	0.505	0.512	2	4769.73	12.32	22.75 ± 0.72	0.064	0.065	4	
4774.73	[Fe II]	4774.42	−19.69	13.19 ± 0.51	0.070	0.071	4	*	*	*	*	*	*	
4777.70	[Fe III]	4777.38	−20.30	17.82 ± 0.21	0.304	0.308	3	4777.97	16.73	24.34 ± 2.76	0.032	0.032	10	
4803.29	N II	*	*	*	*	*	*	4803.46	10.50	18.10 ± 2.08	0.019	0.019	8	
4814.54	[Fe II]	4814.23	−19.37	14.38 ± 0.04	0.393	0.396	2	*	*	*	*	*	*	
4874.50	[Fe II]	4874.18	−19.51	13.84 ± 0.54	0.051	0.051	4	*	*	*	*	*	*	
4861.32	H I	4860.97	−21.47	24.67 ± 0.01	100.000	100.000	2	4861.52	12.45	30.59 ± 0.01	100.000	100.000	2	
4861.32	H I	4859.66	−102.26	14.31 ± 1.90	0.106	0.106	10	*	*	*	*	*	*	Deuterium
4874.50	[Fe II]	4874.18	−19.51	13.84 ± 0.54	0.051	0.051	4	*	*	*	*	*	*	
4881.07	[Fe III]	4880.71	−21.92	18.00 ± 0.01	2.251	2.245	2	4881.30	14.32	20.70 ± 0.17	0.248	0.247	3	

Note. The full version is included in the .tar.gz package, along with the cut 2, combined, and individual blue and red pixel data.
(This table is available in its entirety in machine-readable form.)

Table 10
Atomic Data Set Used for CELs

Ion	Transition Probabilities	Collision Strengths
O^{0}	Wiese et al. (1996)	Bhatia & Kastner (1995)
O^{+}	Froese Fischer & Tachiev (2004)	Kisielius et al. (2009)
O^{2+}	Wiese et al. (1996); Storey & Zeippen (2000)	Storey et al. (2014)
N^{+}	Froese Fischer & Tachiev (2004)	Tayal (2011)
Ne^{2+}	McLaughlin et al. (2011)	McLaughlin et al. (2011)
S^{+}	Podobedova et al. (2009)	Tayal & Zatsarinny (2010)
S^{2+}	Podobedova et al. (2009)	Grieve et al. (2014)
Cl^{+}	Mendoza & Zeippen (1983)	Tayal (2004)
Cl^{2+}	Fritzsche et al. (1999)	Butler & Zeippen (1989)
Ar^{2+}	Mendoza (1983); Kaufman & Sugar (1986)	Galavis et al. (1995)
Ar^{3+}	Mendoza & Zeippen (1982)	Ramsbottom & Bell (1997)
Fe^{+}	Bautista et al. (2015)	Bautista et al. (2015)
Fe^{2+}	Quinet (1996); Johansson et al. (2000)	Zhang (1996)
Fe^{3+}	Froese Fischer et al. (2008)	Zhang & Pradhan (1997)
Ni^{+}	Quinet & Le Dourneuf (1996); Nussbaumer & Storey (1982)	Bautista (2004)
Ni^{2+}	Bautista (2001)	Bautista (2001)
Ca^{+}	Meléndez et al. (2007)	Meléndez et al. (2007)
Cr^{+}	Tayal & Zatsarinny (2020)	Tayal & Zatsarinny (2020)

Table 11
Effective Recombination Coefficients Used for RLs

Ion	Reference
H^{+}	Storey & Hummer (1995)
He^{+}	Porter et al. (2012, 2013)
O^{+}	Pequignot et al. (1991)
O^{2+}	Storey et al. (2017)
C^{2+}	Davey et al. (2000)

Table 12
Comparison of the Observed [Fe III] Intensity Ratios in HH 204 and Theoretical Ones Predicted by the Transition Probabilities of Quinet (1996) and Johansson et al. (2000)

Line Ratio	HH 204	Prediction
3240/3286	3.63 ± 0.81	3.60
3240/3319	3.63 ± 0.86	5.06
3240/8729[a]	11.35 ± 1.06	11.87
3335/3357	1.16 ± 0.20	1.18
3335/8838[b]	6.15 ± 1.00	4.93
4607/4702	0.18 ± 0.01	0.17
4607/4770	0.51 ± 0.01	0.51
4667/4734	0.29 ± 0.01	0.28
4667/4778	0.60 ± 0.03	0.57
4658/4755	5.33 ± 0.15	5.49
4881/4987	6.07 ± 0.17	5.76
5011/5085	5.85 ± 0.32	5.94
5271/5412	10.75 ± 0.39	11.01

Notes.
[a] The emission of [Fe III] λ8728.84 from HH 204 was deblended from the nebular component of [C I] λ8727.13.
[b] The emission of [Fe III] λ8838.14 was deblended from a sky feature.

Table 13
Comparison of the Observed [Fe II] Intensity Ratios in HH 204 and Theoretical Ones Predicted by the Transition Probabilities of Bautista et al. (2015)

Line Ratio	HH 204	Prediction
9052/9399	5.45 ± 0.48	5.49
9052/7927	18.84 ± 1.99	6.91
8892/9227	1.71 ± 0.11	1.80
8892/7874	28.58 ± 4.15	10.64
8892/7687	3.85 ± 0.22	1.48
9268/9034[a]	1.33 ± 0.09	1.28
9268/7733[a]	11.72 ± 1.37	5.08

Note.
[a] [Fe II] λ9267.56 was deblended from sky emission.

Table 14
Comparison between Predicted and Measured [Fe III] Intensity Ratios with the Chosen Atomic Data

λ (Å)	Predicted $I(\lambda)/I(4658)$	Measured $I(\lambda)/I(4658)$	Difference
3239.79	90.3 ± 3.1	84.6 ± 6.3	$-7\% \pm 8\%$
3286.24	25.1 ± 0.9	22.3 ± 4.9	$-13\% \pm 30\%$
3319.27	17.8 ± 0.6	22.9 ± 4.5	$23\% \pm 16\%$
3322.47	...	103.0 ± 7.0	...
3334.95	32.1 ± 1.1	28.8 ± 3.8	$-14\% \pm 17\%$
3356.59	27.2 ± 0.9	24.5 ± 2.0	$-9\% \pm 9\%$
3366.22	14.6 ± 0.5	18.5 ± 2.5	$21\% \pm 12\%$
3371.35	...	67.9 ± 4.4	...
3406.18	...	39.1 ± 3.3	...
4008.34	57.4 ± 0.7	50.0 ± 1.6	$-14\% \pm 3\%$
4046.49	8.2 ± 0.1	7.7 ± 0.7	$-6\% \pm 10\%$
4079.69	14.6 ± 0.2	11.2 ± 0.8	$-30\% \pm 7\%$
4096.68	3.2 ± 0.1	2.3 ± 0.4	$-37\% \pm 30\%$
4607.12	58.5 ± 0.3	60.3 ± 1.5	$2\% \pm 2\%$
4667.11	40.4 ± 0.5	43.1 ± 1.6	$6\% \pm 3\%$
4701.64	338.5 ± 1.9	336.9 ± 10.3	$0\% \pm 3\%$
4734.00	146.1 ± 1.6	150.8 ± 3.4	$3\% \pm 2\%$
4754.81	182.1 ± 0.0	187.3 ± 5.7	$3\% \pm 3\%$
4769.53	115.3 ± 0.7	118.2 ± 3.2	$2\% \pm 2\%$
4777.70	70.3 ± 0.8	71.4 ± 2.4	$0\% \pm 3\%$
4881.07	484.3 ± 2.1	519.0 ± 15.3	$7\% \pm 2\%$
4924.66	6.6 ± 0.2	6.8 ± 0.5	$1\% \pm 7\%$
4930.64	40.3 ± 0.6	43.6 ± 1.7	$7\% \pm 3\%$
4985.88	15.5 ± 0.7	8.1 ± 0.6	$-91\% \pm 15\%$
4987.29	84.1 ± 0.4	85.2 ± 2.3	$1\% \pm 2\%$
5011.41	143.1 ± 1.3	147.4 ± 4.5	$1\% \pm 2\%$
5084.85	24.1 ± 0.2	25.0 ± 1.3	$4\% \pm 5\%$
5270.57	487.8 ± 3.8	525.0 ± 14.5	$6\% \pm 2\%$
5412.06	44.3 ± 0.3	48.9 ± 1.9	$9\% \pm 3\%$
7088.46	1.1 ± 0.1	1.8 ± 0.2	$39\% \pm 6\%$
8728.84	7.6 ± 0.3	7.3 ± 0.4	$-3\% \pm 7\%$
9701.87	24.6 ± 0.7	24.8 ± 1.1	$0\% \pm 5\%$
9942.38	15.9 ± 0.5	18.3 ± 1.4	$13\% \pm 6\%$

Note. The intensities are normalized to I([Fe III]) $\lambda 4658 = 1000$.

9. Table 16. Pixel-to-pixel spatial distribution of the physical conditions and ionic abundances of HH 204 in the UVES red arm spectra.
10. Table 17. Pixel-to-pixel spatial distribution of ionic abundances of HH 204 in the UVES red arm spectra.

Table 15
Spatial Distribution of Physical Conditions and Ionic Abundances along HH 204 as a Function of the Distance from the Bow Shock

Distance (mpc)	n_e([Fe III]) (cm^{-3})	T_e([O III]) (K)	He^+ (λ4471)	O^+	O^{2+}	Ne^{2+}
0.00	21,180 ± 5900	16,790 ± 700	10.50 ± 0.02	8.72 ± 0.14	6.13 ± 0.05	⋯
0.49	19,020 ± 5160	17,200 ± 600	10.46 ± 0.01	8.64 ± 0.12	6.02 ± 0.04	⋯
0.98	19,610 ± 4530	18,510 ± 560	10.46 ± 0.01	8.72 ± 0.10	5.89 ± 0.03	⋯
1.47	21,810 ± 3940	15,620 ± 470	10.46 ± 0.01	8.67 ± 0.10	6.05 ± 0.04	⋯
1.96	15,930 ± 4160	15,200 ± 580	10.43 ± 0.01	8.61 ± 0.09	6.07 ± 0.04	⋯
2.44	16,170 ± 3370	15,880 ± 580	10.41 ± 0.01	8.62 ± 0.07	5.94 ± 0.04	⋯
2.93	14,040 ± 2220	14,730 ± 460	10.39 ± 0.01	8.56 ± 0.07	5.99 ± 0.04	⋯
3.42	17,480 ± 3310	14,660 ± 420	10.38 ± 0.01	8.65 ± 0.08	5.99 ± 0.03	⋯
3.91	15,800 ± 2990	13,990 ± 350	10.39 ± 0.01	8.59 ± 0.10	6.03 ± 0.03	⋯
4.40	13,600 ± 2530	13,480 ± 460	10.41 ± 0.01	8.56 ± 0.08	6.06 ± 0.04	⋯
4.89	14,800 ± 2630	12,430 ± 380	10.38 ± 0.01	8.62 ± 0.08	6.17 ± 0.04	⋯
5.38	13,680 ± 2760	12,020 ± 390	10.38 ± 0.01	8.57 ± 0.08	6.22 ± 0.05	⋯
5.87	12,210 ± 2730	11,910 ± 360	10.41 ± 0.01	8.52 ± 0.08	6.25 ± 0.04	⋯
6.36	13,180 ± 2480	11,300 ± 340	10.41 ± 0.01	8.56 ± 0.06	6.32 ± 0.04	⋯
6.85	12,270 ± 2580	11,600 ± 310	10.44 ± 0.01	8.57 ± 0.09	6.31 ± 0.04	4.99 ± 0.07
7.33	13,740 ± 2610	11,500 ± 390	10.45 ± 0.01	8.61 ± 0.08	6.34 ± 0.05	5.12 ± 0.07
7.82	13,440 ± 2520	11,470 ± 290	10.45 ± 0.01	8.56 ± 0.08	6.36 ± 0.04	5.14 ± 0.06
8.31	14,040 ± 2450	11,630 ± 340	10.45 ± 0.01	8.58 ± 0.07	6.33 ± 0.04	5.14 ± 0.07
8.80	11,630 ± 2200	11,260 ± 250	10.44 ± 0.01	8.51 ± 0.07	6.39 ± 0.03	5.16 ± 0.06
9.29	13,490 ± 2450	11,450 ± 260	10.47 ± 0.01	8.51 ± 0.08	6.41 ± 0.04	5.19 ± 0.05
9.78	11,960 ± 2490	11,230 ± 280	10.52 ± 0.01	8.54 ± 0.07	6.50 ± 0.03	5.25 ± 0.06
10.27	11,400 ± 2390	11,620 ± 220	10.58 ± 0.01	8.52 ± 0.07	6.51 ± 0.03	5.23 ± 0.05
10.76	11,420 ± 2190	12,020 ± 280	10.64 ± 0.01	8.51 ± 0.07	6.49 ± 0.03	5.24 ± 0.05
11.25	9490 ± 1970	11,530 ± 310	10.70 ± 0.01	8.48 ± 0.06	6.62 ± 0.04	5.41 ± 0.06
11.74	10,400 ± 1980	11,710 ± 250	10.75 ± 0.01	8.53 ± 0.07	6.63 ± 0.03	5.41 ± 0.06
12.22	10,330 ± 2020	11,550 ± 200	10.80 ± 0.01	8.53 ± 0.07	6.71 ± 0.02	5.54 ± 0.04
12.71	9740 ± 1970	11,030 ± 240	10.84 ± 0.01	8.50 ± 0.07	6.84 ± 0.03	5.61 ± 0.05

Note. Values derived from the blue arm spectrum. Abundances in units of $12+\log(X^{n+}/H^+)$.

Table 16
Spatial Distribution of Physical Conditions and Ionic Abundances along HH 204 as a Function of the Distance from the Bow Shock

Distance (mpc)	T_e([N II]) (K)	T_e([S III]) (K)	He^+ (λ5876)	He^+ (λ6678)	N^+	O^+ (RLs)	S^+	S^{2+}
0.29	8780 ± 310	9150 ± 190	10.41 ± 0.01	10.57 ± 0.03	7.79 ± 0.06	8.68 ± 0.15	6.82 ± 0.09	6.84 ± 0.03
0.66	8970 ± 340	8780 ± 180	10.43 ± 0.01	10.51 ± 0.03	7.75 ± 0.05	8.87 ± 0.11	6.77 ± 0.08	6.90 ± 0.03
1.02	8670 ± 280	9140 ± 210	10.43 ± 0.01	10.50 ± 0.02	7.80 ± 0.05	⋯	6.82 ± 0.09	6.83 ± 0.03
1.38	8920 ± 300	9500 ± 220	10.42 ± 0.01	10.48 ± 0.02	7.75 ± 0.05	8.75 ± 0.12	6.78 ± 0.08	6.77 ± 0.03
1.74	9100 ± 290	9390 ± 190	10.42 ± 0.01	10.43 ± 0.02	7.71 ± 0.04	⋯	6.73 ± 0.07	6.78 ± 0.02
2.10	8860 ± 290	9050 ± 200	10.41 ± 0.01	10.48 ± 0.02	7.73 ± 0.05	8.57 ± 0.15	6.73 ± 0.08	6.82 ± 0.02
2.46	8980 ± 220	9290 ± 210	10.39 ± 0.01	10.45 ± 0.02	7.73 ± 0.04	8.80 ± 0.09	6.74 ± 0.06	6.82 ± 0.03
2.83	8850 ± 220	9420 ± 170	10.37 ± 0.01	10.43 ± 0.02	7.73 ± 0.03	8.70 ± 0.09	6.72 ± 0.07	6.78 ± 0.02
3.19	8750 ± 230	9250 ± 180	10.37 ± 0.01	10.39 ± 0.02	7.75 ± 0.04	8.72 ± 0.07	6.76 ± 0.07	6.77 ± 0.03
3.55	8790 ± 190	9410 ± 180	10.36 ± 0.01	10.43 ± 0.02	7.75 ± 0.04	8.68 ± 0.07	6.79 ± 0.07	6.75 ± 0.02
3.91	8860 ± 260	9410 ± 180	10.36 ± 0.01	10.42 ± 0.02	7.75 ± 0.04	8.66 ± 0.07	6.78 ± 0.07	6.74 ± 0.03
4.27	8900 ± 230	9390 ± 190	10.37 ± 0.01	10.42 ± 0.02	7.74 ± 0.04	8.74 ± 0.06	6.75 ± 0.06	6.74 ± 0.03
4.64	8800 ± 230	9430 ± 190	10.36 ± 0.01	10.41 ± 0.02	7.75 ± 0.04	8.79 ± 0.06	6.72 ± 0.06	6.73 ± 0.02
5.00	8760 ± 230	9400 ± 190	10.34 ± 0.01	10.40 ± 0.02	7.74 ± 0.04	8.74 ± 0.07	6.72 ± 0.06	6.72 ± 0.03
5.36	8960 ± 220	9480 ± 190	10.36 ± 0.01	10.41 ± 0.02	7.71 ± 0.04	8.72 ± 0.06	6.66 ± 0.06	6.71 ± 0.02
5.72	8880 ± 210	9310 ± 190	10.36 ± 0.01	10.42 ± 0.02	7.72 ± 0.04	8.71 ± 0.06	6.63 ± 0.08	6.74 ± 0.03
6.08	8800 ± 220	9330 ± 180	10.36 ± 0.01	10.42 ± 0.02	7.74 ± 0.04	8.73 ± 0.05	6.67 ± 0.06	6.74 ± 0.03
6.44	8810 ± 220	9280 ± 180	10.38 ± 0.01	10.42 ± 0.02	7.73 ± 0.04	8.64 ± 0.06	6.66 ± 0.07	6.76 ± 0.02
6.81	8760 ± 210	9240 ± 210	10.39 ± 0.01	10.43 ± 0.02	7.72 ± 0.04	8.65 ± 0.06	6.61 ± 0.07	6.76 ± 0.03
7.17	8790 ± 240	9290 ± 200	10.40 ± 0.01	10.44 ± 0.02	7.70 ± 0.04	8.73 ± 0.04	6.61 ± 0.06	6.75 ± 0.03
7.53	8840 ± 220	9480 ± 170	10.42 ± 0.01	10.45 ± 0.02	7.70 ± 0.03	8.56 ± 0.06	6.57 ± 0.06	6.71 ± 0.02
7.89	8830 ± 250	9500 ± 180	10.40 ± 0.01	10.45 ± 0.01	7.68 ± 0.04	8.57 ± 0.06	6.56 ± 0.07	6.71 ± 0.02
8.25	8800 ± 270	9410 ± 190	10.41 ± 0.01	10.46 ± 0.02	7.71 ± 0.04	8.62 ± 0.06	6.58 ± 0.07	6.73 ± 0.02
8.61	8830 ± 220	9360 ± 200	10.41 ± 0.01	10.46 ± 0.02	7.70 ± 0.04	8.64 ± 0.05	6.56 ± 0.07	6.75 ± 0.02
8.98	8870 ± 230	9370 ± 160	10.42 ± 0.02	10.47 ± 0.02	7.70 ± 0.03	8.56 ± 0.10	6.53 ± 0.06	6.77 ± 0.02
9.34	8920 ± 210	9220 ± 180	10.44 ± 0.01	10.48 ± 0.02	7.70 ± 0.03	8.61 ± 0.06	6.53 ± 0.06	6.80 ± 0.02
9.70	8860 ± 210	9410 ± 200	10.45 ± 0.01	10.49 ± 0.01	7.70 ± 0.04	8.63 ± 0.05	6.52 ± 0.06	6.77 ± 0.03

Table 16
(Continued)

Distance (mpc)	T_e([N II]) (K)	T_e([S III]) (K)	He^+ (λ5876)	He^+ (λ6678)	N^+	O^+ (RLs)	S^+	S^{2+}
10.06	8800 ± 210	9570 ± 160	10.47 ± 0.01	10.51 ± 0.01	7.69 ± 0.03	8.60 ± 0.05	6.47 ± 0.05	6.74 ± 0.02
10.42	8730 ± 210	9740 ± 210	10.49 ± 0.01	10.53 ± 0.01	7.69 ± 0.04	8.62 ± 0.06	6.41 ± 0.07	6.70 ± 0.03
10.79	8850 ± 210	9900 ± 200	10.54 ± 0.01	10.59 ± 0.01	7.65 ± 0.04	8.56 ± 0.07	6.34 ± 0.07	6.68 ± 0.03
11.15	8770 ± 210	9890 ± 220	10.59 ± 0.01	10.62 ± 0.02	7.65 ± 0.04	8.56 ± 0.08	6.27 ± 0.07	6.67 ± 0.03
11.51	8820 ± 210	9680 ± 210	10.63 ± 0.01	10.65 ± 0.01	7.64 ± 0.04	8.77 ± 0.11	6.23 ± 0.06	6.72 ± 0.02
11.87	8720 ± 220	9690 ± 190	10.68 ± 0.01	10.71 ± 0.01	7.64 ± 0.04	8.60 ± 0.07	6.24 ± 0.06	6.73 ± 0.03
12.23	8740 ± 200	9840 ± 200	10.73 ± 0.01	10.75 ± 0.02	7.64 ± 0.04	8.75 ± 0.06	6.24 ± 0.08	6.72 ± 0.02
12.59	8860 ± 190	9750 ± 210	10.76 ± 0.01	10.79 ± 0.01	7.60 ± 0.03	8.68 ± 0.09	6.18 ± 0.06	6.73 ± 0.03
12.96	8980 ± 200	9720 ± 190	10.80 ± 0.01	10.82 ± 0.01	7.57 ± 0.03	8.41 ± 0.13	6.12 ± 0.07	6.74 ± 0.02
13.32	8320 ± 270	9880 ± 200	10.82 ± 0.01	10.85 ± 0.01	7.53 ± 0.03	8.67 ± 0.09	6.07 ± 0.05	6.70 ± 0.02

Note. Values derived from the red arm spectrum. Abundances in units of $12+\log(X^{n+}/H^+)$

Table 17
Further Ionic Abundances along HH 204 as a Function of the Distance from the Bow Shock

Distance (mpc)	Cl^+	Cl^{2+}	Ar^{2+}	Ca^+	Cr^+	Fe^+	Fe^{2+}	Ni^+	Ni^{2+}
0.29	4.93 ± 0.05	4.63 ± 0.08	5.66 ± 0.05	3.64 ± 0.05	4.57 ± 0.06	6.35 ± 0.04	6.46 ± 0.06	5.08 ± 0.03	5.05 ± 0.07
0.66	4.92 ± 0.04	4.83 ± 0.08	5.66 ± 0.04	3.66 ± 0.05	4.59 ± 0.06	6.35 ± 0.04	6.42 ± 0.06	5.09 ± 0.03	5.07 ± 0.06
1.02	4.94 ± 0.03	4.74 ± 0.05	5.70 ± 0.04	3.64 ± 0.05	4.71 ± 0.05	6.32 ± 0.05	6.49 ± 0.05	5.08 ± 0.03	5.10 ± 0.05
1.38	4.84 ± 0.04	4.67 ± 0.06	5.64 ± 0.04	3.47 ± 0.06	4.59 ± 0.05	6.27 ± 0.05	6.45 ± 0.06	5.00 ± 0.03	5.06 ± 0.06
1.74	4.80 ± 0.04	4.72 ± 0.04	5.59 ± 0.03	3.54 ± 0.05	4.49 ± 0.04	6.17 ± 0.04	6.40 ± 0.05	4.97 ± 0.03	5.00 ± 0.06
2.10	4.82 ± 0.04	4.86 ± 0.05	5.61 ± 0.04	3.46 ± 0.04	4.53 ± 0.04	6.23 ± 0.05	6.43 ± 0.05	5.00 ± 0.03	5.04 ± 0.05
2.46	4.84 ± 0.04	4.84 ± 0.04	5.60 ± 0.03	3.53 ± 0.05	4.55 ± 0.04	6.26 ± 0.04	6.42 ± 0.04	5.03 ± 0.03	5.07 ± 0.05
2.83	4.82 ± 0.03	4.83 ± 0.04	5.59 ± 0.03	3.51 ± 0.04	4.58 ± 0.03	6.28 ± 0.03	6.46 ± 0.04	5.02 ± 0.03	5.03 ± 0.04
3.19	4.83 ± 0.03	4.80 ± 0.05	5.58 ± 0.03	3.52 ± 0.04	4.59 ± 0.04	6.28 ± 0.03	6.49 ± 0.05	5.07 ± 0.03	5.08 ± 0.05
3.55	4.83 ± 0.03	4.71 ± 0.05	5.56 ± 0.03	3.57 ± 0.04	4.58 ± 0.04	6.28 ± 0.03	6.46 ± 0.04	5.07 ± 0.02	5.05 ± 0.04
3.91	4.83 ± 0.03	4.73 ± 0.04	5.54 ± 0.04	3.56 ± 0.04	4.53 ± 0.04	6.29 ± 0.03	6.47 ± 0.05	5.06 ± 0.03	5.06 ± 0.05
4.27	4.81 ± 0.03	4.69 ± 0.05	5.55 ± 0.03	3.54 ± 0.04	4.49 ± 0.04	6.30 ± 0.03	6.46 ± 0.05	5.05 ± 0.03	5.09 ± 0.05
4.64	4.81 ± 0.03	4.73 ± 0.04	5.56 ± 0.03	3.54 ± 0.03	4.44 ± 0.03	6.32 ± 0.03	6.49 ± 0.04	5.03 ± 0.02	5.11 ± 0.04
5.00	4.80 ± 0.03	4.71 ± 0.04	5.56 ± 0.03	3.55 ± 0.04	4.46 ± 0.04	6.32 ± 0.04	6.50 ± 0.04	5.02 ± 0.03	5.11 ± 0.05
5.36	4.76 ± 0.04	4.68 ± 0.04	5.53 ± 0.03	3.50 ± 0.04	4.41 ± 0.03	6.27 ± 0.03	6.46 ± 0.04	4.99 ± 0.03	5.07 ± 0.04
5.72	4.77 ± 0.03	4.75 ± 0.04	5.55 ± 0.03	3.54 ± 0.04	4.36 ± 0.04	6.27 ± 0.03	6.49 ± 0.04	5.00 ± 0.02	5.12 ± 0.04
6.08	4.76 ± 0.03	4.71 ± 0.05	5.57 ± 0.03	3.55 ± 0.03	4.37 ± 0.04	6.29 ± 0.03	6.51 ± 0.04	5.00 ± 0.02	5.14 ± 0.04
6.44	4.77 ± 0.03	4.76 ± 0.04	5.58 ± 0.03	3.56 ± 0.04	4.34 ± 0.03	6.27 ± 0.03	6.50 ± 0.04	4.99 ± 0.02	5.13 ± 0.04
6.81	4.75 ± 0.03	4.76 ± 0.04	5.60 ± 0.03	3.58 ± 0.04	4.30 ± 0.04	6.26 ± 0.03	6.51 ± 0.04	4.96 ± 0.02	5.12 ± 0.04
7.17	4.71 ± 0.03	4.79 ± 0.04	5.59 ± 0.03	3.55 ± 0.04	4.23 ± 0.04	6.20 ± 0.04	6.48 ± 0.05	4.92 ± 0.03	5.11 ± 0.05
7.53	4.69 ± 0.03	4.76 ± 0.04	5.60 ± 0.03	3.50 ± 0.03	4.18 ± 0.03	6.15 ± 0.03	6.49 ± 0.04	4.88 ± 0.02	5.12 ± 0.04
7.89	4.65 ± 0.03	4.71 ± 0.04	5.59 ± 0.03	3.52 ± 0.03	4.22 ± 0.04	6.12 ± 0.04	6.48 ± 0.05	4.87 ± 0.02	5.13 ± 0.04
8.25	4.67 ± 0.03	4.76 ± 0.04	5.61 ± 0.03	3.55 ± 0.03	4.18 ± 0.04	6.17 ± 0.04	6.52 ± 0.05	4.90 ± 0.03	5.15 ± 0.04
8.61	4.72 ± 0.03	4.77 ± 0.03	5.61 ± 0.03	3.58 ± 0.04	4.25 ± 0.04	6.20 ± 0.03	6.50 ± 0.04	4.92 ± 0.02	5.14 ± 0.04
8.98	4.75 ± 0.04	4.74 ± 0.03	5.61 ± 0.03	3.59 ± 0.04	4.23 ± 0.04	6.21 ± 0.04	6.51 ± 0.04	4.92 ± 0.02	5.18 ± 0.04
9.34	4.74 ± 0.03	4.81 ± 0.03	5.61 ± 0.03	3.60 ± 0.03	4.21 ± 0.03	6.21 ± 0.04	6.49 ± 0.04	4.92 ± 0.02	5.16 ± 0.04
9.70	4.70 ± 0.03	4.79 ± 0.04	5.63 ± 0.03	3.56 ± 0.03	4.20 ± 0.04	6.19 ± 0.03	6.51 ± 0.04	4.90 ± 0.02	5.17 ± 0.04
10.06	4.67 ± 0.03	4.78 ± 0.03	5.64 ± 0.03	3.53 ± 0.04	4.13 ± 0.04	6.13 ± 0.03	6.52 ± 0.04	4.84 ± 0.02	5.18 ± 0.04
10.42	4.58 ± 0.04	4.76 ± 0.04	5.65 ± 0.03	3.48 ± 0.04	3.98 ± 0.04	6.01 ± 0.03	6.54 ± 0.05	4.75 ± 0.02	5.15 ± 0.04
10.79	4.48 ± 0.03	4.68 ± 0.04	5.66 ± 0.03	3.43 ± 0.04	3.72 ± 0.07	5.82 ± 0.03	6.51 ± 0.04	4.64 ± 0.02	5.12 ± 0.04
11.15	4.44 ± 0.03	4.74 ± 0.04	5.72 ± 0.03	3.39 ± 0.04	3.66 ± 0.09	5.72 ± 0.05	6.53 ± 0.04	4.52 ± 0.03	5.16 ± 0.04
11.51	4.42 ± 0.04	4.80 ± 0.03	5.76 ± 0.03	3.34 ± 0.04	3.47 ± 0.10	5.65 ± 0.05	6.52 ± 0.05	4.45 ± 0.03	5.18 ± 0.04
11.87	4.42 ± 0.04	4.81 ± 0.03	5.82 ± 0.03	3.24 ± 0.05	⋯	5.58 ± 0.05	6.53 ± 0.05	4.38 ± 0.03	5.17 ± 0.04
12.23	4.37 ± 0.03	4.78 ± 0.04	5.86 ± 0.04	3.26 ± 0.05	⋯	5.62 ± 0.05	6.52 ± 0.05	4.34 ± 0.02	5.17 ± 0.04
12.59	4.38 ± 0.04	4.76 ± 0.04	5.88 ± 0.03	3.26 ± 0.04	3.50 ± 0.12	5.54 ± 0.05	6.52 ± 0.03	4.28 ± 0.02	5.17 ± 0.04
12.96	4.33 ± 0.12	4.82 ± 0.04	5.90 ± 0.03	3.20 ± 0.05	3.43 ± 0.13	5.58 ± 0.05	6.49 ± 0.04	4.24 ± 0.03	5.13 ± 0.04
13.32	4.29 ± 0.04	4.73 ± 0.04	5.93 ± 0.02	3.22 ± 0.05	⋯	5.42 ± 0.07	6.47 ± 0.03	4.23 ± 0.03	5.14 ± 0.04

Note. Values derived from the red arm spectrum. Abundances in units of $12+\log(X^{n+}/H^+)$.

ORCID iDs

J. E. Méndez-Delgado https://orcid.org/0000-0002-6972-6411
W. J. Henney https://orcid.org/0000-0001-6208-9109
C. Esteban https://orcid.org/0000-0002-5247-5943
J. García-Rojas https://orcid.org/0000-0002-6138-1869
A. Mesa-Delgado https://orcid.org/0000-0003-3776-6977
K. Z. Arellano-Córdova https://orcid.org/0000-0002-2644-3518

References

Abel, N. P., Ferland, G. J., & O'Dell, C. R. 2019, ApJ, 881, 130
Abel, N. P., Ferland, G. J., O'Dell, C. R., & Troland, T. H. 2016, ApJ, 819, 136
Allen, M. G., Groves, B. A., Dopita, M. A., Sutherland, R. S., & Kewley, L. J. 2008, ApJS, 178, 20
Arellano-Córdova, K. Z., Esteban, C., García-Rojas, J., & Méndez-Delgado, J. E. 2020, MNRAS, 496, 1051
Arellano-Córdova, K. Z., Esteban, C., García-Rojas, J., & Méndez-Delgado, J. E. 2021, MNRAS, 502, 225
Badnell, N. R., & Ballance, C. P. 2014, ApJ, 785, 99
Baldwin, J. A., Crotts, A., Dufour, R. J., et al. 1996, ApJL, 468, L115
Bautista, M. A. 2001, A&A, 365, 268
Bautista, M. A. 2004, A&A, 420, 763
Bautista, M. A., Ballance, C. P., & Quinet, P. 2010, ApJL, 718, L189
Bautista, M. A., Fivet, V., Ballance, C., et al. 2015, ApJ, 808, 174
Bautista, M. A., Peng, J., & Pradhan, A. K. 1996, ApJ, 460, 372
Bautista, M. A., & Pradhan, A. K. 1998, ApJ, 492, 650
Bhatia, A. K., & Kastner, S. O. 1995, ApJS, 96, 325
Binder, B. A., & Povich, M. S. 2018, ApJ, 864, 136
Blagrave, K. P. M., Martin, P. G., & Baldwin, J. A. 2006, ApJ, 644, 1006
Blagrave, K. P. M., Martin, P. G., Rubin, R. H., et al. 2007, ApJ, 655, 299
Butler, K., & Zeippen, C. J. 1989, A&A, 208, 337
Cantó, J., Goudis, C., Johnson, P. G., & Meaburn, J. 1980, A&A, 85, 128
Cox, D. P., & Raymond, J. C. 1985, ApJ, 298, 651
Davey, A. R., Storey, P. J., & Kisielius, R. 2000, A&AS, 142, 85
Deharveng, L. 1973, A&A, 29, 341
D'Odorico, S., Cristiani, S., Dekker, H., et al. 2000, Proc. SPIE, 4005, 121
Doi, T., O'Dell, C. R., & Hartigan, P. 2002, AJ, 124, 445
Doi, T., O'Dell, C. R., & Hartigan, P. 2004, AJ, 127, 3456
Escalante, V., Morisset, C., & Georgiev, L. 2012, MNRAS, 426, 2318
Esteban, C., & García-Rojas, J. 2018, MNRAS, 478, 2315
Esteban, C., García-Rojas, J., & Pérez-Mesa, V. 2015, MNRAS, 452, 1553
Esteban, C., Peimbert, M., García-Rojas, J., et al. 2004, MNRAS, 355, 229
Esteban, C., Peimbert, M., Torres-Peimbert, S., & Escalante, V. 1998, MNRAS, 295, 401
Fritzsche, S., Fricke, B., Geschke, D., Heitmann, A., & Sienkiewicz, J. E. 1999, ApJ, 518, 994
Froese Fischer, C., Rubin, R. H., & Rodríguez, M. 2008, MNRAS, 391, 1828
Froese Fischer, C., & Tachiev, G. 2004, ADNDT, 87, 1
Gaia Collaboration, Brown, A. G. A., Vallenari, A., et al. 2018, A&A, 616, A1
Galavis, M. E., Mendoza, C., & Zeippen, C. J. 1995, A&AS, 111, 347
García-Díaz, M. T., & Henney, W. J. 2007, AJ, 133, 952
García-Díaz, M. T., Henney, W. J., López, J. A., & Doi, T. 2008, RMxAA, 44, 181
García-Rojas, J., & Esteban, C. 2007, ApJ, 670, 457
García-Rojas, J., Esteban, C., Peimbert, A., et al. 2005, MNRAS, 362, 301
García-Rojas, J., Esteban, C., Peimbert, A., et al. 2007, RMxAA, 43, 3
García-Rojas, J., Esteban, C., Peimbert, M., et al. 2006, MNRAS, 368, 253
García-Rojas, J., Simón-Díaz, S., & Esteban, C. 2014, A&A, 571, A93
Giannini, T., Antoniucci, S., Nisini, B., Bacciotti, F., & Podio, L. 2015, ApJ, 814, 52
Giannini, T., Nisini, B., Antoniucci, S., et al. 2013, ApJ, 778, 71
Grieve, M. F. R., Ramsbottom, C. A., Hudson, C. E., & Keenan, F. P. 2014, ApJ, 780, 110
Hartigan, P. 1989, ApJ, 339, 987
Hartigan, P., Morse, J. A., & Raymond, J. 1994, ApJ, 436, 125
Hartigan, P., Raymond, J., & Hartmann, L. 1987, ApJ, 316, 323
Hébrard, G., Péquignot, D., Vidal-Madjar, A., Walsh, J. R., & Ferlet, R. 2000a, A&A, 354, L79
Hébrard, G., Péquignot, D., Walsh, J. R., Vidal-Madjar, A., & Ferlet, R. 2000b, A&A, 364, L31
Henney, W. J. 2002, RMxAA, 38, 71
Henney, W. J., & O'Dell, C. R. 1999, AJ, 118, 2350
Johansson, S., Zethson, T., Hartman, H., et al. 2000, A&A, 361, 977
Jones, M. R. 1992, PhD thesis, Rice Univ.
Kaufman, V., & Sugar, J. 1986, JPCRD, 15, 321
Kisielius, R., Storey, P. J., Ferland, G. J., & Keenan, F. P. 2009, MNRAS, 397, 903
Kissler-Patig, M., Pirard, J. F., Casali, M., et al. 2008, A&A, 491, 941
Laha, S., Tyndall, N. B., Keenan, F. P., et al. 2017, ApJ, 841, 3
Liu, X. W., Luo, S. G., Barlow, M. J., Danziger, I. J., & Storey, P. J. 2001, MNRAS, 327, 141
Lodders, K. 2019, arXiv:1912.00844
Lucy, L. B. 1995, A&A, 294, 555
Luridiana, V., Morisset, C., & Shaw, R. A. 2015, A&A, 573, A42
McLaughlin, B. M., Lee, T.-G., Ludlow, J. A., et al. 2011, JPhB, 44, 175206
Meléndez, M., Bautista, M. A., & Badnell, N. R. 2007, A&A, 469, 1203
Méndez-Delgado, J. E., Esteban, C., García-Rojas, J., et al. 2021, MNRAS, 502, 1703
Mendoza, C. 1983, in IAU Symp. 103, Planetary Nebulae, ed. L. H. Aller (Dordrecht: Kluwer), 143
Mendoza, C., & Zeippen, C. J. 1982, MNRAS, 198, 127
Mendoza, C., & Zeippen, C. J. 1983, MNRAS, 202, 981
Mesa-Delgado, A., Esteban, C., & García-Rojas, J. 2008, ApJ, 675, 389
Mesa-Delgado, A., Esteban, C., García-Rojas, J., et al. 2009, MNRAS, 395, 855
Moehler, S., Dreizler, S., LeBlanc, F., et al. 2014a, A&A, 565, A100
Moehler, S., Modigliani, A., Freudling, W., et al. 2014b, A&A, 568, A9
Morisset, C. 2017, in IAU Symp. 323, Planetary Nebulae: Multi-Wavelength Probes of Stellar and Galactic Evolution (Cambridge: Cambridge Univ. Press), 43
Muench, A. A., Lada, E. A., Lada, C. J., & Alves, J. 2002, ApJ, 573, 366
Münch, G., & Wilson, O. C. 1962, ZA, 56, 127
Mundt, R., & Fried, J. W. 1983, ApJL, 274, L83
Nahar, S. N., & Pradhan, A. K. 1996, A&AS, 119, 509
Nisini, B., Antoniucci, S., Alcalá, J. M., et al. 2018, A&A, 609, A87
Nisini, B., Bacciotti, F., Giannini, T., et al. 2005, A&A, 441, 159
Núñez-Díaz, M., Mesa-Delgado, A., Esteban, C., et al. 2012, MNRAS, 421, 3399
Nussbaumer, H., & Storey, P. J. 1982, A&A, 110, 295
O'Dell, C. R. 2009, PASP, 121, 428
O'Dell, C. R. 2018, MNRAS, 478, 1017
O'Dell, C. R., Abel, N. P., & Ferland, G. J. 2020, ApJ, 891, 46
O'Dell, C. R., Abel, N. P., & Ferland, G. J. 2021, ApJ, 907, 119
O'Dell, C. R., & Doi, T. 2003, AJ, 125, 277
O'Dell, C. R., Ferland, G. J., & Henney, W. J. 2001, ApJ, 556, 203
O'Dell, C. R., Ferland, G. J., Henney, W. J., et al. 2015, AJ, 150, 108
O'Dell, C. R., Ferland, G. J., & Peimbert, M. 2017a, MNRAS, 464, 4835
O'Dell, C. R., Hartigan, P., Bally, J., & Morse, J. A. 1997a, AJ, 114, 2016
O'Dell, C. R., Hartigan, P., Lane, W. M., et al. 1997b, AJ, 114, 730
O'Dell, C. R., Kollatschny, W., & Ferland, G. J. 2017b, ApJ, 837, 151
O'Dell, C. R., & Wong, K. 1996, AJ, 111, 846
Osterbrock, D. E., Tran, H. D., & Veilleux, S. 1992, ApJ, 389, 305
Peimbert, M. 1967, ApJ, 150, 825
Pequignot, D., Petitjean, P., & Boisson, C. 1991, A&A, 251, 680
Podobedova, L. I., Kelleher, D. E., & Wiese, W. L. 2009, JPCRD, 38, 171
Porter, R. L., Ferland, G. J., Storey, P. J., & Detisch, M. J. 2012, MNRAS, 425, L28
Porter, R. L., Ferland, G. J., Storey, P. J., & Detisch, M. J. 2013, MNRAS, 433, L89
Quinet, P. 1996, A&AS, 116, 573
Quinet, P., & Le Dourneuf, M. 1996, A&AS, 119, 99
Ramsbottom, C. A., & Bell, K. L. 1997, ADNDT, 66, 65
Raymond, J. C., Chilingarian, I. V., Blair, W. P., et al. 2020, ApJ, 894, 108
Reipurth, B., & Bally, J. 2001, ARA&A, 39, 403
Rodríguez, M. 1999, A&A, 348, 222
Rodríguez, M., & Rubin, R. H. 2005, ApJ, 626, 900
Rosado, M., de La Fuente, E., Arias, L., & Le Coarer, E. 2002, RvMXA, 13, 90
Schwartz, R. D. 1983, ARA&A, 21, 209
Simón-Díaz, S. 2010, A&A, 510, A22
Simón-Díaz, S., García-Rojas, J., Esteban, C., et al. 2011, A&A, 530, A57
Stasińska, G. 1978, A&A, 66, 257
Storey, P. J., & Hummer, D. G. 1995, MNRAS, 272, 41
Storey, P. J., Sochi, T., & Badnell, N. R. 2014, MNRAS, 441, 3028
Storey, P. J., Sochi, T., & Bastin, R. 2017, MNRAS, 470, 379
Storey, P. J., & Zeippen, C. J. 2000, MNRAS, 312, 813
Strom, K. M., Strom, S. E., & Stocke, J. 1983, ApJL, 271, L23

Sutherland, R. S., & Dopita, M. A. 2017, ApJS, 229, 34
Takami, M., Usuda, T., Sugai, H., et al. 2002, ApJ, 566, 910
Tayal, S. S. 2004, A&A, 418, 363
Tayal, S. S. 2011, ApJS, 195, 12
Tayal, S. S., & Zatsarinny, O. 2010, ApJS, 188, 32
Tayal, S. S., & Zatsarinny, O. 2020, ApJ, 888, 10
Tody, D. 1993, in ASP Conf. Ser. 52, IRAF in the Nineties, ed. R. J. Hanisch, R. J. V. Brissenden, & J. Barnes (San Francisco, CA: ASP), 173
Torres-Peimbert, S., Peimbert, M., & Daltabuit, E. 1980, ApJ, 238, 133
van der Werf, P. P., Goss, W. M., & O'Dell, C. R. 2013, ApJ, 762, 101
Verner, E. M., Verner, D. A., Baldwin, J. A., Ferland, G. J., & Martin, P. G. 2000, ApJ, 543, 831
Weilbacher, P. M., Monreal-Ibero, A., Kollatschny, W., et al. 2015, A&A, 582, A114
Wiese, W. L., Fuhr, J. R., & Deters, T. M. 1996, JPCRD, 7, 403
Zel'dovich, Y. B., & Raizer, Y. P. 1967, JAM, 34, 1055
Zhang, H. L. 1996, A&AS, 119, 523
Zhang, H. L., & Pradhan, A. K. 1997, A&AS, 126, 373

5

HH514: evidence of planet formation in the Orion Nebula?

This chapter includes the third article of the series "Photoionized Herbig-Haro objects in the Orion Nebula through deep high-spectral resolution spectroscopy", published in the MNRAS 2022, Volume 514, Number 1, pp.744-761. The article was the main subject of several press releases[a]

In this chapter, we analyse HH514, a microjet located around 25×10^{-3} pc from θ^1 Ori C. It emerges from the proplyd 170-337, showing two evident spatial components: the jet base and a northern knot. HH514 presents the highest radial shift from all the objects analysed in this thesis ($\sim$ 150 km s^{-1}) being the only showing redshift.

Both the jet base and the knot are extremely dense, a factor 40 and 12 denser than the Orion Nebula, respectively. However, HH514 has consistent temperatures with the Orion Nebula given the photoionisation equilibrium. The chemical analysis reveals consistency between the composition of HH514 and the Orion Nebula with the exception of S, Fe and Ni, which are enhanced in HH514. We rule out the possibility that the S/H abundance of HH514, more than twice the solar abundance, may be spurious. We interpret this as evidence of dust destruction of S-bearing dust reservoirs as sulfides (FeS). This is rather a particular case, since such S overabundance has not been observed in previous studies of HHs, neither in those photoionised nor in those that propagate through neutral environments. A possible scenario that could explain

[a] `https://www.iac.es/en/outreach/news/possible-evidence-planet-formation-found-orion-nebula`

the formation of S-rich dust reservoirs is the accretion process from the protoplanetary disk to a central star in the presence of a giant planet/protoplanet immersed in the disk. This cause a pressure bump that can filter the dust particles, accumulating the largest ones, among which would be the sulfides (Kama et al. 2019). By entering these sulfides in the jet launch region, these can be destroyed, explaining the observed sulphur overabundance. This may be indirect evidence of planet formation (and perhaps destruction) in the harsh UV radiated environment of the Orion Nebula.

Monthly Notices of the ROYAL ASTRONOMICAL SOCIETY

MNRAS **514,** 744–761 (2022) https://doi.org/10.1093/mnras/stac1300
Advance Access publication 2022 May 12

Photoionized Herbig–Haro objects in the Orion Nebula through deep high-spectral resolution spectroscopy – III. HH 514

J. E. Méndez-Delgado [1,2]★, C. Esteban [1,2], J. García-Rojas [1,2] and W. J. Henney [3]

[1]*Instituto de Astrofísica de Canarias (IAC), E-38205 La Laguna, Spain*
[2]*Departamento de Astrofísica, Universidad de La Laguna, E-38206 La Laguna, Spain*
[3]*Instituto de Radioastronomía y Astrofísica, Universidad Nacional Autónoma de México, Apartado Postal 3-72, 58090 Morelia, Michoacán, México*

Accepted 2022 May 6. Received 2022 May 5; in original form 2022 April 4

ABSTRACT

We analyse the physical conditions and chemical composition of the photoionized Herbig–Haro object HH 514, which emerges from the protoplanetary disc (proplyd) 170-337 in the core of the Orion Nebula. We use high-spectral resolution spectroscopy from Ultraviolet and Visual Echelle Spectrograph at the *Very Large Telescope* and IFU-spectra from MEGARA at the *Gran Telescopio de Canarias*. We observe two components of HH 514, the jet base and a knot, with $n_e = (2.3 \pm 0.1) \times 10^5 \mathrm{cm}^{-3}$ and $n_e = (7 \pm 1) \times 10^4$ cm^{-3}, respectively, both with $T_e \approx 9000$ K. We show that the chemical composition of HH 514 is consistent with that of the Orion Nebula, except for Fe, Ni, and S, which show higher abundances. The enhanced abundances of Fe and Ni observed in HH objects compared with the general interstellar medium are usually interpreted as destruction of dust grains. The observed sulphur overabundance (more than two times solar) is challenging to explain since the proplyd photoevaporation flow from the same disc shows normal sulphur abundance. If the aforementioned S-overabundance is due to dust destruction, the formation of sulfides and/or other S-bearing dust reservoirs may be linked to planet formation processes in proplyds, which filter large sulfide dust grains during the accretion of matter from the disc to the central star. We also show that published kinematics of molecular emission close to the central star are not consistent with either a disc perpendicular to the optical jet, or with an outflow that is aligned with it.

Key words: ISM: abundances – ISM: Herbig–Haro objects – ISM: individual: Orion Nebula, HH 514.

1 INTRODUCTION

Advances in astrophysical instrumentation in recent decades have allowed detailed observations of internal structures in Galactic star-forming regions. Among them, the observations of small-spatial scale structures in the Orion Nebula have been pioneering. Since the 1990s, with the first images from the *Hubble Space Telescope* (*HST*), dozens of photoevaporating protoplanetary discs (proplyds, O'Dell, Wen & Hu 1993) have been discovered and analysed in the nebula. Proplyds generally have a compact semicircular head with an extended tail that points away from the ionizing source. Their greatest concentration is in the central core of the Orion Nebula Cluster, which contains the four high-mass Trapezium stars, with θ^1 Ori C (O7 Vp; Sota et al. 2011) being the most luminous member and the dominant ionizing source for the nebula. The Trapezium region is illustrated in Fig. 1 with an image that has been high-pass filtered to emphasize sub-arcsecond structures [1 arcsec $\approx$ 0.002 pc for an assumed distance of (410 $\pm$ 10) pc, Binder & Povich 2018]. High-mass Trapezium stars are labelled in blue and proplyds are labelled in white following the nomenclature of Laques & Vidal (1979) for the six closest proplyds to θ^1 Ori C (LV knots) and the coordinate-based names of O'Dell & Wen (1994) for the remaining.

In many of the proplyds in the surrounding areas of θ^1 Ori C, supersonic gas outflows and jets have been observed. Several of them have been classified as Herbig–Haro objects (HHs), some of which are illustrated in Fig. 1. This is the case of HH 514, which originates in the proplyd 170-337 (Bally et al. 1998), located 12.61 arcsec from θ^1 Ori C. A redshifted microjet of size 0.5 arcsec protrudes northwards from the proplyd ionization front and a short chain of redshifted knots are seen at a distance of $\approx$ 4 arcsec along the same axis (Bally, O'Dell & McCaughrean 2000) with proper motions consistent with an origin in 170-337 (O'Dell & Henney 2008). These are, respectively, labelled as 'jet base' and 'knot' in Fig. 1. A blueshifted counterflow is also detected at the base of the jet, but it is much weaker. This is unusual for HH flows in Orion, which tend to be predominantly blueshifted (Henney et al. 2007). A faint fast-moving knot to the S of the proplyd may be associated with this counterjet.

HH 514 is particularly bright in the emission of [Fe III] lines, showing also intense lines of [Fe II], [Ni II], and [Ni III]. In addition, its proximity to θ^1 Ori C and its large propagation velocity make it an excellent laboratory to explore the phenomenon of destruction of dust grains by analysing the abundances of Fe and Ni in the gas. Many HH objects have relatively large gaseous abundances of Fe and Ni, whereas in the rest of the Orion Nebula these abundances are much smaller (Méndez-Delgado et al. 2021b).

In this paper, the third in a series dedicated to photoionized HH objects in the Orion Nebula, we analyse for the first time the physical conditions, chemical composition, and kinematics of HH 514. We use high-resolution spectroscopy from the Ultraviolet and Visual Echelle Spectrograph (UVES) (D'Odorico et al. 2000) of the Very

★ E-mail: jemd@iac.es

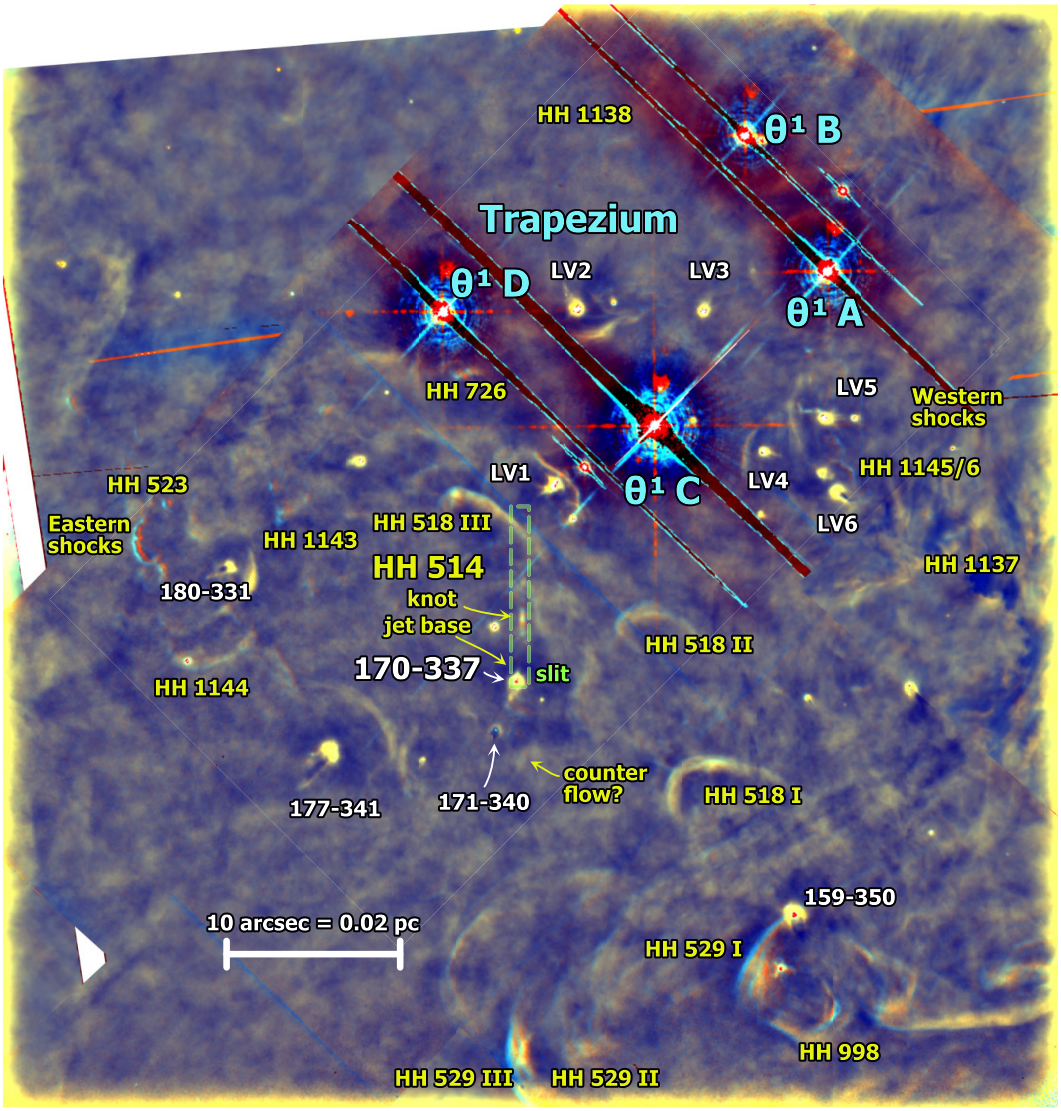

Figure 1. Location of HH 514 within the inner Orion Nebula, showing the position and orientation of the UVES spectrograph slit (dashed green outline). High-mass OB stars are labelled in blue, prominent proplyds are labelled in white, and components of Herbig–Haro flows from O'Dell et al. (2015) are labelled in yellow. Background image is a composite of narrow-band observations with *HST* in the [O III] λ5007 line obtained at three different epochs over a span of 22 yr: 1994 (red channel), 2004 (green channel), 2016 (blue channel). All images are aligned to the astrometric frame defined in Robberto et al. (2013) and have been high-pass filtered with a Gaussian kernel of width 1 arcsec to suppress large-scale brightness variations. Stationary emission features appear yellow–white in this image, while moving features show a prism-like separation: red–green–blue, with blue indicating the leading edge.

Large Telescope and IFU spectra from MEGARA (Gil de Paz et al. 2018) at the Gran Telescopio Canarias (GTC). Given the high spectral and spatial resolution of our observations, we have analysed two velocity components associated with two areas of HH 514: the jet base and a northern knot, completely separated from the emission of the Orion Nebula. Our analysis focuses mainly on estimating the total abundances of Fe and Ni, which seems to be mainly in gaseous phase due to the strong degree of destruction of dust grains in the shock front. We also report an overabundance of S and discuss its possible origin.

In Section 2, we describe the observations and the data reduction process. In Section 3, we derive the physical conditions of each kinematic component. In Section 4, we derive the ionic and total abundances. In Section 5, we discuss our results, focusing on the

Table 1. Main parameters of UVES spectroscopic observations.

Date	Δλ (Å)	Exp. time (s)	Seeing (arcsec)	Airmass
2013-10-30	3100–3885	5, 3 × 180	0.92	1.11
2013-10-30	3750–4995	5, 3 × 600	0.87	1.15
2013-10-30	4785–6805	5, 3 × 180	0.92	1.11
2013-10-30	6700–10 420	5, 3 × 600	0.87	1.15

observed overabundance of S, the total abundances of Fe and Ni, and the kinematic properties of HH 514. In Section 6, we summarize our main conclusions. Finally, in the Appendix A, we add tables of data and figures as supporting material.

2 OBSERVATIONS AND DATA REDUCTION

2.1 High spectral resolution observations

The observations were taken during the nights of 2013 October 29 and 30 under clear conditions using the UT2 (Kueyen) of the Very Large Telescope (VLT) at Cerro Paranal, Chile, with the Ultraviolet Echelle Spectrograph (UVES; D'Odorico et al. 2000). The central coordinates of the 10 arcsec slit are: RA(J2000) = $05^{h}35^{m}16\overset{s}{.}95$, Dec. (J2000) = $-05°23'33.72''$ oriented along the north–south spatial axis as is shown in Fig. 1. The slit width of 1 arcsec provides an effective spectral resolution of $\lambda/\Delta\lambda \approx 6.5$ km s^{-1} in the spectral range between 3100 and 10 400 Å. Analogously to the observations described in the articles on HH 529 II-III and HH 204 (Méndez-Delgado et al. 2021a, b, hereinafter Paper I and Paper II, respectively), three exposures of 150 s each of the star GD71 (Moehler et al. 2014a, b) were taken during the same night under similar conditions to achieve the flux calibration of the science data. The configuration of the instrument and the data reduction procedure are described in detail in Paper I, while the main settings of the observations of HH 514 are shown in Table 1. We define three spatial cuts along the observed slit as shown in Fig. 2, covering the main high-velocity components, which are redshifted by about 150 km s^{-1} from the nebular component. We name the southernmost high-velocity component (within Cut 1) as the jet and the one located in the central cut as the knot. The nebular emission of Cut 1 also contains the emission of the proplyd 170-337. The complete analysis of the physical conditions and chemical composition of this proplyd will be the subject of a future work (Méndez-Delgado et al., in preparation). In this work, we will only mention some results on the abundance of S in 170-337 in Section 5.4, which is relevant for our analysis of HH 514. Panel (b) of Fig. 2 shows several components at intermediate redshifted velocities between that of the nebula and HH 514, which are seen mainly in lines of highly ionized ions such as [O III] or [Ne III]. Unfortunately, their emission is very weak in most spectral lines, so the determination of physical conditions and chemical abundances for those velocity components is not reliable with the present data and they are not studied further here. They may be associated with the HH 518 flow from the proplyd 159-350 (see Fig. 1). In order to increase the contrast of the HH 514 emission, which is rather weak compared to the main nebular background

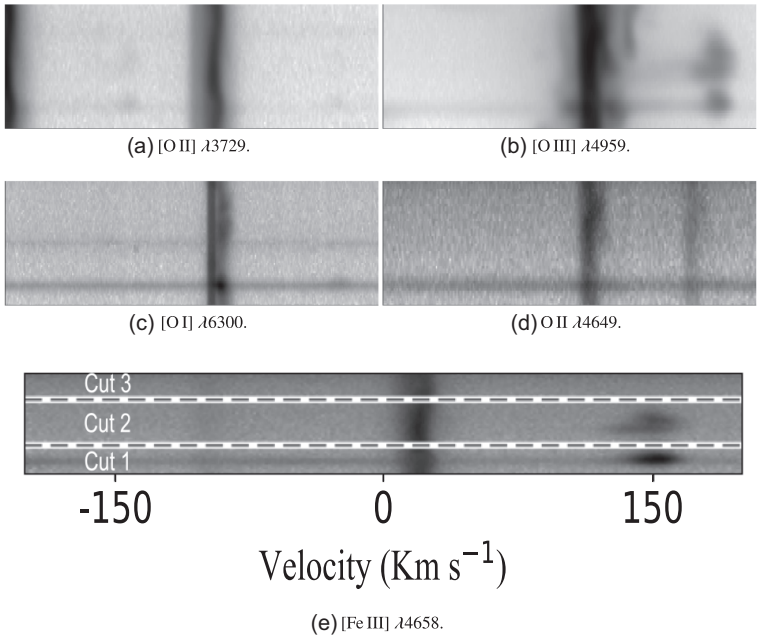

Figure 2. *Upper and middle panels:* Sample of representative lines in the bi-dimensional spectrum. The Y-axis corresponds to the spatial direction (up north, down south, see Fig. 1 for the spatial location of the slit), while the X-axis is the spectral direction. All figures are centred at the rest-frame reference wavelength of each line. *Bottom panel:* Emission of the [Fe III] λ4658.17 line as well as the limits and extension of the different spatial cuts extracted to analyse each velocity component. Cut 1 is at the bottom, which corresponds to the southernmost one. The spatial extension is 2.71, 4.18, and 2.46 arcsec for cuts 1, 2, and 3, respectively. The velocity scale is heliocentric.

Table 2. Reddening coefficients for each component.

	c(H β)	
	Nebular	High velocity
Cut 1	–	0.86 ± 0.05
Cut 2	0.85 ± 0.03	0.75 ± 0.07
Cut 3	0.85 ± 0.02	–

emission, we subtract Cut 3, which contains only background nebular emission, from Cut 1 and Cut 2, rescaling its emission by the number of pixels of each cut. In addition to increasing the contrast of the HH 514 emission, this subtraction procedure permits us to remove sky and ghost contamination from the spectra of the HH object. We estimate the flux of the emission lines, their full width at half-maximum (FWHM), and their central wavelength by Gaussian fittings using the SPLOT task of IRAF[1] (Tody 1993) as is described in detail in Paper I. We achieve the reddening correction using the same procedure described in Paper I and Paper II, using the extinction curve from Blagrave et al. (2007). The resulting values of c(H β) are presented in Table 2. In Table A1, we include the relevant information for some of the emission lines of the spectrum of the jet base, as an example of the tables of the complete spectra that are provided as supplementary material.

2.2 IFU observations

Optical integral-field spectrograph observations of HH 514 were carried out on the night of 2022 February 28 under dark, photometric sky conditions and a seeing of ∼1.2 arcsec using MEGARA (Gil de Paz et al. 2018) at the 10.4 m GTC. The low-resolution (LR) Volume-Phased Holographic (VPH) grism VPH675-LR was used; this grism covers the 6095–7300 Å wavelength range with a spectral dispersion of 0.287 Å pix^{-1} and an effective resolution of $R \sim 5900$. Three 900 s exposures were taken in order to minimize the impact of cosmic rays in the relatively large field of view of MEGARA (12.5 arcsec × 11.3 arcsec). The MEGARA data were reduced using the *megaradrp* v0.11 pipeline (Pascual et al. 2019, 2021). The pipeline uses several python-based recipes to perform bias subtraction, fibre-tracing, flat-field correction, wavelength calibration, and spectra extraction. Sky subtraction was avoided owing to the large size of the Orion Nebula prevented to place any of the MEGARA sky bundles on a nebular emission-free zone of the sky. Flux calibration was also performed using the spectrophotometric standard star HR 1544. The final product is a row-stacked spectrum that is converted into a data cube of 0.2 arcsec square spaxel on spatial dimensions using the *megararss2cube* task of the *megara-tools* suite v0.1.1 (Gil De Paz, Pascual & Chamorro-Cazorla 2020).

3 PHYSICAL CONDITIONS

We use the version 1.1.13 of PyNeb (Luridiana, Morisset & Shaw 2015) and the atomic data set shown in tables 9 and 10 from Paper II to derive the physical conditions of the different gas components analysed in this work. The adopted electron density, n_e, in the nebular components is a weighted average[2] of the resulting values from the collisionally excited line (CEL) diagnostics [O II] λ3726/λ3729, [S II] λ6731/λ6716, [Cl III] λ5538/λ5518, [Fe II] λ9268/λ9052, [Fe III] λ4658/λ4702, and [Ar IV] λ4740/λ4711. In addition, we apply the maximum-likelihood procedure described in section 4.2 of Paper I to derive the physical conditions based on the [Fe III] λλ 4658, 4702, 4734, 4881, 5011, and 5271 lines. As it was commented in Paper I, with the adopted atomic data, [Fe III] diagnostics are not adequately sensitive to density for values smaller than 10^3 cm^{-3}, thus if a considerable part of the observed ionized gas has densities of the order or lower than that value (as it is expected in the nebular components), the resulting n_e may be biased to that of the densest zones along the line of sight. The value of n_e(O II) was derived with the available recombination lines (RLs) of multiplet 1 and the results are highly consistent with the adopted average density.

In the plasma diagnostics of the jet base, there are two possible intersections of the temperature sensitive curve of [N II] λ5755/λ6584 with the density sensitive ones, giving very different values of the electron temperature, T_e. One gives an extremely high density (larger than 10^5 cm^{-3}) (shown in Fig. A1) or an extremely high temperature (higher than 10^5 K at smaller densities than 10^4 cm^{-3}, beyond the scale of Fig. A1). The [Fe III] λ4658/λ4702, [S II] λ4069/λ4076, and [O II] λ7319+20/λ7330 + 31 density diagnostics confirm the first case. In the two studied components of HH 514 we estimate the convergence of $n_e - T_e$ using the [Fe III] λλ 4658, 4702, 4734, 4881, 5011, 5271 CELs. The resulting density in the jet base of HH 514 is $10^{5.37}$ cm^{-3}.

In the case of the northern knot of HH 514, the convergence shows a higher dispersion in $n_e - T_e$ which seems to be due to the mixture of two or more gas components with similar velocities and notably different physical and/or ionization conditions. As it is shown in Fig. A2, the spatial distribution along the slit of the intensity of the [Fe III] λ4658 line centred at a heliocentric velocity of ∼150 km s^{-1} is double-peaked in the northern knot of HH 514, which shows that at least two different gas components moving at a similar velocity are integrated in this part of the HH object. However, the separation into two spatial components results in a very low signal-to-noise spectra. Thus, the physical conditions derived in the knot are expected to be more uncertain than those in the jet base.

Based on the adopted density in each component, we estimate T_e through various diagnostics shown in Table 3. In the nebular components, we define T_e(low) as the weighted average of T_e([N II]), T_e([O II]), and T_e([S II]), while T_e(high) is the weighted average of T_e([O III]), T_e([S III]), and T_e([Ar III]). In both components of HH 514, the estimation of T_e(low) is quite uncertain, given the low critical density of the diagnoses available for this ionization zone and the high density of these objects. Due to this, and considering the similarity between T_e([O III]) in both velocity components, we will adopt the T_e(low) determined for the jet base – the spectrum with the best signal-to-noise ratio – as also representative for the knot.

4 IONIC AND TOTAL ABUNDANCES

We derive ionic abundances of N^+, O^+, S^+, Cl^+, Ca^+, Fe^+, and Ni^+ based on CELs and using T_e(low). We derive the abundances of Cl^{2+} and S^{2+} using T_e ([S III]) and the ionic abundances of O^{2+}, Ne^{2+}, Cl^{3+}, Ar^{2+}, Ar^{3+}, and Fe^{3+} using T_e(high). In the nebular components, we derive the abundance of Fe^{2+} and Ni^{2+} using T_e(low). However, in both components of HH 514, the derived T_e ([Fe III]) indicate a lower temperature than T_e(low). This can be related to the dust destruction process described in detail in Section 5.4, where the filtering and destruction of dust grains increase the relative abundance of metals, cooling the gas. Therefore, in

[1] IRAF is distributed by National Optical Astronomy Observatory, which is operated by Association of Universities for Research in Astronomy, under cooperative agreement with the National Science Foundation.
[2] The weights were defined as the inverse of the square of the error associated with each density diagnostic.

Table 3. Electron densities and temperatures determined from several diagnostics.

Diagnostic	Cut 1 HH 514 jet base	Cut 2 Nebula	Cut 2 HH 514 knot	Cut 3 Nebula
		n_e(cm^{-3})		
[O II] λ3726/λ3729	–	5980^{+1160}_{-870}	–	5610^{+960}_{-800}
[O II] λ7319+20/λ7330 + 31	263000:	–	–	–
[S II] λ6731/λ6716	–	4150^{+1810}_{-1230}	–	4240^{+1400}_{-1030}
[S II] λ4069/λ4076	219000:	–	–	–
[Cl III] λ5538/λ5518	–	7640^{+970}_{-1020}	–	7620^{+1070}_{-960}
[Fe II] λ9268/λ9052	>76000	4500^{+9740}_{-3590}	–	3540^{+9190}_{-2760}
[Fe III] λ4658/λ4702	234000:	8490^{+2490}_{-2350}	57000:	6430^{+2810}_{-2080}
[Ar IV] λ4740/λ4711	–	6730^{+660}_{-690}	–	4800^{+570}_{-690}
O II*	–	5640 ± 510	–	4960 ± 650
[Fe III]*	232000 ± 12000	8600 ± 810	74000 ± 14000	7540 ± 1020
Adopted	**232000 ± 12000**	**6690 ± 940**	**74000 ± 14000**	**5490 ± 1120**
		T_e (K)		
T(He I)	8710:	7790^{+570}_{-480}	6010:	7570^{+490}_{-550}
[N II] λ5755/λ6584	12860^{+1240}_{-1170}	9750^{+230}_{-220}	–	9880^{+230}_{-250}
[O II] λλ 3726+29/λλ7319+20+30 + 31	9180^{+1500}_{-630}	9500^{+740}_{-610}	7830^{+1430}_{-810}	10980^{+1040}_{-1320}
[S II] λλ4069+76/λλ 6716 + 31	20010^{+45030}_{-9150}	9410^{+950}_{-1220}	–	10090^{+2180}_{-1400}
[O III] λ4363/λλ4959 + 5007	8880^{+250}_{-210}	8490^{+90}_{-100}	9330^{+260}_{-230}	8400^{+80}_{-70}
[S III] λ6312/λλ9069 + 9531	8420^{+310}_{-400}	8630^{+330}_{-340}	8230^{+430}_{-560}	8820^{+330}_{-310}
[Ar III] λ5192/λ7136	–	8070^{+190}_{-160}	–	8320^{+230}_{-190}
[Fe III]*	6840 ± 1640	8960 ± 850	8180 ± 1410	7850 ± 830
T_e (low) Adopted	**11370 ± 1820**	**9530 ± 100**	**11370 ± 1820**	**9920 ± 200**
T_e (high) Adopted	**8880 ± 250**	**8430 ± 150**	**9330 ± 260**	**8410 ± 100**

Note. * A maximum likelihood method was used.

HH 514 we derive the abundances of Fe^{2+} and Ni^{2+} using T_e(high). In the case of the abundance of Ca^+, we must take into account the possible coexistence of Ca^+ and H^0, due to its low-ionization potential. Therefore, the derived Ca^+/H^+ may be an upper limit to the real abundance.

As discussed in Paper II, some [Fe II] and [Ni II] lines can be produced mostly by continuum pumping instead of collisional excitation. We make sure that the estimation of the Fe^+ abundance is not affected by fluorescence using lines of the lower a^4F–a^4P levels (λλ 7155, 8892, 9052, 9267) mostly populated by collisions (Baldwin et al. 1996). In the case of Ni^+ the fluorescence effects may be larger, considering that the levels involved in the transitions that give rise to the observed optical lines have the same multiplicity. However, if the density is high enough, collisional excitations may dominate the production of [Ni II] lines. Following the same procedure described in equation 1 from Paper II – based on the equation 8 from Bautista, Peng & Pradhan (1996) – we estimate a critical density of n_{cf} = 55 860 cm^{-3}, from which collisions dominate over fluorescence in the production of [Ni II] λ7378 line at the apparent distance of 12.61 arcsec from θ^1 Ori C. This implies that in both the jet base and the northern knot – regions with densities larger than n_{cf} – we can directly calculate the abundance of Ni^+ based on the intensity of [Ni II] λ7378 line. However, this is not possible in the nebular components, where – due to the much lower density – fluorescence should dominate.

In the UVES spectrum of the jet base of HH 514, we are able to estimate an upper limit for the abundance of Fe^{3+} based on the noise level of the continuum at ∼6743.30 Å, where we would expect the emission of [Fe IV] λ6740. We carefully estimated this upper limit, taking into account that at 6742.91 Å there may be a relatively weak telluric emission line (Hanuschik 2003). However, since Cut 3 was subtracted from Cut 1 – rescaling to the same number of pixels – to increase the contrast between the nebular emission and the HH 514 jet base spectrum, any contamination by telluric lines has been eliminated. In this case, we obtain an upper limit of $12 + \log(Fe^{3+}/H^+) < 6.99$.

To better constraint the flux of the [Fe IV] λ6740 line in the jet base component of HH 514, we search into the MEGARA deep spectra cube (see Section 2.2), analysing the spatial area that comprises the proplyd 170-337 (which includes the emission of the jet base), subtracting the nebular emission from a surrounding area to optimize the contrast of the high-velocity emission – as is indicated in Fig. 3 – as well as remove weak sky features. The resulting 1D-spectrum is shown in Fig. 4, having a higher SNR than the UVES spectra, although with lower spectral resolution. This spectrum allowed us to restrict the upper limit the Fe^{3+} abundance to $12 + \log(Fe^{3+}/H^+) < 6.79$.

In the nebular spectra, we estimate the He^+, C^{2+}, O^+, O^{2+}, and Ne^{2+} abundances using RLs following the same procedure described in Paper I. In the case of the two components of HH 514 analysed in this work, we can only determine the abundances of He^+ from RLs. In this case, the adopted He^+ abundance is an average of the resulting values based on the available He I singlet lines and triplet ones less affected by self-absorption effects (see table D14 from Paper I). The results are shown in Table 4.

To estimate the total abundances of C, N, Ne, S, and Ar, we use the ionization correction factors (ICFs) from Amayo, Delgado-Inglada & Stasińska (2021). These ICFs, based on photoionization models of giant H II regions, are consistent with the schemes shown in

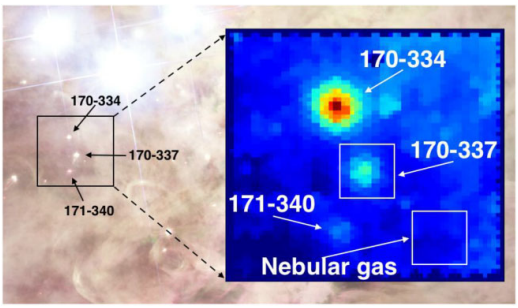

Figure 3. Location of the pointing of MEGARA-IFU observations. The field of view of MEGARA is 12.5 arcsec × 11.3 arcsec and the observations were centred in proplyd 170-337, where the high-velocity component corresponding to the jet base arise. The white rectangles comprise the extracted spaxels to analyse the emission from proplyd 170-337 and those used for the adopted nebular background. The background *HST* image of the Orion Nebula is an RGB composite (red: ACS *F*658*N*+*F*775*W* + *F*850*LP*; green: ACS *F*555*W*; blue: ACS *F*435*W*, Robberto et al. 2013).

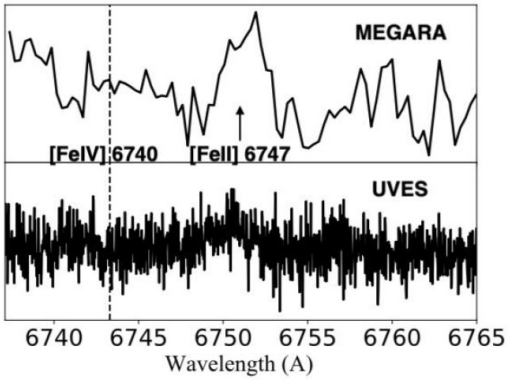

Figure 4. Comparison between MEGARA and UVES one-dimensional spectra of the jet base of HH 514 between 6737 and 6765 Å. The flux units are normalized. In both cases the nebular background was subtracted. The expected location of the [Fe IV] λ6740 emission is indicated with a dashed vertical line. The depth of the MEGARA spectrum allows us to observe [Fe II] λ6747 as well as estimate a tighter upper limit to the [Fe IV] λ6740 emission.

table 10 of Paper I. However, they additionally provide the 1σ limits of their predictions, allowing the formal propagation of uncertainties associated with the ICFs. In our nebular spectra, the calculation of the total abundances of O, Cl, and Fe did not require ICF and were estimated from the sum of their ionic abundances. In the case of Ar, Ar^+ is estimated to contribute only 1 or 2 per cent of the total Ar abundance, having a negligible impact. We estimate the total abundance of Ni as Fe/Ni = Fe^{2+}/Ni^{2+} based on their similar depletion and ionization patterns (Méndez-Delgado et al. 2021b). In the case of the He abundance in the nebular components, we use the ICF of Kunth & Sargent (1983). Since we have a reliable determination of the abundance of O^+ and O^{2+} both with CELs and RLs, we derive the total abundances of He, Ne, and C using the degree of ionization estimated from the abundances of the two ionic species of O determined from RLs.

In the case of the jet base of HH 514, we determine the total abundance of Fe as Fe/H = $Fe^+/H^+ + Fe^{2+}/H^+ + Fe^{3+}/H^+$, summing the estimated upper limit of $12 + \log(Fe^{3+}/H^+) = 6.79$. At first approximation, the total abundance of Fe should be between 7.18 ± 0.02 and 7.33 ± 0.02, where the value of $12 + \log(Fe^{3+}/H^+)$ lies between 0 and 6.79. Rodríguez & Rubin (2005) provide two ICF(Fe) schemes, where the true Fe abundance should be between the limits predicted by both schemes, based on the observed O^+/O^{2+} and Fe^{2+}/O^+ ratios. In our case, both ICFs match in the value of 7.50. Therefore, considering the observational uncertainties in the abundance of O^+, this suggest that the upper limit of the value of Fe^{3+}/H^+ should be close to its expected true value and therefore $12 + \log(Fe/H) \approx 7.33 \pm 0.02$.

It is remarkable that $\log(Ni^+/Fe^+) = -1.20 \pm 0.16$, while $\log(Ni^{2+}/Fe^{2+}) = -1.30 \pm 0.07$, which confirms the conclusions of Méndez-Delgado et al. (2021b) about the similar ionization and depletion patterns of Ni and Fe. Furthermore, this demonstrates that the effects of fluorescence on our Ni^+ abundance determination are negligible, since we would expect stronger continuum pumping effects for [Ni II] than [Fe II]. The estimated total abundances are shown in Table 5.

5 DISCUSSION

5.1 The star/disc/outflow system of 170-337/HH 514

In this section, we combine results from the literature with those of this study to provide a comprehensive view of the multiple components that make up the proplyd 170-337 and its outflows.

5.1.1 The central star and its disc

The central star of 170-337 is of spectral type M2e (Hillenbrand 1997) and its mass and age have been determined from fitting to pre-main-sequence evolutionary tracks, yielding 0.3 M_{odot} and 0.6 Myr, respectively (Boyden & Eisner 2020). It was one of the first Orion proplyds to be detected via the mm-wave dust emission of its protostellar disc (Williams, Andrews & Wilner 2005), with an estimated dust mass of $(23 \pm 5)\ M_\oplus$ (Eisner et al. 2018). The disc has also been detected in the CO 3–2 line (Boyden & Eisner 2020), yielding a disc radius of (44 ± 4) au, which is roughly half of the radius of the proplyd ionization front (90 au, Henney & Arthur 1998). Unfortunately, the gas mass cannot be determined from the CO observations because the line is optically thick.

5.1.2 Launching regions of the jet and the photoevaporation flow

No binary companion to the central star of 170-337 has been detected, either spectroscopically (Tobin et al. 2009) or visually (Duchêne et al. 2018). Therefore, it is likely that both the proplyd and HH flows originate from the same protostellar disc, but the flows must be launched from very different radii.

In the case of the proplyd, an initially neutral photoevaporation flow is driven from the disc surface by FUV radiation from the Trapezium stars (Johnstone, Hollenbach & Bally 1998). For the high radiation fields found in the Orion Nebula, the flow is in the supercritical regime (Adams et al. 2004) in which the sound speed in the FUV-heated gas (≈ 3 km s^{-1}) exceeds the local gravitational escape velocity at the disc surface. For a stellar mass of 0.3 M_{odot} (Section 5.1), this implies radii greater than about 30 au and up to the outer radius of the disc (44 au).

Table 4. Ionic abundances derived in each kinematic component in logarithmic unit with $n(H) = 12$.

Ion	Cut 1 HH 514 jet base	Cut 2 Nebula	Cut 2 HH 514 knot	Cut 3 Nebula
		CELs		
N^+	$6.88^{+0.28}_{-0.13}$	6.89 ± 0.02	$6.23^{+0.27}_{-0.14}$	6.84 ± 0.03
O^+	$7.93^{+0.51}_{-0.18}$	7.81 ± 0.03	$7.40^{+0.49}_{-0.19}$	7.69 ± 0.05
O^{2+}	$8.30^{+0.05}_{-0.04}$	8.37 ± 0.03	$8.45^{+0.05}_{-0.04}$	8.38 ± 0.02
Ne^{2+}	$7.56^{+0.06}_{-0.05}$	$7.84^{+0.04}_{-0.03}$	$7.79^{+0.06}_{-0.05}$	$7.82^{+0.03}_{-0.02}$
S^+	$6.11^{+0.23}_{-0.12}$	5.50 ± 0.04	$5.34^{+0.26}_{-0.14}$	5.45 ± 0.05
S^{2+}	$7.39^{+0.07}_{-0.06}$	$6.86^{+0.05}_{-0.04}$	$7.35^{+0.09}_{-0.07}$	$6.84^{+0.05}_{-0.04}$
Cl^+	–	3.63 ± 0.04	–	3.60 ± 0.04
Cl^{2+}	–	$4.98^{+0.06}_{-0.05}$	–	$4.99^{+0.06}_{-0.05}$
Cl^{3+}	–	3.79 ± 0.03	–	3.92 ± 0.03
Ar^{2+}	6.29 ± 0.04	6.31 ± 0.03	6.19 ± 0.04	6.31 ± 0.02
Ar^{3+}	–	$5.09^{+0.04}_{-0.03}$	–	$5.15^{+0.03}_{-0.02}$
Ca^+	$3.71^{+0.20}_{-0.12}$	–	–	–
Fe^+	6.14 ± 0.05	4.39 ± 0.05	–	4.32 ± 0.02
Fe^{2+}	7.14 ± 0.02	5.28 ± 0.01	6.83 ± 0.04	5.17 ± 0.02
Fe^{3+}	< 6.79	$5.62^{+0.10}_{-0.08}$	–	5.78 ± 0.12
Ni^+	$4.94^{+0.15}_{-0.09}$	–	–	–
Ni^{2+}	$5.84^{+0.07}_{-0.06}$	4.32 ± 0.03	$5.62^{+0.08}_{-0.07}$	4.25 ± 0.04
		RLs		
He^+	10.95 ± 0.04	10.92 ± 0.02	10.96 ± 0.02	10.92 ± 0.02
C^{2+}	–	8.37 ± 0.01	–	8.37 ± 0.01
O^+	–	$8.17^{+0.04}_{-0.03}$	–	8.19 ± 0.05
O^{2+}	–	8.61 ± 0.05	–	8.63 ± 0.05
Ne^{2+}	–	8.04 ± 0.06	–	8.10 ± 0.08

Table 5. Total abundances. The units are logarithmic with $n(H) = 12$.

Ion	Cut 1 HH 514 jet base	Cut 2 Nebula	Cut 2 HH 514 knot	Cut 3 Nebula
		CELs		
N	$7.43^{+0.59}_{-0.32}$	7.64 ± 0.16	$7.36^{+0.58}_{-0.31}$	$7.69^{+0.18}_{-0.16}$
O	8.45 ± 0.16	8.48 ± 0.02	8.49 ± 0.06	8.46 ± 0.02
Ne	$7.75^{+0.19}_{-0.15}$	$7.97^{+0.11}_{-0.10}$	$7.84^{+0.11}_{-0.09}$	$7.92^{+0.09}_{-0.08}$
S	$7.43^{+0.16}_{-0.12}$	$6.92^{+0.07}_{-0.06}$	$7.49^{+0.17}_{-0.14}$	$6.91^{+0.07}_{-0.06}$
Cl	–	5.03 ± 0.05	–	5.04 ± 0.04
Ar	$6.32^{+0.12}_{-0.10}$	$6.34^{+0.06}_{-0.05}$	$6.29^{+0.14}_{-0.12}$	6.34 ± 0.04
Fe	7.33 ± 0.02	5.80 ± 0.07	–	5.89 ± 0.09
Ni	6.03 ± 0.08	4.83 ± 0.08	–	4.96 ± 0.10
		RLs		
He	10.95 ± 0.04	10.95 ± 0.02	10.96 ± 0.02	10.95 ± 0.02
C	–	$8.45^{+0.07}_{-0.06}$	–	$8.45^{+0.07}_{-0.06}$
O	–	8.74 ± 0.04	–	8.76 ± 0.04
Ne	–	$8.17^{+0.13}_{-0.11}$	–	$8.26^{+0.18}_{-0.14}$

In the case of the jet, the much higher flow velocity ($> 100\,km\,s^{-1}$) implies a launch region that is deeper in the gravitational well and closer to the star. Comparison of magnetocentrifugal jet models with observations of the base of HH 212 (Lee et al. 2017) imply that jet launching occurs at disc radii < 0.1 au. Magnetocentrifugal winds may also be launched from intermediate radii of 1 to 10 au but these will be at lower velocities (e.g. Hasegawa et al. 2022).

5.1.3 Kinematics of the star within the Orion Nebula Cluster

The line-of-sight radial velocity of the star can be determined from the systemic velocity of the CO emission (Boyden & Eisner 2020), yielding $(23.8 \pm 0.1)\,km\,s^{-1}$ after converting to the heliocentric frame. This is $-3.7\,km\,s^{-1}$ with respect to the mean velocity of stars in the core of Orion ($27.5\,km\,s^{-1}$, Theissen et al. 2022). The star's tangential velocity in the frame of the cluster can be derived from

proper motion measurements (Kim et al. 2019) as (7.8 ± 1.1) km s^{-1} along PA $= (48 \pm 8)^\circ$. The total space velocity of 170-337 is therefore 8.6 km s^{-1}, which is more than double the 3D velocity dispersion of the cluster (3.7 km s^{-1}; Theissen et al. 2022), making it a candidate for an escaping star. It is included in the escape group ESC1 of Kim et al. (2019), but its total proper motion of 4 mas yr^{-1} is not quite high enough to meet the runaway criterion used in McBride & Kounkel (2019) or Platais et al. (2020).

5.1.4 *Kinematics of the jet*

Proper motion measurements of the jet knot (O'Dell & Henney 2008), after compensating for the proper motion of the star and rescaling to our adopted distance of 410 pc, yield a plane-of-sky tangential velocity of 41 ± 6 km s^{-1}, with a position angle that is consistent with the displacement of the knot from 177-341 (almost due north). Line-of-sight radial velocities can be determined from our spectroscopic measurements (see Table A1) and are found to be approximately the same for the jet base and the knot, with no variation between high- and low-ionization lines, yielding a heliocentric velocity of $(+150 \pm 5)$ km s^{-1}. Subtracting the stellar systemic velocity of 24 km s^{-1} gives a jet propagation velocity of (132 ± 10) km s^{-1} at an inclination of $(-72 \pm 3)^\circ$ to the plane of the sky. Note that the brighter northern side of the flow is inclined away from the observer.

Assuming an ionized sound speed of 11 km s^{-1}, then the isothermal Mach number of the jet is 12 and the Mach angle is 4.8°, which should correspond to the half-opening angle of the ionized portion of the jet after it emerges from the proplyd ionization front. This is consistent with the observed width of the base of the jet in *HST* images (e.g. Fig. 1).

5.1.5 *Mass-loss rates of photoevaporation flow and jet*

The mass-loss rate from the proplyd photoevaporation flow is estimated from model fits to kinematic line profiles (Henney & O'Dell 1999) to be $\approx 8 \times 10^{-7}$ M$_{\rm odot}$ yr^{-1}, with an uncertainty of roughly a factor of two. Bally et al. (2006) include HH 514 in a survey of irradiated jets in the Orion Nebula, calculating a jet mass-loss rate of 6×10^{-7} M$_{\rm odot}$ yr^{-1}, which would make it one of the most massive jets in their survey. However, this estimate is based on analysis of the jet knot and therefore corresponds to a maximum value of the mass-loss, presumably during an outburst phase. Assuming that the current conditions at the jet base are more typical, then a time-averaged jet mass-loss can be estimated by scaling the result from the proplyd photoevaporation flow. Since the densities at the base of the jet and in the proplyd flow are similar (Section 3 and further details in 5.3 below), the mass-loss rate scales as the flow velocity times its solid angle. Assuming a jet half-opening angle of 5° (see previous section) implies a mean jet mass-loss rate of 0.05 times that of the proplyd, yielding 4×10^{-8} M$_{\rm odot}$ yr^{-1} albeit with a large uncertainty. This is similar to but slightly larger than the jet mass-loss rate derived for the closer-in proplyd LV 2 (167-317, Henney et al. 2002).

5.1.6 *Discrepancy between optical jet orientation and CO kinematics*

Assuming that the jet is perpendicular to the disc, then the results of Section 5.1.4 imply that the disc must be close to face-on. In the disc literature, a different inclination convention is used in which the $i_{\rm d}$ is the angle between the rotation axis and the line of sight, meaning that our jet results imply $i_{\rm d} = 18^\circ$ for 170-337. Studies of the mm continuum and line emission (Eisner et al. 2018; Boyden & Eisner 2020) find that the disc has a slight elongation in the north–south direction, which is interpreted as $i_{\rm d} \approx 40^\circ$, but if the jet results are taken at face value then this elongation must be an intrinsic asymmetry rather than an inclination effect. Boyden & Eisner (2020) derive a very low stellar mass (< 0.1 M$_{\rm odot}$) from kinematic disc modelling. However, this value is highly dependent on the disc inclination ($M \sim (\sin i_{\rm d})^{-2}$), so that rescaling to $i_{\rm d} = 18^\circ$ would give 0.3 M$_{\rm odot}$, which is fully compatible with the mass derived from stellar evolution tracks (see Section 5.1.1 above).

A more serious conflict with the CO kinematics concerns the sign and orientation of the observed velocity gradient, which runs north–south with blueshifted CO on the north side (figs 4 and 11 of Boyden & Eisner 2020). This is inconsistent with an origin either in a rotating disc or in an outflow aligned with the optical jet. In the first case, the disc rotation axis would have to be perpendicular to the jet axis. In the second case, one would expect redshifted instead of blueshifted CO on the north side. Two possible explanations for this discrepancy suggest themselves: (1) the source, despite lack of evidence, may in fact be binary, with the optical jet arising from a different star/disc from that seen in CO; (2) the CO emission might arise in neither the disc nor the outflow, but instead in infalling material from the remnants of the surrounding protostellar envelope. Both possibilities seem far-fetched, but in the second case there is a precedent in observations of larger Orion proplyds, where dense neutral filaments are seen within the shadow of the ionization front. Examples include 182-413 (Vicente et al. 2013) and 244-440 (Bally et al. 2000), which are likely to represent transitional stages between Evaporating Gaseous Globules (Hester et al. 1996) and pure photoevaporating discs. Although 170-337 is much smaller, it too may contain remnant envelope material that is still accreting on to the central source. The same phenomenon may explain asymmetrical dust extinction features that are seen in the tails of many proplyds, such as 171-340 (see Fig. 1).

5.2 On the anomalous [S III] emission in HH 514

There are two results for HH 514 included in Tables 3 and 5 that we want to highlight: both components show $T_{\rm e}$ ([S III]) $< T_{\rm e}$ ([O III]), and their S/H ratio is around 0.5 dex higher than the value found in the nebular gas. The abnormally large S abundance seems to rely mainly on the S^{2+} one, which represents 91 per cent of the S/H ratio.

The observed trend of $T_{\rm e}$ ([S III]) goes in the opposite direction to the usual temperature stratification observed in H II regions and simple photoionization models fail to reproduce the observed results (Binette et al. 2012). On the other hand, the overabundance of S is much too large to be produced by errors in the assumed ICF (the abundance of S^{2+} alone is higher than the total S abundance of the Orion Nebula).

In order to be certain that the enhanced S abundance is real, it is necessary to rule out possible systematic errors in the analysis. To that end, in the following subsections we explore some scenarios that could explain the observed results.

5.2.1 *Errors in atomic data for analysing [S III] lines?*

After analysing different sets of transition probabilities and collision strengths of different ions, Juan de Dios & Rodríguez (2017) conclude that the derived ionic abundances can have uncertainties of around 0.1–0.2 dex introduced by the atomic data when density

is lower than 10^4 cm^{-3}, but they can reach values up to 0.8 dex for higher densities. Since both components of HH 514 have extremely high densities, we expect the uncertainties due to atomic data may be amplified in these objects. Given such expectations, we decided to explore the effect of the atomic data used on the S^{2+} abundance.

Instead of following the methodology of Juan de Dios & Rodríguez (2017) of analysing all possible combinations of transition probabilities and collision strengths available, we first focus our attention on transition probabilities, discarding those that give clearly wrong results. If we do not do this in the first place, we may include spurious values in the resulting abundance distribution, which would increase the uncertainties associated with the atomic data. Once this first step is done, we check the available collision strengths, analysing their impact on T_e ([S III]) and the S^{2+} abundance.

We use the observed intensity of [S III] λλ9531, 9069, 8829 lines, arising from the common $^1D_2$ upper level and the [S III] λλ3722, 6312 lines, emitted from the same $^1S_0$ level. Their intensity ratios depend exclusively on the transition probabilities. In Table A2, we compare the aforementioned [S III] line intensity ratios observed in several positions and HH objects of the Orion Nebula and other Galactic H II regions for which we have deep high-spectral resolution spectra with the line ratios predicted by the different atomic data sets.

As it is well known, infrared [S III] λλ9531, 9069 lines can be affected by telluric absorption bands (Noll et al. 2012). In Méndez-Delgado et al. (2021a, b), we mentioned that [S III] λ9069 was affected by telluric absorptions, while λ9531 remained unaffected in the background emission of the Orion Nebula, while in the HHs both lines avoided the absorption bands. Since in this work we are interested in analysing the [S III] λ9531/λ9069 line ratio, we correct the spectra from telluric absorptions around the aforementioned lines. We use the observations of the star GD71 from each data set, normalizing them with the standard tabulated flux. Then, the science spectra were divided by the resulting telluric transmission function around [S III] λλ9531, 9069. The corrected intensities are shown in Table A3.

[S III] λ3722 is usually blended with the H14 Hydrogen Balmer line. We cannot simply subtract the emission of H14 using its theoretical line ratio with respect to other isolated observed H I lines, since it is well known that H I lines from high quantum numbers *n* suffer deviations from case 'B' (Mesa-Delgado et al. 2009; Rodríguez 2020). Even using contiguous lines such as H13 or H15 may introduce important deviations (see fig. A2 of Rodríguez 2020). Therefore, we consider that it is better to use only the observations where the spectral resolution of the data allows the correct Gaussian deblending of the lines, where the resulting FWHM of [S III] λ3722 is consistent with that of the isolated [S III] λ6312 line.

The transition probabilities tested are those available in version 1.1.13 of PyNeb and those from the CHIANTI data base V10 (Del Zanna et al. 2021), named by the following acronyms: LL93-HSC95-MZ82b-KS86 (Mendoza & Zeippen 1982; Kaufman & Sugar 1986; LaJohn & Luke 1993; Heise, Smith & Calamai 1995), MZ82b-HSC95-LL9 (Mendoza & Zeippen 1982; LaJohn & Luke 1993; Heise et al. 1995), FFTI06 (Froese Fischer, Tachiev & Irimia 2006), TZS19 (Tayal, Zatsarinny & Sossah 2019), and CHIANTI (Tayal 1997; Froese Fischer et al. 2006; Hudson, Ramsbottom & Scott 2012). These data encompass all those studied by Juan de Dios & Rodríguez (2017) adding those from TZS19 and CHIANTI. The FFTI06 data file was named as PKW09 in previous versions of PyNeb, alluding to Podobedova, Kelleher & Wiese (2009), who cited Froese Fischer et al. (2006).

As shown in Table A2, the LL93-HSC95-MZ82b-KS86 set of transition probabilities are clearly inconsistent with observations when determining line ratios involving the [S III] λ9531 line from the $^1D_2$-$^3P_2$ transition, for which atomic data are taken from Kaufman & Sugar (1986). This discrepancy forces us to discard the LL93-HSC95-MZ82b-KS86 data set. With respect to the other data sets, the ones most consistent with the observed line ratios are those by FFTI06 and CHIANTI. However, as is shown in Fig. A3, the results obtained with the remaining data sets are not very different for the most important optical transitions ([S III] λλ3722, 6312, 8829, 9069, 9531). In fact, taking the mean and standard deviation of the A-values given by the data sets included in Fig. A3 excluding those from LL93-HSC95-MZ82b-KS86, we obtain $A_{3722} = (7.06 \pm 0.53) \times 10^{-01}$, $A_{6312} = 2.20 \pm 0.08$, $A_{8829} = (6.42 \pm 1.49) \times 10^{-06}$, $A_{9069} = (2.00 \pm 0.13) \times 10^{-02}$, and $A_{9531} = (5.26 \pm 0.35) \times 10^{-02}$. Of these, the one with the largest deviation is A_{8829}, about 23 per cent. In any case, this transition probability has very little impact in the determination of T_e ([S III]) and the S^{2+} abundance if a line different than [S III] λ8829 is used, which is always the case. Moreover, if we discard the data set of TZS19, this deviation is reduced to 4 per cent. Once the LL93-HSC95-MZ82b-KS86 data set is removed, the uncertainties associated with the transition probabilities of the optical lines seem to be around ∼5 per cent considering the consistency between the predictions and the observed line intensity ratios included in Table A2. The previous results indicate that the available sets of transition probabilities for transitions giving rise to [S III] lines show a high degree of consistency. From now on, we adopt the transition probabilities of FFTI06 in our calculations. This was precisely the data set we used in Paper I and Paper II.

Analogously to the previous procedure with transition probabilities, we also check the data sets of collision strengths available in PyNeb: GMZ95 (Galavis, Mendoza & Zeippen 1995), TG99 (Tayal & Gupta 1999), HRS12 (Hudson, Ramsbottom & Scott 2012), GRHK14 (Grieve et al. 2014), and TZS19 (Tayal et al. 2019). These includes all the sets analysed by Juan de Dios & Rodríguez (2017) in addition to TZS19. The CHIANTI data base V10 adopts the same collision strengths as HRS12 by default, so does not need to be considered separately. Comparing the results for the different data sets shown in Fig. A4, we obtain the following mean collision strengths along with their associated dispersion at 10 000 K for the most important [S III] lines: $\Omega_{3722} = (3.65 \pm 0.31) \times 10^{-1}$, $\Omega_{6312} = 1.38 \pm 0.04$, $\Omega_{8829} = (7.64 \pm 0.63) \times 10^{-1}$, $\Omega_{9069} = 2.28 \pm 0.20$, and $\Omega_{9531} = 4.00 \pm 0.26$. The typical dispersion is about ∼8 per cent for most lines, except for [S III] λ6312, where the dispersion is smaller, ∼3 per cent.

One way in which errors in the collision strengths could explain the apparent low T_e ([S III]) and the high S^{2+} abundance in the HH objects is by changing the $\frac{\Omega_{Auroral}}{\Omega_{Nebular}} = \frac{\Omega(3722)+\Omega(6312)}{\Omega(8829)+\Omega(9069)+\Omega(9531)}$ ratio. When $\frac{\Omega_{Auroral}}{\Omega_{Nebular}}$ decreases, T_e ([S III]) increases, for a fixed observed [S III] $\frac{I(\lambda3722)+I(\lambda6312)}{I(\lambda8829)+I(\lambda9069)+I(\lambda9531)}$ ratio. Increasing the value of the denominator in the ratio of collision strengths also decreases the derived abundance of S^{2+}, which is usually determined from the intensity of [S III] λλ9531, 9069 lines. However, modifications in the values of Ω_{8829}, Ω_{9069}, and Ω_{9531} within a dispersion of ∼8 per cent are not enough to account for the discrepant values of T_e ([S III]) and the S^{2+} abundance.

We will try to solve the aforementioned discrepancies exploring the assumption that the collision strengths of the transitions that give rise to [S III] lines are wrong, with Ω_{9531}, Ω_{9069}, and Ω_{8829} being underestimated beyond the dispersion of ∼8 per cent. We will increase the values of Ω_{9531}, Ω_{9069}, and Ω_{8829}, until getting

T_e ([O III]) = T_e ([S III]) in the jet base of HH 514. This may be considered a lower limit since it is expected that T_e ([S III]) is between T_e ([O III]) and T_e ([N II]) (Berg et al. 2020), the latter being generally higher. To achieve this, the collision strengths should be increased about 40 per cent, as we know, five times larger than the dispersion found comparing the available atomic data. In Table A4, we show the T_e ([S III]) and S^{2+} abundances we obtain for each object using the transition probabilities of FFTI06, the different sets of collision strengths considered, and the corresponding value of n_e. In the last column, we include the results obtained increasing by a 40 per cent the Ω_{9531}, Ω_{9069}, and Ω_{8829} values of GRHK14.

Now we discuss what other consequences the increase of 40 per cent in the collision strengths may have. Using these Ω modified values, T_e ([S III]) matches T_e ([O III]) in both components of HH 514,[3] while the modification implies T_e ([S III]) $\approx$ T_e ([N II]) for the Orion Nebula. The latter would imply that the S^{2+} and N^+ ions coexist almost exclusively in the zone of low degree of ionization. However, the large increment we have assumed in the collision strengths are unable to give a *normal*[4] S abundance in the high-velocity components. If we adopt $12 + \log(S/H) = 7.07 \pm 0.03$ from Méndez-Delgado et al. (2021b) as reference, we still have an overestimation of 0.23 dex in the jet base. A similar difference is obtained in the knot. Moreover, this experiment produces a $\log(S/O) = -1.81 \pm 0.06$ for the nebular component, which is inconsistent with the solar value of $\log(S/O) = -1.58 \pm 0.08$ (Lodders 2019). Since both S and O are α-elements, a constant abundance ratio is expected from their common nucleosynthesis. Therefore, following a *reductio ad absurdum* process, we can say that large errors in the collision strengths Ω_{9531}, Ω_{9069}, and Ω_{8829} do not solve the observed discrepancies in T_e ([S III]) and the total S abundance in HH 514.

5.2.2 *Is the [S III] emission affected by the shock?*

HH objects are produced by the interaction of high-velocity flows with the surrounding medium or by internal shocks within the flow. In both cases, gas is initially heated and compressed in a shock front, followed by a non-equilibrium cooling zone in which the gas returns to the photoionization equilibrium temperature while undergoing further compression. The cooling zone may contribute to observed CEL spectrum, but the greatest effect is on highly ionized lines that are not typically seen in H II regions.

In both the jet and knot of HH 514 the low observed line widths of about 20 km s^{-1} (see Table A1) imply that only low-velocity internal shocks are present. For moderate ionization lines such as [S III], the relative contribution is therefore expected to be small (Méndez-Delgado et al. 2021a). Moreover, the emission from the cooling zone, if any, would affect T_e ([S III]) in the opposite direction, increasing the observed [S III] $I(\lambda6312)/I(\lambda9531)$ line intensity ratio that would produce higher temperatures.

5.2.3 *Telluric absorption bands or sky emission?*

There are no other lines arising from sky emission or the Orion Nebula that could be blended with [S III] $\lambda\lambda$6312, 9069, 9531 ($\lambda\lambda$6315.31, 9073.60, 9535.87) lines at the spectral resolution of our spectra. As commented in Section 5.2.1, we correct for telluric absorptions that could affect the intensity of [S III] $\lambda\lambda$9531, 9069 lines in our spectra. Moreover, those [S III] lines fall outside the absorption bands in the spectra of HH 514. In any case, in the presence of absorption bands, their effect on [S III] $\lambda\lambda$9531, 9069 lines would fictitiously increase T_e ([S III]) and decrease the S^{2+} abundance, which is the opposite of what is found.

5.2.4 *Errors in the reddening correction?*

The [S III] $I(\lambda6312)/I(\lambda9531)$ line intensity ratio is highly dependent on the reddening correction. However, if we estimate what reddening coefficient is necessary in order to produce T_e ([S III]) $\geq$ T_e ([O III]), we get $c(H\beta) \geq 1.22$. This is at least 44 per cent higher than the estimated value based on the observed Balmer and Paschen H I lines, which is simply not possible considering the quality of the flux calibration of our data. There is also no evidence of such an increase in $c(H\beta)$ in the MUSE data (Weilbacher et al. 2015), which is consistent with our results. In any case, the derivation of a largely incorrect $c(H\beta)$ value would produce many different and noticeable inconsistencies in our results that are obviously not observed.

5.2.5 *Is the density overestimated?*

Let us suppose that the representative density of the [S III] zone is overestimated and its true value is more similar to that of the Orion Nebula. As can be seen in panel (a) of Fig. A1, this would imply that in the jet base, T_e ([S III]) $\approx$ 10200 K if $n_e \leq 10\,000$ cm^{-3}. However, even assuming that value of T_e ([S III]), the S^{2+} abundance would be still overestimated. A T_e ([S III]) $\approx$ 13000 K would be necessary to obtain a *normal* S^{2+} abundance, which cannot be achieved with any density value.

5.3 Comparison between HH 514 and its associated proplyd

In the previous section, we established that none of the potential systematic biases can plausibly cause the observed [S III] emission from the HH 514 jet, leaving an enhanced sulfur abundance as the most likely explanation. Given that the ionized base of the jet emerges from the ionization front of the proplyd 170-337 (Bally et al. 2000), it is important to compare the abundances in the two components.

In our UVES observations, 170-337 is within Cut 1. We interpolate the nebular emission above and below the zone covered by 170-337 along the slit, so that we can separate the proplyd emission from that of the Orion Nebula. The line intensities used are shown in Table A5. The complete study of 170-337 will be analysed in a future paper (Méndez-Delgado et al., in preparation). By analysing the spectrum, we obtain $n_e \approx 10^{5.85 \pm 0.20}$ cm^{-3} from the n_e([S II]) λ4069/λ4076 diagnostic (no [Fe III] emission lines are detected in 170-337). We use those [S II] lines – that originate from the upper levels ^{2}P – because of their very high critical densities, above the n_e value obtained for the proplyd. This density is close to the value of 1.3×10^6 cm^{-3} found by Henney & O'Dell (1999) for the same proplyd from modelling the Hα surface brightness profile. In Fig. 5, we show the 2D density map obtained with MEGARA from the [S II] λ6731/λ6716 ratio. Lines that come from the intermediate ^{2}D levels of S^+ and have a considerable lower critical density. In Fig. 5, we can see that 170-337 shows a rather low contrast with respect to the surroundings, because the emission of [S II] $\lambda\lambda$6731, 6716 lines is dominated by the background much lower density nebular emission. High-density clumps as the proplyd 170-337 can contribute appreciably to the

[3] This is obviously expected for the jet base, since the increase in the collision strengths was chosen to obtain T_e ([S III]) = T_e ([O III]). The result for the northern knot is independent.

[4] A value consistent with that of the Orion Nebula.

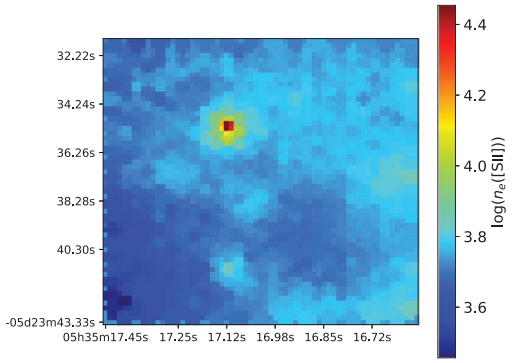

Figure 5. Density map obtained with the intensity ratio [S II] λ6731/λ6716 using the MEGARA-IFU observations (see Fig. 3). This map reveals in a partial way only, the density structures present in the field of view (see the text).

emission of lines arising from the higher levels – as the T_e-sensitive auroral lines – which are less affected by collisional de-excitation. The use of incorrect density diagnostics can lead to wrong estimates of physical conditions and chemical abundances (Méndez-Delgado et al. 2021b).

By adopting the correct density for the ionized layers of 170-337, we obtain T_e ([O III]) ≈ T_e ([S III]) ≈ T_e ([N II]) ≈ 8000 ± 1000 K, in total consistency with the expected values for the gas in photoionization equilibrium within the radiation field of the Orion Trapezium. Although the uncertainties associated with the three temperature diagnostics are high, due to the extremely large density of the proplyd, the convergence of the diagnostics ensures the reliability of the derived physical conditions, yielding the adopted temperature $T_e = (8010 \pm 60)$ K. With the aforementioned physical conditions we obtain 12 + log(S/H) ≈ 7.10 ± 0.04 which is consistent with the value derived by Méndez-Delgado et al. (2021b) for HH 204, representative of the chemical composition of the Orion Nebula. Therefore, the photoionized material of the outer layers of proplyd 170-337 does not show an overabundance of S.

5.4 Implications of the elevated S abundance in HH 514

From Section 5.2, we have ruled out several scenarios that may produce an unrealistic overabundance of S and a low T_e ([S III]). Therefore, it is possible to affirm that the overabundance of S/H in HH 514 is real. Furthermore, neither the surrounding nebula nor the proplyd photoevaporation flow show the same overabundance. The other significant difference between the gas phase abundances in the two flows is the approximately solar Fe and Ni abundance in HH 514, compared with severely depleted abundances in the proplyd (similar to the nebula). This is most simply explained by dust destruction in the HH object, which liberates Fe and Ni to the gas phase, while it remains locked within grains in the case of the proplyd. It is therefore reasonable to suppose that the difference in S abundances might also be related to processes involving dust grains.

It is common to observe relatively high gas-phase Fe and Ni abundances in HH objects, both in photoionized (Blagrave, Martin & Baldwin 2006; Mesa-Delgado et al. 2009; Méndez-Delgado et al. 2021a, b) and neutral (Nisini et al. 2002; Giannini et al. 2015) environments. Depletions with respect to solar abundance of zero to 0.3 dex are typically found, as compared to a depletion of more than 1 dex in the general ISM and H II regions (Rodríguez 2002; Jenkins 2009). This is usually interpreted as evidence for dust reprocessing in the HH shocks themselves, although there is also evidence that some reprocessing must have occurred in the jet launch region (Böhm & Matt 2001; Podio et al. 2009). However, this study is the first to find a supersolar sulphur abundance in an HH object.

It is well known that planetary formation process is capable of building up large grains in proplyds (Beckwith, Henning & Nakagawa 2000). Recently, Kama et al. (2019) have suggested the formation of large sulfide mineral reservoirs during the accretion process from the proplyd to a central star. The presence of a giant planet immersed in the disc can cause a pressure bump that can accumulate the largest dust particles (Pinilla, Benisty & Birnstiel 2012; Birnstiel, Fang & Johansen 2016), among which would be the sulfides. If some mechanism allowed these sulfide grains to preferentially enter the jet flow from the inner disc, and that the grains could subsequently be destroyed, then this could explain the high sulphur abundances that we observe in HH 514. The exact mechanism by which this might be accomplished is unclear however. Simulations of disc winds that include the coupling of different-sized grains to the flow have recently been developed (Rodenkirch & Dullemond 2022), but these do not yet include the effects of external photoevaporation, nor do they include the wind from the innermost disc that gives rise to the fast jet.

5.5 The total abundances of Fe and Ni

In the jet base component of HH 514 we are able to derive the abundances of Ni^+, Ni^{2+}, Fe^+, and Fe^{2+}. As mentioned in Section 4, despite only having an upper limit to the abundance of Fe^{3+}, the ICF schemes of Rodríguez & Rubin (2005) indicate that the total abundance of Fe/H should be close to the sum of the abundances of Fe^+ and Fe^{2+} and the upper limit of Fe^{3+}. Both the total abundances of Ni and Fe in the jet base are a factor 34 higher than in the main emission from the Orion Nebula. Moreover, these values are very close to the reference Solar values from Lodders (2019). However, this does not necessarily mean that all the dust grains containing Fe and Ni have been destroyed. This is also supported by the evidence of thermal dust IR emission from HH 514 (Smith et al. 2005), which suggests the survival of some amount of dust in the object. In connection with Section 5.4, HH 514 is able to destroy the dust reservoirs of S in a planet-forming disc. However, it can also destroy dust grains of zones of the Orion Nebula outside the S reservoirs, with normal S abundance. To estimate the fraction of Fe released from each kind of dust grains, we can assume that the S excess is produced by the destruction of FeS compounds, as suggested by Kama et al. (2019). In addition, NiS compounds should be present as well. For each atom of S released, one atom of Fe or Ni should be released too. Since the S excess will be equal to the difference between the S abundance in HH 514 and the representative value of the Orion Nebula, then

$$\frac{n(\mathrm{S})_{\mathrm{excess}}}{n(\mathrm{H})} \approx \frac{n(\mathrm{Fe{+}Ni})_{\mathrm{excess}}}{n(\mathrm{H})} \approx \frac{1.05 \times n(\mathrm{Fe})_{\mathrm{excess}}}{n(\mathrm{H})} = 1.52 \times 10^{-5},$$

adopting 12 + log(S/H) = 7.07 ± 0.03 (Méndez-Delgado et al. 2021b) for the Orion Nebula. Considering the Fe and Ni abundances obtained in the nebular components, this would imply that of the total abundances of Fe/H and Ni/H in the jet base, ∼67 per cent would come from dust destruction of S reservoirs, ∼30 per cent from the destruction of dust grains of normal S abundance, and ∼3 per cent from Fe and Ni that were already in the gaseous phase.

6 CONCLUSIONS

We analyse the physical conditions and chemical abundances of the photoionized Herbig–Haro object HH 514 and the Orion Nebula using high-spectral resolution spectra taken with UVES at VLT, high-spatial resolution imaging from the *HST*, and deep MEGARA-IFU spectra. Due to the Doppler shift between the emission of the Orion Nebula and HH 514, we independently study the emission of two high-velocity components: the jet base and a knot. These HHs are extremely dense: n_e(HH 514 jetbase) $= 10^{5.37}$ cm^{-3} and n_e(HH 514 knot) $= 10^{4.87}$ cm^{-3}. However, they present temperatures consistent with photoionization equilibrium in the Orion Nebula, T_e ([O III]) $\sim$ 9000 K.

The total abundances of the high-velocity components are fully consistent with the ones derived in the Orion Nebula with the exception of S, Fe, and Ni. In the case of S, the S^{2+} ion comprises 91 per cent of the total abundance. Furthermore, we found that T_e ([S III]) $< T_e$ ([O III]), which is difficult to explain under normal photoionization conditions (Binette et al. 2012). We rule out the possibility that the S overabundance may be a spurious consequence of errors in the atomic data or in the observations. We speculate that it may be due to the preferential incorporation of S-rich dust into the high-velocity jet from the inner disc, which is then returned to the gas phase either in the jet launching region or via internal shocks in the jet. The origin of S-rich dust reservoirs maybe related to the process that Kama et al. (2019) propose to occur in proplyds, which consists of the accumulation of large sulfide dust grains around giant planets during accretion from the disc to the central star.

In the jet base we obtain log(Fe/H)+12 $=$ 7.33 $\pm$ 0.02 and log(Ni/H) + 12 $=$ 6.03 $\pm$ 0.08. These abundances are a factor 34 higher than those derived in the Orion Nebula and are very close to the Solar values (Lodders 2019). We estimate that $\sim$67 per cent of the total Fe/H and Ni/H abundances in the jet base have origin in the destruction of sulfide reservoirs, whereas $\sim$30 per cent would come from the destruction of dust grains with a poorer S content, having just $\sim$3 per cent from Fe and Ni previously present in the gaseous phase. HH 514 destroys dust grains of the Orion Nebula gas more efficiently than other HHs studied in the literature such as HH 202 S, HH 529 II, HH 529 III, and HH 204 (Mesa-Delgado et al. 2009; Méndez-Delgado et al. 2021a, b).

Knowing the relationship between the efficiency of dust destruction and the propagation velocity of the HH object is an important issue. In our series of papers about the chemical content of HH objects, we find that gas-phase Fe/H and Ni/H abundances seem to be correlated with the propagation velocity (being HH 529 the slowest and HH 514 the fastest), which is consistent with studies of HH objects propagating in neutral environments (see fig. 14 from Hartigan et al. 2020). However, it is still not clear if this relation is simply linear or shows a more complex behaviour or even if the dust destruction efficiency reaches a maximum at a given velocity. Some parameters such as the degree of ionization may also play a role. The amount of data is still too limited for addressing this question and analyses of further HH objects are still needed.

Comparison of the optical jet kinematics with the kinematics of a CO molecular emission line close to the central star yields contradictory results. If the molecular line traces the disc rotation, then the jet is perpendicular to the rotation axis, but if the molecular line traces outflow, then the outflow is perpendicular to the jet. We suggest instead that the molecular line may trace inflowing material that is the remnant of the cloud core from which the star formed.

ACKNOWLEDGEMENTS

We are grateful to the anonymous referee for his/her helpful comments. This work is based on observations collected at the European Southern Observatory, Chile, proposal number ESO 092.C-0323(A), and on observations made with the Gran Telescopio Canarias (GTC), installed in the Spanish Observatorio del Roque de los Muchachos of the Instituto de Astrofísica de Canarias, in the island of La Palma. The authors appreciate the friendly communication of Dr. Richard Booth on the planet formation processes. We acknowledge support from the Agencia Estatal de Investigación del Ministerio de Ciencia e Innovación (AEI-MCINN) under grant *Espectroscopía de campo integral de regiones H* II*locales. Modelos para el estudio de regiones H* II*extragalácticas* with reference 10.13039/501100011033. JEM-D thanks the support of the Instituto de Astrofísica de Canarias under the Astrophysicist Resident Program and acknowledges support from the Mexican CONACyT (grant CVU 602402). JG-R acknowledges financial support from the Spanish Ministry of Science and Innovation (MICINN) through the Spanish State Research Agency, under Severo Ochoa Centres of Excellence Programme 2020-2023 (CEX2019-000920-S), and from the Canarian Agency for Research, Innovation and Information Society (ACIISI), of the Canary Islands Government, and the European Regional Development Fund (ERDF), under grant with reference ProID2021010074. The authors acknowledge support under grant P/308614 financed by funds transferred from the Spanish Ministry of Science, Innovation and Universities, charged to the General State Budgets and with funds transferred from the General Budgets of the Autonomous Community of the Canary Islands by the MCIU. The paper has been edited using the Overleaf facility.

DATA AVAILABILITY

The lines measured in the spectra are entirely available in the supplementary material of this article. Table A1 is an example of its content. The rest of information is found in tables or references of this paper.

REFERENCES

Adams F. C., Hollenbach D., Laughlin G., Gorti U., 2004, ApJ, 611, 360
Amayo A., Delgado-Inglada G., Stasińska G., 2021, MNRAS, 505, 2361
Baldwin J. A. et al., 1996, ApJ, 468, L115
Bally J., Sutherland R. S., Devine D., Johnstone D., 1998, AJ, 116, 293
Bally J., O'Dell C. R., McCaughrean M. J., 2000, AJ, 119, 2919
Bally J., Licht D., Smith N., Walawender J., 2006, AJ, 131, 473
Bautista M. A., Peng J., Pradhan A. K., 1996, ApJ, 460, 372
Beckwith S. V. W., Henning T., Nakagawa Y., 2000, in Mannings V., Boss A. P., Russell S. S., eds, Protostars and Planets IV. Univ. Arizona Press, Tucson, p. 533,
Berg D. A., Pogge R. W., Skillman E. D., Croxall K. V., Moustakas J., Rogers N. S. J., Sun J., 2020, ApJ, 893, 96
Binder B. A., Povich M. S., 2018, ApJ, 864, 136
Binette L., Matadamas R., Hägele G. F., Nicholls D. C., Magris C. G., Peña-Guerrero M. Á., Morisset C., Rodríguez-González A., 2012, A&A, 547, A29
Birnstiel T., Fang M., Johansen A., 2016, Space Sci. Rev., 205, 41
Blagrave K. P. M., Martin P. G., Baldwin J. A., 2006, ApJ, 644, 1006
Blagrave K. P. M., Martin P. G., Rubin R. H., Dufour R. J., Baldwin J. A., Hester J. J., Walter D. K., 2007, ApJ, 655, 299
Böhm K.-H., Matt S., 2001, PASP, 113, 158
Boyden R. D., Eisner J. A., 2020, ApJ, 894, 74

D'Odorico S., Cristiani S., Dekker H., Hill V., Kaufer A., Kim T., Primas F., 2000, in Bergeron J., ed., Proc. SPIE Conf. Ser. Vol. 4005, Discoveries and Research Prospects from 8- to 10-Meter-Class Telescopes. SPIE, Bellingham, p. 121
Del Zanna G., Dere K. P., Young P. R., Landi E., 2021, ApJ, 909, 38
Duchêne G., Lacour S., Moraux E., Goodwin S., Bouvier J., 2018, MNRAS, 478, 1825
Eisner J. A. et al., 2018, ApJ, 860, 77
Esteban C., Peimbert M., García-Rojas J., Ruiz M. T., Peimbert A., Rodríguez M., 2004, MNRAS, 355, 229
Esteban C., Carigi L., Copetti M. V. F., García-Rojas J., Mesa-Delgado A., Castañeda H. O., Péquignot D., 2013, MNRAS, 433, 382
Froese Fischer C., Tachiev G., Irimia A., 2006, At. Data Nucl. Data Tables, 92, 607
Galavis M. E., Mendoza C., Zeippen C. J., 1995, A&AS, 111, 347
García-Rojas J., Esteban C., Peimbert M., Rodríguez M., Ruiz M. T., Peimbert A., 2004, ApJS, 153, 501
García-Rojas J., Esteban C., Peimbert A., Peimbert M., Rodríguez M., Ruiz M. T., 2005, MNRAS, 362, 301
García-Rojas J., Esteban C., Peimbert M., Costado M. T., Rodríguez M., Peimbert A., Ruiz M. T., 2006, MNRAS, 368, 253
García-Rojas J., Esteban C., Peimbert A., Rodríguez M., Peimbert M., Ruiz M. T., 2007, Rev. Mex. Astron. Astrofis., 43, 3
Giannini T., Antoniucci S., Nisini B., Bacciotti F., Podio L., 2015, ApJ, 814, 52
Gil de Paz A. et al., 2018, in Evans C. J., Simard L., Takami H., eds, Proc. SPIE Conf. Ser. Vol. 10702, Ground-based and Airborne Instrumentation for Astronomy VII. SPIE, Bellingham, p. 1070217
Gil De Paz A., Pascual S., Chamorro-Cazorla M., 2020, guaix-ucm/megara-tools: Release v0.1.1.
Grieve M. F. R., Ramsbottom C. A., Hudson C. E., Keenan F. P., 2014, ApJ, 780, 110
Hanuschik R. W., 2003, A&A, 407, 1157
Hartigan P., Hillenbrand L. A., Matuszewski M., Borges A. C., Neill J. D., Martin D. C., Morrissey P., Moore A. M., 2020, AJ, 160, 165
Hasegawa Y. et al., 2022, ApJ, 926, L23
Heise C., Smith P. L., Calamai A. G., 1995, ApJ, 451, L41
Henney W. J., Arthur S. J., 1998, AJ, 116, 322
Henney W. J., O'Dell C. R., 1999, AJ, 118, 2350
Henney W. J., O'Dell C. R., Meaburn J., Garrington S. T., López J. A., 2002, ApJ, 566, 315
Henney W. J., O'Dell C. R., Zapata L. A., García-Díaz M. T., Rodríguez L. F., Robberto M., 2007, AJ, 133, 2192
Hester J. J. et al., 1996, AJ, 111, 2349
Hillenbrand L. A., 1997, AJ, 113, 1733
Hudson C. E., Ramsbottom C. A., Scott M. P., 2012, ApJ, 750, 65
Jenkins E. B., 2009, ApJ, 700, 1299
Johnstone D., Hollenbach D., Bally J., 1998, ApJ, 499, 758
Juan de Dios L., Rodríguez M., 2017, MNRAS, 469, 1036
Kama M., Shorttle O., Jermyn A. S., Folsom C. P., Furuya K., Bergin E. A., Walsh C., Keller L., 2019, ApJ, 885, 114
Kaufman V., Sugar J., 1986, J. Phys. Chem. Ref. Data, 15, 321
Kim D., Lu J. R., Konopacky Q., Chu L., Toller E., Anderson J., Theissen C. A., Morris M. R., 2019, AJ, 157, 109
Kunth D., Sargent W. L. W., 1983, ApJ, 273, 81
LaJohn L., Luke T. M., 1993, Phys. Scr, 47, 542
Laques P., Vidal J. L., 1979, A&A, 73, 97
Lee C.-F., Ho P. T. P., Li Z.-Y., Hirano N., Zhang Q., Shang H., 2017, Nat. Astron., 1, 0152
Lodders K., 2019, preprint (arXiv:1912.00844)
Luridiana V., Morisset C., Shaw R. A., 2015, A&A, 573, A42
McBride A., Kounkel M., 2019, ApJ, 884, 6
Méndez-Delgado J. E., Esteban C., García-Rojas J., Henney W. J., Mesa-Delgado A., Arellano-Córdova K. Z., 2021a, MNRAS, 502, 1703 (Paper I)
Méndez-Delgado J. E., Henney W. J., Esteban C., García-Rojas J., Mesa-Delgado A., Arellano-Córdova K. Z., 2021b, ApJ, 918, 27 (Paper II)
Mendoza C., Zeippen C. J., 1982, MNRAS, 199, 1025
Mesa-Delgado A., Esteban C., García-Rojas J., Luridiana V., Bautista M., Rodríguez M., López-Martín L., Peimbert M., 2009, MNRAS, 395, 855
Moehler S., Dreizler S., LeBlanc F., Khalack V., Michaud G., Richer J., Sweigart A. V., Grundahl F., 2014a, A&A, 565, A100
Moehler S. et al., 2014b, A&A, 568, A9
Nisini B., Caratti o Garatti A., Giannini T., Lorenzetti D., 2002, A&A, 393, 1035
Noll S., Kausch W., Barden M., Jones A. M., Szyszka C., Kimeswenger S., Vinther J., 2012, A&A, 543, A92
O'Dell C. R., Henney W. J., 2008, AJ, 136, 1566
O'Dell C. R., Wen Z., 1994, ApJ, 436, 194
O'Dell C. R., Wen Z., Hu X., 1993, ApJ, 410, 696
O'Dell C. R., Ferland G. J., Henney W. J., Peimbert M., García-Díaz M. T., Rubin R. H., 2015, AJ, 150, 108
Pascual S., Cardiel N., Gil de Paz A., Carasco E., Gallego J., Iglesias-Páramo J., Cedazo R., 2019, in Montesinos B., Asensio Ramos A., Buitrago F., Schödel R., Villaver E., Pérez-Hoyos S., Ordóñez-Etxeberria I., eds, Highlights on Spanish Astrophysics X. p. 227
Pascual S., Cardiel N., Picazo-Sanchez P., Castillo-Morales A., Gil De Paz A., 2021, guaix-ucm/megaradrp: v0.11
Pinilla P., Benisty M., Birnstiel T., 2012, A&A, 545, A81
Platais I. et al., 2020, AJ, 159, 272
Podio L., Medves S., Bacciotti F., Eislöffel J., Ray T., 2009, A&A, 506, 779
Podobedova L. I., Kelleher D. E., Wiese W. L., 2009, J. Phys. Chem. Ref. Data, 38, 171
Robberto M. et al., 2013, ApJS, 207, 10
Rodenkirch P. J., Dullemond C. P., 2022, A&A, 659, A42
Rodríguez M., 2002, A&A, 389, 556
Rodríguez M., 2020, MNRAS, 495, 1016
Rodríguez M., Rubin R. H., 2005, ApJ, 626, 900
Smith N., Bally J., Shuping R. Y., Morris M., Kassis M., 2005, AJ, 130, 1763
Sota A., Maíz Apellániz J., Walborn N. R., Alfaro E. J., Barbá R. H., Morrell N. I., Gamen R. C., Arias J. I., 2011, ApJS, 193, 24
Tayal S. S., 1997, At. Data Nucl. Data Tables, 67, 331
Tayal S. S., Gupta G. P., 1999, ApJ, 526, 544
Tayal S. S., Zatsarinny O., Sossah A. M., 2019, ApJS, 242, 9
Theissen C. A., Konopacky Q. M., Lu J. R., Kim D., Zhang S. Y., Hsu C.-C., Chu L., Wei L., 2022, ApJ, 926, 141
Tobin J. J., Hartmann L., Furesz G., Mateo M., Megeath S. T., 2009, ApJ, 697, 1103
Tody D., 1993, in Hanisch R. J., Brissenden R. J. V., Barnes J., eds, ASP Conf. Ser. 52, IRAF in the Nineties. Astron. Soc. Pac., San Francisco, p. 173
Vicente S., Berné O., Tielens A. G. G. M., Huélamo N., Pantin E., Kamp I., Carmona A., 2013, ApJ, 765, L38
Weilbacher P. M. et al., 2015, A&A, 582, A114
Williams J. P., Andrews S. M., Wilner D. J., 2005, ApJ, 634, 495

SUPPORTING INFORMATION

Supplementary data are available at *MNRAS* online.

Table A1. Sample of 15 lines of the HH 514 jet base spectrum.

Please note: Oxford University Press is not responsible for the content or functionality of any supporting materials supplied by the authors. Any queries (other than missing material) should be directed to the corresponding author for the article.

APPENDIX A: SOME EXTRA MATERIAL

Table A1. Sample of 15 lines of the HH 514 jet base spectrum. All line intensity ratios are referred to F(H β) or I(H β) = 100. This is an example of the content found in the supplementary material for all spectra.

λ_0 (Å)	Ion	λ_{obs}(Å)	v_r (km s^{-1})	FWHM (km s^{-1})	F(λ)/F(H β)	I(λ)/I(H β)	Error per cent	Notes
4363.21	[O III]	4365.44	153	19.7 ± 1.4	2.10	2.48	6	
4471.47	He I	4473.78	155	22.4 ± 1.1	4.00	4.54	4	
4596.84	[Ni III]	4599.38	166	10 ± 6	0.24	0.26	38	
4607.12	[Fe III]	4609.42	150	19.8 ± 2.0	1.50	1.62	8	
4658.17	[Fe III]	4660.51	151	18.85 ± 0.07	16.85	18.0	2	
4667.11	[Fe III]	4669.40	147	24.5 ± 2.5	1.69	1.80	8	
4701.64	[Fe III]	4704.00	150	19.4 ± 0.4	8.27	8.69	3	
4734.00	[Fe III]	4736.33	148	21.5 ± 1.2	4.18	4.34	4	
4754.81	[Fe III]	4757.19	150	19.6 ± 1.0	3.39	3.50	4	
4769.53	[Fe III]	4771.92	150	20.4 ± 0.8	3.36	3.45	5	
4777.70	[Fe III]	4780.16	154	17.6 ± 1.7	2.06	2.12	7	
4814.54	[Fe II]	4817.00	153	17 ± 6	0.50	0.51	22	
4861.32	H I	4863.81	154	27.74 ± 0.27	100.0	100.0	2	
4881.07	[Fe III]	4883.58	154	18.4 ± 0.8	4.18	4.15	4	
4930.64	[Fe III]	4933.18	154	20.8 ± 3.4	1.56	1.53	12	blend with [O III] 4931.23

Table A2. [S III] line intensity ratios with a common upper level observed in this paper and other objects from the literature and predicted by theoretical models.

Reference	3722/6312	9531/9069	9531/8829	9069/8829
		Orion Nebula		
Esteban et al. (2004)	–	2.39 ± 0.51	5600 ± 1300	2300 ± 500
Mesa-Delgado et al. (2009)	–	2.32 ± 0.19	–	–
Méndez-Delgado et al. (2021a) Cut 1	0.60 ± 0.03	2.65 ± 0.24	8400 ± 1200	3200 ± 500
Méndez-Delgado et al. (2021a) Cut 2	–	2.84 ± 0.27	7700 ± 900	2730 ± 310
Méndez-Delgado et al. (2021a) Cut 3	–	2.88 ± 0.26	8300 ± 1100	2900 ± 400
Méndez-Delgado et al. (2021a) Cut 4	–	2.50 ± 0.24	7700 ± 1300	3100 ± 500
Méndez-Delgado et al. (2021b) Cut 1 + NIL	–	2.43 ± 0.18	5800 ± 700	2400 ± 270
Méndez-Delgado et al. (2021b) Cut 2	–	2.44 ± 0.22	6800 ± 1200	2800 ± 500
Méndez-Delgado et al. (2021b) NIL	–	2.65 ± 0.46	–	–
This work Cut 2	0.64 ± 0.02	2.69 ± 0.28	7800 ± 1100	2900 ± 400
This work Cut 3	–	2.60 ± 0.27	7400 ± 1000	2800 ± 400
		Photoionized Herbig–Haro Objects		
Mesa-Delgado et al. (2009) HH 202 S	–	2.54 ± 0.22	–	–
Méndez-Delgado et al. (2021a) HH 529 II	–	2.46 ± 0.22	7500 ± 1800	3100 ± 700
Méndez-Delgado et al. (2021a) HH 529 III	–	2.45 ± 0.29	–	–
Méndez-Delgado et al. (2021b) HH 204	–	2.39 ± 0.14	8700 ± 1000	3600 ± 400
This work HH 514 jet base	–	2.60 ± 0.32	–	–
This work HH 514 knot	–	2.55 ± 0.38	–	–
		Galactic H II regions		
García-Rojas et al. (2004) NGC 3576	–	–	–	2500 ± 400
García-Rojas et al. (2005) Sh 2-311	–	2.70 ± 0.21	–	–
García-Rojas et al. (2006) M 16	–	2.43 ± 0.29	–	–
García-Rojas et al. (2006) M 20	–	2.29 ± 0.20	–	–
García-Rojas et al. (2006) NGC 3603	–	–	5900 ± 800	–
García-Rojas et al. (2007) M 8	–	–	–	2700 ± 700
García-Rojas et al. (2007) M 17	–	2.51 ± 0.25	–	–
Esteban et al. (2013) NGC 2579	–	2.18 ± 0.12	–	–
Adopted observed value	**0.62 ± 0.03**	**2.45 ± 0.18**	**7200 ± 1200**	**2900 ± 400**
		Theoretical Predictions		
LL93-HSC95-MZ82b-KS86	0.52	5.52	14963	2710
MZ82b-HSC95-LL93	0.61	2.48	9169	3697
FFTI06	0.54	2.47	8471	3431
TZS19	0.50	2.54	5505	2171
CHIANTI	0.53	2.51	8474	3373

Table A3. [S III] λλ9069, 9531 line intensities with respect to H β = 100.0 observed in this paper and other objects from the literature corrected from telluric absorption bands.

Object	λ9069		λ9531		Reference
	Old	New	Old	New	
Orion Nebula Cut 1	19.7 ± 1.0	32.2 ± 1.9	82.8 ± 5.0	84.7 ± 5.9	Méndez-Delgado et al. (2021a)
Orion Nebula Cut 2	20.8 ± 1.3	32.5 ± 2.3	91.1 ± 5.5	91.4 ± 6.4	
Orion Nebula Cut 3	21.8 ± 1.3	31.8 ± 1.9	91.1 ± 6.4	91.4 ± 6.4	
Orion Nebula Cut 4	22.8 ± 1.4	34.1 ± 2.4	82.5 ± 4.9	85.2 ± 6.0	
Orion Nebula + NIL Cut 1	25.4 ± 1.0	28.6 ± 1.4	69.3 ± 2.8	69.3 ± 3.5	Méndez-Delgado et al. (2021b)
Orion Nebula Cut 2	24.8 ± 1.2	30.7 ± 1.8	74.6 ± 4.5	74.6 ± 5.2	
HH 529 II	40.1 ± 2.4		98.5 ± 6.9		Méndez-Delgado et al. (2021a)
HH 529 III	41.1 ± 3.3		100.4 ± 9.0		
HH 204	36.5 ± 1.5		87.2 ± 3.5		
NIL	26.5 ± 2.9	20.7 ± 2.5	60.6 ± 6.7	55.5 ± 6.6	Méndez-Delgado et al. (2021b)

Table A4. T_e ([S III]) and S^{2+} abundance derived with each set of collision strengths and the transition probabilities from FFTI06. The last column has been determined increasing a 40 per cent the Ω_{9531}, Ω_{9069}, and Ω_{8829} values of GRHK14.

	GMZ95	TG99	HRS12	TZS19	GRHK14	Modified GRHK14
			T_e ([S III])			
HH 514 jet base	8370^{+420}_{-450}	7980^{+400}_{-530}	8410^{+350}_{-390}	7900^{+480}_{-170}	8420^{+310}_{-400}	8840^{+500}_{-560}
HH 514 knot	8200^{+520}_{-510}	7820^{+380}_{-490}	8140^{+450}_{-600}	7750^{+310}_{-670}	8230^{+430}_{-560}	8980^{+570}_{-860}
Nebular Cut 2	8850^{+270}_{-320}	8270^{+280}_{-190}	8650^{+270}_{-280}	–	8630^{+330}_{-340}	9860^{+400}_{-470}
			$12 + \log(S^{2+}/H^{+})$			
HH 514 jet base	$7.35^{+0.07}_{-0.06}$	$7.44^{+0.09}_{-0.07}$	7.39 ± 0.06	$7.47^{+0.08}_{-0.07}$	$7.39^{+0.07}_{-0.06}$	$7.25^{+0.08}_{-0.07}$
HH 514 knot	$7.30^{+0.09}_{-0.07}$	$7.39^{+0.09}_{-0.07}$	$7.36^{+0.10}_{-0.08}$	$7.43^{+0.12}_{-0.09}$	$7.35^{+0.10}_{-0.07}$	$7.14^{+0.12}_{-0.09}$
Nebular Cut 2	$6.76^{+0.05}_{-0.04}$	$6.88^{+0.05}_{-0.04}$	$6.86^{+0.05}_{-0.04}$	–	6.86 ± 0.05	$6.60^{+0.06}_{-0.05}$

Table A5. Intensities ratios of selected lines of the spectrum of proplyd 170-337 after subtracting the emission of the Orion Nebula. c(H β) = 1.16 ± 0.14, $F(H\beta) = 2.54 \times 10^{-13}$(erg cm^{-2} s^{-1}).

λ_0 (Å)	Ion	F(λ)/F(H β)	I(λ)/I(H β)	Error per cent
4068.60	[S II]	3.42	4.72	5
4076.35	[S II]	0.95	1.31	5
4363.21	[O III]	2.66	3.31	4
5754.64	[N II]	6.7	4.82	6
5006.84	[O III]	276	260	2
6312.10	[S III]	3.65	2.20	8
6583.46	[N II]	44.4	24.4	8
9530.60	[S III]	180	43	26

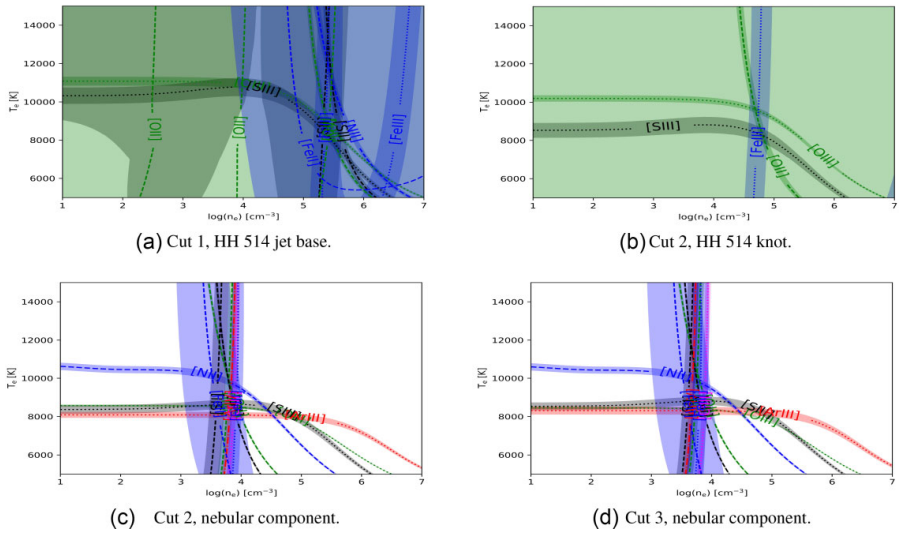

(a) Cut 1, HH 514 jet base. (b) Cut 2, HH 514 knot.

(c) Cut 2, nebular component. (d) Cut 3, nebular component.

Figure A1. Plasma diagnostic plots for the individual analysed components.

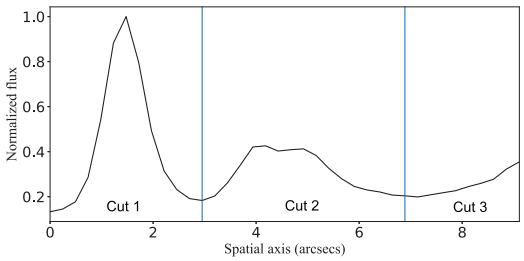

Figure A2. Spatial distribution along the slit of the intensity of [Fe III] λ4658 line centred at a heliocentric velocity of ∼150 km s^{-1}. The emission has been extracted from a window ∼45 km s^{-1} wide.

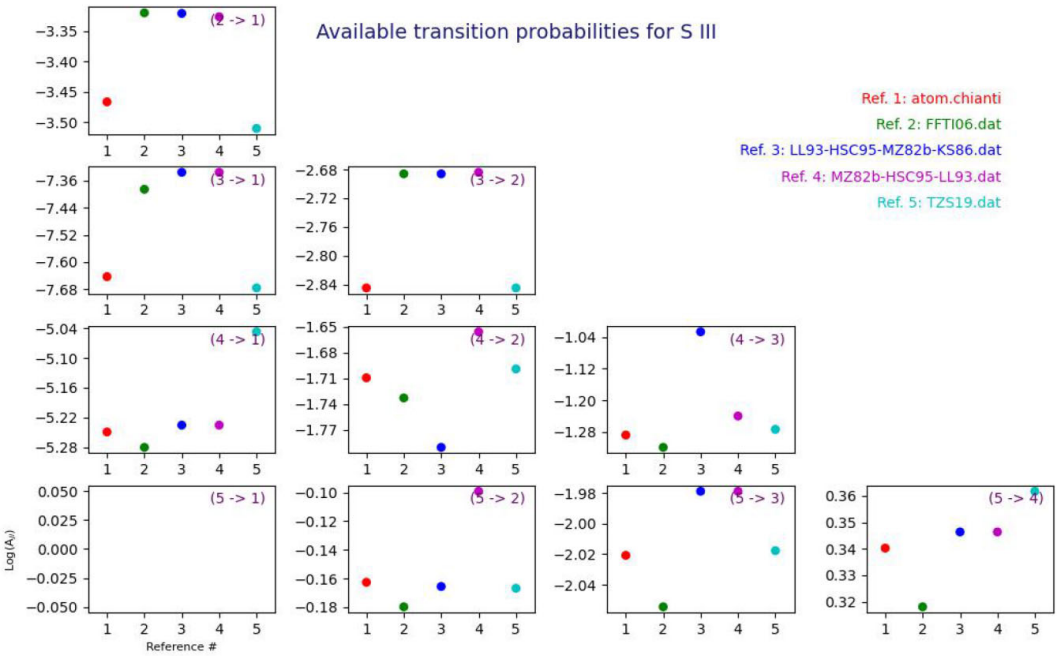

Figure A3. Comparison between the different values of transition probabilities of [S III] transitions given by the references studied in this paper.

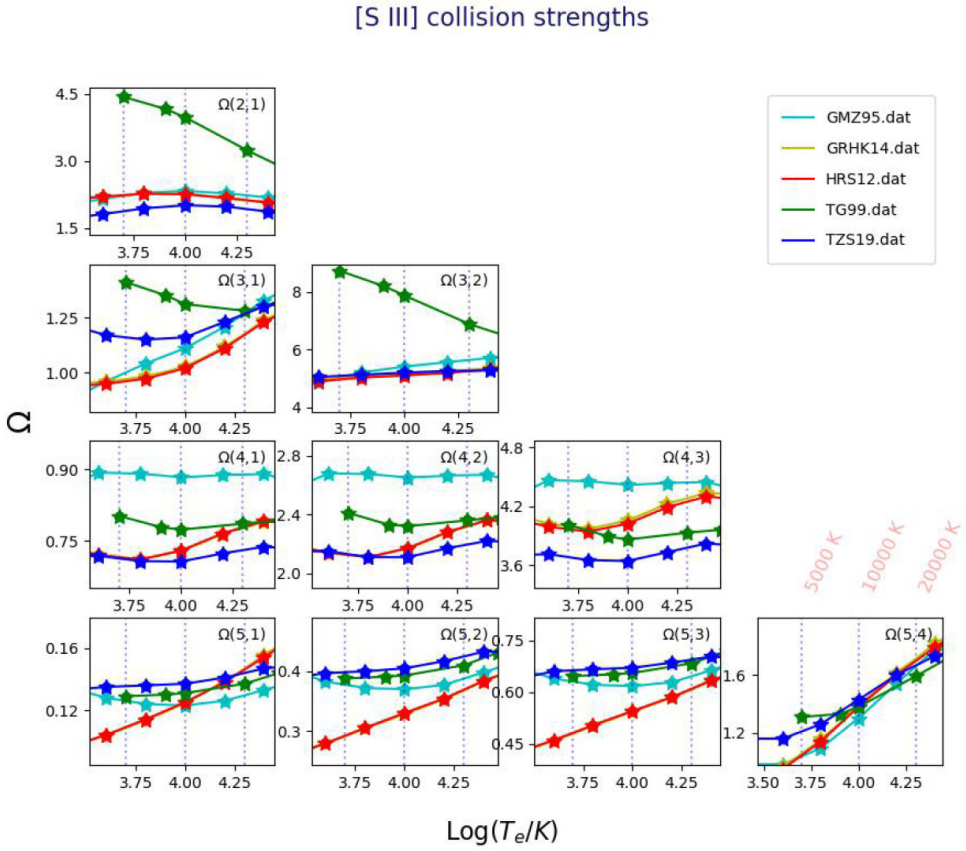

Figure A4. Comparison between the different values of collision strengths of the [S III] transitions given by the references studied in this paper.

This paper has been typeset from a TEX/LATEX file prepared by the author.

6

Conclusions

In this thesis, we analyse a sample of Herbig-Haro (HH) objects flowing within the ionised interior of the Orion Nebula. We mainly use high-spectral resolution spectroscopy from UVES at VLT and high-spatial resolution imaging from HST. Our studies have been presented in a series of refereed papers published in MNRAS and ApJ journals, with the generical title "Photoionized Herbig-Haro objects in the Orion Nebula through deep high-spectral resolution spectroscopy". Each of the three papers are presented in Chapters 3, 4 and 5 of this PhD Thesis and have a large number of individual conclusions on HH529II-III, HH204 and HH514. The interest of some of their results have given rise to several press releases. In this section, I summarise the main results in the global context of this thesis, referring to the objectives presented in Sec. 1.4.

- We show that the ionising radiation field of the Orion Trapezium is sufficient enough to account for most of the ionisation of HH529II-III, HH204 and HH514. This allow us to study their optical spectra as small-scale H II regions. However, some effects of the shock-heating can be observed in the optical emission of some highly ionised species of HH204, which represent less than 1% of the gas. For the HHs of the Huygens region, we estimate that shock contribution to the intensity of [O III] λ5007 (one of the most important optical lines for the cooling of the gas) increases with the propagation velocity up to ~ 20 km s^{-1}, representing up to $\sim 10\%$ of the total flux, after which it starts to decrease. At higher velocities, the post-shock [O III] emission become insensitive to the shock, since the gas cooling is taken mostly by far-ultraviolet (FUV) lines of highly ionised

species such as C III λ1909 or C IV λ1549. For recombination lines such as Hα, the shock heating contribution is negligible as their emissivity decreases with the electron temperature.

- In the HHs, there can be several knots flowing at similar velocities in the frame of reference of the observer. However, their internal velocities with respect to the general jet beam can be different, reaching different match ($\mathcal{M}$) numbers and degrees of compression. This produces density gradients in the observed spectra if each knot is not spatially isolated, which is the most common case, specially in the HHs flowing at small angles with respect to the line of sight. Most of the knots observed in the Orion Nebula have electron densities that exceed the critical densities of some classical diagnostics such as [S II] λ6731/λ6716 or [O II] λ3726/λ3729 ($n_{\rm e} > 10^4$ cm^{-3}). These diagnostics may underestimate the true density of the integrated gas, which can lead to a fictitious overestimation of the temperature. This can be mistakenly interpreted as evidence of shock heating in the optical spectra, which this thesis shows is unlikely in most of the cases, given that the strong radiation field of the Orion Trapezium dominates the ionisation equilibrium.

- The Fe/H and Ni/H ratios in the analysed sample of HHs are higher than the values found in the Orion Nebula. This indicates the destruction of dust grains containing these elements by the shocks. We show that Fe and Ni have similar ionisation and depletion patterns, being $Fe^+/Ni^+ \approx Fe^{2+}/Ni^{2+} \approx$ Fe/Ni. Enhanced emission lines from elements such as Ca and Cr in different ionisation stages were also present in the HHs, suggesting a strong presence of these elements in the destroyed dust. However the calculation of their abundance requires transition probabilities and collision strengths that are still not available. We expect that the existence of our observational spectra stimulate the theoretical study of these atoms. In the case of HH514 there is a high overabundance of S (containing more than two times the solar abundance), probably related to the destruction of S-bearing dust reservoirs, as sulfides.

- In HH529II and HH529III there is a slight ($\sim$ 0.1 dex) overabundance of heavy elements with respect to hydrogen that can not be originated by dust destruction processes because the enhancement also affects noble gases as Ne or Ar. This may indicate the inclusion of H-deficient material in the outer part of the protostellar source of HH529 (probably COUP 666). In the case of HH514, both the jet base and the knot present a very high overabundance of S, which may be related to the destruction

of sulfides accumulated in its source, the protoplanetary disk 170-337. In contrast, HH204 shows consistent abundances with respect to the Orion Nebula in all the elements but Fe and Ni (enhanced by the dust destruction). It is possible that part of the ejected material of the HHs has some chemical inhomogeneities, originated in filtering processes that take place inside the protoplanetary disks. These chemical inhomogeneities can be diluted during the passage of the HHs within the environmental gas, which would explain that HHs closer to their sources such as HH514 and HH529 present larger chemical differences than HH204, which is quite far from its possible origin. This clues should be tested in further analyses.

- Since the shocks that produce HHs compress the gas, increasing the local density, they are able to decrease the local ionisation parameter, and, therefore, the local degree of ionisation of the gas. HH204 is even capable of trap an ionisation front, having a neutral core with strong emissions of neutral species as [O I] or [N I]. The abrupt changes in the physical and ionisation conditions introduced by the presence of some HHs can lead to important errors in the determination of global chemical abundances if they are not properly considered in the calculations. The analysis of a low-resolution spectrum mixing the nebular and the HHs emissions, may give erroneous values of the average physical conditions and chemical abundances that would be not representative of any of the kinematic components. For instance, in the case of HH204 and its nebular surroundings, the classical density diagnostics such as [S II] λ6731/λ6716 or [O II] λ3726/λ3729 underestimate the density, resulting in an overestimate of $T_{\rm e}$, which in turn underestimate most of the chemical abundances, by $\sim$40% in the case of O/H. Since most of the ICF schemes rely on the $O^{2+}/(O^{+}+O^{2+})$ fraction, errors in the total abundances of other elements can be increased.

- Considering the fact that HH objects destroy dust grains and this increases the Fe abundance in the gaseous phase, we propose to use indicators based on ratios of emission lines of this element, such as [Fe III] λ4658/λ4702 to determine more appropriate values of density (and even detect the presence of high-density inclusions) when low-spectral resolution spectra is used. However, other high density clumps such as proplyds, may not emit [Fe III] lines an go unnoticed to this indicator.

- The use of 20 years of HST imaging shows that HH529 is originated in the Orion South region, whereas HH514 is clearly originated in the proplyd 170-337 close to the stars of the Orion Trapezium. The case

of HH204 is more complicated, since at least two different flows may be responsible for driving it. The back-projection of these flows may place the origin of HH204 either at the south of the Orion South or close to the Trapezium. This last scenario had not been considered previously and raises the possibility that the source of HH204 may be a proplyd, as in the case of HH514, which are rather common in that region.

6.1 Future perspectives

This thesis unveiled some internal phenomena of the photoionised HHs of the Orion Nebula, as well as their impact onto the local environment. We have pointed out some global trends that could be relevant in the study of the integrated spectra of H II regions and HH objects. However, some of them require to study a larger sample of objects for their formal demonstration. For instance, we find that the gaseous Fe/H and Ni/H abundances seem to be correlated with the propagation velocity. Nevertheless, more points are required to know if there is a linear trend or a more complex relationship. It is also important to analyse whether the homogeneity of the chemical composition of the HHs (in the less depleted elements) depends on the distance to their sources. A study incluiding more objects could reveal differences between HHs originated from proplyds and those from stellar sources. Finally, this thesis take the first step to analyse the impact of HHs in the study of the integrated spectrum of the Orion Nebula. By using IFU spectra, we can distinguish the spaxels containing HHs, just from the strong emission in [Fe II] or [Fe III] lines that the dust destruction associated with these objects generates. Then, we can compare the derived chemical composition of the Orion Nebula with and without the spaxels with HHs to estimate their impact. An important refinement of this study is to consider the proplyds, whose densities can reach values up to $\sim 10^6$ cm^{-3}, which enhances the emission of T_e-sensitive auroral lines. This study is important to better understand the chemical abundances derived in H II regions in both, Galactic and extragalactic contexts, which are always idealised as Strömgren spheres. Future large scale spectroscopic surveys as the Local Volume Mapper (LVM) of the Sloan Digital Sky Survey (SDSS) V may be key to this future study.

Bibliography

Astropy Collaboration, Price-Whelan, A. M., Sipőcz, B. M., et al. 2018, AJ, 156, 123. doi:10.3847/1538-3881/aabc4f

Astropy Collaboration, Robitaille, T. P., Tollerud, E. J., et al. 2013, A&A, 558, A33. doi:10.1051/0004-6361/201322068

Avila, G., Rupprecht, G., & Beckers, J. M. 1997, Proc. SPIE, 2871, 1135. doi:10.1117/12.269000

Ballester, P., Modigliani, A., Boitquin, O., et al. 2000, The Messenger, 101, 31

Bally, J., Sutherland, R. S., Devine, D., et al. 1998, AJ, 116, 293. doi:10.1086/300399

Bazer, J. & Ericson, W. B. 1959, ApJ, 129, 758. doi:10.1086/146673

Bhatia, A. K. & Kastner, S. O. 1995, ApJS, 96, 325. doi:10.1086/192121

Binder, B. A. & Povich, M. S. 2018, ApJ, 864, 136. doi:10.3847/1538-4357/aad7b2

Blagrave, K. P. M., Martin, P. G., & Baldwin, J. A. 2006, ApJ, 644, 1006. doi:10.1086/503830

Blagrave, K. P. M., Martin, P. G., Rubin, R. H., et al. 2007, ApJ, 655, 299. doi:10.1086/510151

Bohm, K. H. 1983, Rev. Mex. Astron. Astrofis., 7, 55

Butler, K. & Zeippen, C. J. 1989, A&A, 208, 337

Canto, J., Goudis, C., Johnson, P. G., et al. 1980, A&A, 85, 128

Canto, J. 1985, Lecture Notes in Physics, Berlin Springer Verlag, 181. doi:10.1007/3-540-15991-6_92

D'Odorico, S., Cristiani, S., Dekker, H., et al. 2000, Proc. SPIE, 4005, 121. doi:10.1117/12.390133

Esteban, C., Peimbert, M., García-Rojas, J., et al. 2004, MNRAS, 355, 229. doi:10.1111/j.1365-2966.2004.08313.x

Falle, S. A. E. G. & Raga, A. C. 1993, MNRAS, 261, 573. doi:10.1093/mnras/261.3.573

Fehrenbach, C. 1977, A&AS, 29, 71

Ferland, G. J., Henney, W. J., O'Dell, C. R., et al. 2016, Rev. Mex. Astron. Astrofis., 52, 261

Fritzsche, S., Fricke, B., Geschke, D., et al. 1999, ApJ, 518, 994. doi:10.1086/307328

Froese Fischer, C., Tachiev, G., & Irimia, A. 2006, Atomic Data and Nuclear Data Tables, 92, 607. doi:10.1016/j.adt.2006.03.001

Froese Fischer, C. & Tachiev, G. 2004, Atomic Data and Nuclear Data Tables, 87, 1. doi:10.1016/j.adt.2004.02.001

Galavis, M. E., Mendoza, C., & Zeippen, C. J. 1995, A&AS, 111, 347

García-Rojas, J. & Esteban, C. 2007, ApJ, 670, 457. doi:10.1086/521871

Goudis, C. 1982, Astrophysics and Space Science Library, Dordrecht: Reidel, 1982. doi:10.1007/978-94-009-7712-9

Grieve, M. F. R., Ramsbottom, C. A., Hudson, C. E., et al. 2014, ApJ, 780, 110. doi:10.1088/0004-637X/780/1/110

Haro, G. 1952, ApJ, 115, 572. doi:10.1086/145576

Haro, G. 1953, ApJ, 117, 73. doi:10.1086/145669

Hartigan, P., Morse, J. A., & Raymond, J. 1994, ApJ, 436, 125. doi:10.1086/174887

Hartigan, P., Raymond, J., & Hartmann, L. 1987, ApJ, 316, 323. doi:10.1086/165204

Hebb, M. H. & Menzel, D. H. 1940, ApJ, 92, 408. doi:10.1086/144230

Henney, W. J., O'Dell, C. R., Zapata, L. A., et al. 2007, AJ, 133, 2192. doi:10.1086/513074

Henney, W. J. 2002, Rev. Mex. Astron. Astrofis., 38, 71

Herbig, G. H. 1950, ApJ, 111, 11. doi:10.1086/145232

Herbig, G. H. 1951, ApJ, 113, 697. doi:10.1086/145440

Huygens, C. 1659, Cristiani Hugenii... Systema Saturnium sive de causis mirandorum Saturni phaenomenon et comite ejus planeta novo, by Huygens, Christiaan, 1659.. doi:10.3931/e-rara-3178

Kama, M., Shorttle, O., Jermyn, A. S., et al. 2019, ApJ, 885, 114. doi:10.3847/1538-4357/ab45f8

Kaler, J. B. 1967, ApJ, 148, 925. doi:10.1086/149219

Karttunen, H., Kröger, P., Oja, H., et al. 2017, Fundamental Astronomy, ISBN 978-3-662-53044-3. Springer-Verlag Berlin Heidelberg, 2017. doi:10.1007/978-3-662-53045-0

Kaufman, V. & Sugar, J. 1986, Journal of Physical and Chemical Reference Data, 15, 321. doi:10.1063/1.555775

Kisielius, R., Storey, P. J., Ferland, G. J., et al. 2009, MNRAS, 397, 903. doi:10.1111/j.1365-2966.2009.14989.x

Laques, P. & Vidal, J. L. 1979, A&A, 73, 97

Luridiana, V., Morisset, C., & Shaw, R. A. 2015, A&A, 573, A42. doi:10.1051/0004-6361/201323152

Mendoza, C. 1983, Planetary Nebulae, 103, 143

Mesa-Delgado, A., Esteban, C., García-Rojas, J., et al. 2009, MNRAS, 395, 855. doi:10.1111/j.1365-2966.2009.14554.x

Mesa-Delgado, A., Esteban, C., & García-Rojas, J. 2008, ApJ, 675, 389. doi:10.1086/524296

Mundt, R. 1985, Lecture Notes in Physics, Berlin Springer Verlag, 160. doi:10.1007/3-540-15991-6_91

Méndez-Delgado, J. E., Amayo, A., Arellano-Córdova, K. Z., et al. 2022, MNRAS, 510, 4436. doi:10.1093/mnras/stab3782

Méndez-Delgado, J. E., Esteban, C., García-Rojas, J., et al. 2021, MNRAS, 502, 1703. doi:10.1093/mnras/stab068

Méndez-Delgado, J. E., Esteban, C., García-Rojas, J., et al. 2022, MNRAS, 514, 744. doi:10.1093/mnras/stac1300

Méndez-Delgado, J. E., Henney, W. J., Esteban, C., et al. 2021, ApJ, 918, 27. doi:10.3847/1538-4357/ac0cf5

Nisini, B., Antoniucci, S., Alcalá, J. M., et al. 2018, A&A, 609, A87. doi:10.1051/0004-6361/201730834

Núñez-Díaz, M., Mesa-Delgado, A., Esteban, C., et al. 2012, MNRAS, 421, 3399. doi:10.1111/j.1365-2966.2012.20565.x

O'Dell, C. R., Hartigan, P., Bally, J., et al. 1997, AJ, 114, 2016. doi:10.1086/118622

O'Dell, C. R., Hartigan, P., Lane, W. M., et al. 1997, AJ, 114, 730. doi:10.1086/118507

O'Dell, C. R., Wen, Z., & Hu, X. 1993, ApJ, 410, 696. doi:10.1086/172786

O'Dell, C. R. & Wen, Z. 1992, ApJ, 387, 229. doi:10.1086/171074

Osterbrock, D. E. 1958, PASP, 70, 399. doi:10.1086/127245

Osterbrock, D. E. & Ferland, G. J. 2006, Astrophysics of gaseous nebulae and active galactic nuclei, 2nd. ed. by D.E. Osterbrock and G.J. Ferland. Sausalito, CA: University Science Books, 2006

Patra, S., Karr, J.-P., Hilico, L., et al. 2018, Journal of Physics B Atomic Molecular Physics, 51, 024003. doi:10.1088/1361-6455/aa9b92

Pauli, W. 1925, Zeitschrift fur Physik, 31, 765. doi:10.1007/BF02980631

Peimbert, M., Luridiana, V., & Peimbert, A. 2007, ApJ, 666, 636. doi:10.1086/520571

Peimbert, M. 1967, ApJ, 150, 825. doi:10.1086/149385

Podobedova, L. I., Kelleher, D. E., & Wiese, W. L. 2009, Journal of Physical and Chemical Reference Data, 38, 171. doi:10.1063/1.3032939

Raga, A. C., Cantó, J., & Rodríguez-González, A. 2020, The Physics of the Interstellar Medium. Online Book

Raga, A. C., Canto, J., Binette, L., et al. 1990, ApJ, 364, 601. doi:10.1086/169443

Raga, A. C., Reipurth, B., Castellanos-Ramírez, A., et al. 2015, AJ, 150, 105. doi:10.1088/0004-6256/150/4/105

Reipurth, B. & Bally, J. 2001, ARA&A, 39, 403. doi:10.1146/annurev.astro.39.1.403

Schwartz, R. D. 1983, ARA&A, 21, 209. doi:10.1146/annurev.aa.21.090183.001233

Schwartz, R. D. 1975, ApJ, 195, 631. doi:10.1086/153364

Spitzer, L. 1949, ApJ, 109, 337. doi:10.1086/145141

Storey, P. J., Sochi, T., & Badnell, N. R. 2014, MNRAS, 441, 3028. doi:10.1093/mnras/stu777

Storey, P. J. & Hummer, D. G. 1995, MNRAS, 272, 41. doi:10.1093/mnras/272.1.41

Storey, P. J. & Hummer, D. G. 1995, MNRAS, 272, 41. doi:10.1093/mnras/272.1.41

Storey, P. J. & Zeippen, C. J. 2000, MNRAS, 312, 813. doi:10.1046/j.1365-8711.2000.03184.x

Strömgren, B. 1939, ApJ, 89, 526. doi:10.1086/144074

Tayal, S. S. 2011, ApJS, 195, 12. doi:10.1088/0067-0049/195/2/12

Tayal, S. S. & Zatsarinny, O. 2010, ApJS, 188, 32. doi:10.1088/0067-0049/188/1/32

Taylor, K. & Munch, G. 1978, A&A, 70, 359

Tody, D. 1993, Astronomical Data Analysis Software and Systems II, 52, 173

Wiese, W. L., Fuhr, J. R., & Deters, T. M. 1996, Atomic transition probabilities of carbon, nitrogen, and oxygen : a critical data compilation. Edited by W.L. Wiese, J.R. Fuhr, and T.M. Deters. Washington, DC : American Chemical Society ... for the National Institute of Standards and Technology (NIST) c1996. QC 453 .W53 1996. Also Journal of Physical and Chemical Reference Data, Monograph 7. Melville, NY: AIP Press

Zel'dovich, Y. B. & Raizer, Y. P. 1967, New York: Academic Press, 1966/1967, edited by Hayes, W.D.; Probstein, Ronald F.

Agradecimientos

Cuando llegué al camino de la física, nada fue más grato que encontrarme con sabios profesores y amistades nobilísimas. Agradezco a la Dra. Magali Folch por haberme presentado a los Drs. William Lee y Manuel Peimbert. Sin duda, esto fue un hecho crucial para descubrir mi vocación por la Astronomía. Reconozco a Manuel por haberme enseñado tanto durante los años en que fui su ayudante de investigación. Mi reconocimiento trasciende la esfera académica, pues tengo bien presente su calidad humana y su preocupación por los problemas nacionales. Quiero destacar mi profunda admiración por la Dra. Silvia Torres quien, a través del ejemplo y las palabras, me impulsó a buscar la excelencia en aras del desarrollo humano. Tuve la fortuna de contar con el apoyo de la Dra. Catalina Stern para asistir a conferencias, escuelas y congresos y así explotar todas mis capacidades e intereses.

Llegar a las Islas Canarias fue una gran aventura. En ella tienen un espacio destacado los Drs. César Esteban y Jorge García Rojas. A ellos agradezco su mentoría y sobre todo su amistad. Fueron varios años de buenos momentos y charlas exquisitas sobre todos los temas, desde la física hasta la historia. En esta travesía conocí a mi amiga, la Dra. Karla Arellano, quien siempre me hizo sentir cercano a la idiosincrasia mexicana. Tengo la bendición de contar con muchos y muy buenos amigos. Mis notables camaradas, Pablo Aguilar, Pedro Derrant, Francisco Morales, Omar Apud, Juan Tafoya, Diana Pineda, Ayoze Álvarez, Alberto Álvarez Saavedra, Paul González y Romeo Barajas merecen una mención especial por su fraternidad y presencia durante los años de tesis. La brevedad de mis palabras contrasta con el gran cariño que les tengo.

La vida me brindó la riqueza de contar con una familia amorosa. A ellos les debo más de lo que pudiese pagar y gracias a sus sacrificios este trabajo se ha materializado. A mis padres Ricardo y Margarita, a mis hermanos Gemma y Ricardo y a mi primo Bladimir les dedico estas líneas con todo mi corazón. A Žofia le agradezco estar presente en momentos muy difíciles.

Finalmente, destaco el compromiso y apoyo institucional de México y España a lo largo de mis estudios profesionales, desde la licenciatura hasta el doctorado. Sin la educación pública, laica, gratuita y de calidad de la Universidad Nacional Autónoma de México (UNAM) y los fondos del Consejo Nacional de Ciencia y Tecnología (CONACyT) esto no hubiese sido posible. El Instituto de Astrofísica de Canarias (IAC) y la Universidad de La Laguna (ULL) me brindaron las herramientas educativas y financieras para desarrollar las investigaciones plasmadas en este trabajo.

José Eduardo Méndez Delgado